

Impact of Alkali Treatments on the Surface and Interface Properties of Chalcopyrite Thin-Film Solar Cell Absorbers

Von der Fakultät 1 - MINT - Mathematik, Informatik, Physik,
Elektro- und Informationstechnik
der Brandenburgischen Technischen Universität Cottbus–Senftenberg
zur Erlangung des akademischen Grades eines

Doktors der Naturwissenschaften

(Dr. rer. nat)

genehmigte Dissertation
vorgelegt von

M.Sc.

Penghui Yang

geboren am 06.02.1988 in Shandong, China

Vorsitzender: Prof. Dr. Götz Seibold

Gutachter: Prof. Dr. Ingo Flege

Gutachter: Prof. Dr. Marcus Bär

Tag der mündlichen Prüfung: 19. Mai 2020

Abstract

This thesis focuses on the investigation and characterization of the surfaces and interfaces of chalcopyrite-based Cu(In,Ga)Se₂ (CIGSe) thin film solar cells using various x-ray and electron spectroscopies. In particular, the impact of alkali post deposition treatments (PDT) on the chemical and electronic surface and interface structure of CdS/CIGSe absorbers is studied.

The structure of “real world” CdS/CIGSe interfaces and how they are impacted by different alkali PDTs was investigated by a combination of different x-ray spectroscopies. The interface formation is characterized by studying sample sets with different CdS thicknesses. The chemical environment for indium and cadmium is revealed by deriving the modified Auger parameter $\alpha'(In)$ and $\alpha'(Cd)$ using the kinetic energy of most prominent Auger line together with the binding energy of the chosen core level. A more complex situation is found for CdS/CIGSe samples that underwent NaF+KF PDT, where a K-In-Se compound is initially present on top of the chalcopyrite absorber. The conversion of the K-In-Se type species into a Cd-In-(O,OH,S,Se) interface compound is recorded at short CBD-CdS deposition times. It appears the majority of K that is present at the surface of the NaF+KF PDT CIGSe absorber is dissolved in the CBD and partially re-deposited as K-O type species. The Cd/S ratio clearly deviates from the stoichiometry expected for CdS, and a Cd(O,OH,S)-like compound is likely formed. The electronic structure of CdS/CIGSe interface is similarly more complex for the NaF+KF PDT compared to the NaF PDT case, where only Cd(O,OH,S) buffer was formed.

In an attempt to shed more light into this complex situation, the impact of evaporated alkali metals (K, Rb, Cs) on the surface structure of CIGSe was studied in-system by synchrotron-based hard x-ray photoelectron spectroscopy (HAXPES), aiming at understanding the underlying mechanism of the interfacial effect of alkalis on the performance of CIGSe devices. In the case of K deposition, two K species are observed by x-ray absorption near-edge structure (XANES) and HAXPES, one of which species disappears at high annealing temperature. Furthermore, three new In contributions (In-O and K-In-Se, metallic In species) can be observed after K evaporation. The evolution of

chemical contribution supports the formation of a K-In-Se and Cu-poor CIGSe (1:3:5) bilayer structure that is similar to what was reported for “real world” NaF+KF PDTs. Deposition of heavy alkali metals (Rb, Cs) induced the formation of alkali selenide phases after alkali evaporation and during low temperature annealing. Similar chemical changes as seen for the K composition (i.e. presence of metallic In, In-O, and alkali-O) are observed. However, detailed analysis of the Alk/Se ratio and composition provide direct evidence for the formation of a Alk-(In)-Se and (Cu,Alk)(In, Ga)Se₂ bilayer.

The insights from these studies promise to provide crucial aid to fully exploit alkali pre-treatments in scientific and industrial CIGSe production, and will deliberate use of this means of surface/interface tailoring to push efficiencies even further.

Zusammenfassung

Diese Dissertation konzentriert sich auf die Untersuchung und Charakterisierung der Ober- und Grenzflächen in Chalkopyrit-basierten Cu(In,Ga)Se_2 (CIGSe) Dünnschicht-Solarzellen mit verschiedenen Röntgen- und Elektronenspektroskopien. Insbesondere werden die Auswirkungen von Alkali-Nachbehandlungen (post deposition treatments, PDT) auf die chemischen und elektronischen Oberflächen- und Grenzflächenstrukturen in CdS/CIGSe Schichtstapeln untersucht. Die Eigenschaften von "realen" CdS/CIGSe Grenzflächen und wie verschiedene Alkali-PDTs diese beeinflussen, wurde durch eine Kombination verschiedener Röntgenspektroskopien untersucht. Die Ausbildung der Grenzfläche wurde mittels einer CdS-Dickenserie untersucht. Die chemische Umgebung von Indium und Cadmium wurde durch die Betrachtung der modifizierten Auger-Parameter $\alpha'(\text{In})$ und $\alpha'(\text{Cd})$ identifiziert. Für CdS/CIGSe-Proben bei denen der CIGSe Absorber vor der CdS Abscheidung einer NaF+KF PDT unterzogen wurde finden wir eine komplizierte Grenzflächenstruktur. Die K-In-Se-Verbindung die sich durch das PDT zunächst auf dem Chalkopyritabsorber ausbildet wandelt sich in der Anfangsphase der CdS Abscheidung im chemischen Bad in eine Cd-In-(O,OH,S,Se) Grenzflächenverbindung um. Zudem scheint es, dass die Mehrheit des vorhandenen Kalium, sich im chemischen Bad löst und teilweise als K-O Verbindung wieder auf dem CIGSe Absorber abgelagert wird. Das Cd/S Verhältnis weicht deutlich von der für CdS erwarteten Stöchiometrie ab, und es bildet sich wahrscheinlich eine Cd(O,OH,S) ähnliche Verbindung für lange Abscheidezeiten aus. Die elektronische Struktur der CdS/CIGSe Grenzfläche ist für den NaF+KF PDT Fall ähnlich komplexer als im NaF PDT-Fall, wo wir quasi eine abrupte Grenzfläche zwischen Absorber und Cd(O,OH,S) Puffer finden.

Um mehr Licht in diese komplexe Situation zu bringen, wurden entsprechende Modellsystem untersucht. Hierfür wurden die Alkalimetalle (K, Rb, Cs) direkt auf die Oberflächenstruktur von CIGSe aufgedampft und im gleichen Vakuumsystem mittels synchrotron-basierter Hart-Röntgen-Photoelektronenspektroskopie (HAXPES) untersucht. Nach der Abscheidung von Kalium konnten wir zwei K Spezies identifizieren, von denen eine bei hohen Temperaturen thermischer Nachbehandlung verschwindet. Darüber hinaus können drei neue In-Verbindungen (In-O und K-

In-Se, metallisches In) nach der Abscheidung von K beobachtet werden. Die Entwicklung der chemischen Struktur mit höher werdenden Temperaturen während der thermischen Nachbehandlung unterstützt das Bild einer K-In-Se/Cu-arme CIGSe (1:3:5) Doppelschicht-Struktur – ist also ganz ähnlich was für “reale” NaF+KF PDT CIGSe Proben berichtet wird. Die Abscheidung von schweren Alkalimetallen (Rb, Cs) induziert die Bildung von Alkaliselenidphasen. Ähnliche chemische Veränderungen wie im K-Experiment (d.h. Vorhandensein von metallischem In, In-O und Alkali-O) werden auch hier beobachtet. Eine detaillierte Analyse des Alk/Se-Verhältnisses und der Zusammensetzung liefert jedoch direkte Beweise für die Bildung einer Alk-(In)-Se/(Cu,Alk)(In, Ga)Se₂ Doppelschicht.

Die Erkenntnisse aus dieser Arbeit können dazu beitragen, Alkali-Vorbehandlungen auch in der industriellen CIGSe-Produktion einzusetzen und voll auszuschöpfen. Ein bewusstes Nutzen der identifizierten Oberflächen-/Grenzflächenanpassung könnte die Wirkungsgrade entsprechender Solarzellen sogar noch steigern.

Declaration of Academic Integrity

I declare that this dissertation titled

**'Impact of Alkali Treatments on the Surface and Interface Properties of Chalcopyrite
Thin-Film Solar Cell Absorbers'**

and the work presented in it are my own. I confirm that this work was done wholly or mainly while in candidature for a research degree at this University. No part of this thesis has previously been submitted for a degree or any other qualification at this University or any other institution. This thesis is my first submission for a PhD degree at any institution. Where I have consulted the published work of others, this is always clearly attributed. Where I have quoted from the work of others, the source is always given. With the exception of such quotations, this thesis is entirely my own work. I have acknowledged all main sources of help. Already published or submitted parts of this thesis are clearly indicated.

Place, Date

Penghui Yang

Contents

Abstract	I
Zusammenfassung	III
Declaration of Academic Integrity	V
Contents	VII
1. Introduction	1
2. (Thin-film) photovoltaics considerations	3
2.1 Chalcopyrite-based thin film solar cells	3
2.1.1 Physical principles of solar cell devices.....	3
2.1.2 Characterization of solar cell devices.....	4
2.2 Device structure	5
2.2.1 Substrates	6
2.2.2 Back contact	6
2.2.3 Absorber layer	7
2.2.4 Buffer layer.....	8
2.2.5 Front contact	8
2.3 Chalcopyrite absorber properties	9
2.4 Sample preparation	9
2.5 Motivation and background	10
3. Experimental methods	13
3.1 Photoelectron spectroscopy (PES)	14
3.2 X-ray Auger electron spectroscopy (XAES)	16
3.3 X-ray emission spectroscopy (XES) and X-ray absorption spectroscopy (XAS)	17
3.4 Instrument and experimental setups	18
3.4.1 Lab-based instrument.....	18
3.4.2 Synchrotron-based instrument	19
3.4.2.1 Synchrotron radiation.....	19
3.4.2.2 Instrumentation and experimental details	23
3.5 Data analysis	24

3.5.1 Peak fitting and analysis details.....	24
3.5.2 Analysis details.....	25
4. Impact of NaF PDT and NaF+KF PDT on the chemical and electronic structure of CdS/Cu(In, Ga)Se₂ thin film solar cell absorbers	27
4.1 Introduction.....	27
4.2 Impact of KF PDT on Cu(In,Ga)Se ₂ surface.....	28
4.2.1 Surface chemical structure.....	28
4.2.2 Modified auger parameter analysis.....	30
4.3 Impact of KF PDT on CdS/Cu(In,Ga)Se ₂ interface.....	34
4.3.1 Interface chemical structure.....	34
4.3.1.1 Survey and detail spectra.....	34
4.3.1.2 “CdS” thickness calculation.....	40
4.3.1.3 Modified auger parameter analysis.....	43
4.3.1.3.1 Indium modified auger parameter analysis.....	45
4.3.1.3.2 Cadmium modified auger parameter analysis.....	48
4.3.2 Soft X-ray emission spectroscopy.....	54
4.3.2.1 Se M _{4,5} X-ray emission spectroscopy.....	54
4.3.2.2 S L _{2,3} and Se M _{2,3} X-ray emission spectroscopy.....	58
4.3.4 Summary.....	64
4.4 Impact of alkali treatments on the electronic structure of CdS/CIGSe interface.....	65
4.4.1 Valence band spectra.....	65
4.4.2 Interface energy level alignment.....	67
4.4.3 Summary.....	73
5. Impact of alkalis on the surface structure of Cu(In,Ga)Se₂ studied on in-system prepared model systems	75
5.1 Sample preparation.....	76
5.1.1 Argon treatment.....	76
5.1.2 Alkali evaporation.....	76
5.1.3 Annealing treatment.....	77
5.2 HAXPES spectra comparison.....	78
5.3 Impact of potassium treatments on the chemical structure of CIGSe absorbers.....	82

5.3.1 X-ray absorption of the potassium K-edge	82
5.3.2 Surface chemical structure.....	83
5.3.3 Direct chemical structure comparison with CIGSe samples undergoing NaF+KF PDT	91
5.4 Impact of rubidium/cesium treatments on the chemical and electronic structure of CIGSe absorbers.....	93
5.4.1 Surface chemical structure.....	93
5.4.2 Detail evolution of chemical composition upon Rb/Cs deposition	102
5.4.3 Direct chemical structure comparison with RbF-PDT CIGSe (CIGSe ^{RbF}) samples	110
5.5 Electronic structure of alkali/CIGSe (Alkali= K, Rb, Cs) and direct comparison with PDT CIGSe samples	112
5.6 Summary.....	115
6. Conclusion and Outlook	117
Appendix	121
A.1. Direct In MNN spectra comparison	121
A.2. Cu 3p background correction	122
A.3 HAXPES spectra	127
A.3.1 HAXPES survey spectra	127
A.3.2 Direct comparison of HAXPES VBM spectra.....	128
B.1 In 4p background correction for K/CIGSe series.....	130
B.2 Cross sections.....	131
B.3 In 4p background correction for Rb/CIGSe and Cs/CIGSe sample series	132
B.4 Cu 3p fitting spectra of Rb/CIGSe sample series	134
B.5 The direct comparison of realigned-VBM spectra for alk/CIGSe and PDTs CIGSe samples....	135
Bibliography	137
Acknowledgements	147

1. Introduction

The growing energy demand of human society is forcing us to seek new, reliable energy sources. It is well-known that greenhouse gas emissions will lead to significant global warming. Solar energy is clean and safe for the environment and can produce energy at low costs without producing carbon dioxide (CO₂) emissions. Photovoltaics (PV) convert sunlight directly into electricity using solar cells. In the last few decades, it is a rapidly growing and increasingly important renewable alternative to conventional fossil and nuclear electricity generation. Since the discovery of a p–n junction Si PV device was reported in 1950s^[1], the solar cell technologies have undergone revolutionary developments. The most important factor in determining the cost of silicon products is the cost of the Si wafer used for the fabrication of solar cells. It has been recognized that cheaper solar cells can be produced only if cheaper materials and lower cost technologies are utilized^[2].

The I–III–VI chalcopyrite materials have some very desirable properties for photovoltaic application. CuInSe₂ (bandgap: 1.0 eV) has been proved to be a leading candidate for photovoltaic applications because of the excellent absorption coefficient of $3\sim 6\times 10^5/\text{cm}$ and the ability to form high-quality junctions. Superior performance of photovoltaic devices can be achieved when the optical absorption properties at the junction is matched to the solar spectrum by increasing the bandgap. Alloying with Ga and/or S increases the CuInSe₂ bandgap allowing for high-efficiency devices. The efficiency and stability of these devices are very promising, but there are several parameters limiting large-scale production of such devices.

When manufacturing thin film solar cells based on Cu(In,Ga)Se₂ (CIGSe) absorber layer, one of the critical components is the buffer layer which is positioned between CIGSe absorber and ZnO window layer. CdS buffer layers prepared by chemical bath deposition (CBD) generally resulting in the highest-performing CIGSe solar cells. CIGSe and CdS buffer layers result in efficient heterojunction solar cells because they have compatible lattice structures with acceptable lattice mismatches and favorable differences in electron affinities, resulting in favorable energy alignments. The recent laboratory-scale record efficiencies for CIGSe thin-film solar cells have been realized using alkali fluoride postdeposition treatments (PDT) after the deposition of the CIGSe absorber layer, reaching 22.6%^[3] power conversion efficiency for co-evaporated CIGSe, 22.9%^[4] for a sequential absorber deposition process. Recently, a 23.35% conversion efficiency was achieved for a 1cm² cell^[5].

The goal of this dissertation is to reveal the impact of alkali treatments on the chemical and electronic structure of the absorber surface, and how it influences the buffer/CIGSe interface formation.

The work is presented in the following order:

Chapter 2 discusses the physical principles behind the operation of solar cell devices. The configuration of thin film chalcopyrite-based solar cell devices and the function of the various layers based on chalcopyrite solar cells are further explained.

Chapter 3 covers the working principles behind the different spectroscopic techniques in this dissertation. Details of the data evaluation applied to characterize the surfaces and interfaces are also included.

Chapter 4 focuses on the effect of alkali post-deposition treatment on the chemical and electronic structure of a “real world” buffer/CIGSe interface.

Chapter 5 discusses the impact of evaporated alkali metals on the surface structure of CIGSe studied on in-system prepared model systems, aiming at understanding the underlying mechanism of the interfacial effect of alkalis on the performance of CIGSe devices.

2. (Thin-film) photovoltaics considerations

In this chapter, a concise overview of the physical principles behind solar cell device performance is presented. Current density-voltage (jV)-curve characterization is introduced along with important solar cell performance parameters that can be obtained from this method. Each component layer in chalcopyrite-based solar cells and the role it plays in the device is described. The possible loss mechanisms occurring throughout the device are also discussed, with a special emphasis on carrier recombination in the absorber layer and at the buffer/absorber interface.

2.1 Chalcopyrite-based thin film solar cells

2.1.1 Physical principles of solar cell devices

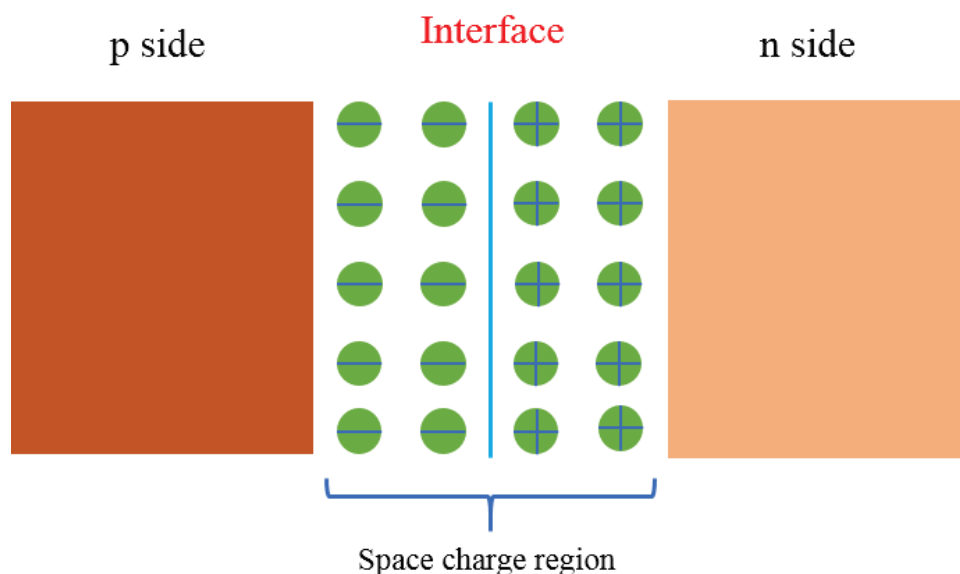


Figure 2.1. Schematic diagrams showing changes across a p-n junction predicted by the depletion approximation model.

Solar cells are made of semiconductor materials which can produce a "photoelectric effect" when exposed to sunlight. In practice, almost all photovoltaic energy conversion devices use semiconductor materials to form a p-n or p-i-n junction.

Normally p-n junctions are formed by joining p-type and n-type semiconductor materials. Since the p-type region has a high hole concentration and the n-type a high electron concentration, both majority carrier types diffuse over the junction driven by the concentration difference at the p-n contact. After electrons diffuse from the n region, positively charged donor atoms are left behind. Similarly, as holes diffuse from the p region, they uncover negatively charged acceptor atoms. The net positive and negative charges in the n and p regions induce an electric field in the region, in the direction from the positive to the negative charge, or from the n to the p region, this region is called the space charge region (SCR). The charged regions are shown in Figure 2.1.

2.1.2 Characterization of solar cell devices

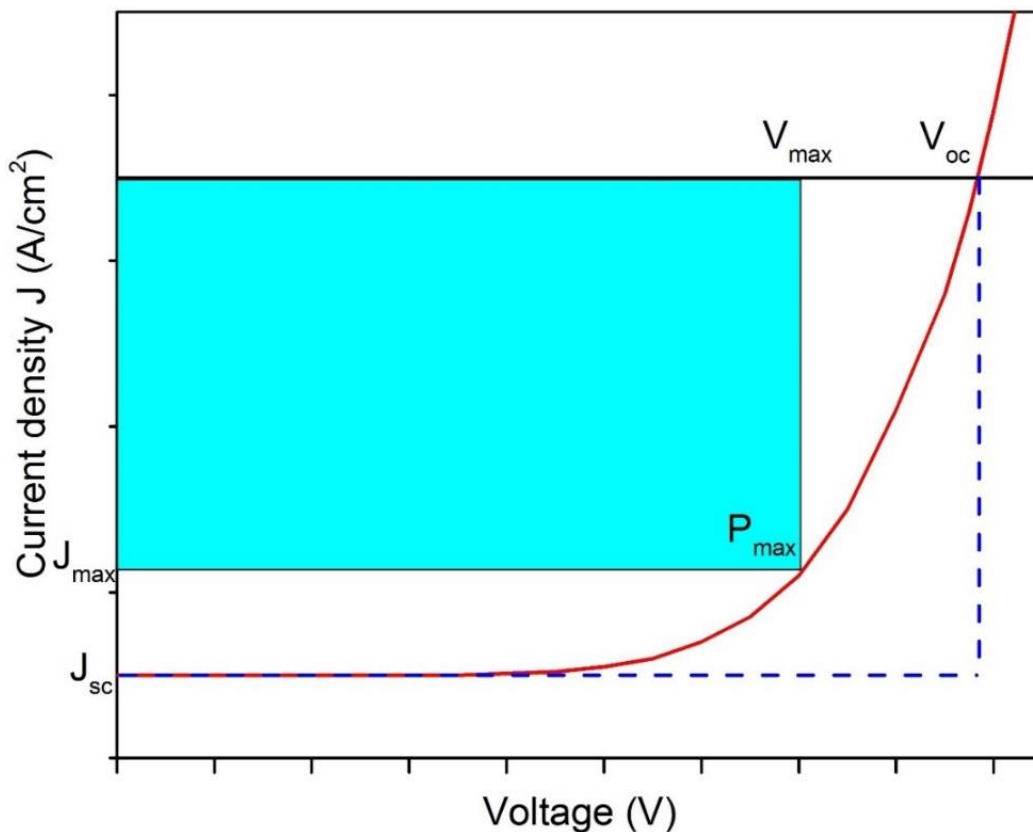


Figure 2.2. Exemplary J-V curve of a solar cell under sun/light illumination.

One important characterization used to describe a solar cell is electrical current density versus voltage (J-V) relationship, which is shown in Figure 2.2.

From the J-V curves, the cell's short circuit current density J_{sc} , and open-circuit voltage V_{oc} can be identified. Solar cell parameters like the current density J_{max} and voltage V_{max} at the maximum power point P_{max} and the fill factor (FF) are related according to the formulae:

$$P_{max} = V_{max} \times J_{max} = FF \times V_{oc} \times J_{sc} \quad (2.1)$$

$$FF = \frac{P_{max}}{V_{oc} \times J_{sc}} \quad (2.2)$$

The most important solar cell performance parameter is the conversion efficiency, which can be defined as the ratio between the P_{max} and the power of the sunlight at which the solar cell is illuminated (P_{in}). According to equation 2.1: the efficiency can be expressed as:

$$\eta = \frac{P_{max}}{P_{in}} = \frac{FF \times V_{oc} \times J_{sc}}{P_{in}} \quad (2.3)$$

The performance parameters of a photovoltaic cell can be affected by many factors, like the incident solar radiation spectrum, the resulting operating temperature of the cell, and so on. The standard reference spectrum for standard measuring conditions is an air mass 1.5 global (AM 1.5G) solar spectrum with a total irradiance of 1000 W/m^2 [6], and the standard reporting conditions (SRC) specified device operating temperature is $25 \text{ }^\circ\text{C}$ [7].

2.2 Device structure

The most common structure for CIGSe solar cells usually consists of the substrate, back contact, the p-type absorber, the n-type buffer layer, the transparent front contact, anti-reflective coating (ARC), and metal-grid. Each layer and the respective interfaces influence the performance of a such solar cell. A schematic diagram of a CIGSe based solar cell is shown in Figure 2.3.

In this cell configuration, MgF_2 acts as an anti-reflective coating layer and light enters the cell through transparent conduction oxide (TCO). Typically, a bilayer of TCO consists of a thin (50~100 nm) intrinsic ZnO layer and a thick (200~400 nm) Al: ZnO layer. A heterojunction is

formed between CdS buffer layer and the CIGSe absorber layer. Mo back contact is deposited on the substrate.

The working principle of the CIGSe solar cell can be described as follows: the n-type CdS buffer/window layer transmits light to the absorber where electron–hole pairs are generated. Due to a built-in electric field across the p–n junction interface between absorber and buffer/window layer: photogenerated electrons move from the p-type absorber to the n-type buffer layer and are collected by the n-type electrode; holes are swept away from the n-type buffer layer to the p-type absorber layer and collected by the p-type electrode, which is the Mo back contact. Each layer of the CIGSe solar cells will be shown in detail next.

2.2.1 Substrates

Glass is the most commonly used substrate since the first report on CIGSe in 1974^[8], but efforts are being made to develop flexible solar cells on metal foils and polyimide (PI) foils. The difficulties with metal foils are their rough surfaces and the diffusion of impurities into the absorber layer. The limitation of PI foils is their thermal stability; the cells on this substrate must be processed below 500 °C. Therefore, glass is still the first option for a CIGSe solar cell substrate. It is well known that a small amount of sodium incorporated into absorber layer is needed to enhance the cell efficiency^[9-10]. The traditional way to introduce sodium into CIGSe absorber layer is to allow the Na diffusion from the substrate (e.g. SLG glass) through the back contact^[9]. To block the Na diffusion, an additional layer (e.g. Al₂O₃) can be coated on the glass substrate to serve as a diffusion layer for alkali atoms; this is done so that the alkali can be introduced in a controlled manner during absorber formation.

2.2.2 Back contact

Molybdenum (Mo) is the most common metal used as a back contact for chalcopyrite-based solar cells. Normally the Mo is deposited by sputtering or e-gun evaporation. The most common techniques are direct current (DC) sputtering and radio frequency (RF) sputtering. DC sputtering is a well-established industrial process with high throughout capability and requires a cheaper set up cost, whereas RF sputtering can deposit a more reflective Mo thin films but with additional expense on RF power supplies and impedance matching network.^[11] DC sputtered Mo films have

more favorable physical properties while RF sputtered Mo films have more favorable electrical properties. An intermediate MoSe₂ layer is generally formed during CIGSe deposition, the CIGSe/Mo hetero contact including the MoSe₂ layer leads to a favorable Ohmic-type contact by the evaluation of dark I-V measurement at lower temperature^[12-13]. This interfacial layer doesn't appear to degrade the device performance.

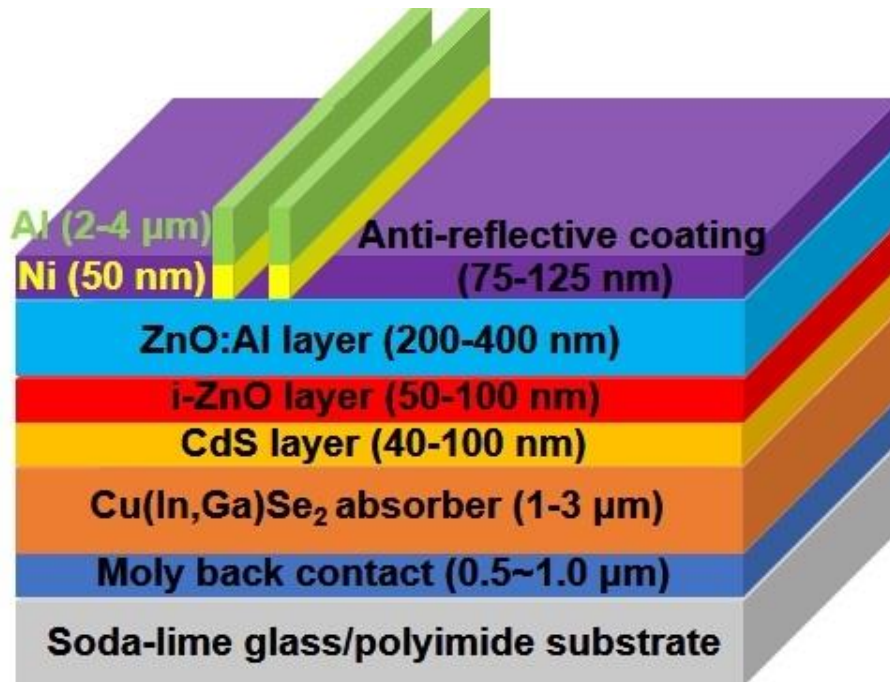


Figure 2.3. Schematic cross-section of a chalcopyrite-based thin film solar cell. The approximate thickness of each layer is also included.

2.2.3 Absorber layer

Different deposition methods can be used to deposit CIGS thin films. The most promising deposition methods for the commercial manufacture of modules can be divided into two approaches to get solar cells with high performance. The first one is “co-evaporation”: simultaneous evaporation of all the elements to the heated substrate from multiple sources where selenium (Se) is supplied during the whole deposition process. The primary advantage of co-evaporation is the good control over film composition and the band gap by changing In-Ga ratios^[14-15]. However, the Se evaporation source is not easy to control at high temperature.

The second approach^[16] is a two-stage deposition process where Cu/In/Ga elements are sputtered onto the substrate and then annealed in a chalcogen-containing (Se and/or S) atmosphere for the formation of CIGS or Cu(In,Ga)(S,Se) (CIGSSe) films. Normally, sputtering for the first step is suitable for industrial production and large area deposition. During the second stage, a chalcopyrite material (CIGS, CIGSSe) is formed by annealing/reactive annealing or rapid thermal processing (RTP) of the metal (Cu/In/Ga) precursor stack using the selenization/sulfurization process. The two-step process will take longer than the absorber preparation by co-evaporation due to diffusion kinetics.

2.2.4 Buffer layer

CdS is the most widely employed buffer layer, usually deposited by chemical bath deposition (CBD) technique. In comparison to physical vapor deposition (PVD) techniques, it provides a superior device performance, partly due to the improvement in the interface chemistry. CdS layers are processed in an alkaline aqueous solution of the following constituents^[17]: a complexing agent (normally ammonia), a cadmium salt (e.g. Cd(CH₃COO)₂) and a sulfur precursor (thiourea). The role of ammonia is to supply the ligand for the metal ions and to control the hydrolysis of thiourea via PH. The absorber film is immersed in the bath solution with three constituents for a few minutes at a deposition temperature of 60-80°C. The reaction formula^[18] is given by



However, because of the common CdS layer with a band-gap energy of about 2.42 eV^[19] limits the level of optimum performance of the cells, one of the major objectives in the field of CIGS technology remains the development in the production line of Cd-free alternative buffer layers.

As an alternative to the traditional CdS buffer, films based on Zn compounds or In compounds^[20-24] are studied with the aim to replace the heavy metal compared CdS with a non-toxic, non-hazardous material.

2.2.5 Front contact

Conductivity (for the transportation of the photo-generated current to the external circuit with minimum resistance losses) and transparency (transmission of light to the underlaying layer) are two conditions which need to be considered for the electronic front contact layer. A transparent

conducting oxide (TCO) is the best choice for good device performance, three main materials are used for front contact layers: SnO_2 , $\text{In}_2\text{O}_3:\text{Sn}$ (ITO), and ZnO . High deposition temperatures are needed for SnO_2 which can damage the underlying CIGSe device layer. Considering the lower cost for the whole device, ZnO is the most common material used.

2.3 Chalcopyrite absorber properties

Compared to crystalline silicon (c-Si) wafer based solar cells, CIGS technology is highly competitive and involves less raw materials, cost, and time. CIGSe module production requires a lower thermal budget ($550\text{ }^\circ\text{C}$) than c-Si ($1100\text{ }^\circ\text{C}$), and CIGSe solar cells can be monolithically integrated during cell processing, whereas in Si-wafer based solar cells, monolithic integration is not possible.

Chalcopyrite semiconductors have direct band gaps (E_g) leading to large absorption coefficients $\alpha > 10^4\text{ cm}^{-1}$ above the band gap. This fact makes these materials very suitable as absorber materials in thin-film solar cells, as only thicknesses of about $1\text{-}2\text{ }\mu\text{m}$ (almost 100 times less than the thickness of the c-Si wafer^[16]) are needed to absorb most of the band gap light from the solar spectrum, without the need for light trapping. The variable band gap of $\text{CuIn}_{1-x}\text{Ga}_x\text{Se}_2$ monotonically with Ga content can be described by^[25]: $E_g(x) = 0.13x^2 + 0.55x + 1.0$. The high efficiencies with chalcopyrite solar cells have been achieved with a Ga content around 0.35^[26]. It has been found^[27-28] that alloying with Ga mainly reduces the electron affinity of $\text{Cu}(\text{In}_{1-x}\text{Ga}_x)\text{Se}_2$ leading to an upward shift of the conduction band whereas the valence band stays at the same energetic position. This fact is important to consider when constructing band diagrams of CIGSe heterojunction devices.

2.4 Sample preparation

The chalcopyrite absorbers with alkali fluoride PDT studied in chapter 4 of this thesis were prepared at the Laboratory for Thin Films and Photovoltaics of the Swiss Federal Laboratories for Materials and Science Technology (Empa) as described in Ref.^[26] using a low-temperature multistage process (i.e. suitable CIGSe for PI substrates, although glass was used). They are grown

on a glass substrate coated with an Al_2O_3 diffusion barrier and 600 nm thick molybdenum back contact. The glass substrates have a diffusion barrier so that sodium diffusion into the absorber from the glass is avoided. The roughly 2 μm thick CIGSe absorber layers are grown by co-evaporation in a high-vacuum chamber equipped with Cu, In, Ga, and Se effusion cells.

In order to study the impact of alkalis, an in-situ NaF-PDT was applied after the CIGSe growth ($\rightarrow\text{CIGSe}^{\text{NaF}}$) as in Ref. [26] to fully exploit the impact of Na. Additionally, half of $\text{CIGSe}^{\text{NaF}}$ samples were subsequently treated with a KF-PDT ($\rightarrow\text{CIGSe}^{\text{NaF+KF}}$) after the NaF-PDT in the presence of selenium. A bare sample of both was retained, and then different thickness CdS buffer layers were grown on the remaining absorbers by a CBD method according to Ref. [26]. The deposition temperature was 70°C , and the samples were immersed in the solution for different deposition times: 5s, 30s, 1min, 2 min, 4min, 8min (only for NaF+KF PDT), 15min, and 24 min (only for NaF PDT). All samples prepared at EMPA were sealed in a N_2 -filled glove bag which was attached to the deposition chamber and opened in glovebox attached to ultra- high vacuum (UHV) system at HZB.

The chalcopyrite samples studied in chapter 5 of this thesis were prepared at PVcomB Laboratory in Helmholtz-Zentrum Berlin für Materialien und Energie (HZB). They are grown on a glass substrate coated with a diffusion barrier and molybdenum back contact. The CIGSe absorber layers are grown by co-evaporation in a high-vacuum chamber equipped with Cu, In, Ga, and Se effusion cells at high temperature.

2.5 Motivation and background

Recently, (heavy) alkali fluoride postdeposition treatments (PDTs) led to a boost in power conversion efficiencies for Cu(In,Ga)Se_2 (CIGSe) – based solar cells, now being well above 20%. [3, 5, 26, 29] After it was discovered that the incorporation of sodium – which usually diffuses from the commonly used soda-lime glass (SLG) substrate into the absorber during the absorber preparation at elevated temperature – into the CIGSe absorber improved solar cell performance, [9-10] the PDT was developed to deliberately incorporate sodium into CIGSe films deposited on alkali-free (flexible) substrates. [30] Recently, PDTs have also been used to incorporate other alkalis (heavier

than Na) into CIGSe.^[3, 26, 31] A combined, sequential NaF+KF PDT of CIGSe absorbers prepared at low temperature (to facilitate the use of flexible, e.g. polyimide, substrates) leads to an improvement of solar cell performance; mainly due to an increase of the short-circuit current.^[26] This is explained by the fact that the NaF+KF PDT enables a significant reduction of the CdS layer thickness – the standard buffer layer in CIGSe – based solar cells – without compromising interface quality preventing the commonly observed losses in open-circuit voltage and fill factor.^[32] As a consequence, the parasitic absorption in the UV regime due to the CdS is dramatically reduced, benefitting the short-circuit current. Furthermore, a pronounced NaF+KF PDT – induced modification of the CIGSe surface was observed: Several groups report on the presence of K^[26, 29, 33] accompanied with significant Cu^[34-35] and Ga^[26] depletion, the formation of a K–In–Se type surface species^[33, 36-38], and a related pronounced band gap widening at the absorber surface^[39-41]. However, only little is known about how this NaF+KF PDT induced absorber surface modification impacts the interface formation between CdS (the standard buffer layer in CIGSe-based solar cells) and the absorber. Reinhard et al.^[29] show that the K signal at the surface of a NaF+KF PDT CIGSe surface is significantly reduced upon rinsing in diluted aqueous ammonia and that the Cd signal after a respective partial electrolyte treatment is significantly higher for NaF+KF PDT CIGSe surfaces compared to similarly treated CIGSe absorbers that only underwent a NaF PDT or no PDT at all. While the CdS/CIGSe interface was not specifically addressed, the findings related to the aqueous ammonia rinse and the Cd partial electrolyte treatment could be relevant for the processes dominating the early stages of the CdS chemical bath deposition (CBD) process. Nicoara et al. study the impact of a KF-PDT on the aging of CIGSe surfaces and its interface with CdS, focusing on very short (1 min) CBD times^[42]. Together with Lepetit et al.,^[36] they speculate on the formation of an interface layer with a Cd–In–(S,O/OH)₄ composition.

Considering the importance of the CdS/CIGSe interface for the device performance, it is crucial to study the interface formation between CdS buffer and CIGSe absorber and how e.g. this is influenced by a KF PDT. This will be important to gain a detailed insight in the underlying mechanism of the apparent beneficial role of performing a KF PDT on the solar cell performance, i.e., enabling a significant reduction of the CdS buffer layer thickness. Consequently, we studied

the structure of the CdS/CIGSe interface and how it is impacted by different alkali PDTs by a combination of different x-ray spectroscopies. The interface formation is investigated by studying sample sets with different CdS thicknesses.

Moreover, heavy alkali elements (eg. Rb, Cs) were also introduced to the solar cell to modify the solar cell performance recently^[3]. T. Kodalle^[43] reported the effect of RbF PDT on the material and device properties of CIGSe, which show strong evidence that an Rb/Na-containing In-Se layer is formed at the surface during the RbF-PDT. N. Nicoara^[44] investigate the early stages of the CdS growth on RbF-PDT CIGSe absorbers which suggest that different CdS-CBD times (< 2 min and > 3min) lead to a complete different interface region. The study of the impact of RbF PDT on the electrical structure^[31] indicate that the RbF-PDT leads to an additional downward band bending in the CIGSe absorber upon interface formation with the CdS buffer. The formation and migration energies of the alkali metal impurities was calculated^[45] and several secondary phases could be formed during the PDT process. The results show that the theoretical impact of light alkali metal and heavy alkali metals could be different for the structure of absorber layer. To study the chemical structure and derive insights into the mechanism for underlying the formation of the heavy alkali/CIGSe surface, we investigated the impact of evaporated potassium/rubidium/cesium metal on the structure of CIGS studied on in-system prepared model systems in comparison with alkali fluoride treated CIGSe absorber surface to gain detailed insight.

3. Experimental methods

In this chapter, the theoretical descriptions and explanations of the various measurement techniques used in this thesis are explained. Photoelectron spectroscopy (XPS, HAXPES) with soft and hard X-rays is the principal characterization technique used, through which the surface chemical and electronic structure of semiconductor surfaces can be determined. Furthermore, the chemical properties of samples in the surface near-bulk region are probed via soft x-ray emission spectroscopy (XES) and x-ray absorption spectroscopy (XAS). The data evaluation and analysis methods are also described in this chapter.

Measurement techniques with the corresponding depth sensitivity and the probed electronic states are shown in Table 3.1. More details about different techniques are shown in the following.

Table 3.1 Overview of x-ray spectroscopic methods

Measurement technique	Detection of	Probed electronic states	Depth sensitivity
X-ray Photoelectron spectroscopy (XPS)	Electrons	Core levels + Occupied valence levels	Surface
X-ray excited Auger Electron Spectroscopy (XAES)	Electrons	Auger transitions	Surface
Hard X-ray Photoelectron Spectroscopy (HAXPES)	Electrons	(Deep) Core levels + Occupied valence levels	Near-surface bulk
X-ray Absorption Spectroscopy (XAS)	X-ray photons (fluorescence yield) /electrons (electron yield)	Unoccupied states	(Near-surface) bulk
X-ray Emission Spectroscopy (XES)	X-ray photons	Occupied states	Near-surface bulk

3.1 Photoelectron spectroscopy (PES)

Photoelectron spectroscopy is based on the external photoelectric effect, in which electrons are removed by electromagnetic radiation from a surface. The phenomenon of photoemission was first discovered by Hertz in 1887^[46] and in 1905 Einstein provided a theoretical description that involved the quantum nature of light^[47].

During the photoemission process, an electron gets excited from the initial states ψ_i to final states ψ_f . The transition probability P_{i-f} between electron states (initial ψ_i and final ψ_f) can be calculated by Fermi's Golden rule^[48]:

$$P_{i-f} \propto \frac{2\pi}{h} |\langle \psi_i | \Delta | \psi_f \rangle|^2 \delta(E_f - E_i - h\nu) \quad (3.1)$$

where h is Planck's constant, δ function describes the energy conservation law, Δ is the perturbation operator, and E_i and E_f are the initial and final state energy, respectively.

Under the Koopmans theorem (i.e., the frozen orbital approximation)^[48-49], it is assumed that orbitals of the initial (i.e., N-electron system) and final (i.e., N-1-electron system) are identical. For the photoemission process, the simplified equation describing the photoionization process is

$$E_K = h\nu - E_B - \phi \quad (3.2)$$

where E_B is the binding energy (E_B) of the electron, $h\nu$ is the energy of the X-ray photons being used, E_K is the kinetic energy (E_K) of the electron as measured by the instrument and the work function $\phi = E_{\text{vac}} - E_F$ as the difference between the Fermi level (E_F) and the vacuum level (E_{vac}).

This equation is essentially a conservation of energy equation.

For interpretation, PES can be explained by a simple three-step model. In the first step photoionization takes place when the photon is absorbed and an electron is excited. In the second step, this electron travels through the sample to the surface. Finally, in the third step the electron escapes into the vacuum where it is detected. Figure 3.1a illustrates the photoemission process.

PES is also used to study the valence band (VB) region and determine the valence band maximum (VBM). PES measurements need to be performed in ultrahigh vacuum (UHV) chamber to minimize surface contamination and get meaningful conclusions; photoelectrons ejected from the sample do not lose their KE through collisions with particles en route to the electron analyzer. When excited with X-rays from a lab source: Mg K_α (1253.56 eV) and Al K_α (1486.58 eV) radiation, PES is

generally denoted as "XPS"; When excitation energy $h\nu_{\text{ex}}$ is higher than 2 keV, PES is generally denoted as "Hard X-ray photoelectron spectroscopy (HAXPES)". Varying the excitation energy will change the energy of the detected photoelectrons and thus is a method to tune the depth from where the electrons will escape the material. Figure 3.2 illustrates the relation between excitation energy and inelastic mean free path (IMFP). With a relatively low photon energy, the photoelectrons will get low kinetic energy therefore that will not be able to escape from deeper in the material. Higher photon energy gives higher kinetic energy and increase the depth from where the electrons can be emitted, then the measurement becomes more bulk sensitive.

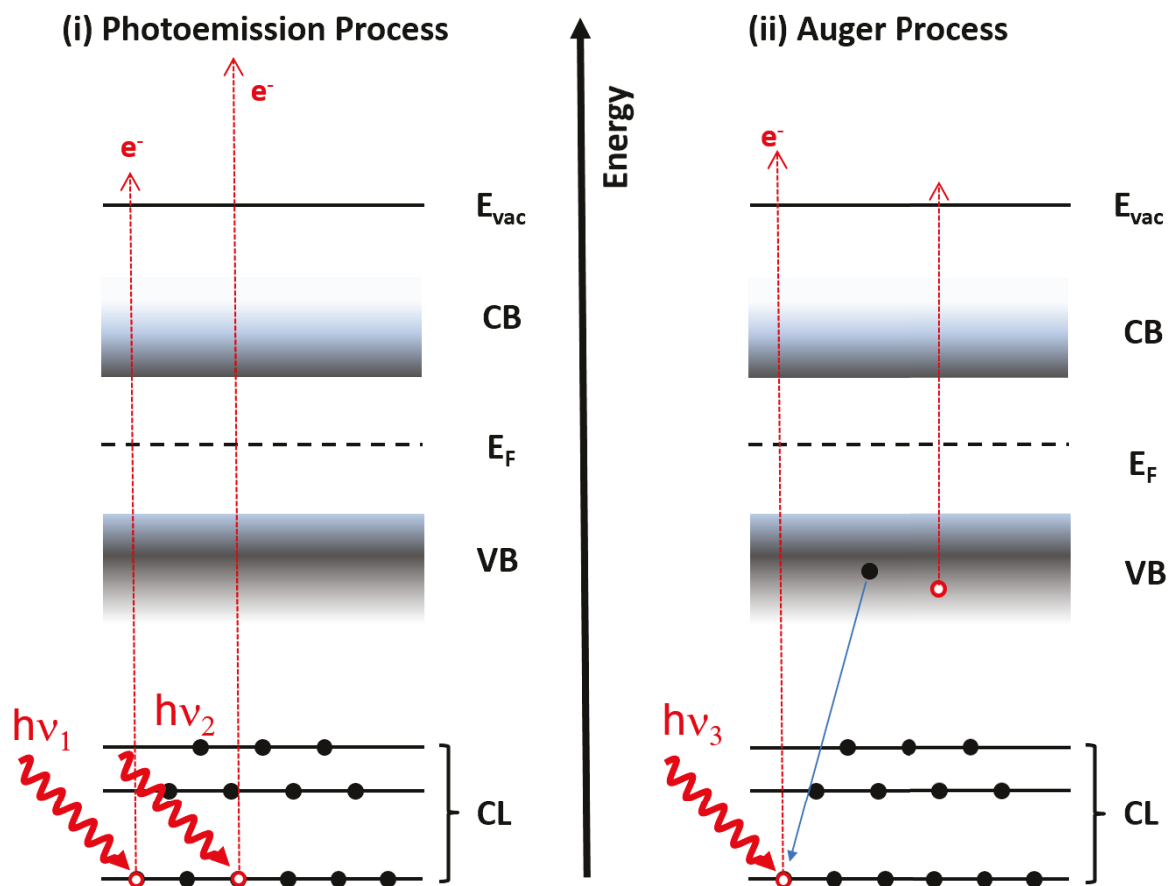


Figure 3.1. (i) Schematic of the photoemission process where photons with different excitation energy $h\nu_1/h\nu_2$ excite electrons from core levels (CL). (ii) Schematic of the Auger process showing the electronic recombination of the CL hole.

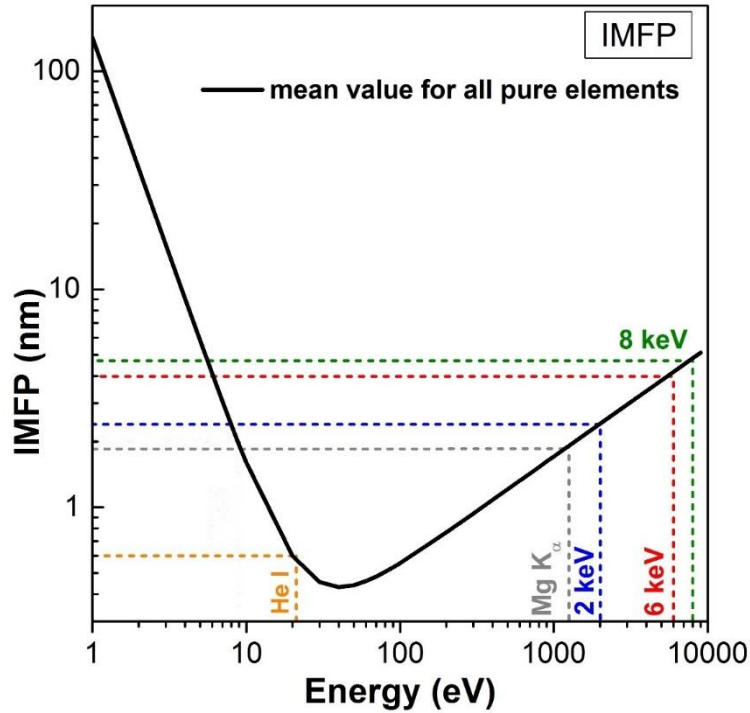


Figure 3.2. Universal curve of the inelastic mean free path of electrons in a solid as a function of electron kinetic energy. Adapted from Ref. ^[50].

3.2 X-ray Auger electron spectroscopy (XAES)

During PES measurements, two different spectral lines can be detected that are related to different emission processes following x-ray excitation: i) photoemission lines which was explained above, and ii) Auger lines. In the Auger process: the core hole that is left behind after the photoemission process is filled by an electron from a higher sub shell; the extra amount of energy is transferred to another electron which is knocked out of the material. The Auger process is shown in Figure 3.1 ii). The notation of XAES lines is: element, the three principal quantum numbers of the electrons participating in the process and a subscript representing the angular momentum, spin quantum number, and their coupling like Cd M₄N₄₅N₄₅.

Combining the XPS core lines and XAES Auger lines, the modified Auger parameter can be calculated, which is useful to ascertain the chemical environment of a detected element. The relation of the discussed energetic variables ^[51-52] is:

$$\alpha' = E_B(\text{core level}) + E_K(\text{Auger Line}) \quad (3.3)$$

where E_B is the binding energy (E_B) of the core level of the detected element, E_K is the kinetic energy of the Auger line of the detected element. Because α' are the sum of PES and XAES lines

(in E_B and E_K , respectively), this value is independent of effects such as charging and band-bending, which cancel out in the calculation.

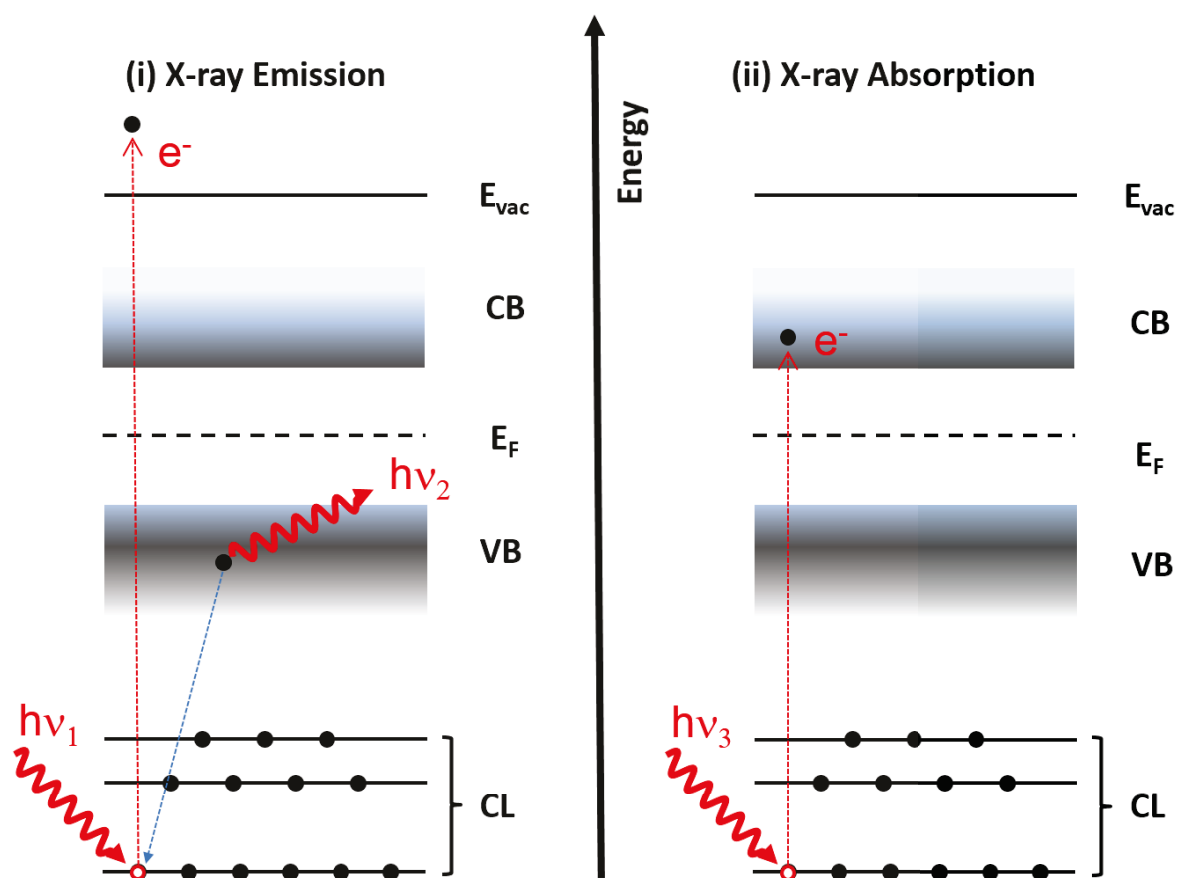


Figure 3.3. (i): Schematic of x-ray emission, photon with the energy $h\nu_1$ excites an electron above the vacuum level E_{vac} ; photo-generated hole gets filled with an electron of lower binding energy emitting a photon of $h\nu_2$. (ii): Schematic of x-ray absorption, photon with the energy $h\nu_3$ excites an electron into an unoccupied state of the conduction band (CB).

3.3 X-ray emission spectroscopy (XES) and X-ray absorption spectroscopy (XAS)

XES is a photon-in-photon-out technique and thus its probing depth is not limited by the IMFP of photoelectrons like PES. A schematic diagram of this emission process is shown in Figure 3.3. Excitation can be achieved at a certain energy and the X-ray emission can be determined by an X-ray energy dispersive spectrometer.

X-ray absorption spectroscopy (XAS) is a well-established analytical technique used extensively for the characterization of semiconductors in solid or liquid, crystalline or amorphous, bulk or

nanoscale form and it can be a photon-in-photon-out technique like XES depending on detection mode. XAS can be used to study the unoccupied states, by varying the photon energy $h\nu_{\text{ex}}$ to excite a core level electron into an unoccupied state in the CB.

Several different modes are available for different absorption experiments: transmission model, fluorescence yield (FY), and electron yield (EY). The most common one in terms of quality of signal and acquisition time for a spectrum is the transmission model. Normally, ion chambers are necessary to be equipped as detectors for this mode to measure the incident (I_0) and transmitted flux (I_t). Moreover, a reference metal foil can be added behind the sample between the second and third ion chamber to measure the reference flux (I_{flux}) at same time. This set is required for intensity calibration and checking the stability of the experiment condition. The total fluorescence yield (TFY) mode using e.g. a channeltron detector captures all emitted photons also unwanted transitions for the specific experiment. Partial Fluorescence Yield (PFY) with an energy-discriminating detector will be able to count only the photons in the energy range of interest and dismiss scattered photons. All the emitted electrons can be measured by the Total Electron Yield (TEY) mode by means of electron multipliers or by a grid close to the sample surface. By introducing an electron energy analyzer to select only the element-characteristic Auger electrons, the Partial Electron Yield (PEY) model can be performed. The EY modes are much more surface sensitive since their information depth are limited by IMFP of the involved chemicals.

3.4 Instrument and experimental setups

3.4.1 Lab-based instrument

Laboratory-based XPS measurements, non-monochromatized Mg K_{α} (1253.56 eV) and Al K_{α} (1486.58 eV) radiation and a SPECS PHOIBOS 150 MCD-9 were used to characterize core levels and Auger lines. The excitation source was a XR50 SPECS twin anode x-ray source. All the measurements are performed in the analysis chamber with pressure lower than 10^{-9} mbar. The electron energy analyzer was calibrated according to D. Briggs et al.^[51]. Calibration checks and excitation energy calibrations are usually done with Au 4f peaks measured on a clean Au foil. Figure 3.4 illustrates schematic of an XPS spectrometer.

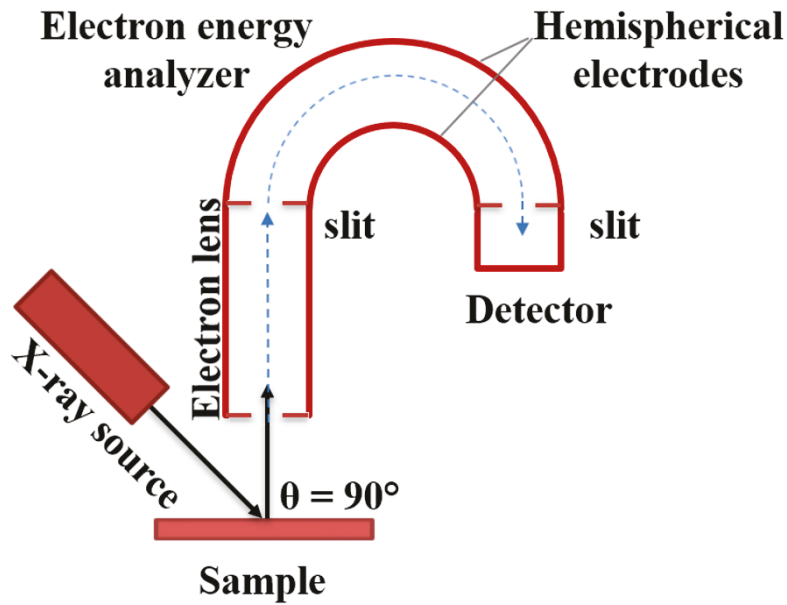


Figure 3.4. Schematic of an XPS spectrometer.

The energy resolution of a hemispherical analyzer can be described as follows:

$$\Delta E = \frac{s \cdot E_{pass}}{R_0} \quad (3.4)$$

Where E_{pass} is pass energy, s is the width of entrance slit (in mm) and R_0 is the hemisphere radius. For survey spectra, a pass energy of 50 eV was used for survey spectra measurement and 30 eV pass energy was used for the collection of the XPS core level and Auger line spectra. The energy resolution was approximately 1 eV.

3.4.2 Synchrotron-based instrument

3.4.2.1 Synchrotron radiation

A synchrotron is a type of particle accelerator, in which the accelerating particle beam consists of electrons traveling around a fixed closed-loop path. The radiation is emitted when the charged particle is accelerated. The electrons are accelerated to close to the speed of light and stored in a storage ring.

Synchrotron radiation is generated when relativistic electrons are accelerated (i.e. if they undergo a change of direction) in a magnetic field. Normally, three types of magnetic structures (bending magnets, undulator, and wigglers) are used for synchrotron radiation. Bending magnets are needed to produce the closed path motion in the storage ring resulting in a radiation spectrum that is very

broad. Better beam quality and significantly higher brilliance can be achieved when wiggler and undulator-type insertion devices ^[53] are installed in special straight sections.

An undulator consists of a periodic structure of dipole magnets with relatively weak magnetic field. The periodicity resulting in the electron motion characterized by small angular excursions (undulations), the amplitude of this undulation would be small because of the weak magnetic fields and respective radiation cone is narrow, allowing constructive interference of the emitted photons. The principal of wiggler magnets is basically the same as of undulator magnets but with stronger magnetic fields. Due to the stronger fields, the oscillation amplitude is larger and the resultant radiation core is broader, which also result in similar radiation spectrum as that of bending magnets but with high photon flux and a shift to hard x-rays.

Different monochromators are suitable for different energy ranges: grating monochromators work for lower photon energy range while crystal monochromators are better for higher photon energy. The transition point is, effectively, slightly above the Si K-edge absorption (i.e. around 2 keV). The end station is located at the end of the beamline where the measurements can be performed. Between the storage ring and the beamline end station, the light will pass the monochromator, mirrors, gratings and slits and then focus on the sample.

An electron experiencing radial acceleration as it travels around a circle emits radiation through a broad angular pattern which is compressed on Lorentz transformation from one frame of reference to another. The Lorentz factor γ ^[54] needs to be taken into account, which is related to the velocity of the particle v and the speed of light c :

$$\gamma = \frac{1}{\sqrt{1 - \frac{v^2}{c^2}}} \quad (3.5)$$

For highly relativistic electrons, Figure 3.5 show bending magnets radiation is emitted tangentially when an electron traverses a curved path, in a narrow radiation cone of half width $\theta \cong 1/2\gamma$. This simple description about how radiation occurs at x-ray wavelengths is based on the estimation of time duration of the radiation signal observation and Heisenberg's uncertainty principle for photon energy: $\Delta E \cdot \Delta T \geq \hbar/2$; ΔT is the time duration during which one detects radiation, and ΔE is the uncertainty in observed photon energies. Therefore,

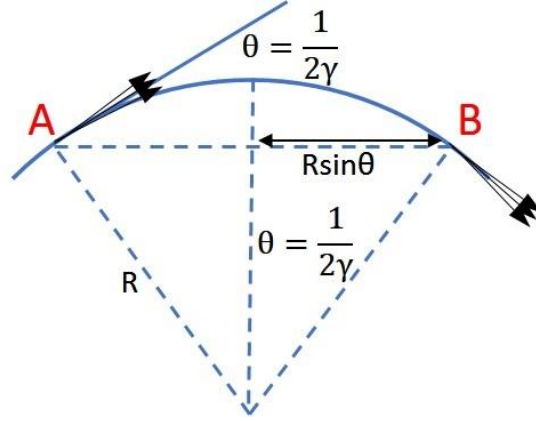


Figure 3.5. Scheme of bending magnets radiation in a narrow cone with half angle θ . Points A and B are the states before and after radiation and electrons transmitted. Adapted from Ref. [54].

$$2\Delta T = T_e - T_r \quad (3.6)$$

As the electron comes within an angle θ , T_e is the transit time for electron from point A to point B while radiation signal will be detected after a transit time of the light, T_r . Note that $T_e = \frac{R \cdot 2\theta}{v}$,

$T_r = \frac{2R \cdot \sin\theta}{c}$, $\beta = v/c$, and use small angle approximation, the expression becomes:

$$\Delta E \geq \frac{2\hbar c \gamma^3}{R} \quad (3.7)$$

If radius R with an expression with γ and the magnetic field $R \approx \gamma m c / e B$, where B_0 is the magnetic flux density, m is the electron rest mass, we have

$$\Delta E \geq \frac{2e\hbar B_0 \gamma^2}{m} \quad (3.8)$$

For highly relativistic electrons, it is convenient to express the total electron energy E_e in terms of γ and the electron rest energy, mc^2 , as

$$\gamma = \frac{E_e}{mc^2} \quad (3.9)$$

The critical energy E_c , defined as the photon energy that divides the synchrotron radiation emission into two parts of equally radiated power, is related to the magnetic flux density B_0 of the bending magnet:

$$E_c = \frac{3e\hbar B_0 \gamma^2}{2m} \quad (3.10)$$

If charged particles in synchrotron light sources is electrons, this simplifies to:

$$E_c(\text{keV}) = 0.6650 E_e^2(\text{GeV}) B_0(\text{T}) \quad (3.11)$$

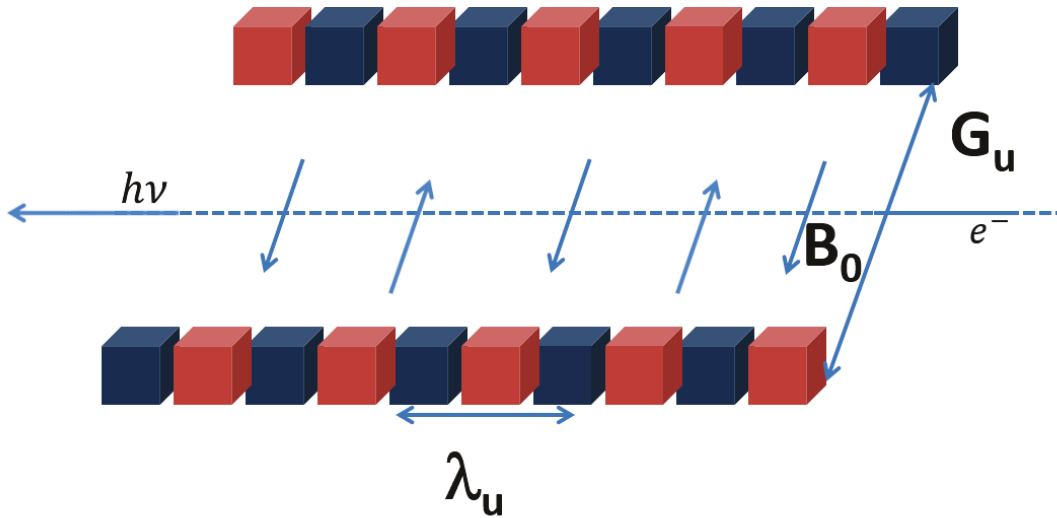


Figure 3.6. Schematic of insertion device with alternating polarity of permanent magnets. B_0 is a magnetic field density.

As we discussed above, insertion devices must be included in the straight sections of the storage ring to get higher brilliant light. Figure 3.6 illustrates the basic principles of these devices, consisting of stacks of pairs of permanent magnets with alternating polarity. The λ_u is the undulator frequency determined by the distance between magnets of the same polarity determines. G_u is the undulator gap (the distance between two arrays of magnets).

The insertion devices make the travelling path of particles oscillate by the alternating magnetic configuration. The difference between wiggler and undulator has been explained before. But for different conditions, a parameter will be introduced to select different insertion devices, which is non-dimensional magnetic strength K . That can be described as^[54]:

$$K = \frac{E\lambda_\mu B_0}{2\pi mc} = 0.9337 \cdot B_0(T)\lambda_u(cm) \quad (3.12)$$

If $K \gg 1$, the insertion device is referred to as a wiggler. The large amplitude of the oscillations mean that radiation emission cones are too far apart to overlap and interfere with each other. For factor $K \ll 1$, an undulator need to be set which can produce constructive interference and increased intensity of a specific energy. In this case, photon energy can be changed by changing the undulator gap.

3.4.2.2 Instrumentation and experimental details

BESSY II

BESSY II employs an electron gun to generate a 70 kV electron beam, the beam is accelerated over a microtron and a synchrotron to its final energy of 1.7 GeV before injection in the main storage-ring.

The KMC-1 beamline at BESSY II is equipped with a bending magnet and a crystal monochromator that uses three different crystals: Si (422), Si (111) and Si (311), allowing the energy to be adjusted between 2 and 10 keV. The Si (111) crystal is used for the data collection in this thesis. Schematic of the main HIKE end station at KMC-1 at BESSY II is shown in Figure 3.7. The electron analyzer is in a direction that is close to the surface normal of the sample (the beam and the spectrometer are at a 90-degree angle). The light is coming from the right side in Figure 3.7. Samples can be introduced via the load-lock chamber and transferred to the analysis chamber in UHV. Argon ion sputtering used for cleaning and annealing for thermal treatment can be performed in the analysis chamber of HIKE. The prep- chamber is used for sample preparation; the evaporation experiment in this thesis is done in this chamber. The evaporator is installed on the bottom of this chamber. The end station is equipped with a Scienta R4000 hemispherical electron energy analyzer. For the HAXPES measurements were performed at BESSY II, a pass energy of 500 eV was used for all survey spectra and 200 eV for all detail spectra. In addition, potassium K edge XAS spectra were measured changing photon energies between 3600 and 3660 eV in fluorescence yield mode. XAS measurements^[55] were carried out using a standard chamber equipped with a solid state fluorescence detector. The excitation energy was calibrated by measuring multiple Au 4f spectra of a grounded clean Au foil and setting the Au 4f_{7/2} binding energy equal to 84.00 eV at the start and end of the HAXPES and XAS measurement.

ALS

The ALS storage rings has energy E_e values of 1.9 GeV and a critical energy E_c of 2.4 keV, respectively, so it is most intense in soft x-ray regime.

X-ray emission spectroscopy (XES) measurements at the Se M_{4,5} and the S L_{2,3}/Se M_{2,3} edges were performed using the Soft X-ray Fluorescence (SXF) spectrometer installed at beamline 8.0.1 of the Advanced Light Source (ALS), Lawrence Berkeley National Laboratory^[56]. The base pressure of

the SXF analysis chamber was $\leq 1 \times 10^{-9}$ mbar. The energy scales of the XES spectra were calibrated using elastically scattered photons in the range of 100–120 eV in second diffraction order of the spectrometer for the Se $M_{4,5}$ energy window. For transport to the ALS, the samples were sealed under N_2 -atmosphere. However, during introduction into the SXF UHV chamber, the samples were shortly (< 5 min) exposed to ambient air.

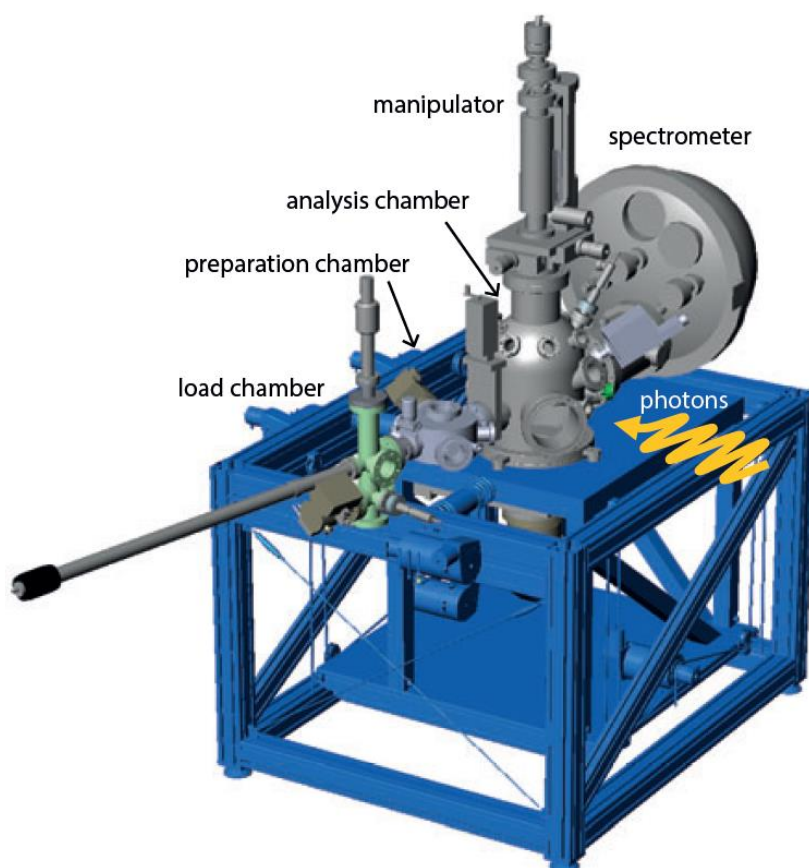


Figure 3.7. Schematic of the HIKE end station at KMC-1 at BESSY II. Adapted from Ref. ^[57].

3.5 Data analysis

3.5.1 Peak fitting and analysis details

The curve fit analysis of the PES data is conducted by iterative fitting by the least-squares method with the Fityk software^[58].

Core levels notation for XPS uses the nomenclature nlj where n is the principal quantum number, l is the angular momentum quantum number, s is the spin angular momentum number and can be $\pm\frac{1}{2}$ and j is the total angular momentum quantum number (where $j = l + s$). All orbital levels except

the s levels ($l = 0$) give rise to a doublet with the two possible states having different binding energies, which is known as spin-orbit splitting. The peaks will also have specific area ratios based on the degeneracy of each spin state, i.e. the number of different spin combinations that can give rise to the total j (see Table 3.2).

Table 3.2. Spin-orbit splitting j values and peak area ratios.

Subshell	j values		Area Ratio
s	1/2		
p	1/2	3/2	1:2
d	3/2	5/2	2:3
f	5/2	7/2	3:4

In addition to the ratio of spin-orbit splitting ratio, the spin-orbit separation energy also needs to be considered as a fitting constraint. For the measured series of photoemission spectra which are simultaneously fitted, the full-width-half-maximum (FWHM) of the curve fit peaks are coupled to the same value for the photoemission line.

The core level positions were determined using fits with linear background and Voigt profiles. The Voigt function is a convolution of Gaussian and Lorentzian functions: Lorentzian function accounting for the lifetime broadening of the peak, caused by the existence of core holes under x-ray bombardment and Gaussian function mainly describes the experimental broadening.

Finally, the number of employed fit peaks are minimized; additional peaks are only used if a physical reason is found (i.e., peak broadening due to the presence of new chemical species). Curve fit analysis was used to determine the intensity and the number of spectral contributions in a measured PES line.

3.5.2 Analysis details

To calculate surface compositions, the fitted areas of core levels must be taken into account first. For qualify the main cation, three influential factors are: the respective photoionization cross-sections, the IMFP of the photoelectrons, and the transmission function of the electron analyzer as they also have a direct impact on the measured signal. For shallow core levels analysis, only

photoionization cross-sections were used since the IMFP and the transmission function are nearly identical in this small energy range.

In the investigation of solids, we are mostly interested to observe chemical shifts. The nature of the chemical shift gives us information about chemical bonding. There can also be a chemical shift between surface atoms and bulk atoms in a solid due to the different amounts of neighboring atoms. The linear extrapolation of the leading edge is used to determine valence band maximum (VBM) measured with HAXPES.

4. Impact of NaF PDT and NaF+KF PDT on the chemical and electronic structure of CdS/Cu(In, Ga)Se₂ thin film solar cell absorbers

4.1 Introduction

Alkali treatments of CIGSe absorber surfaces have a beneficial impact on the device performance^[26, 59]. In a solar cell device, several interfaces are formed in the process and one of the most crucial interfaces is between the absorber and the buffer layer^[60-65]. A combined, sequential NaF+KF PDT of CIGSe absorbers prepared at low temperature (to facilitate the use of flexible, e.g. polyimide, substrates) leads to an improvement of solar cell performance; mainly due to an increase of the short-circuit current^[26, 66]. This has been attributed on the NaF+KF PDT enabling a significant reduction of the CdS buffer layer thickness without the commonly observed losses in open-circuit voltage and fill factor. The surface of NaF+KF PDT/CIGSe absorbers on flexible substrates was already studied in detail^[33], but the impact on interface formation when a buffer layer is added on top is not totally understood yet. In this subsection, surface-sensitive PES and XAES measurements are used to monitor the surface/interface formation of the CdS/CIGSe^{PDT} heterointerface as a function of CBD time (i.e., CdS layer thickness).

First, the impact of such treatments on the chemical structure will be discussed and compared to the results based on alkali treated samples on flexible substrates. Second, the chemical structure and electronic structure of CdS deposition on alkali treated CIGSe samples will be shown and discussed.

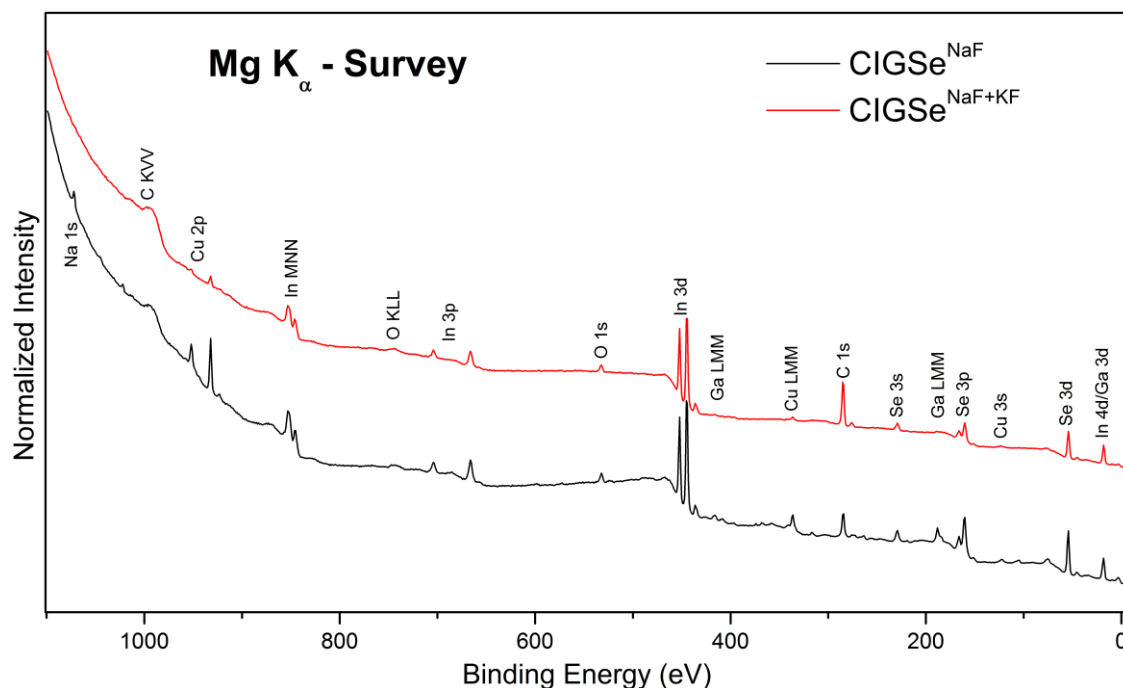


Figure 4.1. Survey spectra of a CIGSe^{NaF} (black), and a CIGSe^{NaF+KF} (red) CIGSe absorber measured with an excitation energy of $h\nu=1253.56$ keV (Mg K $_{\alpha}$). The core level and Auger lines are marked. Spectra are vertically offset for clarity.

4.2 Impact of KF PDT on Cu(In,Ga)Se₂ surface

4.2.1 Surface chemical structure

Figure 4.1 shows the survey spectra of the samples with different PDT treatment of the respective CIGSe absorbers (NaF PDT for CIGSe^{NaF} and NaF+KF PDT for CIGSe^{NaF+KF}) measured with Mg K $_{\alpha}$. CIGSe^{NaF} and CIGSe^{NaF+KF} refer to NaF and NaF+KF PDT CIGSe samples, respectively. All expected absorber-related core level and Auger lines are present. Cu- and Ga-depletion for the CIGSe^{NaF+KF} can be observed, which is in agreement with Ref. [33]. In and Se signals also decrease but not as strongly as Cu and Ga. The alkali elements Na (for CIGSe^{NaF} absorber) and K (for CIGSe^{NaF+KF} absorber) can be observed. No F signals are detected for either sample. Additionally,

C 1s and O 1s are detected, most likely due to surface contamination, and will be discussed in detail later.

Figure 4.2 displays Cu 2p_{3/2}, In 3d_{3/2}, Ga 2p_{3/2}, Se 3s, Na 1s, and C 1s/K 2p regions of the PDT/CIGSe sample series with the respective fits recorded with an excitation energy of $h\nu=1253.56$ eV. The core levels are simultaneously fitted with Voigt profiles and linear backgrounds; the backgrounds have been subtracted in all figures. Gaussian-Lorentzian function is linked for all the core level spectra in the fitting process. All the spectra related to CIGSe can be fitted with one species. Note the different magnification factors, which give direct indication for Cu and Ga depletion. We use the In 3d_{3/2} line from Figure 4.2b (and not the more intense 3d_{5/2} XPS peak) to avoid the Mg K _{α 3,4}-excited 3d_{3/2} satellite lines that overlap with the 3d_{5/2} peak. The K 2p peaks of a given spin-orbit doublet were constrained to share the same FWHM, and the intensity ratio of the peaks in a doublet were set to obey the $2j+1$ multiplicity rule. The doublet separations of K 2p were fixed to 2.70 eV^[67]. In comparison to the CIGSe^{NaF} series, there is a shift of ~ 0.1 eV to lower binding energies for the CIGSe^{NaF+KF} samples for In 3d and Se 3s. This shift is not the same as the other absorber cation's core levels spectra of this series, possibly indicating a different chemical environment for In+Se derived from the NaF+KF PDT sample.

To derive the absorber surface composition, we have used the shallow core level lines of the absorber elements (Cu 3p, Se 3d, In 4d, Ga 3d; neither alkali elements nor C and O are included in this analysis, the related spectra are shown later in Figure 4.6). Due to the very similar kinetic energy of the related photoelectrons, we are able to neglect the variations in electron analyzer transmission function and IMFP on signal intensity, and hence only correct for the different photoionization cross sections^[68] for quantification. The surface Cu:(In+Ga):Se compositions are $\approx 1.0:2.8:3.9$ and $\approx 1.0:6.8:9.8$ for the bare CIGSe^{NaF} and CIGSe^{NaF+KF} absorbers, respectively. We find a different degree of surface Cu-deficiency, in agreement with Refs.^[26, 29, 33, 69-70]. Similarly to our previous report, we attribute the heavier Cu depletion of the CIGSe^{NaF+KF} absorbers to the formation of a K-In-Se type species on top of the CIGSe absorber^[33]. The Ga/(Ga+In) (GGI) ratio is derived to be (0.22 ± 0.05) and (0.04 ± 0.05) for CIGSe^{NaF} and CIGSe^{NaF+KF}, respectively. This confirms previous XPS studies of the impact of KF PDTs on the chemical CIGSe surface

structure,^[26, 33] suggesting that employing a NaF+KF PDT does not only lead to a strong Cu- but also Ga-depletion near the absorber surface. In a previous report^[71], TEM results suggest that Alk-In-Se components form only when indium is present.

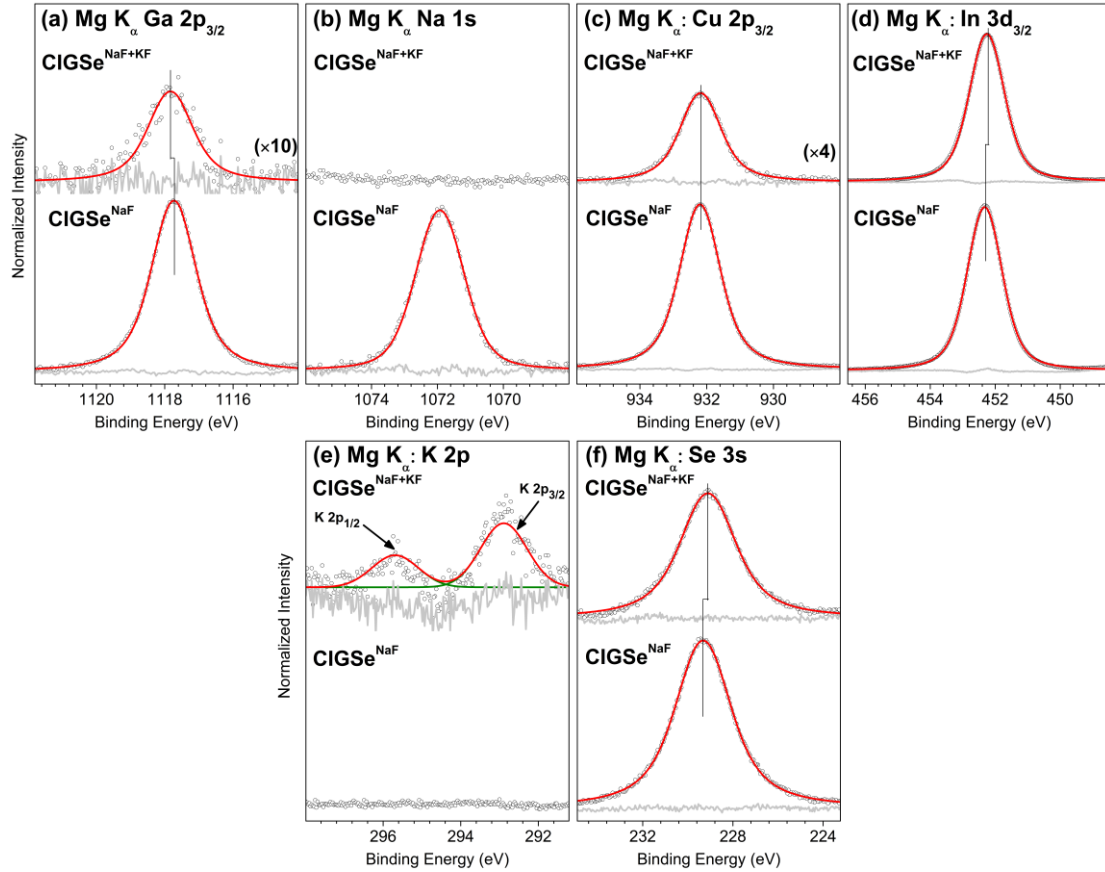


Figure 4.2. XPS detail spectra of the (a) Ga $2p_{3/2}$, (b) Na $1s$, (c) Cu $2p_{3/2}$, (d) In $3d_{3/2}$, (e) K $2p$, and (f) Se $3s$ of the PDT/CIGSe sample series, as normalized to background intensity. Solid lines indicate peak centers determined by curve fit analysis. All spectra were measured using Mg K_{α} excitation. Vertical offsets are added for clarity. Note the different magnification factors.

4.2.2 Modified auger parameter analysis

For a more direct examination of the impact of alkali treatments, especially on the chemical speciation of the $\text{CIGSe}^{\text{NaF}}$ and $\text{CIGSe}^{\text{NaF+KF}}$, we use the In $M_{45}N_{45}N_{45}$ Auger lines. A different shape can be observed for the In $M_{45}N_{45}N_{45}$ Auger line for the $\text{CIGSe}^{\text{NaF}}$ and $\text{CIGSe}^{\text{NaF+KF}}$ sample (See Appendix A.1). It is reported^[33] that a K-In-Se interface layer was observed for $\text{CIGSe}^{\text{NaF+KF}}$ absorber on flexible polyimide foils. Therefore, we use the sum of the narrowest $\text{CIGSe}^{\text{NaF}}$ reference spectra to represent the In $M_{45}N_{45}N_{45}$ spectrum of $\text{CIGSe}^{\text{NaF+KF}}$ absorber.

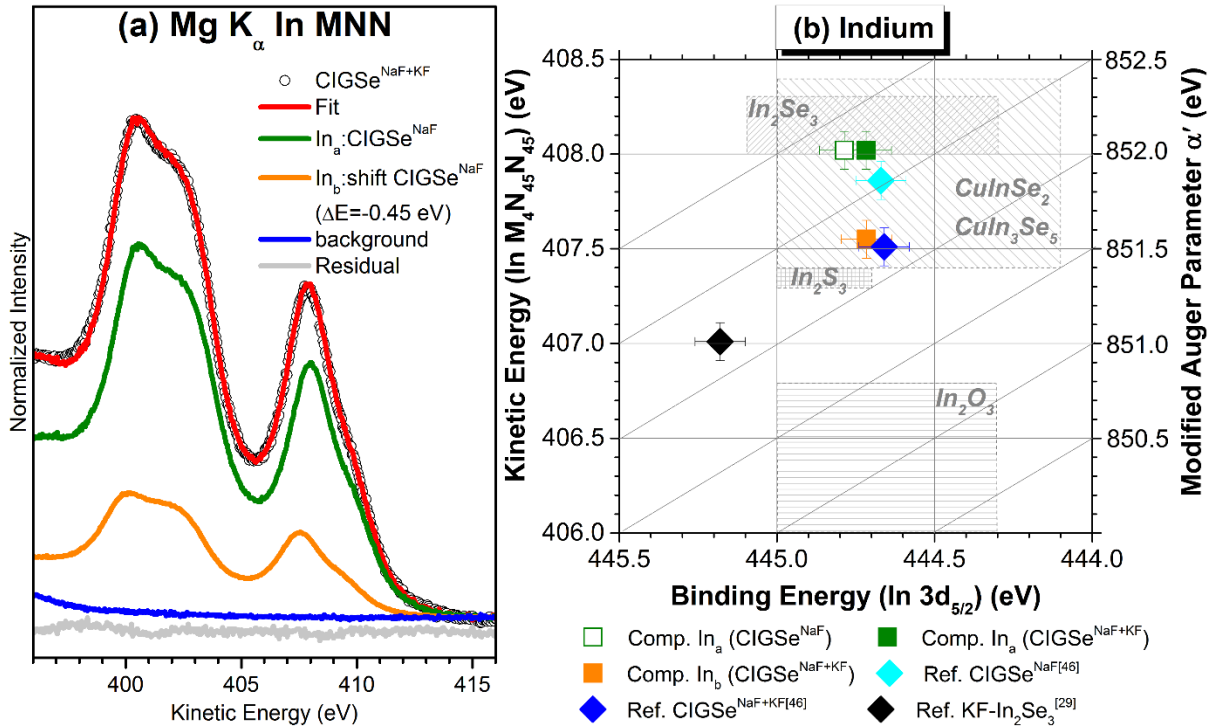


Figure 4.3. (a) $\text{In M}_{45}\text{N}_{45}\text{N}_{45}$ XAES line of the $\text{CIGSe}^{\text{NaF}}$ and $\text{CIGSe}^{\text{NaF+KF}}$ sample with their spectra analysis. The reference spectra used to fit the $\text{CdS/CIGSe}^{\text{NaF+KF}}$ spectra are the (shift and scaled) In MNN spectra of $\text{CIGSe}^{\text{NaF}}$ absorber and a background spectrum (from thickest $\text{CdS/CIGSe}^{\text{NaF+KF}}$ sample) spectra; (b) Evolution of the modified Auger parameter (α') of In [i.e., the sum of the binding energy (E_B) of the $\text{In } 3d_{5/2}$ photoemission line and the kinetic energy (E_K) of the $\text{In M}_{45}\text{N}_{45}\text{N}_{45}$ Auger line] with increasing CdS CBD time. The $\text{KF-In}_2\text{Se}_3$ reference data point was adopted from Ref. [33]. For comparison, reference position area for In_2Se_3 , CuInSe_2 , CuIn_3Se_5 , In_2S_3 , and In_2O_3 compounds (as derived based on data in Ref. [52, 72-78] are indicated). The error bars are dominated by the uncertainty in the determination of the energy position of the individual components.

The $\text{In M}_{45}\text{N}_{45}\text{N}_{45}$ (MNN) XAES lines representation of $\text{CIGSe}^{\text{NaF+KF}}$ sample by (shifted and scaled) $\text{CIGSe}^{\text{NaF}}$ are displayed in Figure 4.3a, every spectrum was normalized to same area. A small shift (0.12 eV) to lower kinetic energy can be observed for $\text{CIGSe}^{\text{NaF+KF}}$ in Figure A.1.1. To investigate the difference, an original ($\times 0.75$) and shifted ($\times 0.25$) In MNN spectrum from $\text{CIGSe}^{\text{NaF}}$ sample were used to represent the In MNN Auger spectrum of the $\text{CIGSe}^{\text{NaF+KF}}$ sample. This suggests that In mainly present in a chalcopyrite environment; the shift/broadening is probably due to a second indium species at the surface. The residues of the fit are also shown below the spectrum. When shifts in binding energy (for core levels) and kinetic energy (for Auger lines) are combined to the modified Auger parameter (α'), it is a powerful tool for the identification of different chemical environments^[79]. Based on the fitting results, the computed $\text{In } \alpha'$ values for the investigated sample

series are presented in Figure 4.3 b, along with reported $\text{In } \alpha'$ values for four reference data regions, In_2Se_3 , CuIn_xSe_y , In_2S_3 , and In_2O_3 region.

In previous reports, the In MNN Auger kinetic energies of In_2Se_3 are located between 408.0 - 408.3 eV [52, 73]. Corresponding In $3d_{5/2}$ binding energies can be found between 444.3 and 445.1 eV [52, 72-73]. Similarly, for CuInSe_2 we find 408.4 eV [72] and 443.9 eV [73] - 445 eV [74]; for CuIn_3Se_5 we find 407.4 eV [52] and 444.1 eV - 444.8 eV [52, 73]; for In_2S_3 we find 407.3 - 407.4 eV [52, 78] and 444.7 - 445 eV [51-52, 78]; for In_2O_3 we find 406.0 - 406.8 eV [75-76] and 444.4 - 445 eV [72, 77]. Note that the doublet separation between In $3d_{3/2}$ (used in the analysis) and In $3d_{5/2}$ (for which reference values are reported) is 7.54 eV [80] and was considered when computing the modified Auger parameters derived from the measured data.

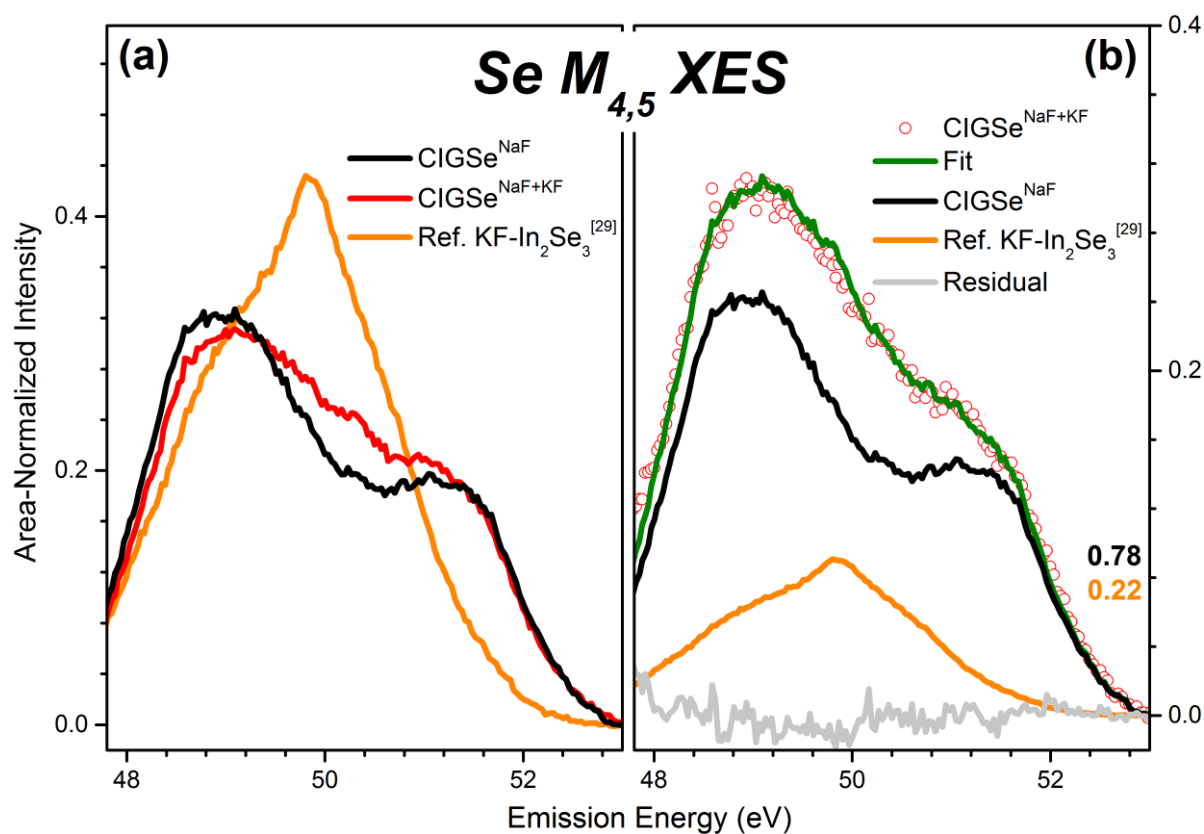


Figure 4.4. (a) Se $M_{4,5}$ emission spectrum of the $\text{CIGSe}^{\text{NaF}}$, $\text{CIGSe}^{\text{NaF+KF}}$, Reference KF-PDT In_2Se_3 samples [33]; (b) The Se $M_{4,5}$ XES spectrum of bare $\text{CIGSe}^{\text{NaF+KF}}$ absorber is represented by a spectral sum of $0.78 \cdot \text{CIGSe}^{\text{NaF}}$ and $0.22 \cdot \text{KF-PDT } \text{In}_2\text{Se}_3$. The difference between data and sum (residual) is also shown.

According to all the reference range and data points, the sample treated with NaF PDT in our experiment shows $\text{In } \alpha'$ values in the range of CuIn_xSe_y , which is from chalcopyrite. The two data points (In_a and In_b) from the represented $\text{CIGSe}^{\text{NaF+KF}}$ spectra are also shown. In_a α' value are close

to the values of $\text{CIGSe}^{\text{NaF}}$, and $\text{In}_b \alpha'$ value (852.26 eV) is similar as the $\text{KF-In}_2\text{Se}_3$ reference (852.19 eV), which suggest that the second In compound is a K-In-Se type species as in Ref.^[33].

To directly probe the impact of different PDTs on the local density of occupied Se-derived valence states, Se $M_{4,5}$ XES spectra were measured and fitted. Figure 4.4a displays the Se $M_{4,5}$ XES spectra of different PDT-treated CIGSe absorbers along with the KF-PDT In_2Se_3 reference sample^[33]. Comparing the respective spectra from different alkali-treated samples, the NaF PDT differs from the $\text{CIGSe}^{\text{NaF+KF}}$ in shape. The $\text{CIGSe}^{\text{NaF+KF}}$ absorber shows a more distinctive shape between 49 - 51.5 eV emission energy and an additional emission feature in this region. The Se $M_{4,5}$ XES spectra for KF treated In_2Se_3 have a feature at around 50 eV, which can explain the difference. The weighted sum of $0.78 \times \text{NaF-PDT CIGSe}$ and $0.22 \times \text{KF-In}_2\text{Se}_3$ represents well the $\text{CIGSe}^{\text{NaF+KF}}$ spectrum in Figure 4.4b. The difference (residual) between data and sum is also shown for clarity. This is a direct evidence and support for the formation of a K-In-Se type species.

As was found for the alkali-rich and alkali-poor NaF+KF PDT absorber in Ref. ^[33], we conclude that also a K-In-Se type surface compound is formed on the surface in this case. The result based on this sample is quantitatively located between alkali-rich and alkali-poor, and the difference can be attributed to normal variability of PDT process as well as to the refinement over time.

4.3 Impact of KF PDT on CdS/Cu(In,Ga)Se₂ interface

4.3.1 Interface chemical structure

4.3.1.1 Survey and detail spectra

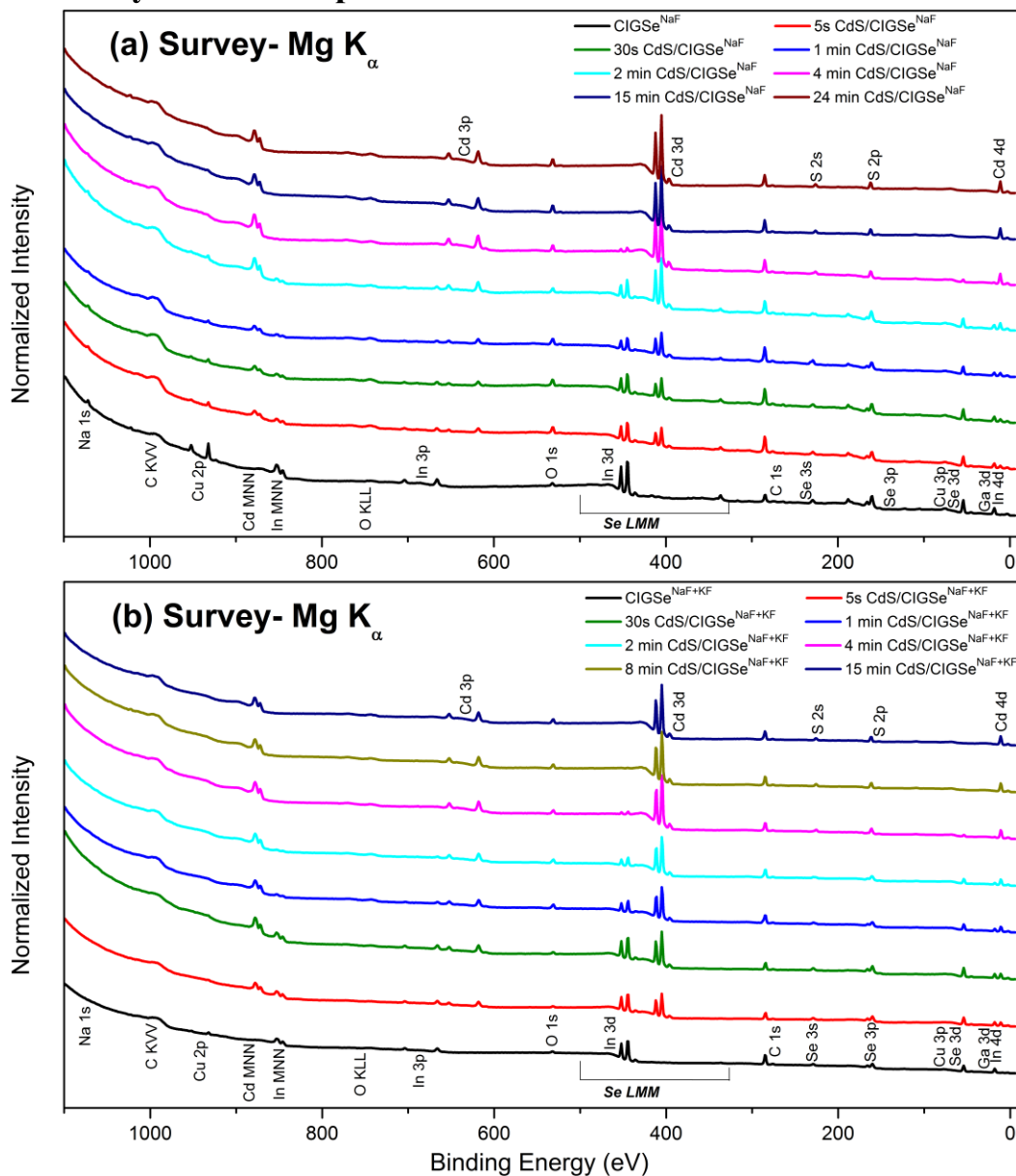


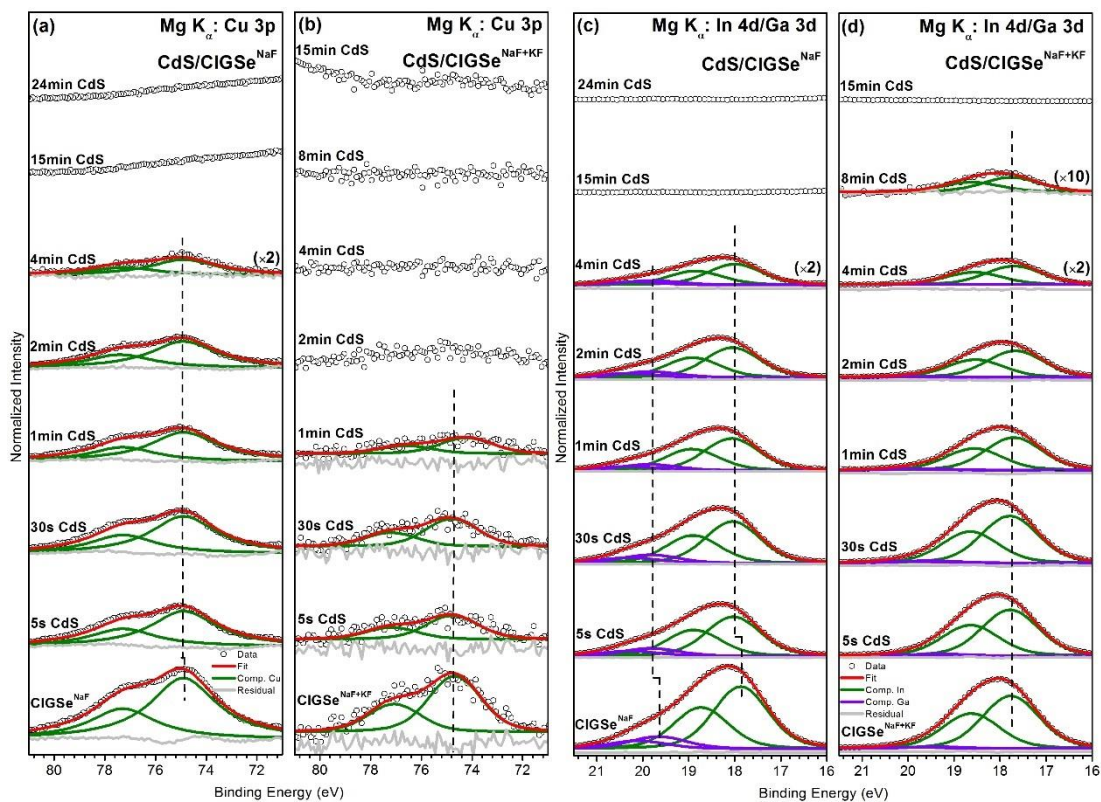
Figure 4.5. XPS survey spectra (normalized to background at a binding energy of 0 eV) of (a) CdS/CIGSe^{NaF} and (b) CdS/CIGSe^{NaF+KF} (deposition time varied between 0 and 24(15) min). All prominent photoemission and Auger lines are labeled. Spectra are vertically offset for clarity.

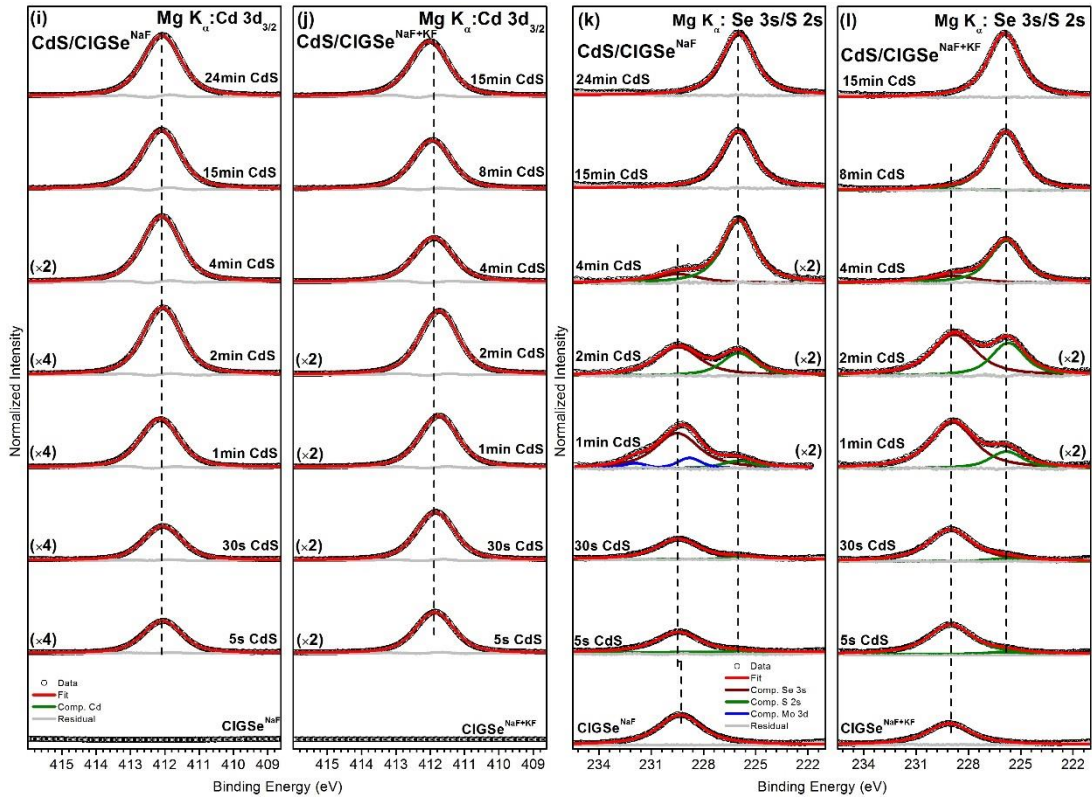
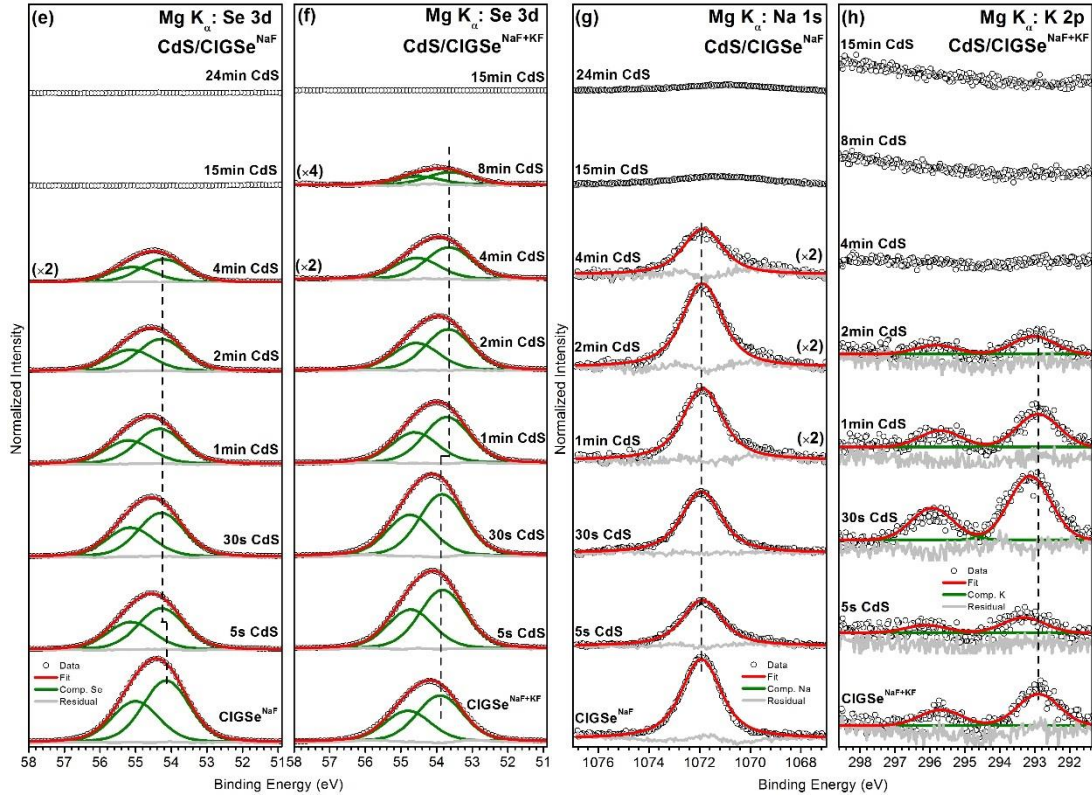
In the following section, the characterization of the chemical structure of the CIGSe absorber after CdS deposition will be presented. Sects. 4.2 based on bare CIGSe^{NaF} and CIGSe^{NaF+KF} is a foundation for this section. First, surface-sensitive PES experimental results are given. Then, X-ray emission spectroscopy measurements are presented and discussed.

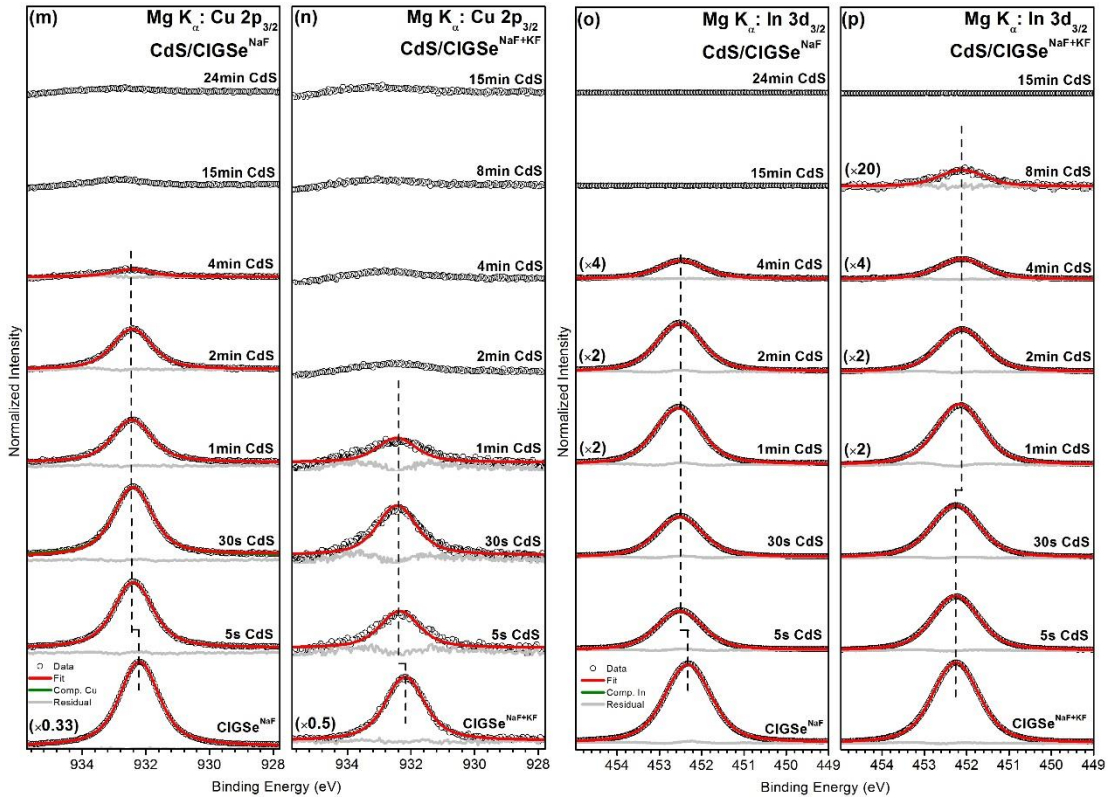
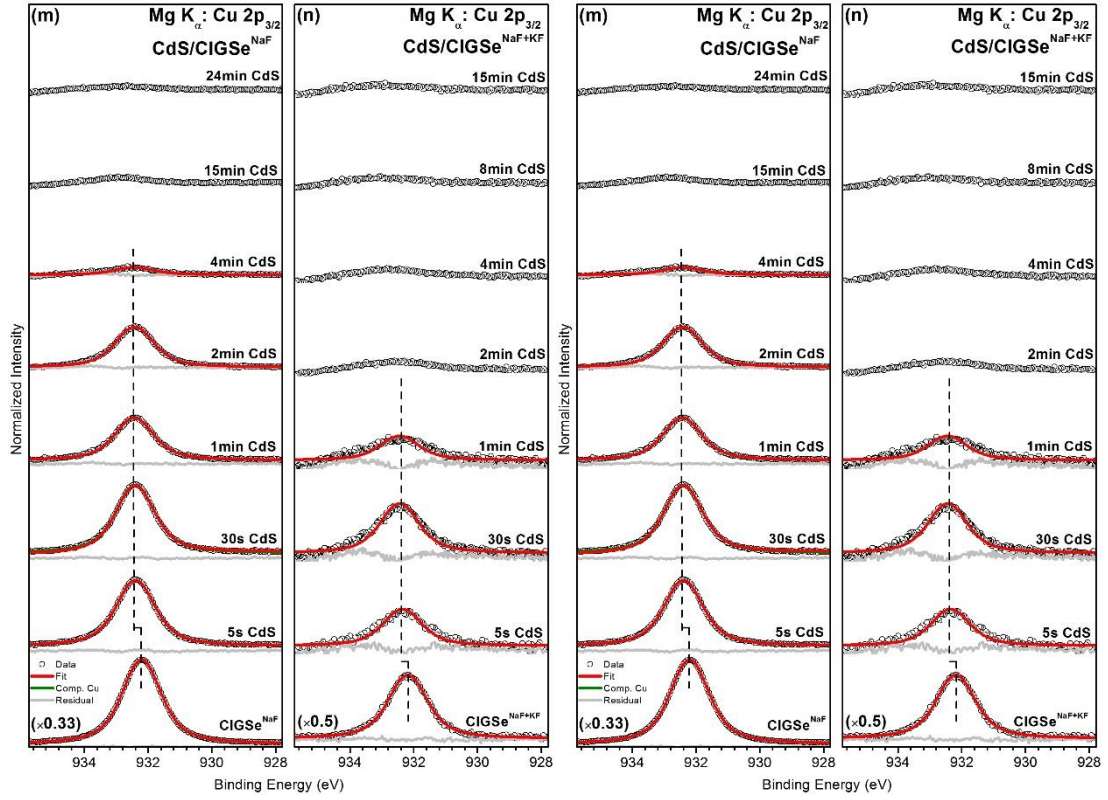
To study the impact of a NaF+KF PDT on the chemical structure of the CdS/CIGSe interface, a CdS thickness series was prepared by CBD (CdS/CIGSe^{NaF+KF}) and studied by XPS, XAES, and XES. In order to isolate the effect of potassium, the CdS/CIGSe^{NaF+KF} data are compared to the measurements of corresponding CdS/CIGSe samples for which the absorber was only subject to a NaF PDT (CIGSe^{NaF}). The XPS survey spectra of the two CdS/CIGSe sample series are shown in Figure 4.5. As expected, all Cu, In, Ga, Se, Cd, and S photoemission and Auger lines are present. The Cu, In, Ga, and Se peaks decrease in intensity, and Cd and S peaks increase with increasing CBD time, as expected. A Na-related XPS signal (most prominently the Na 1s line at 1071 eV binding energy) can only be observed for CdS/CIGSe^{NaF} samples. In addition, the presence of substantial C- and O-related XPS and XAES signals suggest surface contamination and/or incorporation of C and O into the deposited absorber and buffer layers (as discussed below). Cu signal intensity of the bare CIGSe^{NaF+KF} is significantly lower than for the CIGSe^{NaF} absorber, consistent with a strong surface depletion as previously reported^[26, 29, 69].

For more detailed chemical and electronic structure information, higher-resolution detail spectra were measured and are displayed – along with curve fitting results in Figures 4.6. The detail spectra of the background normalized Cu 3p, In 4d/Ga 3d, Se 3d, Na 1s (only for CdS/CIGSe^{NaF}), K 2p (only for CdS/CIGSe^{NaF+KF}), Cd 3d, Se 3s/S 2s, Cu 2p, In 3d, Ga 2p, and O 1s photoemission lines as a function of increasing CBD time and for different PDT treatments are shown. The Cu 3p spectra are shown after In 4p and Cd 4p background correction (see Appendix A.1). As expected, most of absorber related signals decrease and the CdS buffer related signals increase in intensity with CBD time. All fits of a particular data set and for a particular photoemission line have been performed simultaneously using Voigt profiles with the same coupled Lorentz and Gauss widths. In case of spin-orbit doublet fits, the multiplicity rule (2j+1) is obeyed and the doublet separation for Cu 3p, In 4d, Ga 3d, and Se 3d was set to 2.39 eV^[81], 0.86 eV^[82], 0.46 eV^[83], and 0.83eV^[84], respectively. The fit also included a linear background. Note that the Cd 3d_{3/2} and In 3d_{3/2} lines were chosen to fit instead of the more prominent respective 3d_{5/2} lines to avoid the Mg K_{α3,4}-excited 3d_{3/2} satellite lines that overlap with the 3d_{5/2} peak. All spectra but the O 1s line could be fit with one component. For O 1s more than one contribution (O_a and O_b for CdS/CIGSe^{NaF}; O_a, O_b, and O_c

for CdS/CIGSe^{NaF+KF}) was needed for a satisfactory representation. Feature O_a at about 531.7 eV can be assigned to metal oxides^[85-87], as e.g. In₂O₃^[85], Ga₂O₃^[86], or CdO^[87]. Feature O_b located at 532.7 eV can be attributed to adsorbed hydroxyl species^[88] and/or Cd(OH)₂^[89]. The third component O_c between 530.0 and 530.8 eV, which is only present in the data set of the CdS/CIGSe^{NaF+KF} series, is attributed to potassium-oxygen bonds, presumably with a mixed stoichiometry between K₂O and K₂O₂^[90]. Note the small blue contribution to the Se 3s fit for the 1min CdS/CIGSe^{NaF} (Figure 4.6 k&l) is attributed to a Mo 3d signal from the back contact presumably made accessible to the XPS analysis by accidental sample scratching during sample mounting. Furthermore, the broad signal detected at around 933 eV in Figure 4.6 m and n for thicker CdS samples (i.e. ≥ 15 min for CdS/CIGSe^{NaF} and ≥ 2 min for CdS/CIGSe^{NaF+KF}) is ascribed to a Cd MNN background rather than to Cu 2p_{3/2}.







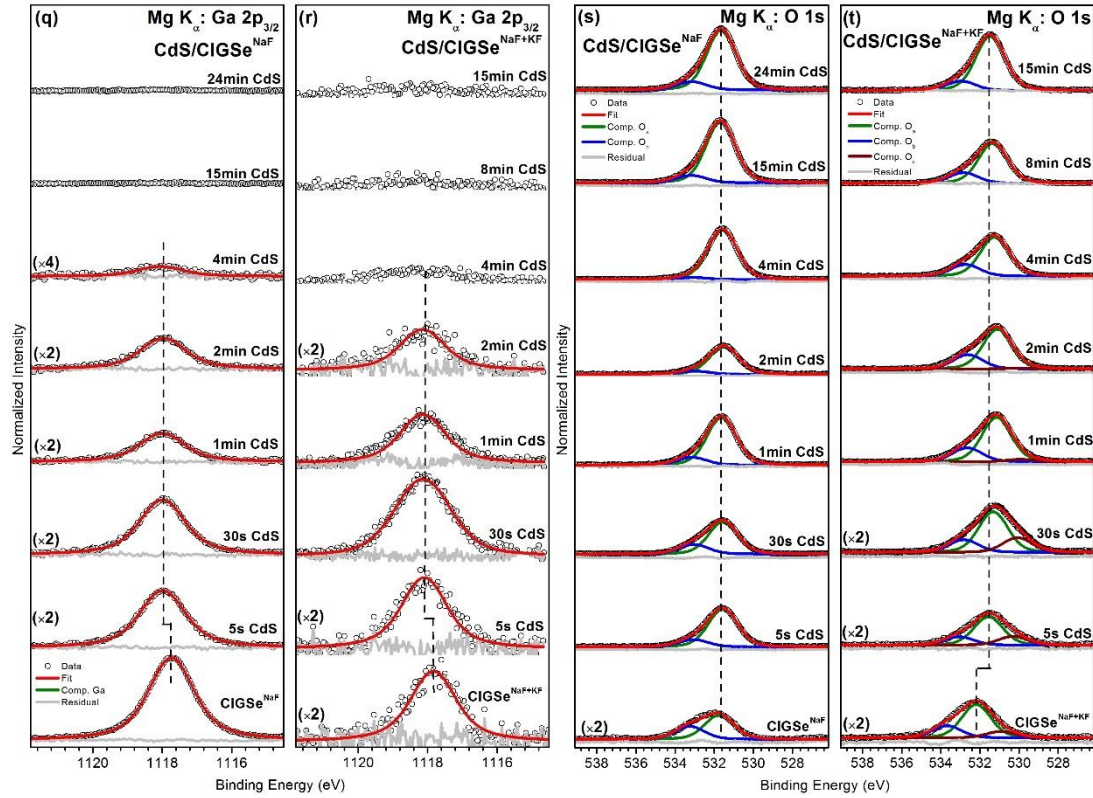


Figure 4.6. Cu 3p (a/b), In 4d&Ga 3d (c/d), Se 3d (e/f), Na 1s (g), K 2p (h), Cd 3d (i/j), Se 3s/S 2s (k/l), Cu 2p(m/n), In 3d (o/p), Ga 2p(q/r), and O 1s (s/t) XPS data with respective Voigt fits of the CdS/CIGSe^{NaF} (a, c, e, g, i, k, m, o, q, s) and CdS/CIGSe^{NaF+KF} (b, d, f, h, j, l, n, p, r, t) sample series, measured with excitation energies of 1253.56 eV (Mg K_α). All spectra are displayed after subtraction of a linear background. For each fit, the residual is shown as well. Note the different magnification factors. Spectra are vertically offset for clarity.

For the CdS/CIGSe^{NaF} series, there is a shift of ~ 0.2 eV to higher binding energies for the samples with CdS compared to the bare absorber; this same shift is also seen in the other absorber related core levels (i.e., Cu, Ga, Se) of this series. The In 3d_{3/2} binding energy of the CIGSe^{NaF+KF} is < 0.1 eV lower than that of the CIGSe^{NaF}, and the changes in the CdS/CIGSe^{NaF+KF} series are more complex – despite still being modelled with a single Voigt – with a shift of ~ 0.15 eV to lower binding energy after 30s CBD. This shift is not reproduced in the other absorber cations' core level spectra of this series; the Cu and Ga 2p of the CdS/CIGSe^{NaF+KF} series rather undergo a similar shift (~ 0.2 eV to higher binding energy after CdS deposition) to what is seen in the CdS/CIGSe^{NaF} series. All the variation for every element indicates more complex situation than in the CdS/CIGSe^{NaF+KF} series.

4.3.1.2 “CdS” thickness calculation

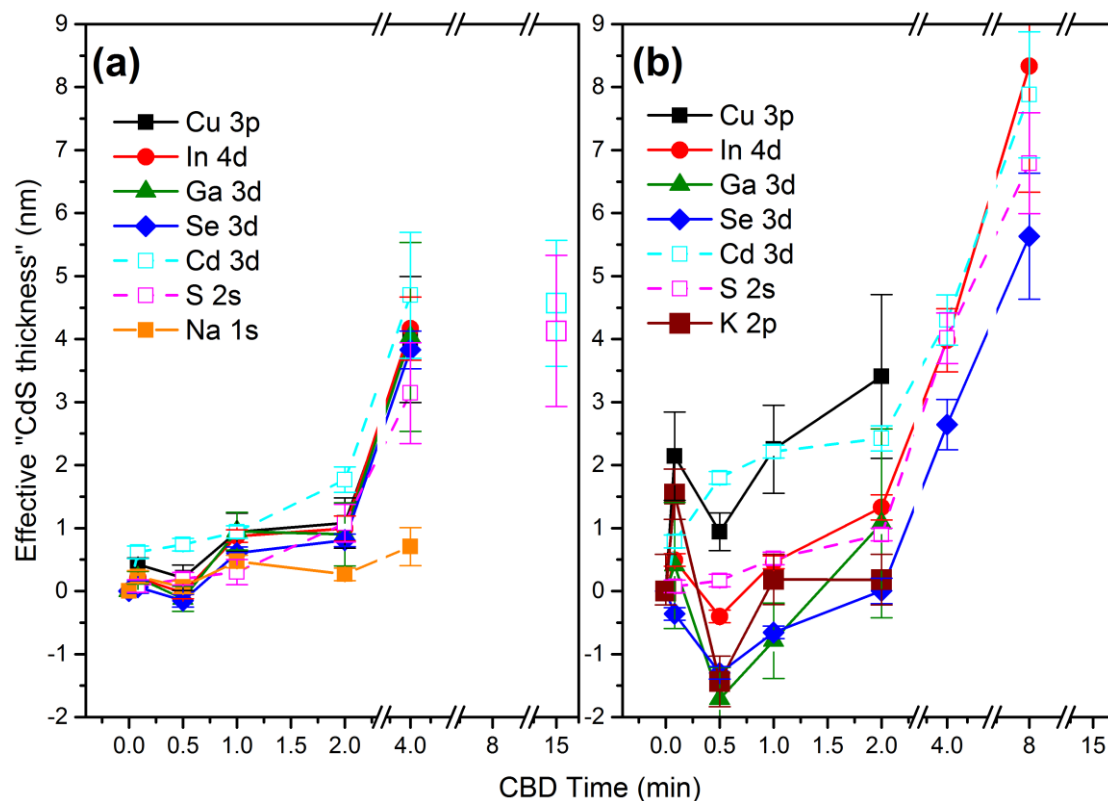


Figure 4.7. Evolution of the effective "CdS" layer thicknesses for the CdS/CIGSe^{NaF} (a) and CdS/CIGSe^{NaF+KF} (b) samples with increasing CBD time. The thickness values have been calculated based on the fit results in Figures 4.6, and the respective inelastic mean free path (IMFP, calculated by TPP2M^[91]).

Next, we discuss the chemical structure at the CdS/CIGSe interface and how it is influenced by the different PDTs. To do so, we consider the effective CdS thickness values calculated from the attenuation of each absorber shallow core level line (and from the increasing intensity of the Cd and S lines), assuming that the CdS components cover the CIGSe^{PDT} absorber; these element-specific thicknesses are displayed as functions of CBD time in Figure 4.7.

The evolution of the intensity of the absorber (mainly attenuation) and buffer (increasing amount of material) related lines with CBD-CdS treatment periods is used to estimate the effective thickness of the attenuating buffer layers. Based on the fitting results of the (shallow) core level spectra (Figures 4.6 a-l), the buffer layer thickness is calculated based on the IMFP of the respective photoelectrons in CdS.^[91] For absorber layer related elements, the intensity I^{abs} attenuated due to the increasing buffer layer and the effective buffer layer thickness d^{buf} are related – considering the used measurement geometry – according to the following formula:

$$I^{abs} = I_0 \times e^{-\frac{d^{buf}}{IMFP}} \quad (4.1)$$

where I_0 is the intensity of the lines of the bare CIGSe substrate. For this approach it is assumed that the buffer grows homogeneously layer-by-layer.

Similarly, for buffer layer related elements, the effective buffer thickness d^{buf} and the intensity of the increasing buffer-related photoemission lines I^{buf} are related according to:

$$I^{buf} = I_1 \times (1 - e^{-\frac{d^{buf}}{IMFP}}) \quad (4.2)$$

Here I_1 is the intensity of the buffer-related photoemission lines for the thickest buffer layer (i.e., 24 min CdS/CIGS^{NaF} and 15 min CdS/CIGS^{NaF+KF}). The used IMFP values (in CdS) for the respective core level photoelectrons are shown in Table 4.1.

Table 4.1. Calculated inelastic mean free path for the different photoelectrons in CdS according to the TPP2M formula^[91].

Photoelectrons (excited with Mg K α)	Inelastic mean free path [nm]
In 4d (E _K = 1236.6 eV)	2.325
Ga 3d (E _K = 1233.6 eV)	2.321
Se 3d (E _K = 1193.6 eV)	2.262
Cu 3p (E _K = 1173.6 eV)	2.233
S 2s (E _K = 1023.6 eV)	2.008
K 2p (E _K = 957.6 eV)	1.933
Cd 3d (E _K = 838.6 eV)	1.738
Na 1s (E _K = 178.6 eV)	0.642

The effective element-specific thicknesses derived for the CdS/CIGSe^{NaF} samples increase with CBD time and agree for all elements within the error bar as shown in Figure 4.7a. Note that the thickness plateau above 4 min CBD time is caused by the saturation of the Cd 3d and S 2s signal (i.e., after 4 min CBD, the layer is "infinitely" thick compared to the XPS information depth) and thus does not accurately represent the true CdS thickness but rather shows the limitation of this approach. The Na-related effective thickness agrees for short CBD times up to 1 – 2 min, but indicates a significantly lower thickness value for a CBD time of 4 min. This can be explained by redeposition (from the chemical bath) or diffusion (from the CIGSe^{NaF} absorber). Based on this preliminary examination of the effective thickness calculations, it appears that the buffer layer

grows without strong interfacial interaction between absorber and buffer elements. This is in contrast to our previous reports^[62] in which we see a S/Se intermixing at the CdS/CIGSe interface. However, this difference could be explained by a different absorber surface structure formed during the low-temperature deposition process (compared to the absorbers from a high-temperature deposition process studied in the past). It is also important to note that the CIGSe^{NaF} deposition process was not optimized to produce the best-performing cells, rather it was as similar as possible to the CIGSe^{NaF+KF} process; the absorber surface structure of an optimized CIGSe^{NaF} may differ in a significant enough way that S/Se intermixing could occur.

The effective element-specific thicknesses derived for the CdS/CIGSe^{NaF+KF} samples are shown in Figure 4.7b. The direct comparison with the thickness values derived for the CdS/CIGSe^{NaF} samples shows clear differences. After a CBD time of 5 s the derived thicknesses have all increased except for the Se-based values, with the largest thicknesses (exceeding that derived for the CdS/CIGSe^{NaF} samples) determined for Cu and K, i.e., the intensity of the Cu 3p and K 2p lines have decreased most. From 5 s to 30 s CBD time, the thickness values based on the intensity evolution of the absorber elements (including K) then decrease to an extent that they even result in “negative thicknesses” calculated for In, Ga, K, and Se. The drop is biggest for K and very similar for all other absorber elements. These negative values arise due to the increase of the respective XPS line intensities to values above that measured for the bare CIGSe^{NaF+KF} absorber, indicating significant chemical interaction involving these elements during that CBD period. For a CBD time of 1 min and longer all thickness values increase steadily (with some variation for K-based values – indicating a more complex situation, as discussed below), as expected for regular buffer layer growth. Furthermore, we observe a different behavior for the Cd and S derived thickness values. Especially for CBD times below 2 min, the Cd-based thicknesses are significantly larger than the S-based thicknesses and the corresponding thickness in the CdS/CIGSe^{NaF} series. This difference indicates that at early stages of CdS CBD on CIGSe^{NaF+KF}, Cd is deposited not (only) as stoichiometric CdS but might (also) be incorporated into the upper surface of the CIGSe^{NaF+KF} absorber and/or present in other chemical forms.

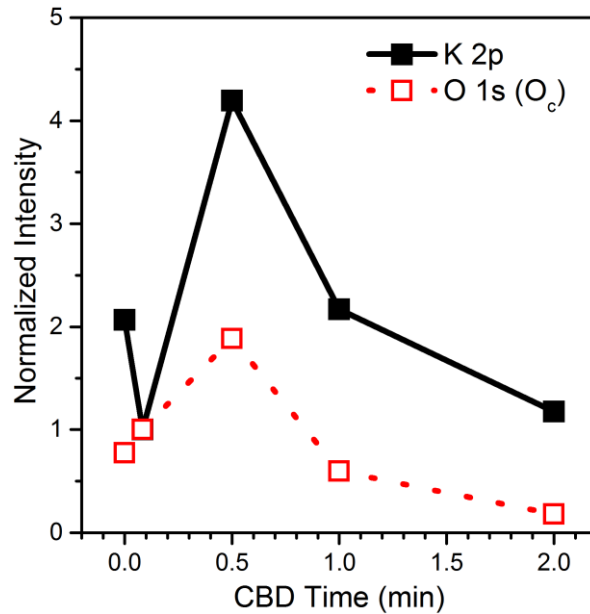


Figure 4.8. Intensity evolution of the K 2p (black) and O_c species (red) with increasing CBD time, normalized to the respective intensity values derived for the 5s CdS/CIGSe^{NaF+KF} sample.

As shown in Figure 4.6 s and t, there is a clear difference between the O 1s spectra of the two CdS/CIGSe sample sets. In the CdS/CIGSe^{NaF+KF} series, an additional low-binding energy O 1s component (O_c) appears for CBD times ≤ 2 min. In the same CBD regime, we find a clear K 2p signal (Figure S5b) on the respective samples. Comparing the intensity evolution of the K 2p_{3/2} peak to that of the O 1s feature O_c in Figure 4.8, a clear correlation is revealed for CBD times ≥ 5 s suggesting the presence of O-K bonds (see also discussion in conjunction to Figure 4.6h, above). The deviation for the bare absorber can be explained by potassium being present in a different chemical environment (i.e. a K-In-Se type species). The significant intensity variation of the K 2p (and the O 1s (O_c)) line in the early stages of the CBD process indicates a complicated process probably involving dissolution and redeposition, or possibly diffusion. Furthermore, it should be considered that the formation of K-O bonds in this CBD time regime could very well be an artifact of sample preparation (i.e., retrieving the samples after the given time in the CBD solution with subsequent rinsing).

4.3.1.3 Modified auger parameter analysis

As in chapter 4.2 for the bare CIGSe absorbers, In and Cd modified Auger parameters are used to identify their chemical states in the CdS/CIGSe series. Figure 4.9 shows the Cd M₄₅N₄₅N₄₅/In

$M_{45}N_{45}N_{45}$ XAES lines as a function of CdS-CBD time for the $CdS/CIGSe^{NaF}$ and $CdS/CIGSe^{NaF+KF}$ series. In Auger spectra appear at high kinetic energy range ($E_K=395\text{ eV}-415\text{ eV}$) and Cd Auger spectra locate at lower kinetic energy ($E_K=365\sim 390\text{ eV}$). The significant overlap of the two Auger structures complicates the results, and a careful procedure must be followed to ensure that (especially) the present of In MNN does not produce artifacts in the analysis of the Cd MNN.

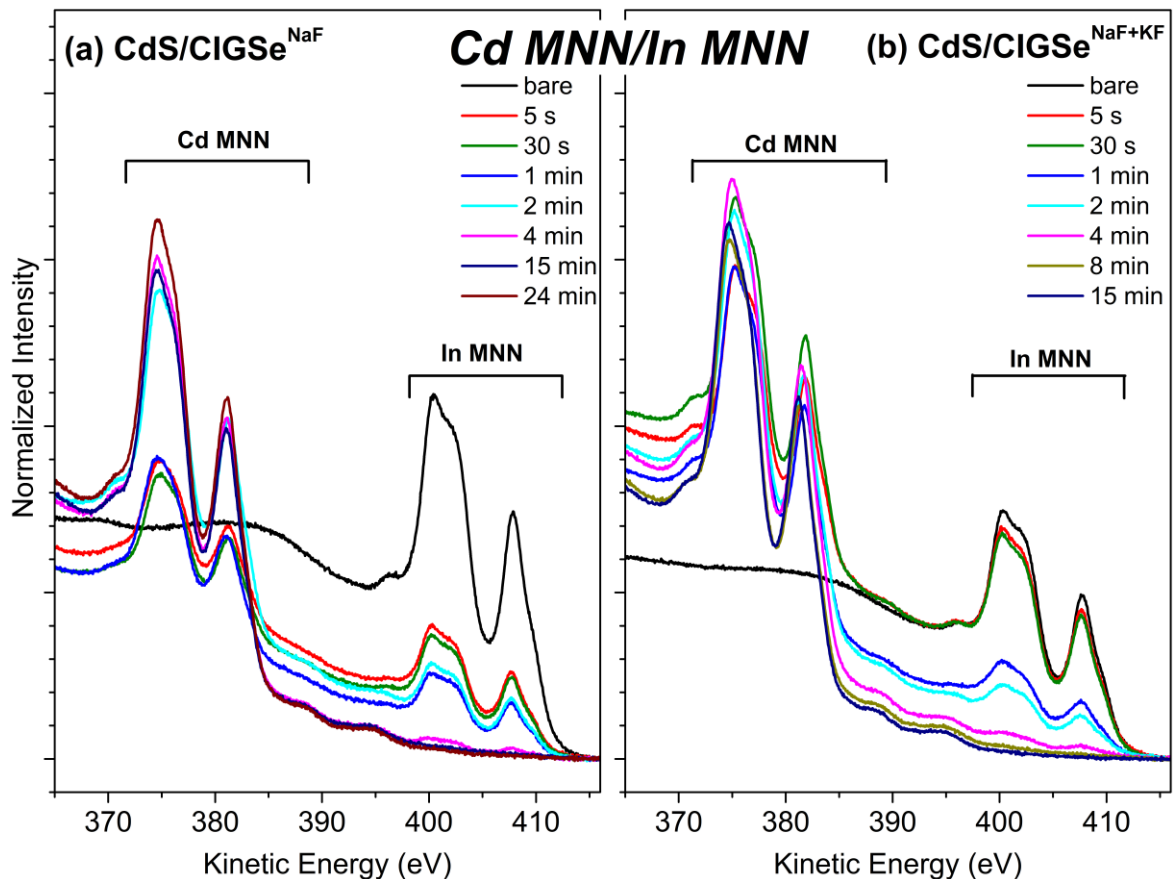


Figure 4.9. Evolution of the background normalized Cd $M_{45}N_{45}N_{45}/In\ M_{45}N_{45}N_{45}$ XAES spectra with increasing CdS-CBD time. All spectra were measured using Mg K_{α} (1253.56 eV) excitation.

From the first glance of Cd $M_{45}N_{45}N_{45}/In\ M_{45}N_{45}N_{45}$ XAES spectra, it is observed that In MNN decreases faster and Cd increases (with In MNN background) slower for $CdS/CIGSe^{NaF}$ series, which indicates different Cd/In environments or content compared to the NaF PDT series. The detail Cd $M_{45}N_{45}N_{45}$ spectra analysis is affected by In $M_{45}N_{45}N_{45}$ spectra significantly. Hence, In MNN spectra must be considered first, and then subtracted from the Cd MNN spectra before they can be analyzed.

4.3.1.3.1 Indium modified auger parameter analysis

In Figure 4.6, each measured In $3d_{3/2}$ spectrum was fitted by a single Voigt function, all with the same Gaussian and Lorentzian contributions. The spectral shape of the In MNN of the CdS/CIGSe^{NaF} samples is largely independent of CdS deposition, in agreement with the unchanging In $3d_{3/2}$ (Figure 4.6o/p). Thus, for this series, all In MNN spectra can be represented by the sum of the (scaled and shifted) In MNN spectrum of the bare CIGSe^{NaF} absorber (component In_a) and a suitable (Cd MNN induced) background spectrum (i.e., the spectrum of the 24 min – CdS/CIGSe^{NaF} sample). In contrast, the In MNN spectra of the CdS/CIGSe^{NaF+KF} series do change in spectral shape upon CdS deposition and with CdS deposition time (see Figure 4.10b). In order to analyze these spectra, we use the In MNN spectra of the bare CIGSe^{NaF} absorber (which has the narrowest shape and thus is used as a reference spectrum presenting one In species) to fit the In MNN spectra of the CdS/CIGSe^{NaF+KF} sample set. In this procedure, each spectrum can be reproduced as a sum of two contributions (plus 15 min CdS/CIGSe^{NaF+KF} background spectrum) – one at almost constant energy position corresponding to the CIGSe^{NaF} In_a position (and thus also attributed to species In_a) and a second species which shifts as a function of CBD time, attributed to In_b, In_c, and In_d. In order to identify these components, we consult the modified Auger parameter next.

As in Chapter 4.2, the calculated In modified Auger parameters (α') of indium for both PDT series and related In-compounds reference boxes are shown in Figure 4.11. Hence, for the CdS/CIGSe^{NaF+KF} series, the shifted contributions to the XAES spectra (components In_a – In_d) are treated as distinct chemical species, because the lack of a shift in the corresponding In $3d_{3/2}$ spectra gives them a distinct value of α' . The direct comparison with α' values for related In-compounds reveals that component In_a is attributed to a similar chalcopyrite type environment for both CdS/CIGSe sample series. Note that the α' value for the CdS/CIGSe^{NaF} samples lie on the same diagonal as the values of the bare absorbers, although the binding energy value falls slightly outside the reference box defined by published binding energies.

The modified Auger parameter of component In_b, which is only found for the bare CIGSe^{NaF+KF} absorber, agrees – within experimental uncertainty – with that of the K-In-Se – type species, described in our earlier study^[33]. For the 5s and 30s CdS/CIGSe^{NaF+KF} the In_c species appear in the Auger spectra, while the core level spectra remain at the same binding energy as the bare absorber.

The α' value of In_c suggests the formation of an In-containing interface species in this CBD time regime. Note that the relative contributions of In_a and In_c are nearly constant for the two spectra. Component In_d is found for 1, 2, 4 min $\text{CdS}/\text{CIGSe}^{\text{NaF+KF}}$ samples and can clearly be attributed to the formation of In-O bonds. After 1 min CBD time, the chemical environment of In ceases to change, and there is only a decrease in the corresponding XPS/XAES intensities consistent with attenuation of the signal by the growing buffer layer.

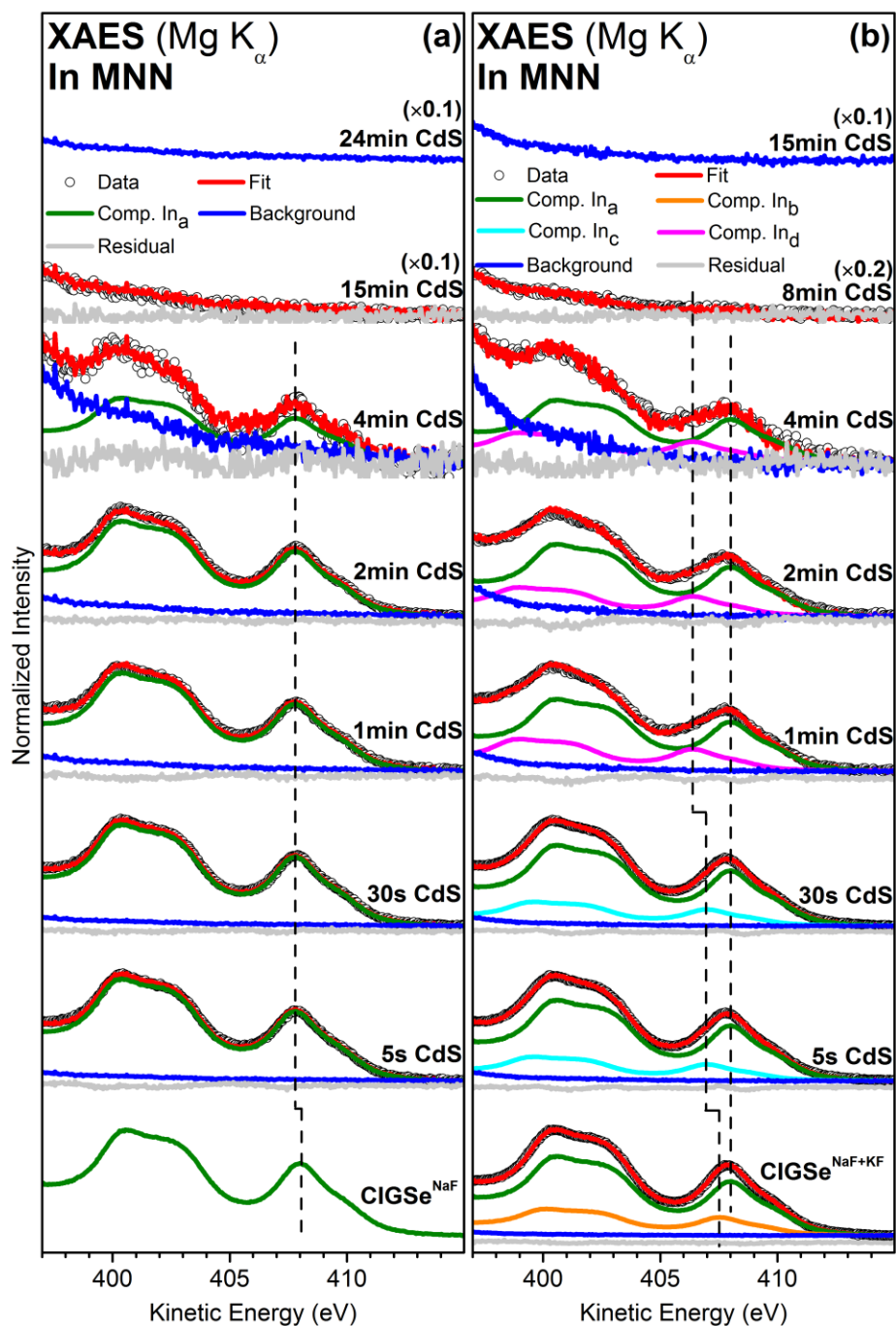


Figure 4.10. In $M_{45}N_{45}N_{45}$ XAES spectra of the CdS/CIGSe^{NaF} (a) and CdS/CIGSe^{NaF+KF} (b) sample series together with their spectral analysis. The reference spectra summed up to represent the data are the (scaled and shifted) In MNN spectra of bare CIGSe^{NaF} absorber and a suitable (Cd MNN induced) background spectrum (i.e., the spectrum of the 24 min – CdS/CIGSe^{NaF} sample and the 15 min – CdS/CIGSe^{NaF+KF} sample, respectively). For the CdS/CIGSe^{NaF} spectra, one In MNN component (In_a) and the background spectrum is sufficient to achieve a reasonable agreement, while for the CdS/CIGSe^{NaF+KF} data four different In MNN components (In_a, In_b, In_c, and In_d – with at most two at the same time) are required. All spectra were measured using Mg K_α excitation. Vertical offsets are added for clarity.

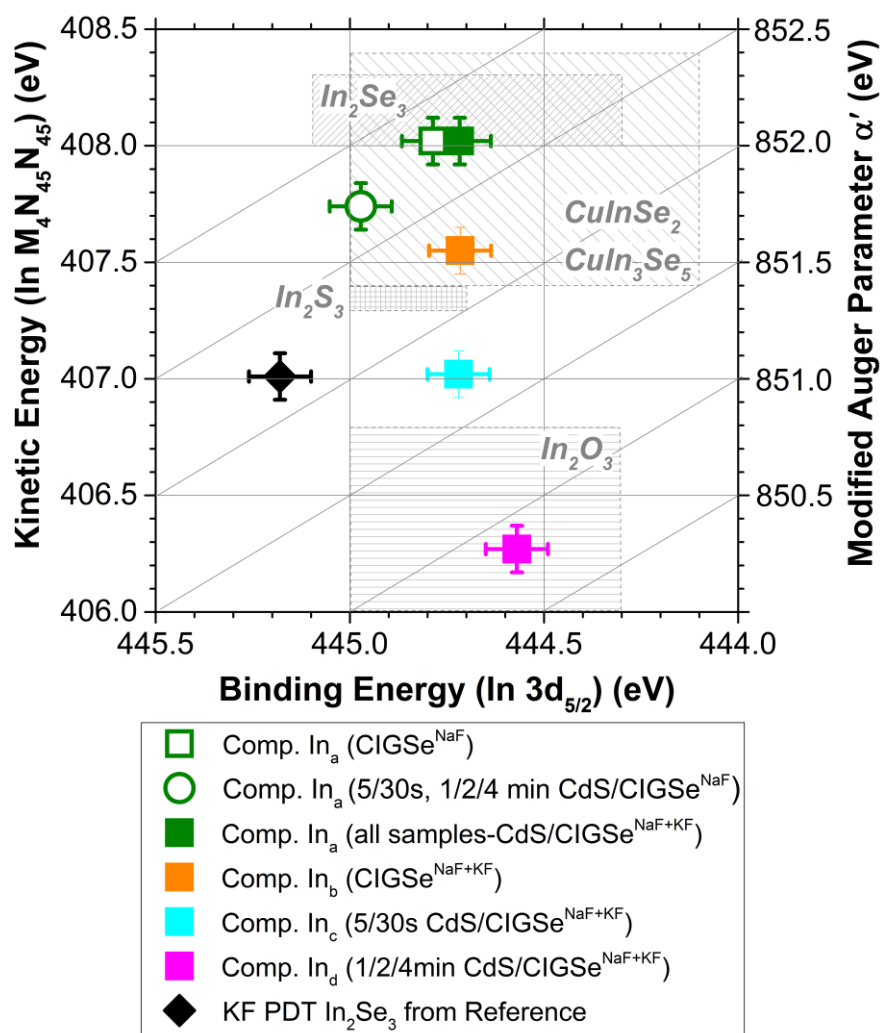


Figure 4.11. Evolution of the modified Auger parameter (α') of In [i.e., the sum of the binding energy (E_B) of the In 3d_{5/2} photoemission line and the kinetic energy (E_K) of the In M₄₅N₄₅ Auger line] with increasing CdS CBD time. The KF-In₂Se₃ reference data point was adopted from Ref. [33]. For comparison, reference position area for In₂Se₃, CuInSe₂, CuIn₃Se₅, and In₂O₃ compounds (as derived based on data in Ref. [52, 72-77]) are indicated. The error bars are dominated by the uncertainty in the determination of the energy position of the individual components.

4.3.1.3.2 Cadmium modified auger parameter analysis

To study the interface formation from the viewpoint of the deposited buffer layer, the Cd modified Auger parameters α' (calculated in similar fashion to the In parameters above) are discussed next. Since the Cd $M_{45}N_{45}N_{45}$ spectra (E_K : 370 eV~390eV) are significantly influenced by the In $M_{45}N_{45}N_{45}$ (E_K : 395 eV~415eV) spectra, In $M_{45}N_{45}N_{45}$ spectra were subtracted according to the fitting results depicted in Figure 4.10, which included the Cd MNN background. The subtraction details are visualized in Figure 4.12.

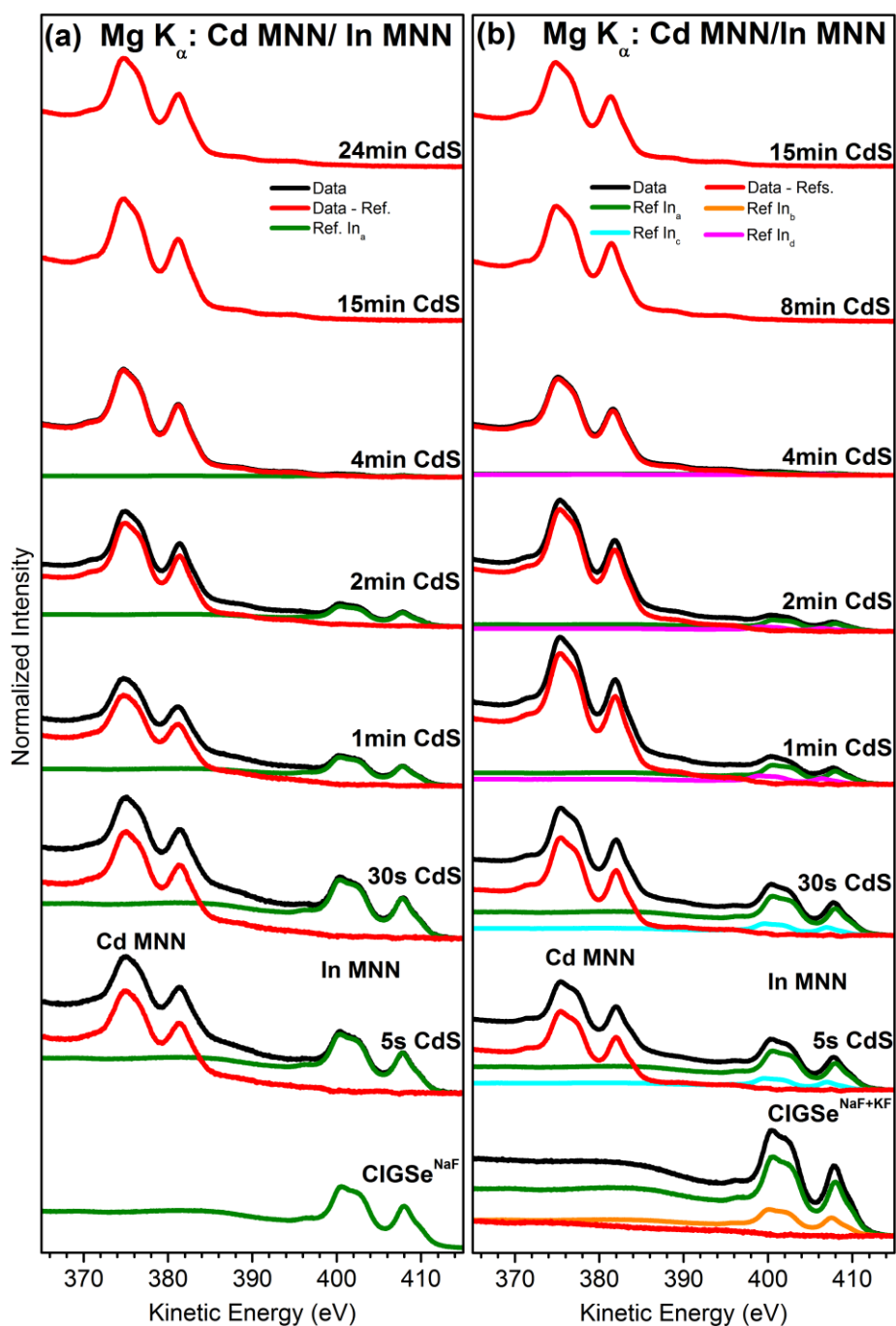


Figure 4.12. In MNN background-corrected Cd $M_{45}N_{45}N_{45}$ XAES lines of the CdS/CIGSe^{NaF} (a) and CdS/PDT/CIGSe^{NaF+KF} (b) sample series with increasing CBD time, measured using Mg K_{α} excitation. Vertical offsets are added for clarity. The reference spectra representing component Cd_a or Cd_b are properly scaled and shifted Cd MNN spectra of the thickest sample per sample set (i.e., the spectrum of the 24 min CdS/CIGSe^{NaF} sample and that of the 15 min CdS/CIGSe^{NaF+KF} sample are used as single-species references).

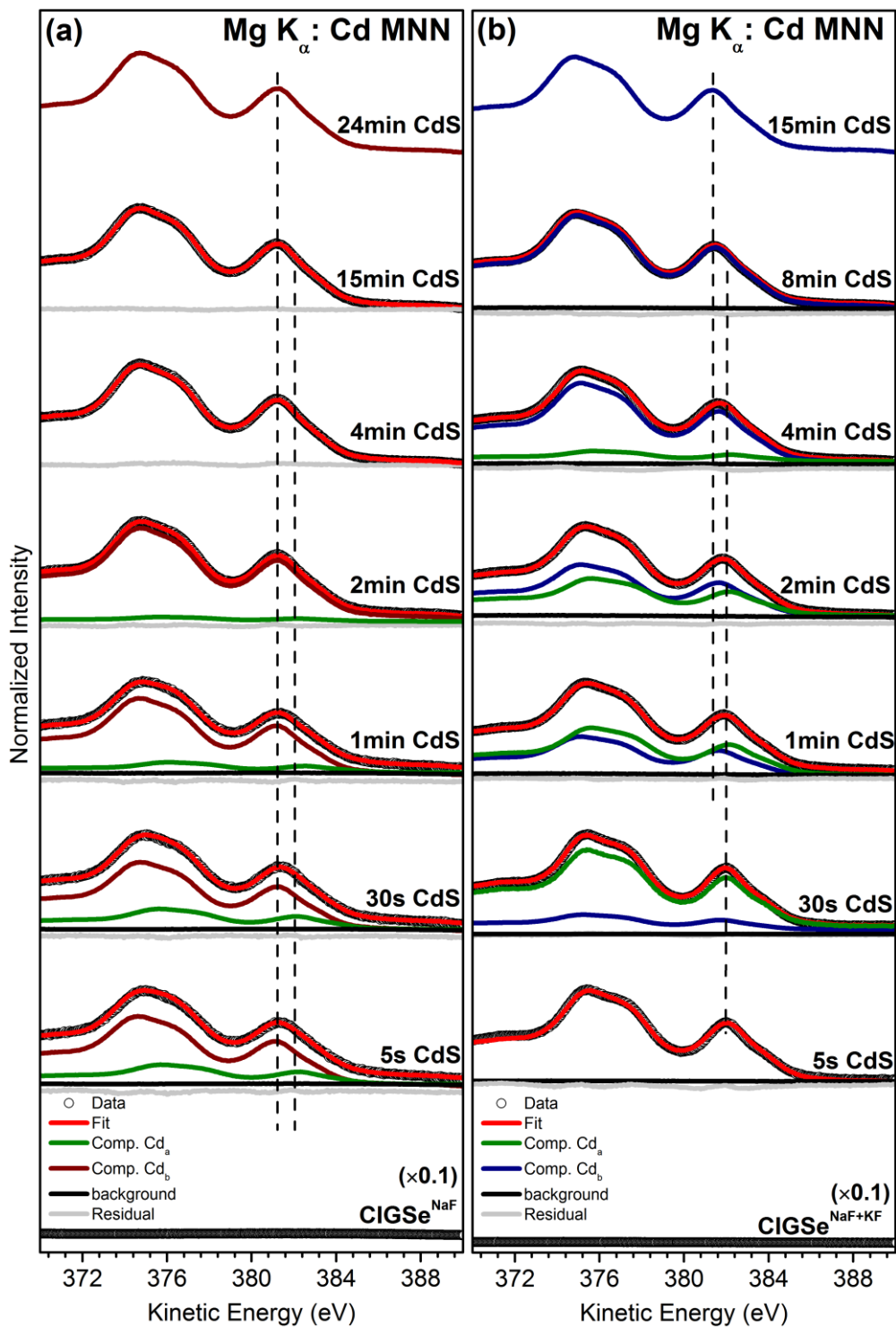


Figure 4.13. In MNN background-corrected Cd $M_{45}N_{45}N_{45}$ XAES lines of the CdS/CIGSe^{NaF} (a) and CdS/PDT/CIGSe^{NaF+KF} (b) sample series with increasing CBD time, measured using Mg K_{α} excitation. Vertical

offsets are added for clarity. The reference spectra representing component Cd_a or Cd_b are properly scaled and shifted Cd MNN spectra of the thickest sample per sample set (i.e., the spectrum of the 24 min CdS/CIGSe^{NaF} sample and that of the 15 min CdS/CIGSe^{NaF+KF} sample are used as single-species references).

After In M₄₅N₄₅N₄₅ background correction, peak-area-normalized Cd M₄₅N₄₅N₄₅ spectra were fitted and are shown in Figure 4.13. Since Cd MNN Auger spectra of the thickest samples for each data set (i.e. the spectrum of the 24 min CdS/CIGSe^{NaF} sample and the spectrum of the 15 min CdS/CIGSe^{NaF+KF} sample) have the same spectral shape and are the narrowest, these spectra were also used as single-species references to (properly scaled and shifted) fit all other Cd MNN Auger spectra.

For the Cd modified Auger parameter, we followed a similar procedure. We combined the following kinetic energies of Cd MNN Auger and corresponding binding energies of Cd 3d_{5/2} peaks: for CdSe 381.20 eV – 381.90 eV^[92-93] and 404.80 - 405.45 eV^[52, 93-94]; for CdS 381.00 – 381.6 eV^[52, 95] and 405.00 – 405.40 eV^[96-97]; for Cd(OH)₂ 379.90 – 380.7^[95, 98] and 405.10 - 405.60 eV^[98-100]; for CdO 382.1 - 382.7 eV^[95, 101-102] and 404.00 – 405.2 eV^[52, 101-102]. Note that also in this case the doublet separation between Cd 3d_{5/2} and Cd 3d_{3/2} of 6.75 eV^[103] has to be considered for the measured data.

For both CdS/CIGSe^{NaF} and CdS/CIGSe^{NaF+KF} series, two distinct components defined initially as Cd_a and Cd_b are needed to explain the spectra, but the relative quantities vary distinctly between the two series, confirming that the buffer deposition proceeds quite differently depending on PDT. For the CdS/CIGSe^{NaF+KF} series, a strong Cd_a signal forms in the first stage of CBD (i.e., for the 5 s sample). In the discussion of Figure 4.7b, we described how Cd was deposited without corresponding quantities of S in the early stages of CBD; it strongly indicates that other Cd compounds are formed at the interface. This is corroborated by the α' values for Cd_a in Figure 4.14b, which are directly compared to α' values for related Cd-compounds^[52, 92-98, 100-102] (CdSe, CdS, CdO, and Cd(OH)₂). Within the experimental uncertainty, we find an agreement between the modified Auger parameter of CdSe and that of Cd_a (at least for CBD times up to 2 min). However, the fact that due to a seemingly high E_K of the respective Cd MNN spectra, the Cd_a α' values are located outside the indicated CdSe box (i.e., being more in agreement with what would be expected for Cd-O bonds, in particular for the 4 min CdS/CIGSe^{NaF+KF} sample), indicating that the interface

compound has a more complex chemical structure than pure CdSe. For larger CBD times, a second species, Cd_b is present, and the relative Cd_a contribution decreases in a way that is consistent with what would be seen from an interface species, i.e. the Cd_a signal is attenuated by a capping (buffer) layer of increasing thickness. After 8 min CBD, the Cd_a contribution is effectively zero, and the spectra again represent a single phase, Cd_b, characteristic of the completed buffer layer. Based on the comparison and agreement of the α' values for Cd_b with that of CdS, we attribute it to Cd-S bonds. (However, note that the composition of the buffer layer is more complex than pure CdS, as will be discussed below.)

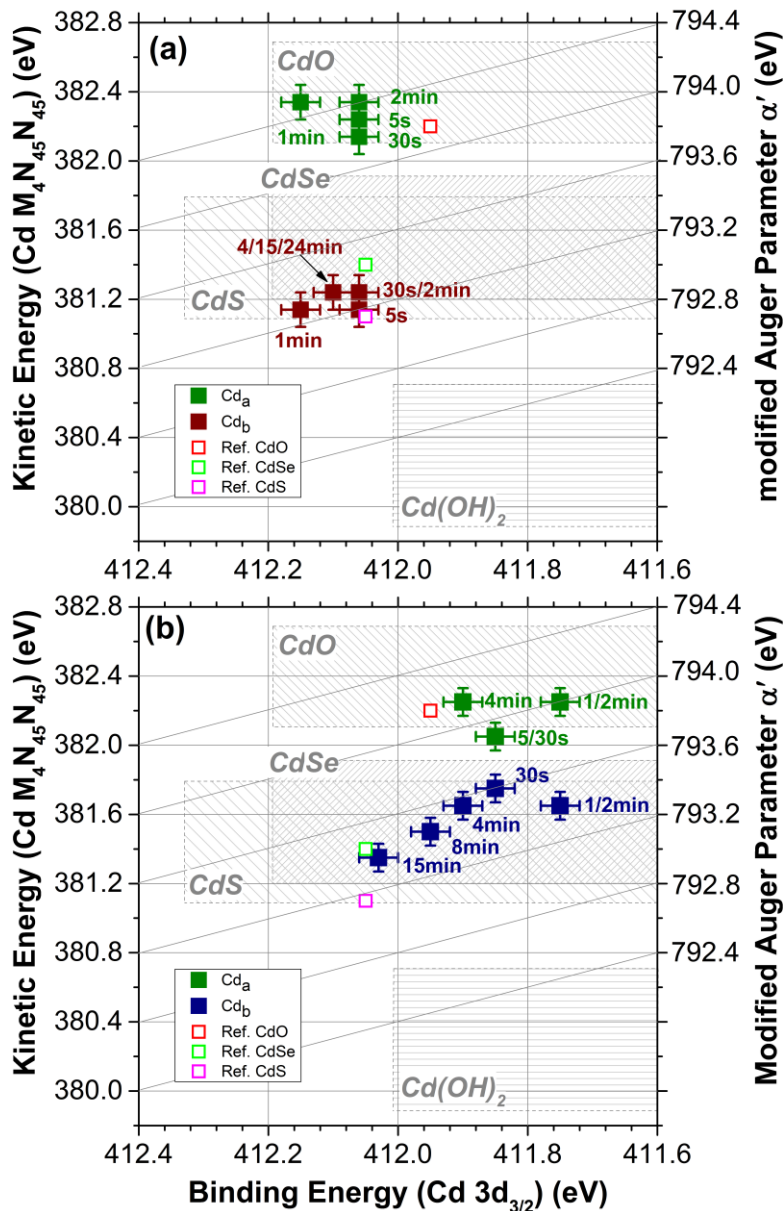


Figure 4.14. Evolution of the modified Auger parameter (α') of Cd [i.e., the sum of the binding energy (E_B) of the Cd 3d_{3/2} photoemission line and the kinetic energy (E_K) of the Cd M₄N₄₅N₄₅ Auger line] with increasing CBD time: (a) for the CdS/CIGSe^{NaF} and (b) for the CdS/CIGSe^{NaF+KF} sample set. Reference positions for CdO, CdS, CdSe, and Cd(OH)₂ compounds are indicated^[52, 92-98, 100-102]. The error bars are dominated by the uncertainty in the determination of the energy position of the individual components.

For the CdS/CIGSe^{NaF} series, we find the Cd MNN Auger spectrum of the 5s CBD CdS/CIGSe^{NaF} sample in Figure 4.14a is more complex than the corresponding CdS/CIGSe^{NaF+KF} spectrum, as it already requires two contributions for an adequate description. We again label these components Cd_a and Cd_b, and their general behavior is similar to that of the corresponding components in the CdS/CIGSe^{NaF+KF} described above, with some differences in specifics. In the CdS/CIGSe^{NaF} series, Cd_a is only a relatively small contributor and disappears completely after 2 min CBD, and again it appears consistent with a species formed at the interface. (Since Cd_a seems to form exclusively in the induction period of the CdS CBD process, it might very well be possible that Cd_a forms only in the early stages of CBD and would no longer be present if the process was not interrupted; i.e., it may be an artifact of the non-standard CBD process used to produce the “thin” buffer layers for this experiment.).

The values of α' , coupled with the higher Cd 3d binding energies, indicate that in this series Cd_a is likely a CdO species, unlike the corresponding species formed at the CdS/CIGSe^{NaF+KF} interface, as depicted in Figure 4.14b. When Cd_b is formed, it is much more uniform in Cd 3d binding energy and α' than the corresponding data in Figure 4.14b, and falls very close to expected values for CdS. The presence of Cd_b in all spectra, including for very short CBD times, is in agreement with the discussion of Figure 4.7a. The analysis of the Cd Auger parameter does not suggest that Cd(OH)₂ is present in significant amounts in either of the sample sets, however, the respective O 1s spectra in 4.6s/t, does show a high binding energy component (O_b) at approx. 532.7 eV, which we attribute to hydroxyl groups. The ratio of O_a (the main O 1s peak in Figure 4.6s/t, attributed to oxides) to O_b indicates that the amount of hydroxide present is small relative to the oxide content ([12 ± 2]% for the 2 – 24 min CdS/CIGSe^{NaF} samples and [25 ± 3]% for the 2 – 15 min CdS/CIGSe^{NaF+KF} samples). The hydroxide and its corresponding spectral signature (if present) is expected to appear in the measurement of all samples, including the “single species” reference curve used to fit the Cd MNN

curves. Thus, as long as the hydroxide content is relatively stable, the Auger spectra analysis method is not sensitive to $\text{Cd}(\text{OH})_2$, potentially explaining why no $\text{Cd}(\text{OH})_2$ species is specifically identified.

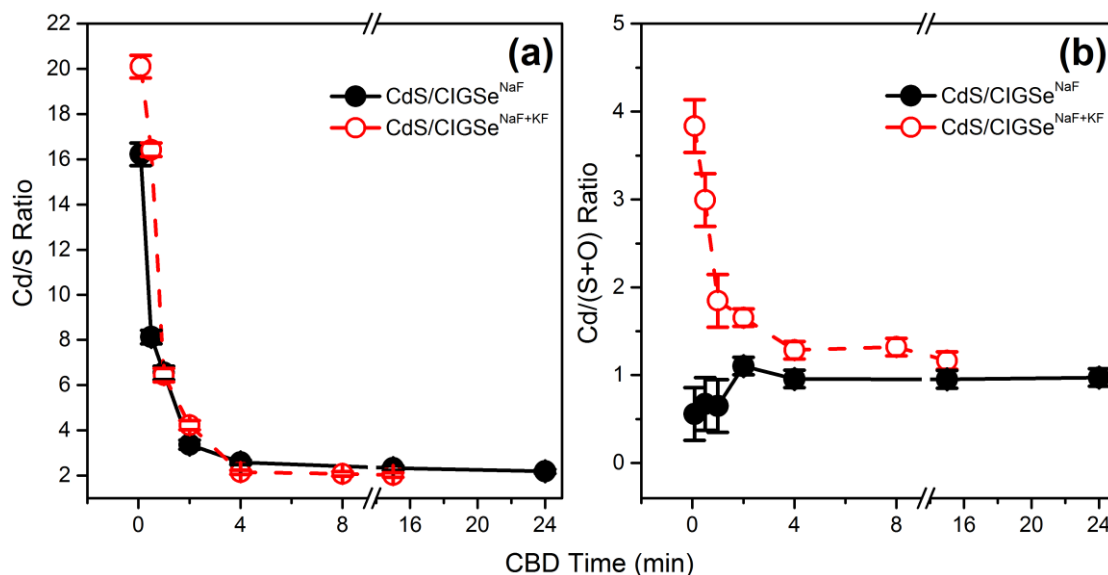


Figure 4.15. Evolution of (a) the Cd/S ratio and (b) Cd/(S+O_{a+b}) ratio with increasing CBD time. The ratios were derived based on the fit results in Figures 4.6 i-l and s/t, corrected by the respective inelastic mean free path (IMFP calculated by TPP2M^[91]), analyzer transmission function, and photoionization cross section^[68] values.

The Cd/S ratio (derived from the Cd 3d and S 2s spectra in Figures 4.6 i-l) clearly deviates from the stoichiometry expected for CdS independent of performed PDT, as shown in Figure 4.15 a. For short CBD times, the ratio is quite large, and we attribute this to the formation of S-free (or poor) Cd species at the interface (as indicated in Figure 5 and related discussion). However, even for long CBD times, we find Cd/S ratios of approximately 2 for both sample sets, indicating that the buffer material is not stoichiometric CdS. When the Cd/(S+O_{a+b}) ratio is calculated instead, the expected cation/anion ratio of approximately 1 is derived for CBD times > 2 min, suggesting that the buffer is better described as a Cd(O,S) like compound. The S 2s (Figure 4.6 k/l) indicate that the mixed phase forms without S-O (i.e., sulfate) bonds, which would be indicated by a clear peak at high binding energy as reported for S 2p^[104]. For short CBD times, the Cd/(S+O_{a+b}) is still quite large for the CdS/CIGSe^{NaF+KF} sample set, as was the Cd/S ratio, in agreement with the formation of additional Cd-Se bonds at the interface as discussed in conjunction with Figures 2 and 5. For the

CdS/CIGSe^{NaF} series, the Cd/(S+O_{a+b}) ratio is below 1 for CBD times shorter than 2 minutes, indicating that the (hydr)oxide features O_{a+b} in the O 1s spectra are not exclusively related to Cd.

4.3.2 Soft X-ray emission spectroscopy

This part will focus on x-ray emission spectroscopy to directly probe the occupied local density of states to provide element-specific information. Se M_{4,5} XES and Se M_{2,3}/S L_{2,3} XES spectra was used to identify the chemical environment of selenium and sulfur.

4.3.2.1 Se M_{4,5} X-ray emission spectroscopy

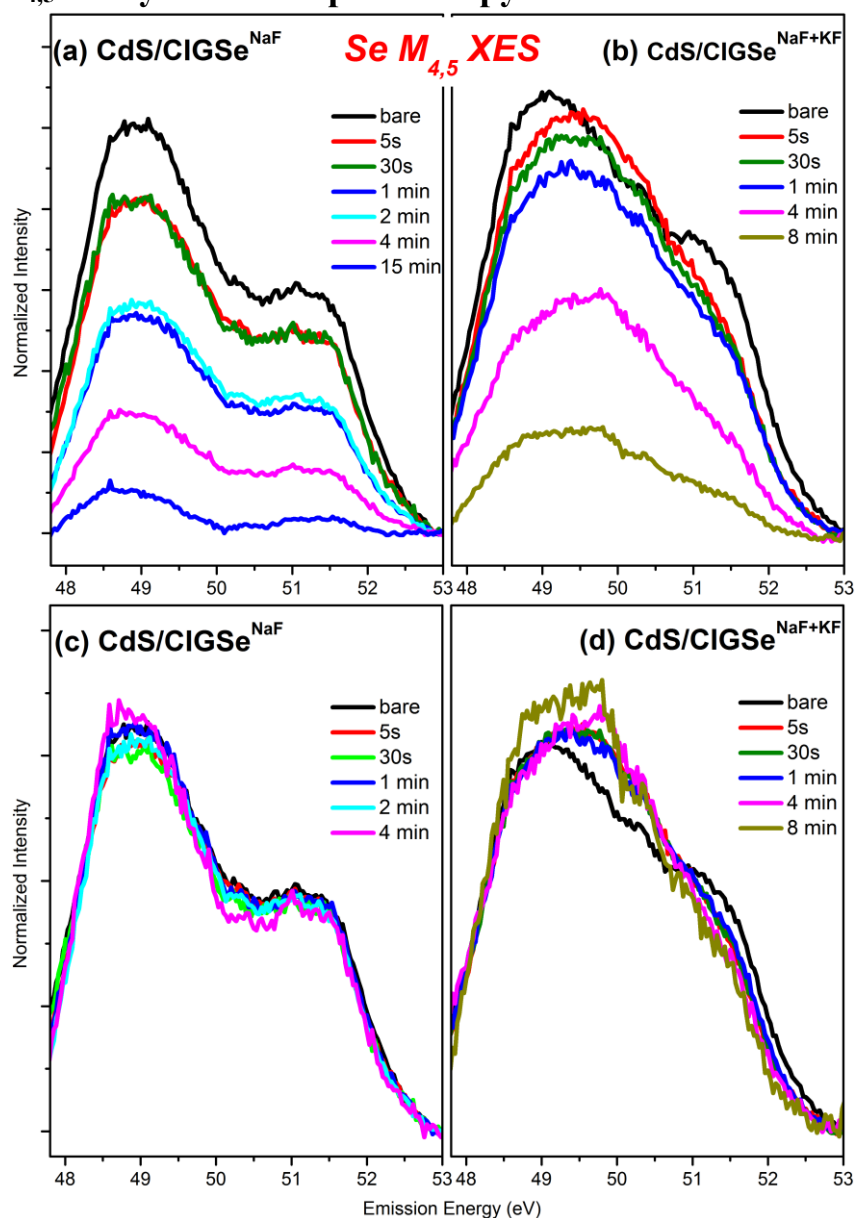


Figure 4.16. Background and area normalized Se M_{4,5} XES spectra of the CdS/CIGSe^{NaF} (a, c) and CdS/CIGSe^{NaF+KF} (b, d) sample series.

In order to get insight into the chemical nature of this potentially formed surface layer, we performed complementary Se $M_{4,5}$ XES measurements. The background normalized Se $M_{4,5}$ XES spectra of the $\text{CdS/CIGSe}^{\text{NaF}}$ and $\text{CdS/CIGSe}^{\text{NaF+KF}}$ sample sets are shown in Figure 4.3.12 a) and b). The sharp drop off of intensity below ~ 48.5 eV is an artifact of the measurement; the spectra were measured on a Rowland-circle geometry spectrometer, and the chosen energy range approached the edge of what was measurable. Thus, the low-energy region of the spectrum was recorded very inefficiently, inducing the observed drop. In reality, the shape of the spectrum in this region would be similar to the region ~ 152 eV in the analogous Se $M_{2,3}$ spectra (Figure 4.19).

The spectra are produced through relaxation of a Se 3d core-ionized excited state; in a simple picture, a (4p-like) valence electron decays into the 3d core hole, leading to emission of a photon. The energy-resolved spectrum of the measured photons is therefore related to the Se projected density of occupied states. The spectra of the bare CIGSe absorbers are similar to what was previously observed^[33] for similarly prepared samples. For the $\text{CIGSe}^{\text{NaF}}$ series, the CBD process leads only to a decreased intensity of the XES signals without a change in spectral shape (confirmed by area normalized spectra in Figure 4.16c) suggesting the Se chemical environment is dominated by the absorber. For the $\text{CdS/CIGSe}^{\text{NaF+KF}}$ series, there is a drop in intensity and a clear change in spectral shape in the CBD treated samples compared to the bare absorber, but the shape of all CBD treated samples remains the same, corroborated by the area-normalized spectra in Figure 4.16d. The difference in the Se $M_{4,5}$ spectra between $\text{CIGSe}^{\text{NaF}}$ and $\text{CIGSe}^{\text{NaF+KF}}$ absorbers is consistent with our previous observations^[33] and can be explained by formation of a K-In-Se layer in the latter case. The CBD-induced changes in the $\text{CIGSe}^{\text{NaF+KF}}$ series spectra suggest that this layer is modified due to buffer deposition; the $\text{CdS/CIGSe}^{\text{NaF+KF}}$ spectra do not however simply resemble those of the $\text{CIGSe}^{\text{NaF}}$ series, suggesting that a significant quantity of a different Se-containing material is formed in the former case. To identify the new Se compound, we attempt to reconstruct the measured $\text{CdS/CIGSe}^{\text{NaF+KF}}$ spectra with a superposition of reference spectra of $\text{CIGSe}^{\text{NaF}}$, $\text{KF-In}_2\text{Se}_3$, and CdSe in Figure 4.17. Note that all the spectra (including reference spectra) for fitting are area normalized. As previously published and discussed above, the $\text{CIGSe}^{\text{NaF+KF}}$ spectrum can be modelled as a sum of the spectra of $\text{CIGSe}^{\text{NaF}}$ and of a KF-treated In_2Se_3 sample (considered as

being representative for the chemical structure of a K-In-Se type species) with the relative contributions falling between those derived from the previously published alkali-poor and alkali-rich spectra.^[38] The spectra of the CdS/CIGSe^{NaF+KF} series can be presented as a sum of the spectra of the bare CIGSe^{NaF} and a CdSe reference (see Figure 4.17). However, due to the broadness of the spectra, other fit models can also be successfully applied: an equally good fit can be obtained from a sum of bare CIGSe^{NaF+KF} and CdSe reference spectra (see 4.18). In the CIGSe^{NaF} + CdSe model, the relative contribution of the CdSe to the fit is larger than in the CIGSe^{NaF+KF} + CdSe model. In conclusion, based on this analysis we cannot distinguish whether the K-In-Se type species is present at the CdS/CIGSe^{NaF+KF} interface or whether it is dissolved/modified (partially or completely) in the chemical bath.

However, based on the discussion around Figure 4.8, it appears that the majority of the K that is present at the surface of the CIGSe^{NaF+KF} absorber is dissolved in the CBD, and is only present in the measurements of the CdS/CIGSe^{NaF+KF} samples as K-O type species. In that case, the K-In-Se compound would no longer be present (or only present in greatly reduced quantities), and so of the two Se M_{4,5} XES fit models described above, we would favor the CIGSe^{NaF} + CdSe model for representing the CdS/CIGSe^{NaF+KF} data.

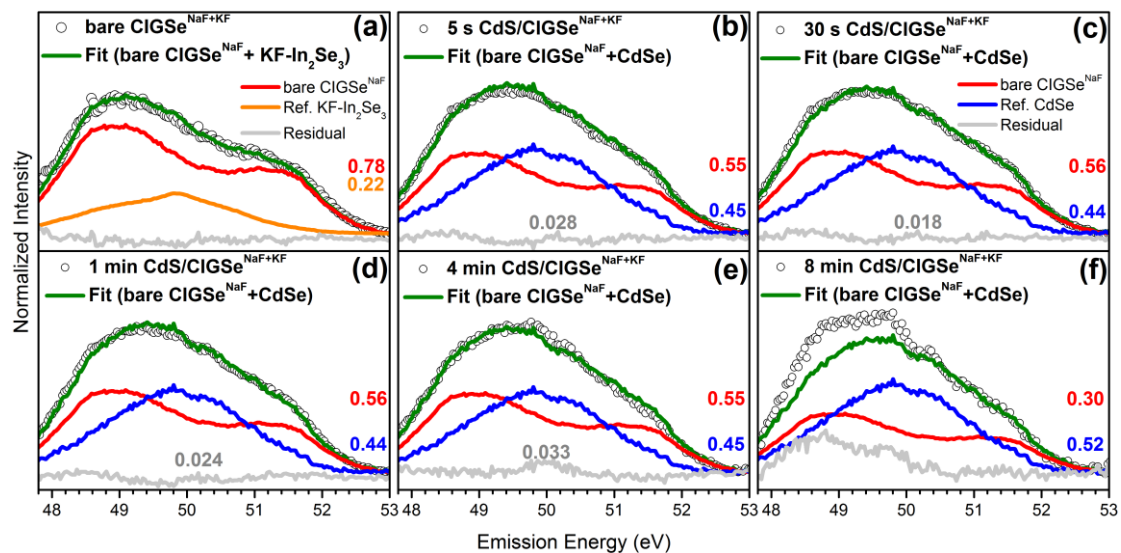


Figure 4.17. Se M_{4,5} XES spectra of the CdS/CIGSe^{NaF+KF} sample set (CBD time: 0s (a), 5 s (b), 30 s (c), 1 min (d), 4 min (e), and 8 min (f)) represented by a spectral sum (green) of the spectra of CIGSe^{NaF} (red), KF-PDT In₂Se₃ (orange) and CdSe (blue). The quantified values for the spectral contributions and the

residuals are also shown. Furthermore, the absolute area of the spectral residuals is stated as measure for the goodness of the fit.

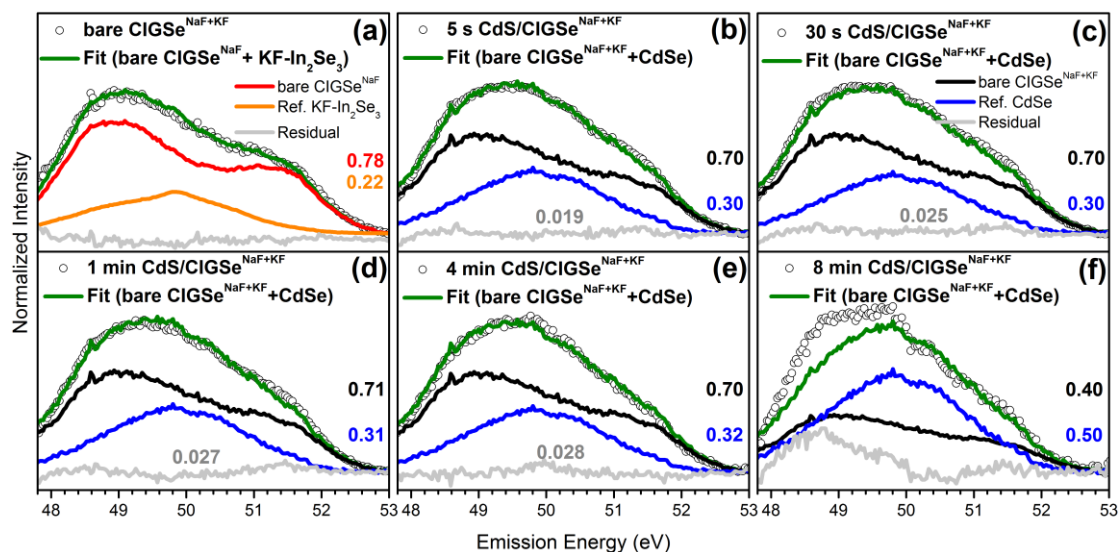


Figure 4.18. The Se $M_{4,5}$ XES spectrum of the $\text{CIGSe}^{\text{NaF+KF}}$ sample (a) is represented by a spectral sum (green) of the spectra of $\text{CIGSe}^{\text{NaF}}$ (red) and KF-PDT In_2Se_3 (orange) as shown in Figure 4.17a. The Se $M_{4,5}$ XES spectra of the $\text{CdS/CIGSe}^{\text{NaF+KF}}$ sample set (CBD time: 5 s (b), 30 s, (c), 1 min (d), 4 min (e), and 8 min (f)) is represented by a spectral sum (green) of the spectra of $\text{CIGSe}^{\text{NaF+KF}}$ (black) and CdSe (blue). The quantified values for the spectral contributions and the residuals are also shown. Furthermore, the absolute area of the spectral residuals is stated as measure for the goodness of the fit.

The fact that the Se $M_{4,5}$ XES does not show significant spectral shape changes for CBD times > 5 s is in agreement with the formation of an In- and Se-containing interface species and an additional Se-free In species for CBD times ≥ 1 min. There is a slight discrepancy in the comparison, because as stated above (and shown in Figure 4.10) it would appear that the interface species In_b disappears after 30s CBD time to be replaced by In_c . However, the fit method applied to the In MNN was to use the minimum possible number of distinct components, and so the fit would be improved by including three components – $\text{In}_{a,b,c}$ – in the fits for CBD of more than one minute. The uncertainty in the model means that it is not in contradiction with the Se $M_{4,5}$ results, even more so considering that the Se $M_{4,5}$ spectrum of In_2Se_3 [33] is very similar to that of CdSe (Figures 4.17 and 4.18). Thus, the spectral Se $M_{4,5}$ fingerprint of In-Se bonds could already be accounted for in the $\text{CIGSe}^{\text{NaF}} + \text{CdSe}$ fit model shown above.

4.3.2.2 S $L_{2,3}$ and Se $M_{2,3}$ X-ray emission spectroscopy

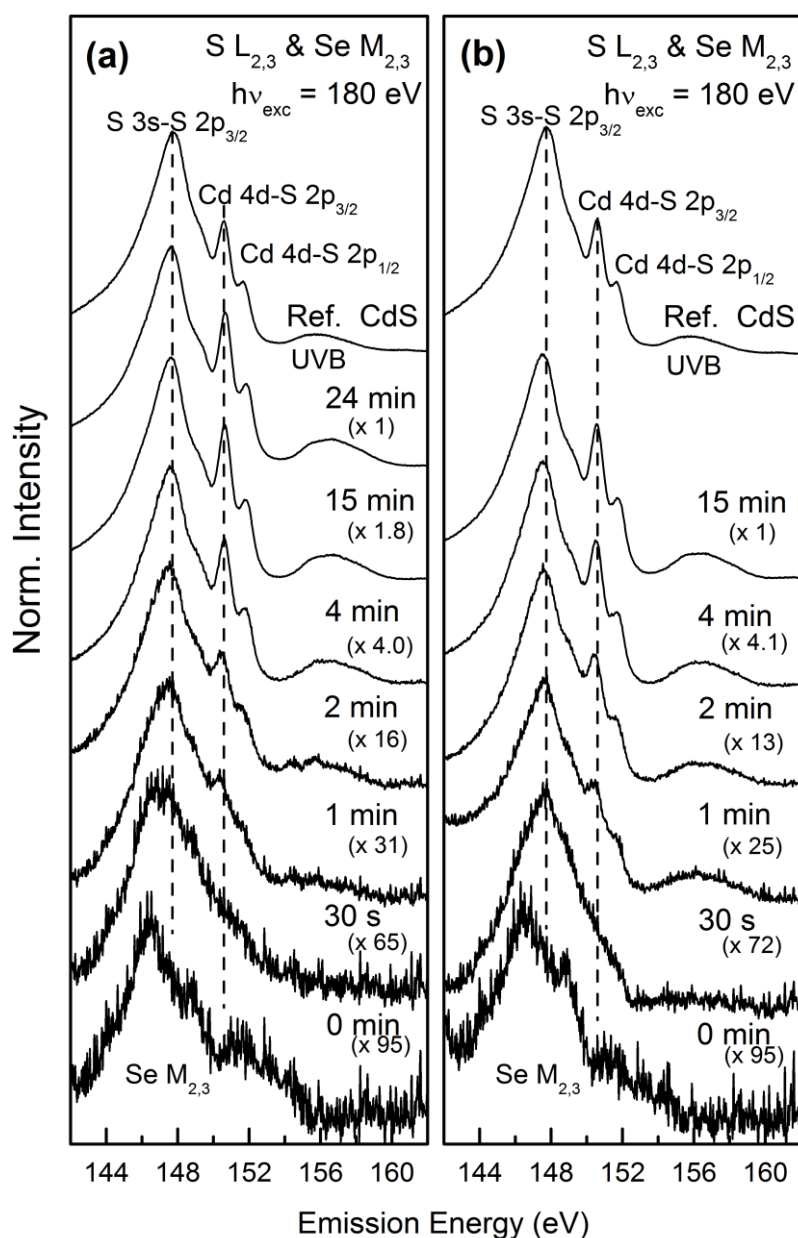


Figure 4.19. Background-normalized Se $M_{2,3}$ /S $L_{2,3}$ XES spectra of the CdS/CIGSe^{NaF} (a) and CdS/CIGSe^{NaF+KF} (b) samples with increasing CdS-CBD time. CdS reference spectrum^[19] was added for comparison. The spectra are shown on different magnification scales (as indicated) and are vertically offset to allow for easy comparison.

To further characterize the chemical structure at the buried CdS/CIGSe interface and how it changes with different PDT, S $L_{2,3}$ /Se $M_{2,3}$ XES were measured (see Figure 4.19). The broadness and low cross-section of the Se $M_{2,3}$ make it less useful than the Se $M_{4,5}$ as an indicator of chemical structure of Se, but the S $L_{2,3}$ has been shown to be extremely sensitive to the valence band and chemical structure^[105-106] of S. As in the overlapping XPS spectra in Figure 4.6 k and l, the S signal

intensity increases while the Se signal is attenuated as CdS thickness increases, as expected. The relative intensities of the S and Se related signals are influenced by a number of factors including fluorescence yield^[107], ionization cross section, depth dependence, etc., and so the specific S/Se signal ratios in XPS and XES will be quite different for the same sample.

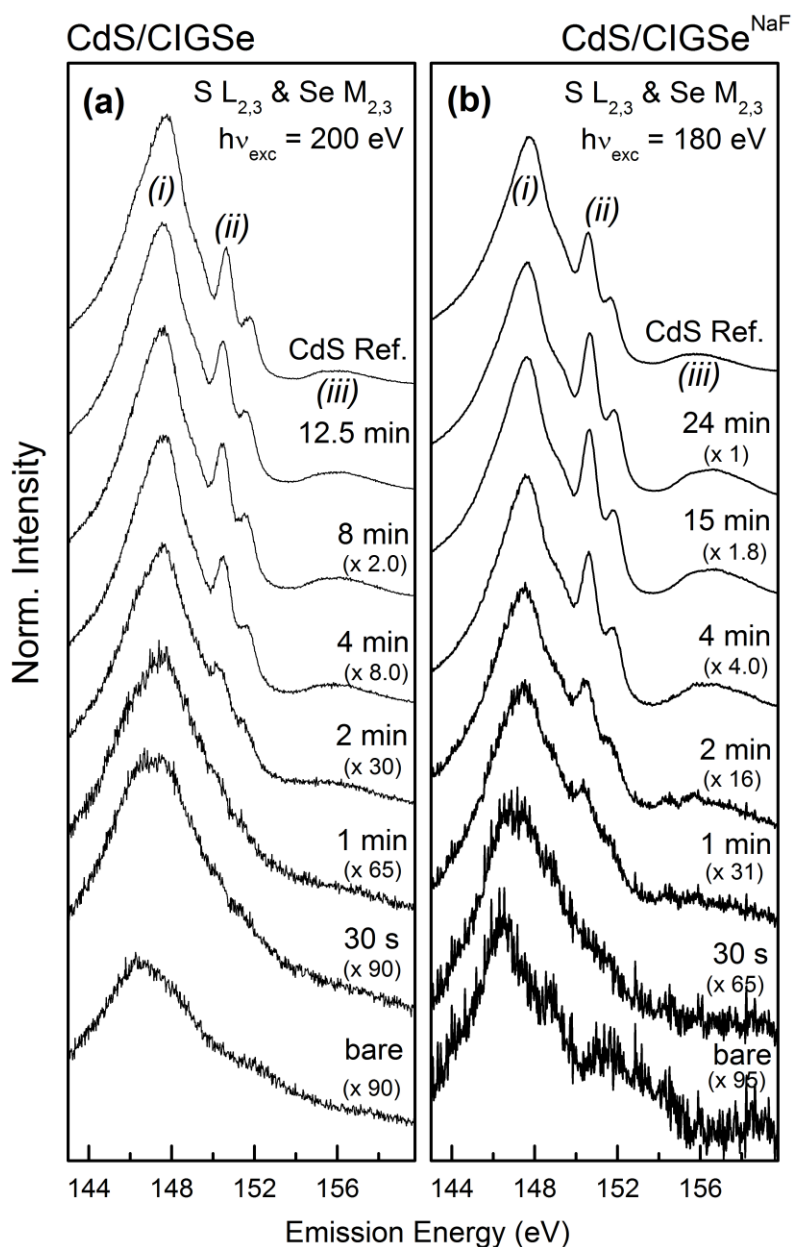


Figure 4.20. S L_{2,3}/Se M_{2,3} XES spectra of K-free CdS/CIGSe samples as a function of CBD time prepared based on high-temperature processed ((a), modified from ref ^[63]; copyright 2010 American Institute of Physics) and low-temperature processed ((b), compare to Figure 6a of this study) CIGSe absorber. The main features are labeled (i)–(iii). Spectra are normalized to equal peak height above background and vertically offset for clarity. Note the different magnification factors.

For the $\text{CIGSe}^{\text{NaF}}$ and $\text{CIGSe}^{\text{NaF+KF}}$ absorbers, the dominant emission feature is attributed to the Se $M_{2,3}$ emission. The energy difference between the main peak and high-emission energy shoulder is 5.7 eV, corresponding to the Se 3p doublet separation^[108]. Independent of employed PDT, the S $L_{2,3}$ spectra of samples with long CBD times closely resemble the CdS reference spectrum, which has been reported many times previously^[63, 107], as expected based on the XPS and XAES data described above. The S $L_{2,3}$ spectrum of CdS is composed of emission caused by S $3s \rightarrow 2p$ transitions, Cd $4d \rightarrow S$ 2p transitions, and Cd $5s \rightarrow S$ 2p transition from the upper valence band (UVB)^[109]. For ease of comparison, all spectra were multiplied by appropriate scaling factors to be presented with similar intensity. While spectra are essentially identical to the CdS reference spectra for CBD times longer than 4 min, the samples with thinner (30s - 2 min CBD time) CdS overlayers are quite different. Most prominently the emission from Cd $4d \rightarrow S$ 2p transitions seems to be almost entirely absent in the spectra of both the CdS/ $\text{CIGSe}^{\text{NaF}}$ and the CdS/ $\text{CIGSe}^{\text{NaF+KF}}$ sample sets. In the past, this has been interpreted as indication that sulfur is deposited without forming S-Cd bonds^[63, 110] or that the CdS deposited during the early stages of the CBD process has a poorly defined physical structure (i.e., different bond lengths and angles), which would result in a broadening of the Cd $4d \rightarrow S$ 2p emission features to an extent where they disappear in the noise floor of the measurement^[107].

Considering the direct comparison of the S $L_{2,3}$ data of the CdS/ CIGSe sample set from Ref. ^[63] (that indicates the deposition of sulfur without the formation of S-Cd bonds) with our data in Figure 4.20. The main difference in the sample sets is the fact that the absorbers of the different series were prepared in different temperature regimes. While the absorbers of this study have been prepared at low temperatures (to facilitate the employment of flexible polyimide type substrates), the absorber used in the previous study was deposited at higher temperatures. In addition, for the low temperature processed CIGSe absorber of the current study a PDT was performed, while for the high temperature processed absorbers of the previous study one relied on the diffusion from the soda-lime glass as the sole sodium source. Nevertheless, at first sight, the spectra look very similar. The main features are associated with^[107] (i) S 3s states, (ii) Cd 4d-derived bands (i.e., Cd $4d \rightarrow S$ $2p_{3/2}$, and Cd $4d \rightarrow S$ $2p_{1/2}$ transitions, respectively), and (iii) the upper valence band (UVB).

However close inspection of the spectra, in particular those that represent samples with buffer layers that have been deposited within short (i.e., 1 and 2 min) CBD times, reveals that the Cd 4d-derived features are differently pronounced. In the old data set, the Cd 4d-derived features are (almost) completely missing (for the 1 min CdS/CIGSe sample) and significantly reduced in intensity (for the 2 min CdS/CIGSe sample) compared to the spectra of the respective CdS/CIGSe^{NaF} samples of this study. Previously, the apparent presence of S-related spectral intensity without the presence of the Cd 4d-derived features was interpreted as a CBD-CdS process induced S-deposition without the deposition of Cd / the formation of S-Cd bonds. In this particular case, it was concluded that $(\text{In}_{1-x}\text{Ga}_x)_y\text{S}_z$ type interface layers between CdS and the CIGSe absorber is formed.^[63] However, the related finding that the buffer layer contains a significant amount of oxygen (Figure 4.15), does not lead to the formation of sulfates as the distinct spectral signature of $-\text{SO}_4^{2-}$ bonds^[111] is not observed in any S L_{2,3} spectra, in agreement with the XPS and XAES data. In order to study the impact of the different PDTs on the chemical interface structure, i.e. aiming at determining whether or not the chemical species formed at the CdS/CIGSe interfaces (e.g., species In_c in Figure 4.10b and 4.11 as well as species Cd_a in Figure 4.14) contain S, the S L_{2,3} XES spectra of the CdS/ CIGSe^{NaF} and the CdS/CIGSe^{NaF+KF} samples for short CBD times are inspected. To do so, the 30 s and 4 min spectra (normalized to same height) from Figure 4.19 are directly compared in Figure 4.21. The spectra of the 4 min CdS/CIGSe samples with different PDT are dominated by the spectral signature of CdS, and the spectra do not differ significantly between series. However, for the 30s sample, there are small differences between the CIGSe^{NaF} and CIGSe^{NaF+KF} series. Most prominent is the redistribution of spectral intensity at the maximum of the spectra to higher emission energies when comparing the normalized spectrum of the 30s CdS/CIGSe^{NaF+KF} sample with that of the 30s CdS/CIGSe^{NaF} sample.

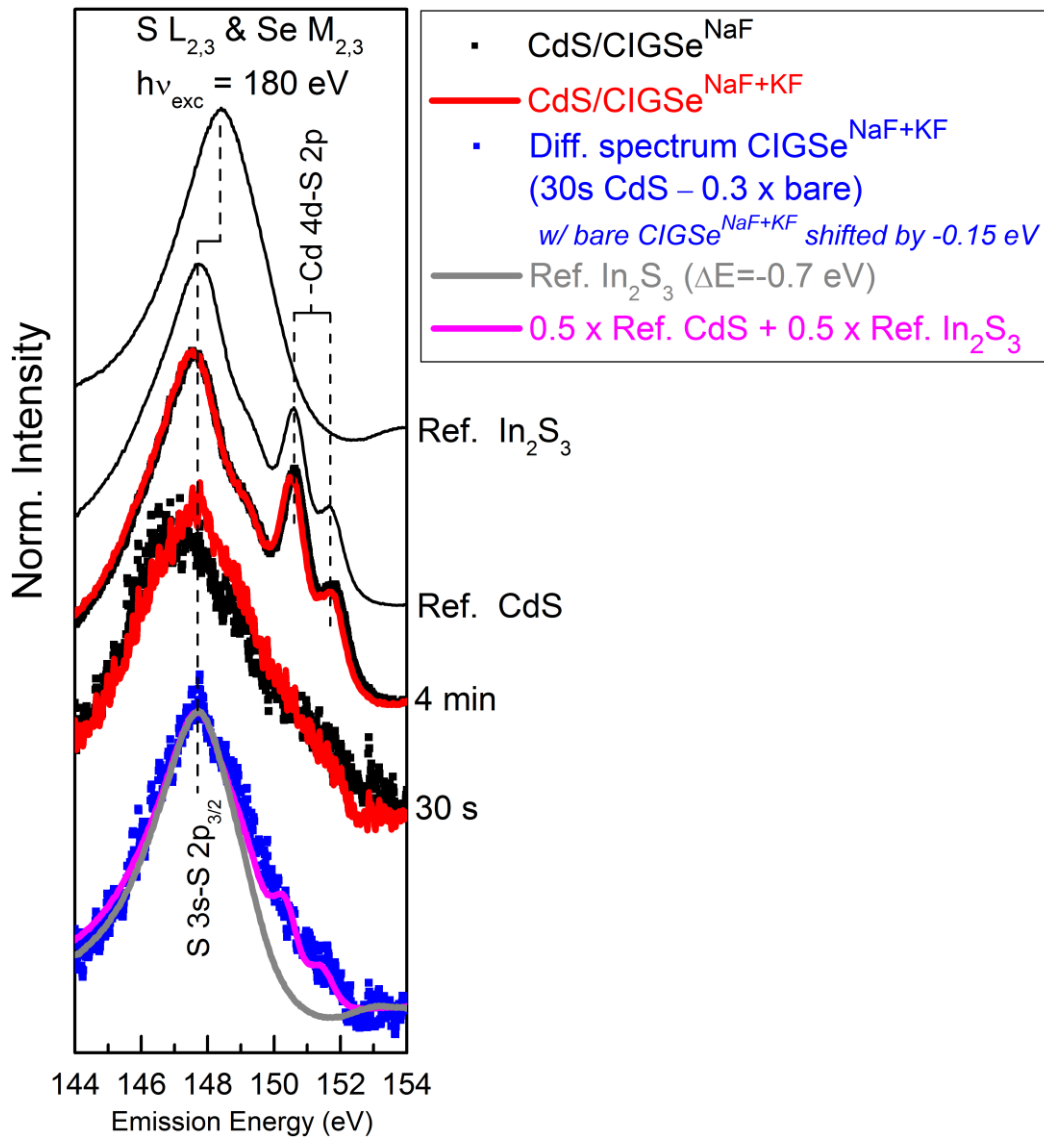


Figure 4.21. Direct comparison of four selected Se $M_{2,3}/S L_{2,3}$ XES spectra (30s and 4 min for both series) and the difference between bare and 30s $CdS/CIGSe^{NaF+KF}$ are shown. A model "CdIn₂S₄" reference spectrum were produced by the S $L_{2,3}$ spectrum of $0.5 \times CdS + 0.5 \times In_2S_3$. All samples were excited at $h\nu = 180 \text{ eV}$. Dashed lines are added as guides for spectral features and main features are labeled. CdS and In_2S_3 reference spectra^[19] was added for comparison.

We attribute this to the spectrum of the 30s $CdS/CIGSe^{NaF}$ sample being dominated by the Se $M_{2,3}$ emission of the CIGSe absorber, while the spectrum of the 30s $CdS/CIGSe^{NaF+KF}$ sample shows a higher contribution of a CdS signature, in agreement with the discussion in conjunction with Figure 4.7. Reasonable difference spectra can be computed using Se $M_{2,3}$ contributions of up to 30% (see Figure 4.21). The comparison with the S $L_{2,3}$ spectrum of a In_2S_3 reference spectrum^[19] (shifted by -0.7 eV to align with the low-energy slope of the difference spectrum) indicates the presence of

additional spectral intensity between 151 and 153 eV, i.e. the region which is dominated by Cd 4d→S 2p emission features. Considering a model "CdIn₂S₄" reference spectrum, which is constructed by adding 0.5 × S L_{2,3} (CdS) and 0.5 × S L_{2,3} (In₂S₃), we find a good agreement with the difference spectrum. The clearly identifiable Cd 4d→S 2p emission features in the "CdIn₂S₄" reference spectrum and their absence in the (noisier) difference spectrum is again attributed to a poorly defined physical structure. Thus, we find indications for the formation of S-Cd *and* S-In bonds at the interface of the CdS/CIGSe^{NaF+KF} but not at the CdS/CIGSe^{NaF} interface (or at least in smaller quantities). Based on our analysis of the In and Cd XPS and XAES data, we relate this Cd-In-S containing interface compound to species In_c (see Figure 4.10b and 4.11) and to some extent to species Cd_a (see Figure 4.14). Note that the position of the related α' (In) between that of In₂S₃ and In₂O₃ (see Figure 4.11) suggests that oxygen is also incorporated in this compound. Considering all the XPS, XAES, and XES results (i.e. detail spectra and affiliated species), it is possible to make some clear statements about the structure at the CdS/CIGSe^{NaF} and CdS/CIGSe^{NaF+KF} interface, as shown in Table 4.2

Table 4.2. Interface formation of CdS/CIGSe^{NaF} (a) and CdS/CIGSe^{NaF+KF} (b) based on XPS, XAES and XES results (detail spectra and affiliated species).

(a) CdS/CIGSe ^{NaF}	Se M _{4,5} XES	In MNN	Cd MNN	Se M _{2,3} / S L _{2,3} XES	O 1s XPS
bare	CIGSe	CIGSe	---	---	
5 s	CIGSe	CIGSe	CdO	---	Cd(O, OH)
30 s	CIGSe	CIGSe	CdO + CdS	CIGSe	Cd(O, OH)
1 min	CIGSe	CIGSe	CdO + CdS	CdS	Cd(O, OH)
2 min	CIGSe	CIGSe	CdO + CdS	CdS	Cd(O, OH)
4 min	CIGSe	CIGSe	CdO + CdS	CdS	Cd(O, OH)
15 min	---	---	CdS	CdS	Cd (O, OH)
24 min	---	---	CdS	CdS	Cd (O, OH)

(b) CdS/CIGSe ^{NaF+KF}	Se M _{4,5} XES	In MNN	Cd MNN	S L _{2,3} XES	K 2p/O 1s
bare	CIGSe + K-In-Se	CIGSe +K-In-Se	---	---	
5 s	CIGSe+ CdSe	CIGSe + S-In?	CdSe/CdO	Cd-In-S	K-O + Cd (O, OH)
30 s	CIGSe+ CdSe	CIGSe+ S-In?	CdSe/CdO + CdS	Cd-In-S	K-O + Cd(O, OH)
1 min	CIGSe + CdSe	CIGSe + In-O	CdSe + CdO +CdS	CdS	K-O + Cd(O, OH)
2 min	CIGSe + CdSe	CIGSe + In-O	CdSe + CdO +CdS	CdS	K-O + Cd(O, OH)
4 min	CIGSe + CdSe	CIGSe + In-O	CdSe + CdO +CdS	CdS	Cd(O, OH)
8 min	CIGSe + CdSe	---	CdS + CdO	CdS	Cd(O, OH)
15 min	---	---	CdS + CdO	CdS	Cd(O, OH)

4.3.4 Summary

X-ray photoelectron spectroscopy (XPS), x-ray excited Auger electron spectroscopy (XAES), and soft x-ray emission spectroscopy (XES) were used to investigate the impact of different alkali post-deposition treatments (PDTs) on the chemical structure of the CdS/CIGSe interface. In order to identify the role of potassium in interface formation, the results on buffer/absorber samples sets have been compared that underwent a NaF or a NaF+KF PDT prior CdS deposition. For both sample sets we find – independent of PDT – the buffer layer to be best described by a Cd(O,OH,S) compound rather than to be a pure CdS buffer. However, while the buffer/CIGSe^{NaF} structure is formed without major interfacial interaction, significant elemental redistribution involving Cd, In, K, S, and Se in the proximity of the buffer/CIGSe^{NaF+KF} heterojunction is revealed. In detail, we suggest that a mixed Cd-In-(O,OH,S,Se) type layer with probably some Cd-In and (S,O)-Se composition gradients is formed in the early stages of the CBD-CdS process presumably due to modification/conversion of the K-In-Se layer present on the CIGSe^{NaF+KF} surface. This interface

layer enables the employment of thinner CdS buffer layers and thus the reduction of parasitic absorption, (partly) explaining the beneficial impact of the NaF+KF PDT on corresponding solar cells.

4.4 Impact of alkali treatments on the electronic structure of CdS/CIGSe interface

This section focuses on the influence of different alkali treatments (i.e., NaF PDT and NaF+KF PDT) on the electronic structure (i.e., the band alignment) of CdS/CIGSe interfaces. HAXPES at 2keV (HAXPES) was used to investigate the valence band structure.

4.4.1 Valence band spectra

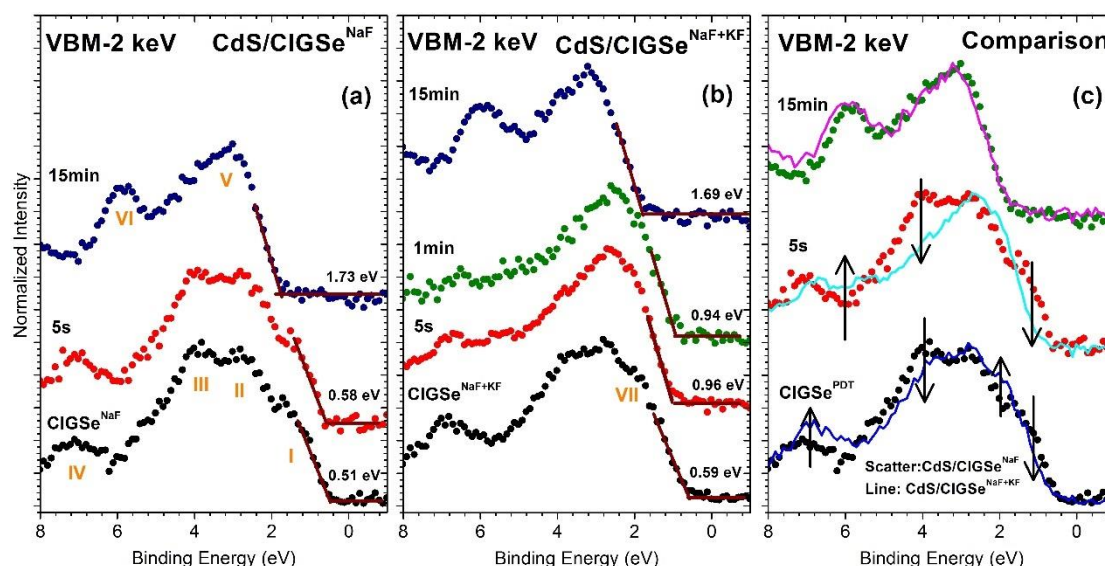


Figure 4.22. HAXPES valence band spectra of the CdS/CIGSe^{NaF}(a), CdS/CIGSe^{NaF+KF}(b) of CIGSe absorbers with different CdS thickness at $h\nu=2$ keV. Panel c shows the direct comparison of selected VBM spectra. Linear extrapolation of the leading edges is used to determine the position of the valence band maxima. Label I-VII mark particular spectral regions.

The impact of different alkali treatments with different CdS thickness (i.e. deposition time) on chemical structure are described in chapter 4.3, the PDT treatments also impact the valence band region and the VBM. To derive the bulk electronic structure, the valence band spectra measured at 2 keV of all the investigated samples are shown in Figure 4.22 a and b. Linear extrapolation of the

leading edge is used to determine the respective VBM values for all valence band spectra. Measurements were performed at HIKE endstation, which is described in section 3.3.2.

For the CdS/CIGSe^{NaF} series, the derived VBM values are 0.51, 0.58, and 1.73 (+/- 0.10) for the CIGSe^{NaF}, 5s and 15 min CdS/CIGSe^{NaF} sample, respectively. The short CBD process (5s) leads to a similar VBM spectra shape suggesting the VB is dominated by the absorber, which agrees with our previous chemical structure results in chapter 4.3. As discussed in the previous chapter, the 1 min CdS/CIGSe^{NaF} sample was inadvertently scratched during sample preparation (mounting), and thus only 5s sample's valence band spectrum is considered. For the CdS/CIGSe^{NaF+KF} series, the VBM values are 0.59, 0.96, 0.94, and 1.69 (+/- 0.10) for the CIGSe^{NaF+KF}, 5s, 1 min, and 15 min CdS/CIGSe^{NaF+KF} sample, respectively. The obvious change in spectral shape and VBM position of the CBD treated samples compared to the bare absorber can be observed clearly in Figure 4.22 b, which indicates a more complex situation compared to the CIGSe^{NaF} samples (in agreement with the finding in chapter 4.3). The valence band spectra (Figure 4.22 a and b) show several different features (labeled I-VII), which we attribute according to the reported references [40, 70, 112-114] and summarize in Table 4.3. We ascribe features I–VII to (I) antibonding hybridized Se p – Cu d states, (II) nonbonding Se p states, (III) bonding hybridized Se p – Cu d states, (IV) In s/Ga s derived states, (V/VI) hybridized S 3s and S 3p states, and (VII) Se p states in KInSe₂, respectively. Feature VII is more visible when the CIGSe^{NaF} and CIGSe^{NaF+KF} spectra were compared directly, as shown in Figure 4.22 c. All the spectra were normalized to the same height for direct comparison. For CIGSe^{NaF} and CIGSe^{NaF+KF} sample, the decrease of feature I and III is induced by Cu and Ga depletion and the increase of feature VII can be attributed to the existence of K-In-Se species, while the change of feature IV can be explained by In↑ and Ga ↓. After 5s CBD, an obvious difference can be observed: the VBM shifts to high binding energies compare to CIGSe^{NaF+KF}, feature III is reduced, and the feature VI is increased; most properties due to the appearance of the Cd-In-S layer (see discussion about Figure 4.21). The most significant Cu depletion also contributes to the VBM shift to high binding energies (i.e. disappearance of the feature I). For thick CdS samples (15min CBD time), similar VBM spectra indicated similar chemical structure in agreement with our previous discussion in chapter 4.3. The direct comparison of the VBM spectra of our PDT samples

with the alkali-poor and alkali-rich data published in Ref.^[50] are shown in Figure A.3.2 and A.3.3. While the VBM spectrum of our CIGSe^{NaF} sample fits quite well with the data published on alkali-rich CIGSe^{NaF}^[50], the data of our CIGSe^{NaF+KF} sample is very similar to the alkali-poor CIGSe^{NaF+KF} data published in Ref.^[50], in agreement with our discussion in conjunction with Figure 4.16.

Table 4.3. Features attribution in Figure 4.22

Feature	Binding Energy (eV)	Attribution
I	1.65	antibonding hybridized Se p – Cu d states ^[114]
II	2.8	nonbonding Se p states ^[114]
III	3.8	bonding hybridized Se p – Cu d states ^[114]
IV	7.0	In s/Ga s derived states ^[114]
V/VI	3.0/6.0	Hybridized S 3s and S 3p states ^[112]
VII	1.8 – 3.0	Se p states in KInSe ₂ ^[70]

4.4.2 Interface energy level alignment

In order to determine the energy level alignment, the band bending that occurs at the heterointerface due to the CdS deposition must be taken into account^[115]. The valence/conduction band offset (VBO/CBO) can be calculated by the following formula^[19]:

$$VBO = VBM_{CdS} - VBM_{CIGSe} + IIBB \quad (4.3)$$

$$CBO = CBM_{CdS} - CBM_{CIGSe} - IIBB \quad (4.4)$$

The IIBB is monitored by the detected shifts in the binding energy position of related XPS lines (Cu 2p_{3/2}, In3d_{5/2}, Ga 2p_{3/2}, Se 3d, Cd 3d_{3/2}) in samples with intermediate CdS buffer thicknesses (5s and/or 1min deposition). Table 4.4 shows the derived peak center values for Cu 2p_{3/2}, In3d_{5/2}, Ga 2p_{3/2}, Se 3d, Cd 3d_{3/2} of the bare CIGSe^{PDT}, 5s, 1 min (only for CIGSe^{NaF+KF}), and 15 min CdS/CIGSe^{PDT} samples (data see Figure 4.6).

For these thin (≤4min) samples, the absorber and the buffer layer core level lines can still be detected at the same time, for thicker CdS layers, only buffer layer signals can be detected. The IIBB was calculated using Kraut's method^[115], which can be expressed as^[19]:

$$IIBB = [E_{a,i}^0 - E_{a,i}^t] + [E_{b,j}^t - E_{b,j}^f] \quad (4.5)$$

where $E_{a,i}^0$ is the BE-position of an absorber-related PES line in the bare absorber; $E_{a,i}^t$ is the BE-position of an absorber-related PES line after a CBD time t , $E_{b,j}^t$ is the BE-position of a buffer-related PES line after a CBD deposition time t ; and $E_{b,j}^f$ is the core level position of a buffer-related PES line after deposition of the final CdS layer.

Table 4.4. The peak position of the respective Cu, In, Ga, Se and Cd core level lines in binding energy measured with $h\nu=1253.56$ keV. An error margin of ± 0.10 eV is assumed.

Samples	Binding Energy	$E_B(\text{Cu } 2p_{3/2})$ $h\nu=1253.56\text{eV}$	$E_B(\text{In } 3d_{3/2})$ $h\nu=1253.56\text{eV}$	$E_B(\text{Ga } 2p_{3/2})$ $h\nu=1253.56\text{eV}$	$E_B(\text{Se } 3s)$ $h\nu=1253.56\text{eV}$	$E_B(\text{Cd } 3d_{3/2})$ $h\nu=1253.56\text{eV}$	$E_B(\text{S } 2s)$ $h\nu=1253.56\text{eV}$
	CIGSe ^{NaF}	932.20	452.33	1117.74	229.32	---	---
5s CdS/CIGSe ^{NaF}	932.39	452.51	1117.99	229.44	412.07	225.91	
15min CdS/CIGSe ^{NaF}	---	---	---	---	412.11	226.01	
CdS/CIGSe ^{NaF+KF}	932.19	452.26	1117.83	229.11	---	---	
5s CdS/CIGSe ^{NaF+KF}	932.37	452.26	1118.10	229.01	411.87	225.93	
1min CdS/CIGSe ^{NaF+KF}	932.45	452.17	1118.15	228.90	411.75	225.82	
15min CdS/CIGSe ^{NaF+KF}	---	---	---	---	412.03	225.93	

In total, 12 values of IIBB were computed by using combinations of the selected CIGSe and CdS lines for CdS/CIGSe^{NaF} (8 values) and CdS/CIGSe^{NaF+KF} (8 values) series, respectively. All the used data for this calculation are marked (bold). The complete set of IIBB values are displayed in Figure 4.23. Note that the only suitable absorber-related lines for CdS/CIGSe^{NaF+KF} series were the Cu 2p_{3/2} and Ga 2p_{3/2}, as a result of the discovered interface formation involving In, Se, Cd, and S. The average IIBB-values of the analysis are -0.26 ± 0.14 and -0.40 ± 0.14 for CdS/CIGSe^{NaF} and CdS/CIGSe^{NaF+KF} sample series (as denoted by the dashed line in Figure 4.23), respectively.

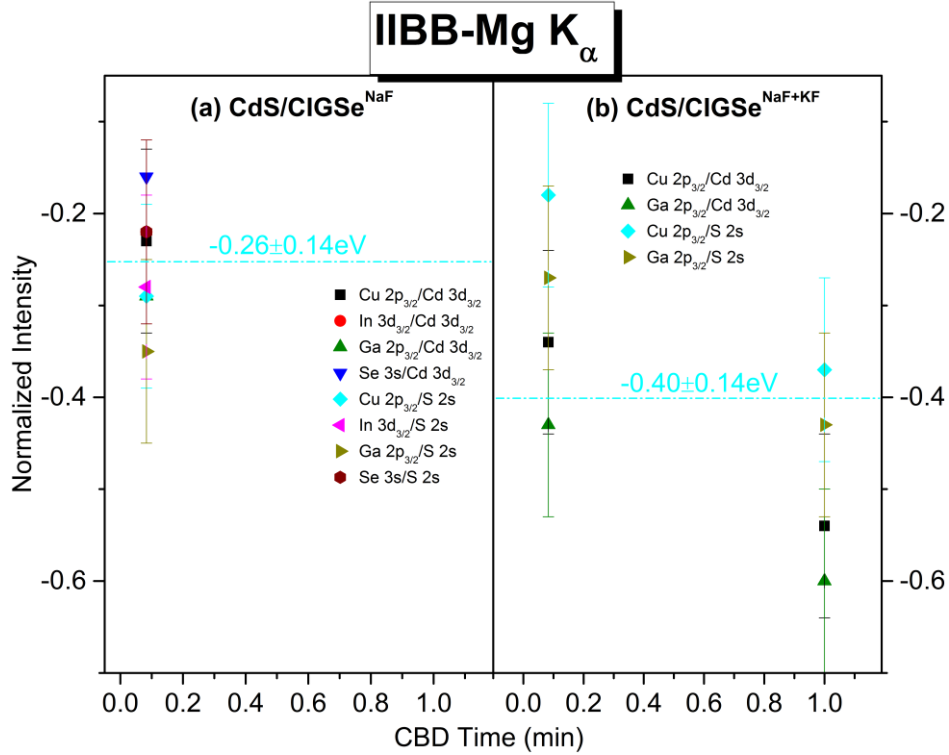


Figure 4.23 Interface-induced band bending (i.e., IIBB) as determined by combining core-level positions of the $\text{CIGSe}^{\text{NaF}}$ absorber sample, the 5s $\text{CdS/CIGSe}^{\text{NaF+KF}}$ sample (the “new” bare $\text{CIGSe}^{\text{NaF+KF}}$ sample), the sample with the thicker CdS (15 min) layer, and two samples with intermediate CdS layer thicknesses (5s $\text{CdS/CIGSe}^{\text{NaF}}$ and 5s/1min $\text{CdS/CIGSe}^{\text{NaF+KF}}$ samples).

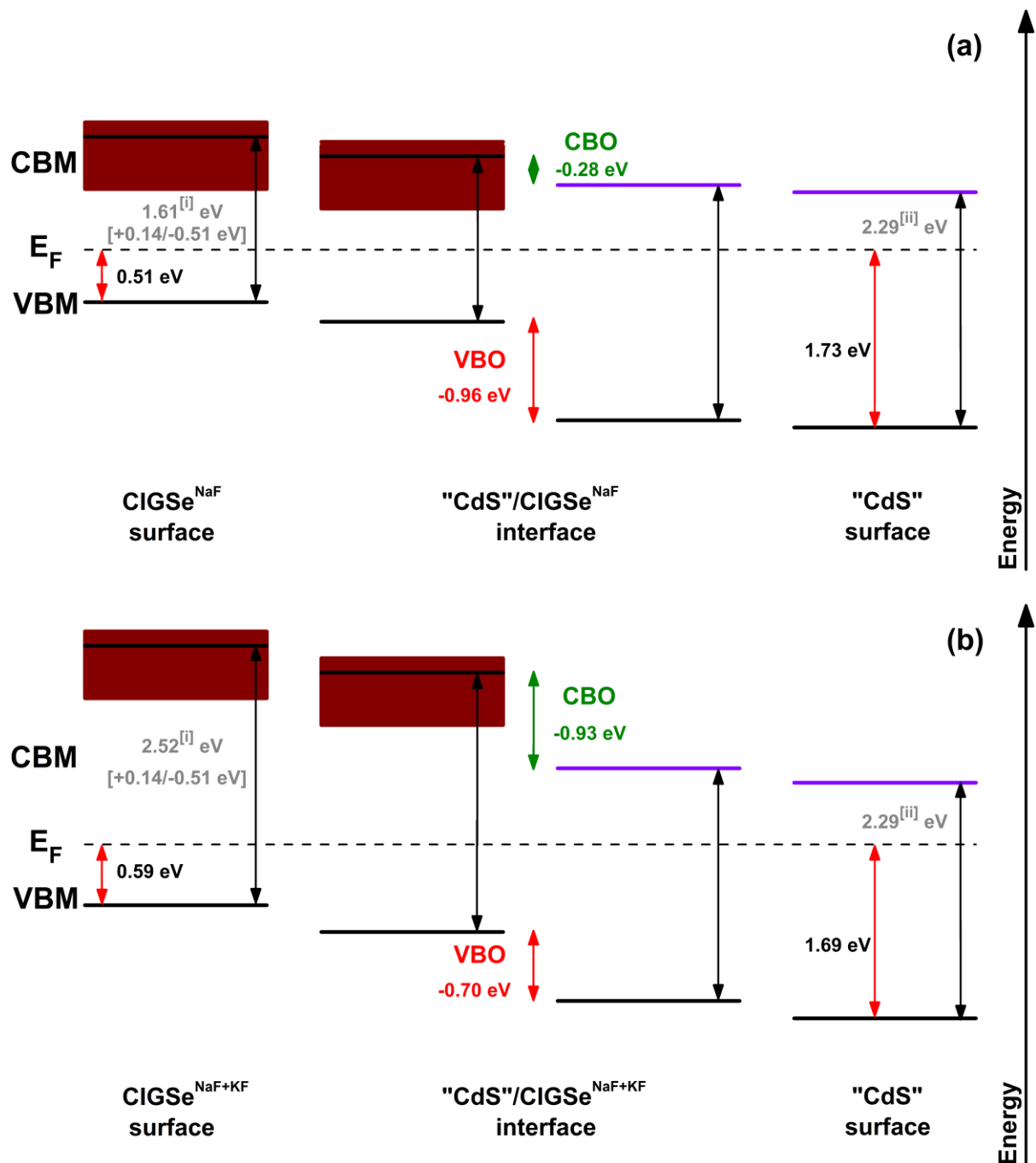
The VBO are calculated by using the formula 4.3, and are ascertained to be -0.96 ± 0.14 and -0.70 ± 0.14 eV for $\text{CdS/CIGSe}^{\text{NaF}}$ series and $\text{CdS/CIGSe}^{\text{NaF+KF}}$ series, respectively. Using reference (bulk) bandgap data from literature, approximate CBO are also calculated to complete the whole band alignment picture. Considering the bulk band gap energies of CdSe (2.3 eV^[116]), CdO (2.16 – 2.6 eV^[117-118]), CdS (2.42 eV^[119]), Cd(S,O) (2.29 eV^[119]), CdIn₂S₄ (2.35 eV^[120]), and Cd(OH)₂ (2.74 – 3.59 eV^[118, 121-122]), i.e. components related to the identified Cd-In-(O,OH,S,Se) interface species, we can speculate about the energy level alignment at the Cd-In-(O,OH,S,Se)/CIGSe interface. For our sample series, the near-surface band gap for the $\text{CIGSe}^{\text{NaF}}$ sample is reported to be as large as 1.61 eV^[40]; while the surface band gap for the $\text{CIGSe}^{\text{NaF+KF}}$ sample is reported to be 2.52 eV^[40]. According to the chemical finding in chapter 4.3, the top layer after long CBD (≥ 15 min) is Cd(S,O) and the optical band gap for 15 min Cd(S,O) sample is 2.29 eV^[119]. For $\text{CdS/CIGSe}^{\text{NaF}}$ series, considering the conduction band maximum (CBM) data points from the references (1.61 eV^[40] and 2.29 eV^[119]), the calculated CBO edge value for $\text{CdS/CIGSe}^{\text{NaF}}$ series

is -0.28 ($-0.14/+0.51$) eV, as shown in Figure 4.24a. A small “cliff” like CBO can be observed at the CdS/CIGSe^{NaF} interface. The band schematic for CdS/CIGSe^{NaF+KF} is shown in Figure 4.24b. Note that the reported VBM value (1.10 eV^[40]) for bare CIGSe^{NaF+KF} sample is much larger than that (0.59 eV) of our sample, which is likely related to the different alkali amount (we have much less potassium than the reference). The optical band gap for 15 min CdS/ CIGSe^{NaF+KF} sample is 2.29 eV^[119]. A significant “cliff” like CBO (-0.93 eV) appears in the approximation of the CdS/CIGSe^{NaF+KF} interface, which is in conflict to the optimal CBO range for high efficiency CIGSe and which is reported to be $0\sim 0.4$ eV^[123]. As the corresponding solar cells are working well and have high performance^[124], this CBO approximation for the CdS/CIGSe^{NaF+KF} interface does probably not represent the reality; sources of error and possible corrections are discussed below. Note that all the band gap values of bare PDT samples are larger than the lowest bulk value (~ 1.15 eV) determined by quantum efficiency (QE) measurements^[26, 40]. The band gap widening at the surface of high-efficiency chalcopyrite absorbers is related to a decrease in p-d interband repulsion related to the Cu-deficient surface composition^[125] caused by formation of a Cu-free/poor phase or surface.

The extensive modification of the K-In-Se layer on the CIGSe absorber and formation of a Cd-In-(O,OH,S,Se) – type compound as discussed in chapter 4.3 would impact the energy level alignment at this crucial interface; after exposure to short chemical bath the CIGSe^{NaF+KF} should be more like that of the bare CIGSe^{NaF} (as the K-In-Se layer is supposed to be washed away). Therefore, we combine the results of bare CIGSe^{NaF}, 5s CdS/CIGSe^{NaF+KF}, and 15 min CdS/CIGSe^{NaF+KF}, as shown in Figure 4.24c to approach the realistic picture. We estimate the band gap of the 5s CdS/CIGSe^{NaF+KF} sample to be $2.16 \sim 2.6$ eV based on the related (very common) optical band gap values for CdS^[119], CdO^[117-118], CdSe^[116], and CdIn₂S₄^[120] compounds. The band gap of the Cd(OH)₂ species is not included since it is not the dominant contribution here (see O 1s spectra in Figure 4.6t).

Considering the chemical modification/conversion after short CdS deposition, the band gap of the 5s CdS/CIGSe^{NaF+KF} sample is likely dominated by the Cd-In-(O,OH,S,Se) – type compound. Therefore, the conduction band alignment at the heterointerface would reveal a “spike” CBO with

the experimental uncertainty compared to that of CdS/CIGSe^{NaF} sample series. This is much close to the reported electronic band alignment of high-efficiency CIGSe solar cells.^[126]



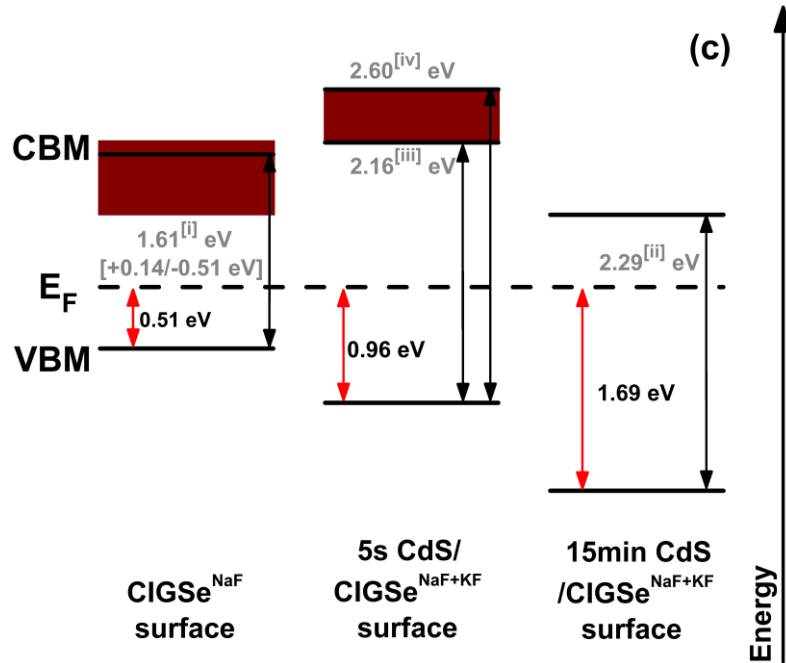


Figure 4.24. Schematic diagram of the CdS/CIS heterointerface electronic band alignment with different alkali treatment (a: CdS/CIGSe^{NaF}; b: CdS/CIGSe^{NaF+KF}; c: CIGSe^{NaF} and CdS/CIGSe^{NaF+KF}). The left and right sides display the electronic surface band gap (as derived by HAXPES and reference) for the bare PDT treated CIGSe absorber and the CdS/CIGSe^{PDT} buffer, respectively. The middle shows the electronic band alignment after considering interface-induced band bending effects. The uncertainty VBO and CBO are estimated to be -0.96 ± 0.25 eV and -0.47 ± 0.25 eV. The reference i-iv in this figure are correspond to 40, 118, 116, and 117, respectively.

According to p-n junction band alignment simulation^[123], a “cliff”-like CBO enhances interface recombination (e.g. the recombination between electrons in the conduction band of the buffer and holes in the valence band of CIGSe), especially in the presence of interface defects and/or a high interface recombination velocity, resulting in a significantly decreased V_{oc} . The parameters of cells related to our samples (V_{oc} : 0.696 eV for CIGSe^{NaF} and 0.718 eV for CIGSe^{NaF+KF}^[124]) provide some support for the diagrams in 4.24 a and c. A thin interface layer (here represented by 5s CdS/CIGSe^{NaF+KF}) may act as a passivation layer reducing recombination, which could explain the improved performance by an increased charge selectivity more efficiently repelling holes from the absorber.

In order to back up this line of argumentation with experimental data, inverse photoemission spectroscopy measurements (in order to directly probe the conduction band minimum) should be performed to directly access CBM. Furthermore, in order to have direct access to the modified

electronic interface structure when the K-In-Se type species is converted into the Cd-In-(O,OH,S,Se) compound, we would suggest to study CIGSe^{NaF+KF} absorbers before and after Cd partial electrolyte treatments (see e.g. ref.^[127], basically a CdS CBD-type process without the sulfur source) to mimic the early stages of the CBD process.

4.4.3 Summary

To conclude this section, we have used photoelectron spectroscopy with an excitation energy of $h\nu=2$ keV to characterize the electronic structure of CdS/CIGSe with different PDT treatment. The valence band offset (-0.96 and $-0.70 (\pm 0.14)$ eV for CdS/CIGSe^{NaF} and CdS/CIGSe^{NaF+KF}, respectively) can be observed at the CdS/CIGSe interface. At the CdS/CIGSe^{NaF} interface, a small “cliff”-like conduction band offset ($-0.28 (-0.14/+0.51)$ eV) was determined according to the reference band gap data. A significant CBO (-0.93 eV) was determined at the CdS/CIGSe^{NaF+KF} interface, which is in conflict with working high efficiency chalcopyrite-based solar cells. Considering a realistic picture of the CdS/CIGSe^{NaF+KF} (i.e. chemical change, interface band bending), the re-compared conduction band alignment indicating the presence of an interface layer reveals the formation of a passivation layer, which is in agreement with the parameters change of corresponding solar cells in the previous report.

5. Impact of alkalis on the surface structure of Cu(In,Ga)Se₂ studied on in-system prepared model systems

In this chapter, the impact of alkali (K, Rb, Cs) metal deposition and annealing on the surface structure of chalcopyrite-based thin-film solar cell absorbers will be discussed. Alkali treatments (alkali fluoride) of CIGSe absorber surfaces have gained more and more interest due to the beneficial impact on the device performance, but the mechanism of their influence on the chemical, and electronic structure is not yet fully understood, especially for the heavy alkalis (Rb, Cs). Hard x-ray photoelectron at the HIKE endstation BESSY II KMC-1 was used to study model alkali-CIGSe systems prepared in-system.

In the first part, the sample preparation, including all the treatments, will be explained and discussed. Second, the effect of alkali treatment on the chemical structure of those absorbers will be explored, separately. In particular, the influence of alkalis on the chemical surface structure is derived, suggesting possible chemical mechanisms. Finally, the effect on the electronic structure is addressed.

5.1 Sample preparation

This section focuses on the study of compound formation during in-situ annealing of the alkali/CIGSe model system. We monitored the surface and interface structure using photoelectron spectroscopy with an excitation energy of $h\nu=2$ keV and how it changes upon in-situ annealing in order to mimic the thermal input similar to PDT conditions. The bare samples (CIGSe/Mo/barrier/glass) were prepared by PVcomB at the Helmholtz-Zentrum Berlin für Materialien und Energie GmbH by co-evaporation method.

5.1.1 Argon treatment

Before alkali deposition, low energy ion treatments (200 eV) were conducted to remove surface contaminants from the CIGSe sample, (i.e., carbon and oxygen). A high-purity argon gas was used to produce an ion beam which impinges on the sample surface for sample cleaning. The ion treatments produce an exchange of energy and momentum between the colliding ions and the atoms of the sample's surface, inducing collision cascades in the sample. When recoils of the collision cascades reach the surface of the sample with energies greater than the energy binding the surface atoms (adatoms) to the material, atoms (adatoms) are ejected from the sample. The kinetic energy of ion treatments conducted on absorber substrates was confined to 200eV to maintain the ion beam energy below the sputter energy threshold to prevent damage of the sample. This can be considered as an ion-stimulated cleaning process rather than a classical sputter process. To ensure the complete cleaning of all the bare samples, three angles (45° , 90° , 135°) between sample and ion gun were used during the Ar^+ ion treatment. For these three different angles, the treatment was performed for about 30 minutes for each angle.

5.1.2 Alkali evaporation

After sample cleaning by argon treatment, alkalis were evaporated onto the cleaned CIGSe surface. The evaporation times were: i) 1 h for potassium (K) evaporation, ii) 20 min for rubidium (Rb) evaporation, and iii) 20 min for cesium (Cs) evaporation. The release of alkali metals is controlled by the amount of current passed through the dispenser.

The whole evaporation experiment was performed in the prep-chamber between load-lock and analysis chamber at HIKE end station, which is shown in Figure 3.6. The evaporator was attached to the bottom of the prep-chamber and the distance from the getter element to the sample is about 4 cm. Commercially alkali getter elements from SAES getter company^[128] were used. The pressure in the prep-chamber during the evaporation process was varied between 1×10^{-8} mbar and 1×10^{-7} mbar. A DELTA ELETRONIKA Power Supply SM 70-22 was used as current supply. The evaporation current in our experiments is 6.5 A for all the alkali elements.

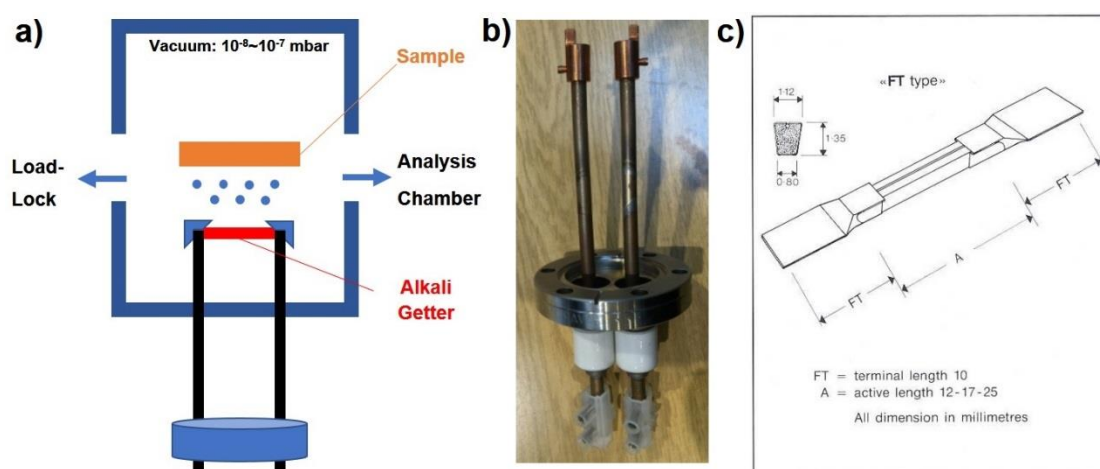


Figure 5.1 a) Schematic of the prep-chamber used for the evaporation experiment, b) picture of evaporator, c) alkali getter model^[128].

5.1.3 Annealing treatment

The annealing is carried out in the analysis chamber at HIKE end station. The heater is integrated into the manipulator in the analysis chamber behind the sample position. The heating rate was set to $5 \text{ }^\circ\text{C}/\text{min}$. The temperature of the treated samples was monitored by a thermocouple attached to the manipulator. The pressure in the analysis chamber was lower than 5×10^{-7} mbar during the entire annealing treatment. Each alkali treated sample was annealed at five different temperatures ($100 \text{ }^\circ\text{C}$, $150 \text{ }^\circ\text{C}$, $200 \text{ }^\circ\text{C}$, $250 \text{ }^\circ\text{C}$, $300 \text{ }^\circ\text{C}$) for 1h, sequentially. After the sample cooled down to around $50 \text{ }^\circ\text{C}$, HAXPES measurements were performed on the sample in the HIKE end station. This procedure was repeated for the next subsequential (higher) temperature.

Note that after annealing step at 250°C, K/CIGS and Rb/CIGSe samples were stored in the load-lock at EMIL for 31 and 34 days, separately, then the 300°C annealing step and related HAXPES measurements were performed on these samples.

5.2 HAXPES spectra comparison

Figure 5.2 shows the hard X-ray photoelectron spectroscopy (HAXPES) survey spectra of the three alkali/CIGSe sample series with an excitation energy of $h\nu = 2$ (2.1) keV. As expected, all Cu, In, Ga, Se, and alkali (K, Rb, and Cs after deposition) related photoemission and Auger lines are present. Before alkali evaporation, the survey spectra of the bare absorbers show no big difference. Besides Cu, In, Ga, and Se related signals, only minor C and O related signals can be observed, demonstrating the effectiveness of the cleaning treatment. The spectra of the CIGSe samples with evaporated alkalis are shown in Figure 5.2.b, we find a decreased intensity of the absorber related core level lines and strong alkali signals (most prominent K 2p, Rb 3d, and Cs 3d). Two different excitation energies are used for the measurement of the Rb/CIGSe sample because the Rb Auger lines overlap with O 1s when measured with 2 keV and overlapped with In 3d signals when measured with 2.1 keV. The oxygen signals increase after alkali evaporation. Since the annealing and measurement for K and Rb at 300°C were taken after a long time stored in UHV system, here 250°C samples were chosen for the comparison in Figure 5.2.c.

A significant depletion of the Cu 2p photoemission line can be observed after annealing; detail spectra of Cu 2p_{3/2}, In 4d/Ga 3d, and Se 3d are compared in Figure 5.3. Cu 2p was chosen because of the overlapping of Cu 3p and Cs 4d lines. After alkali evaporation, a Cu 2p attenuation is clear and spectra are broader especially after Rb/Cs evaporation. Figure 5.3.b shows In 4d/Ga 3d spectra. The shape of the spectra of the bare samples are similar, but broaden after alkali evaporation and annealing. For the Rb/CIGSe and Cs/CIGSe, new peaks appear at low binding energy which can be assigned to Rb 4p and Cs 5p. The peak located at about 16.7 eV appear for all three alkali/CIGSe samples and can attributed to a new In species. This In 4d contribution varies, prominently due to different alkali amount. The main In 4d peak shifts to high binding energy and the peak for the K/CIGSe is narrower than that for the Rb/CIGSe & Cs/CIGSe samples. This change of the chemical

environment of In is more significant for heavy alkali metals. Note that the K 3p signal (~17 eV) overlaps with the In 4d and Ga 3d peaks. Note that In 4d/Ga 3d intensity of the bare CIGSe absorber is different indicating different In/Ga surface ratios. The Se 3d spectra are displayed in Figure 5.3c. Similar to the In 4d/Ga 3d spectra, the shapes of the Se 3d spectra are getting broader after alkali evaporation and then getting narrower after annealing. The new Se contribution located at low binding energy is different for the different alkali elements, which is probed related to the different alkali amounts on the samples.

According to these first comparison results, the respective shallow core levels and the results of their fit analysis are discussed in the next two sections in detail: first the findings related to the K/CIGSe series are addressed. Then the results on the Rb/CIGSe and Cs/CIGSe samples are discussed.

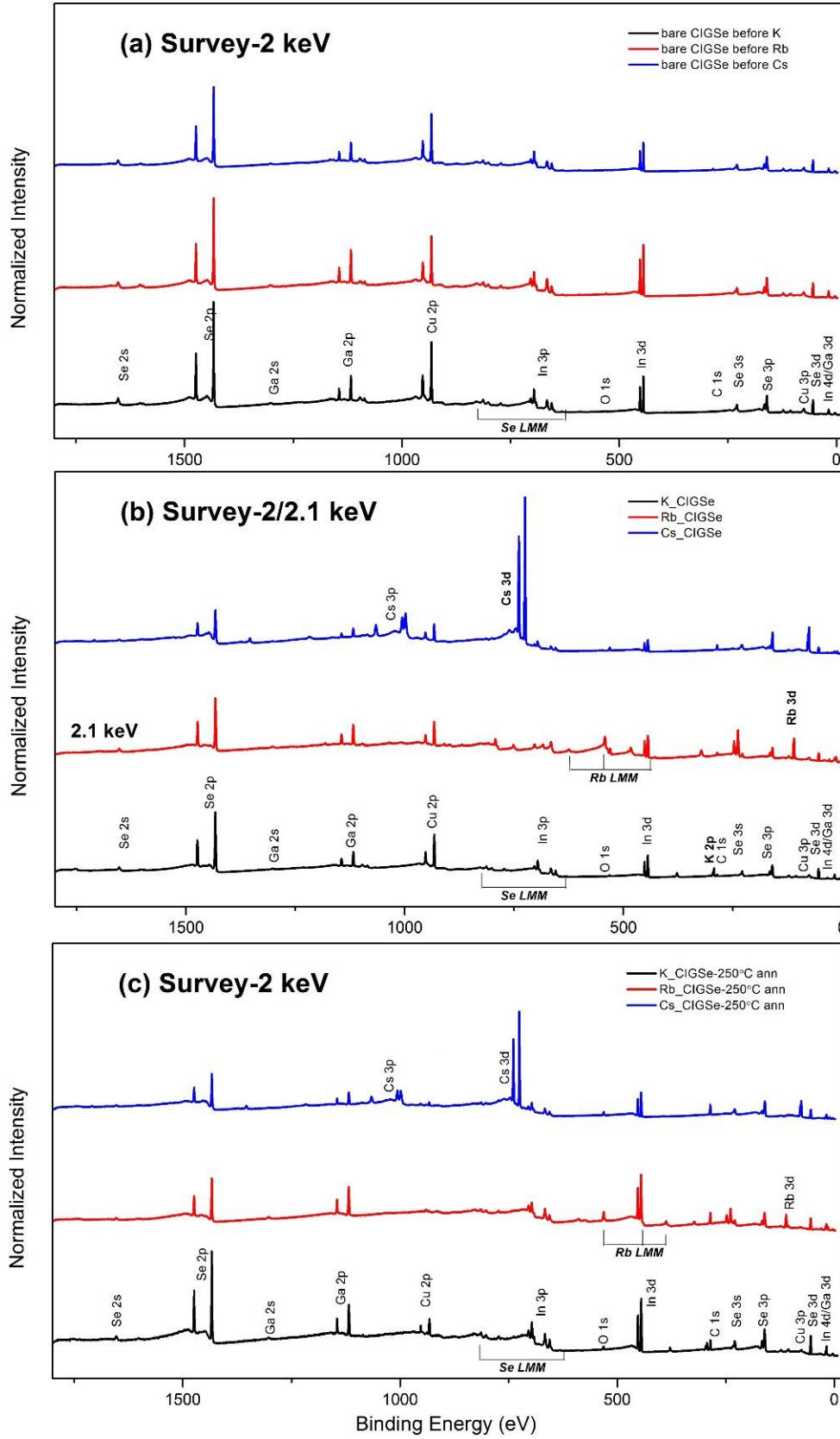


Figure 5.2. 2 keV survey spectra of bare, alkali/CIGSe, and annealed alkali/CIGSe absorbers (K: black; Rb: red; Cs: blue). For the spectra of the Rb/CIGSe sample, an excitation energy of 2.1 keV is used. The most prominent core level and Auger lines are marked.

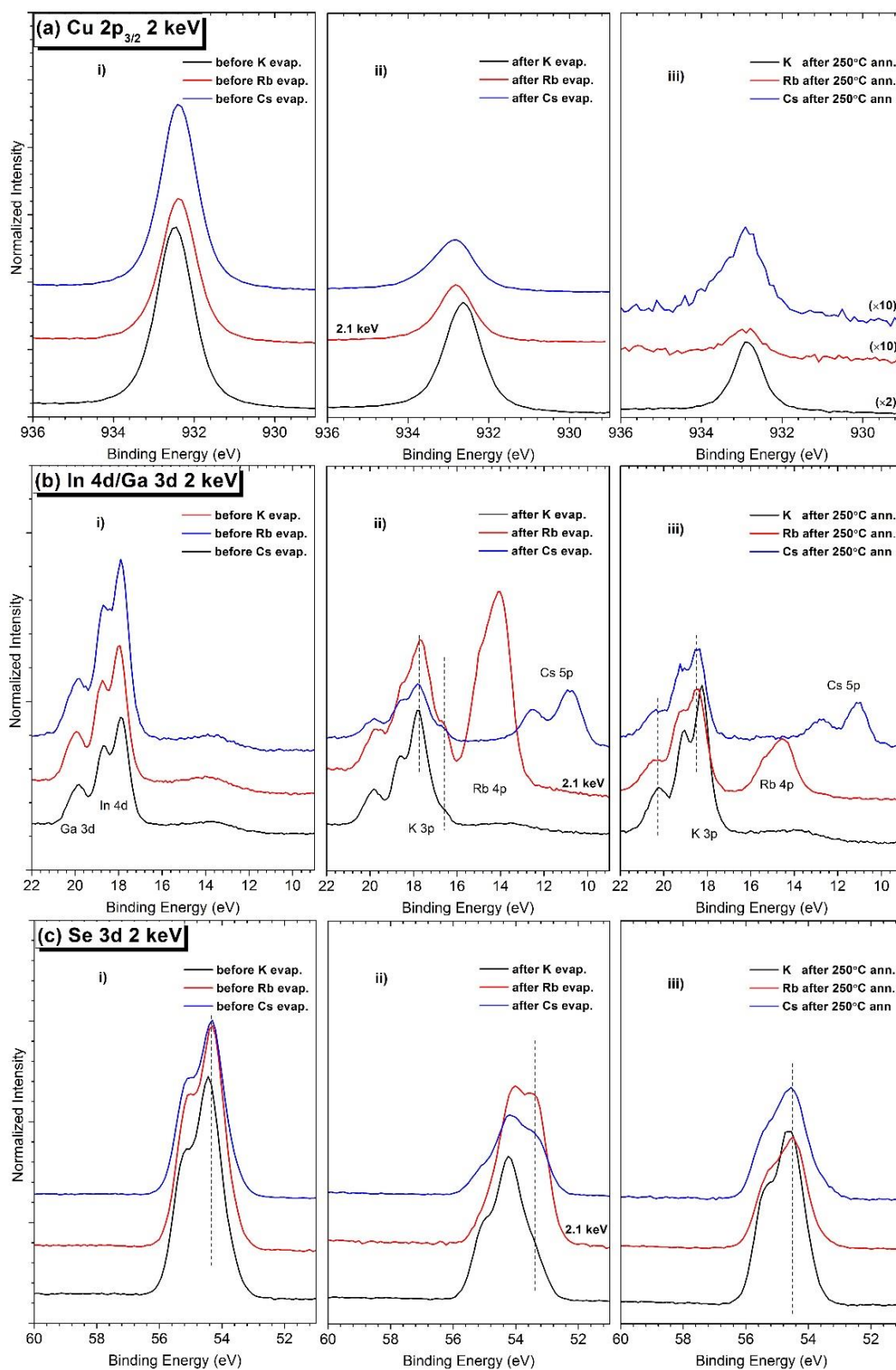


Figure 5.3. HAXPES detail spectra of the (a) Cu 2p_{3/2}, (b) In 4d/Ga 3d, (c) Se 3d regions of the bare CIGSe (i), alkali/CIGSe (ii), and annealed alkali/CIGSe (iii) sample series, as normalized to background intensity. All spectra were measured using 2/2.1 keV excitation. Vertical offsets are added for clarity.

5.3 Impact of potassium treatments on the chemical structure of CIGSe absorbers

5.3.1 X-ray absorption of the potassium K-edge

This subchapter will focus on x-ray absorption spectroscopy to directly probe the unoccupied local density of states to provide element-specific information. X-ray absorption near-edge structure (XANES) spectroscopy is a synchrotron-radiation-based technique that is sensitive to oxidation state, coordination, and site distortion (i.e., bond lengths and angles). The features of x-ray absorption spectra can be correlated directly with excited states created by absorption of x-ray photons, accessible from the ground state by selection rules.

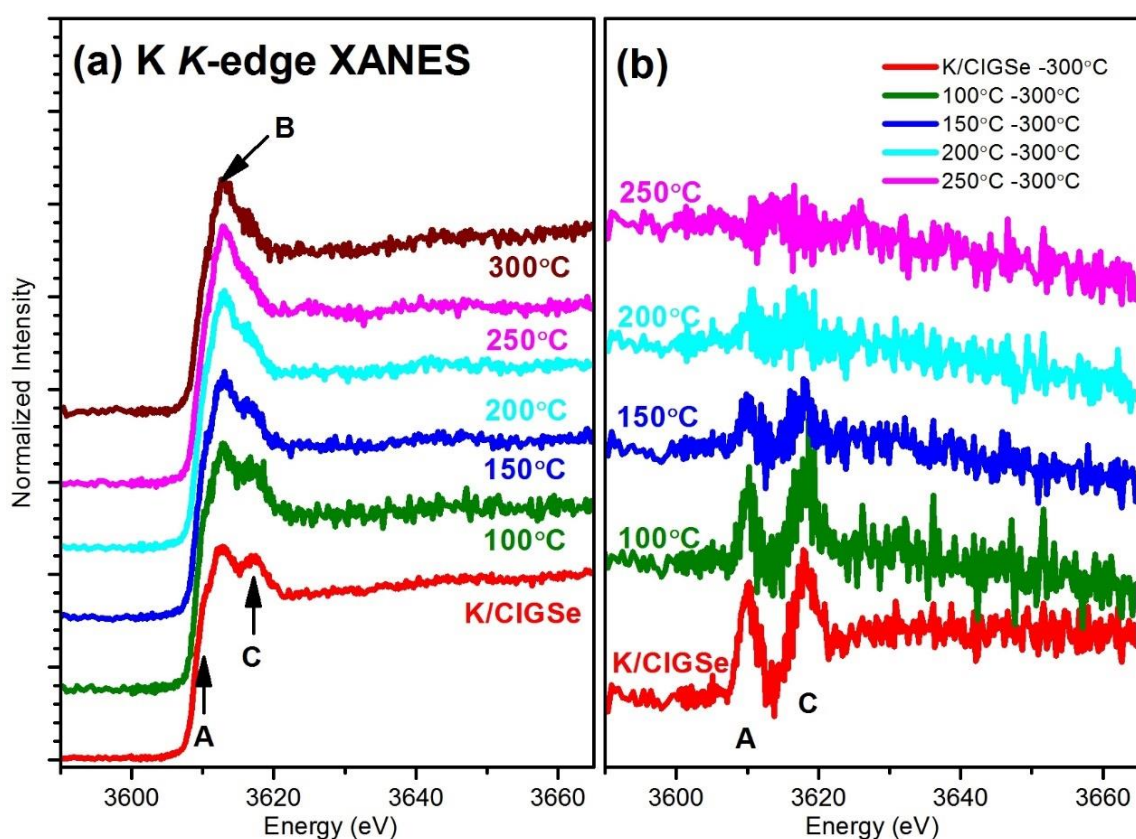


Figure 5.4. (a) The X-ray absorption spectra of K K-edge of the the bare CIGSe sample (bottom), K evaporated CIGSe and the annealing temperature series (temperature varied between 100 and 300 °C); (b) the spectral difference between K/CIGSe and annealing sample series, all the spectra was normalized to same edge jump before subtraction was performed.

Figure 5.1 shows the K K-edge spectra of our K/CIGSe samples. The spectra have similar features A (~3610 eV), B (~3612.5 eV), and C (~3618 eV), corresponding to the excitations from K 1s to 4p^[129]-based occupied states. A series of potassium K-edge XANES spectra of references samples with different coordination numbers were reported^[130] previously. Comparison of our spectra with the references suggest K is 6 coordinated for our samples independent of annealing. Features A and C decrease with increasing annealing temperature while feature B mainly stays constant, which indicates the presence of two K species of which one decreases and disappears after 200 °C annealing. To further identify the K species, HAXPES measurement are performed for K/CIGSe sample series with an excitation energy of $h\nu = 2$ keV, as discuss below.

5.3.2 Surface chemical structure

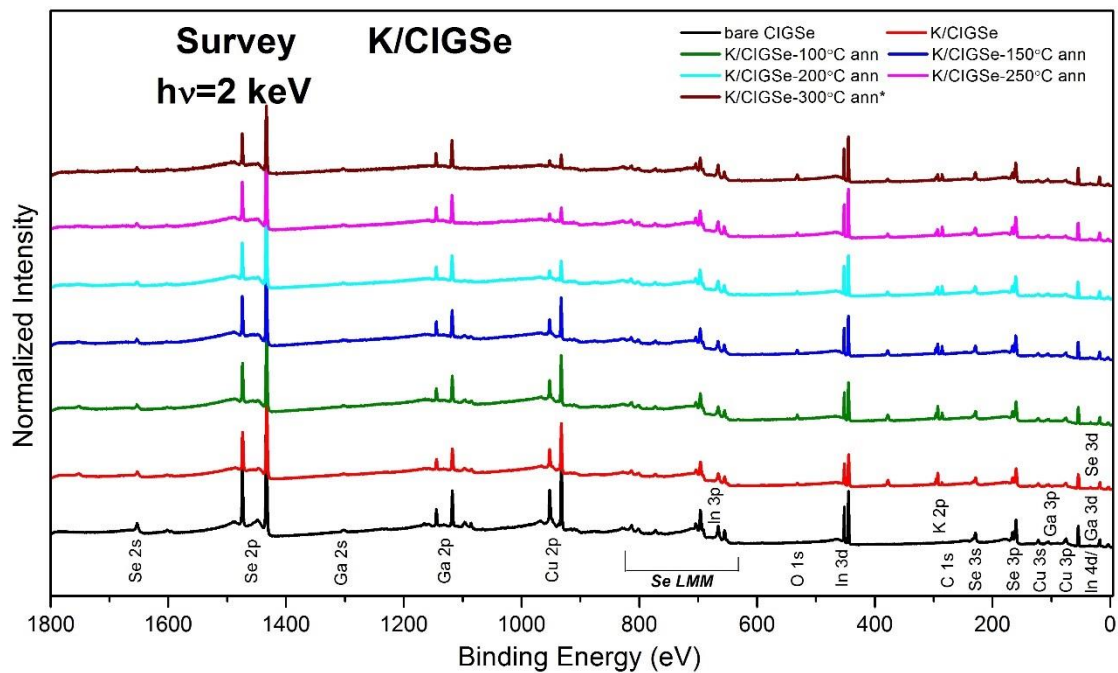
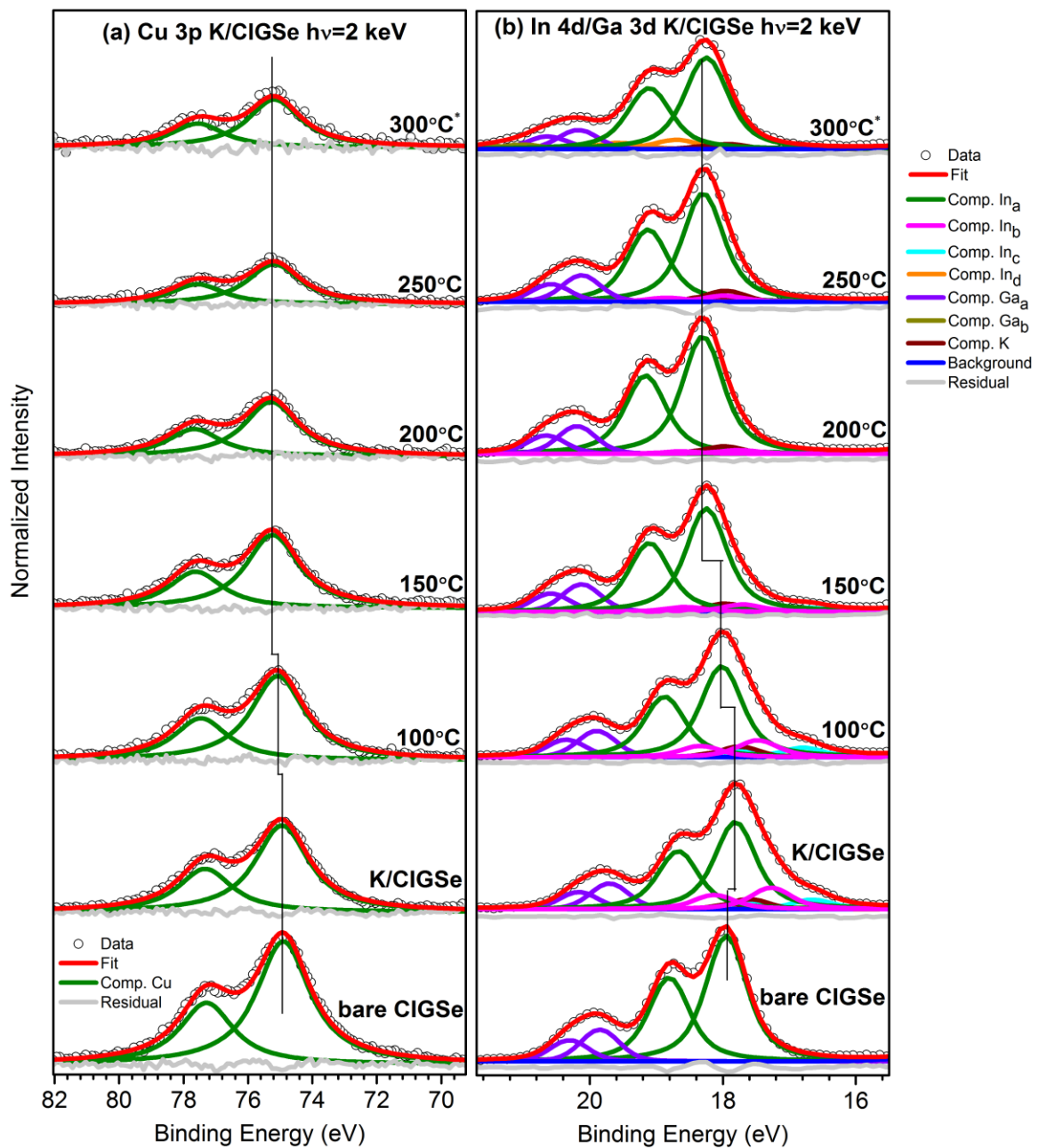


Figure 5.5. XPS survey spectra (normalized to equal intensity at a binding energy of 0 eV) of the bare CIGSe sample (bottom), K/CIGSe and the annealing temperature series (temperature varied between 100 and 300 °C), recorded with an excitation energy of $h\nu = 2$ keV. All prominent photoemission and Auger lines are labeled. Spectra are vertically offset for clarity. "*" mark means the annealing and measurement at 300 °C were performed 31 days later after that of the 250 °C sample (stored in Vacuum).

Following chapter 5.2, HAXPES measurements for the K/CIGSe series were performed before and after potassium evaporation and after each annealing step. The survey spectra of potassium treated

CIGSe absorber recorded with an excitation energy of $h\nu=2$ keV are shown in Figure 5.5. As expected, all Cu, In, Ga, Se, and K photoemission and Auger lines are present. The Cu and K peaks decrease in intensity, and the In, Ga, and Se peaks decrease first and then increase with increasing annealing temperature. In addition, rather substantial C-, and O-related XPS signals increase significantly after K evaporation and annealing. C and O signals are attributed to a surface contamination layer, formed presumably by gettering of residual gas remaining in the vacuum of the preparation and analysis chamber of HIKE by the highly reactive (metallic) potassium.



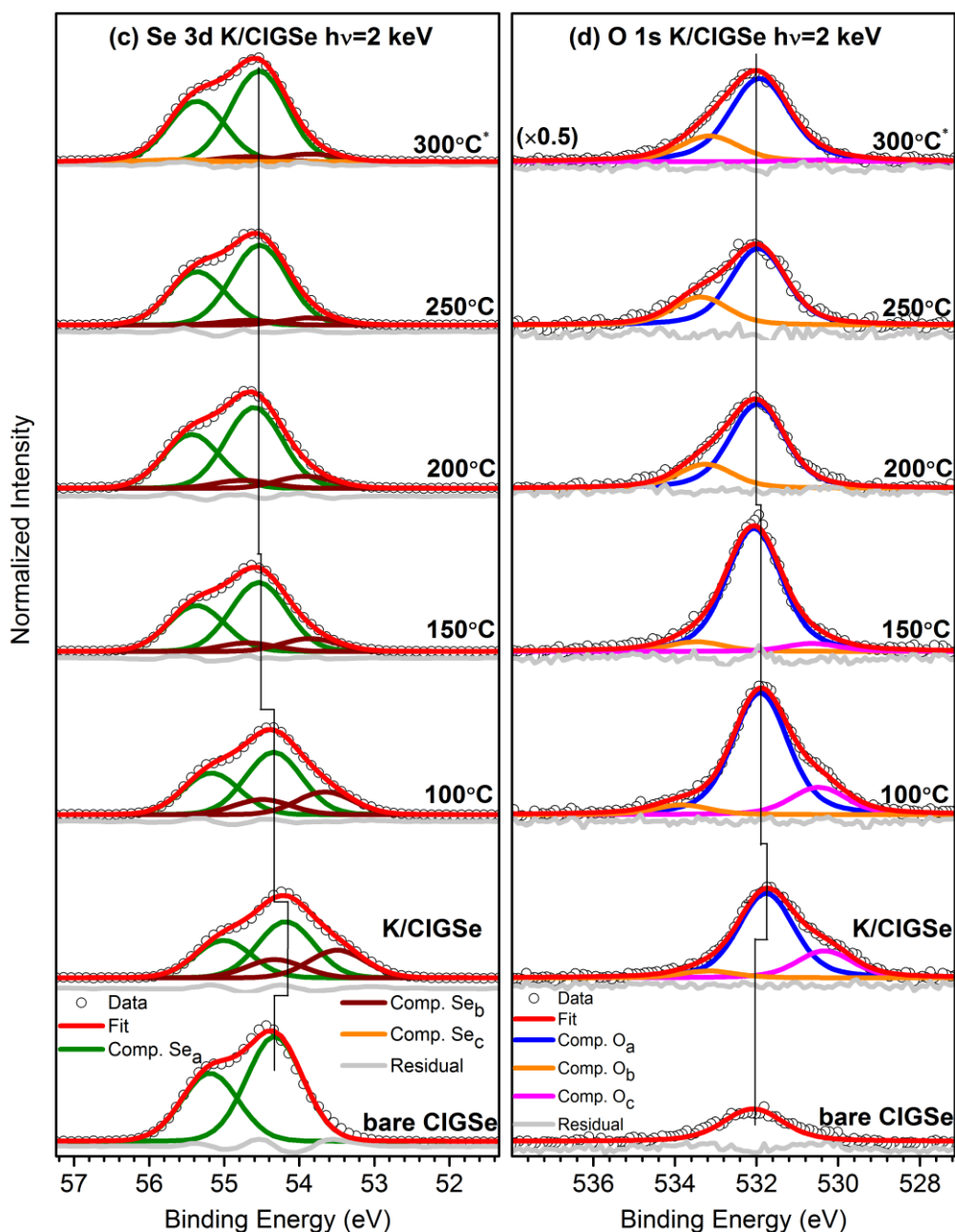


Figure 5.6. HAXPES data of K/CIGSe sample series, recorded with an excitation energy of $h\nu = 2$ keV: In 4p corrected Cu 3p (a), In 4d/Ga 3d/K 3p (b), Se 3d (c) and O 1s (d) detail spectra. The respective fits with Voigt profiles (doublets) and the residuals of the fits are also displayed. Note the different magnification factors.

Figure 5.6 shows the fits of the In 4p corrected Cu 3p (a), In 4d/Ga 3d/K 3p (b), Se 3d (c) and O 1s (d) spectra taken at 2 keV for the K/CIGSe sample series. Details of the In 4p background correction procedure are shown in Appendix B.1. The doublet separations of Cu 3p, In 4d, Ga 3d, and Se 3d were fixed to 2.39 eV^[81], 0.86 eV^[82], 0.46 eV^[83] and 0.83 eV^[84], respectively. The Cu 3p spectra can be fitted by one Cu species for all the samples. For other elements, more than one species is

required for some samples to obtain a nice fit. For the bare CIGSe absorber, the Cu 3p_{3/2} at 74.9 eV, In_a 4d_{5/2} at 17.87 eV, Ga_a 3d_{5/2} at 19.76 eV, Se_a 3d_{5/2} at 54.33 eV contributions represent the chemical surface of the chalcopyrite absorber^[131-132]. The experimental uncertainty is ±0.05 eV for all the values.

The Cu 3p peak shifts to high binding energy after sample annealing, but no obvious shape change can be observed. Figure 5.6 b shows the K 3p/In 4d/Ga 3d spectra with the respective fitting. The In 4d/Ga 3d gets broader after K evaporation and two additional peaks appear at low binding energy (In_b & In_c). In order to analyze these spectra in detail, we use the fit parameters from the In 4d/Ga 3d spectra of the 250 °C annealed K/CIGSe sample (which has the narrowest shape and thus is used as a reference spectrum representing one In/Ga species) to fit the In 4d/Ga 3d/K 3p spectra of the K/CIGSe sample set with fixed doublet separation and coupled Lorentzian-Gaussian widths. Following this procedure, more than one In and Ga species is needed for all In 4d/Ga 3d/K 3p spectra of the K/CIGSe samples, labelled In_a, In_b, In_c, In_d, Ga_a, and Ga_b.

As discussed above, In_a is attributed to the chalcopyrite absorber; In_b (In 4d_{5/2}: 17.27eV) could be K-In-Se or In-Se, In_c (In 4d_{5/2}: 16.76eV) can be assigned to metallic indium^[133] and decreases with increasing annealing temperature. After long storage time in vacuum, a fourth In peak appears after 300 °C annealing (In_d-In 4d_{5/2}: 18.69eV), which we ascribe to surface contamination (In-O). can be attributed to the In-O bonds. The melting point of In is 156.5 °C, which can explain the disappearance of In_c at 200 °C. The shifts and decrease of In_a and In_b after K deposition and annealing are attributed to chemical changes. Note that the K 3p is linked in area and position to the more prominent K 3s signal (E_B: 33.78eV) because of the significant overlap between the In 4d and K 3p lines, taking into account the respective cross-section ratio^[134] for the area and a fixed energy separation for all the spectra. Se detail fitting spectra are shown in Figure 5.6c. After K evaporation, a new component (Se_b: 53.50 eV) can be observed at lower BE, which can be related to the chemical change induced by K evaporation. The attribution of this Se species is not immediately clear, but the binding energy agrees well with the reported data of selenides^[135]. The main Se species shift tendency is similar to that of In in Figure 5.6b, which is an indication for a similar chemical environment change.

For a detailed analysis of the influence of alkali treatments on the chemical structure, the effect of surface contamination/oxidation must be discussed. Thus, O 1s spectra was fitted and shown in Figure 5.6 d. For the O 1s spectra, there are multiple fit contributions (O_a for the bare cleaned CIGSe; O_a , O_b , and O_c for K/CIGSe and annealing samples) needed for a satisfactory representation. Feature O_a at a binding energy of 532.05 eV (531.77 eV after K evaporation) and feature O_b at 533.22 eV clearly indicates the presence of chemisorbed oxygen (i.e. C=O) in the samples. Feature O_c at 530.35 eV can be attributed to metal-oxygen bonds.

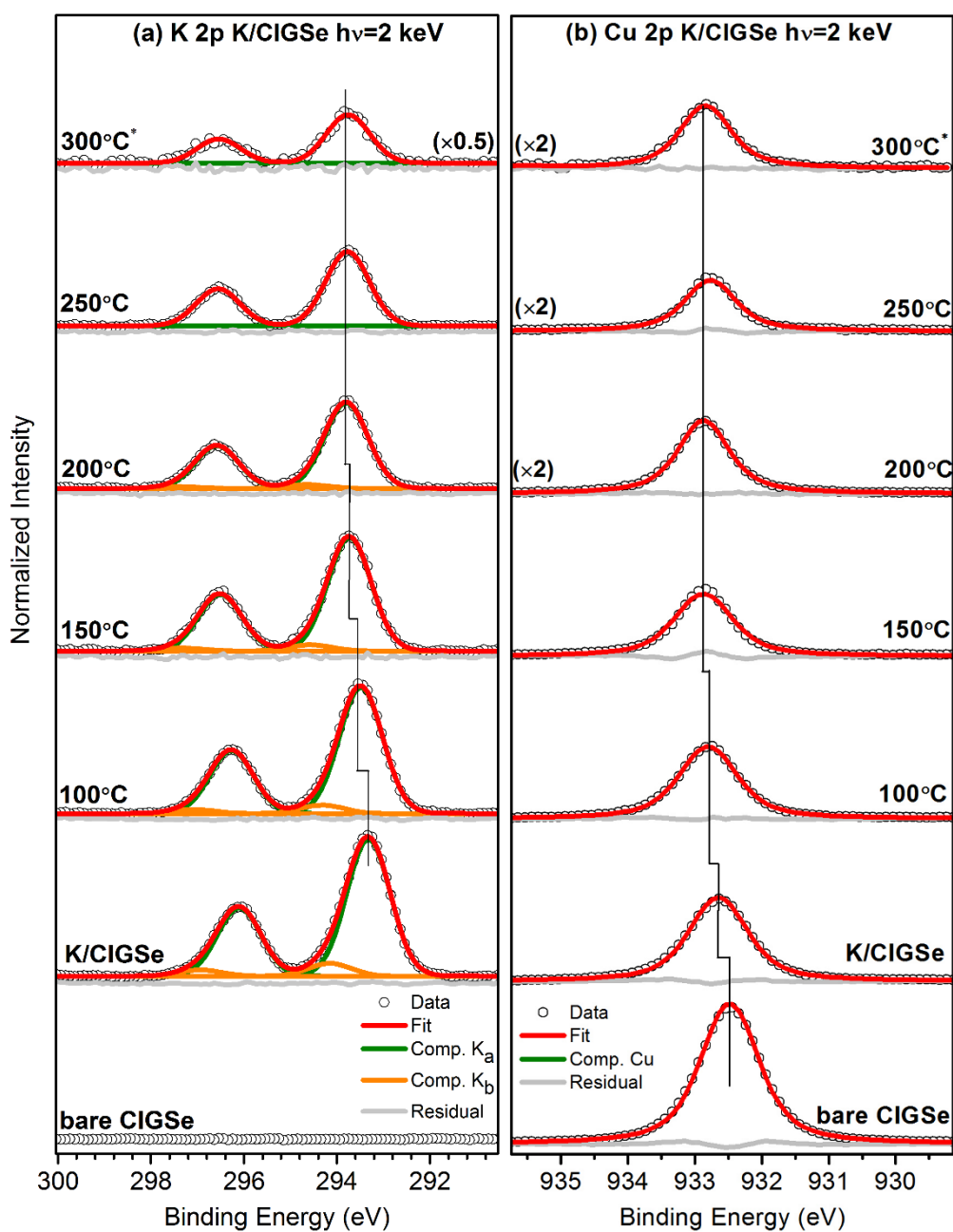


Figure 5.7. K 2p (a) and Cu 2p_{3/2} (b) HAXPES data of K/CIGSe sample series, recorded with an excitation energy of $h\nu = 2$ keV. The respective fits with Voigt profiles (doublets) and the residuals of the fits are also displayed. Note the different magnification factors.

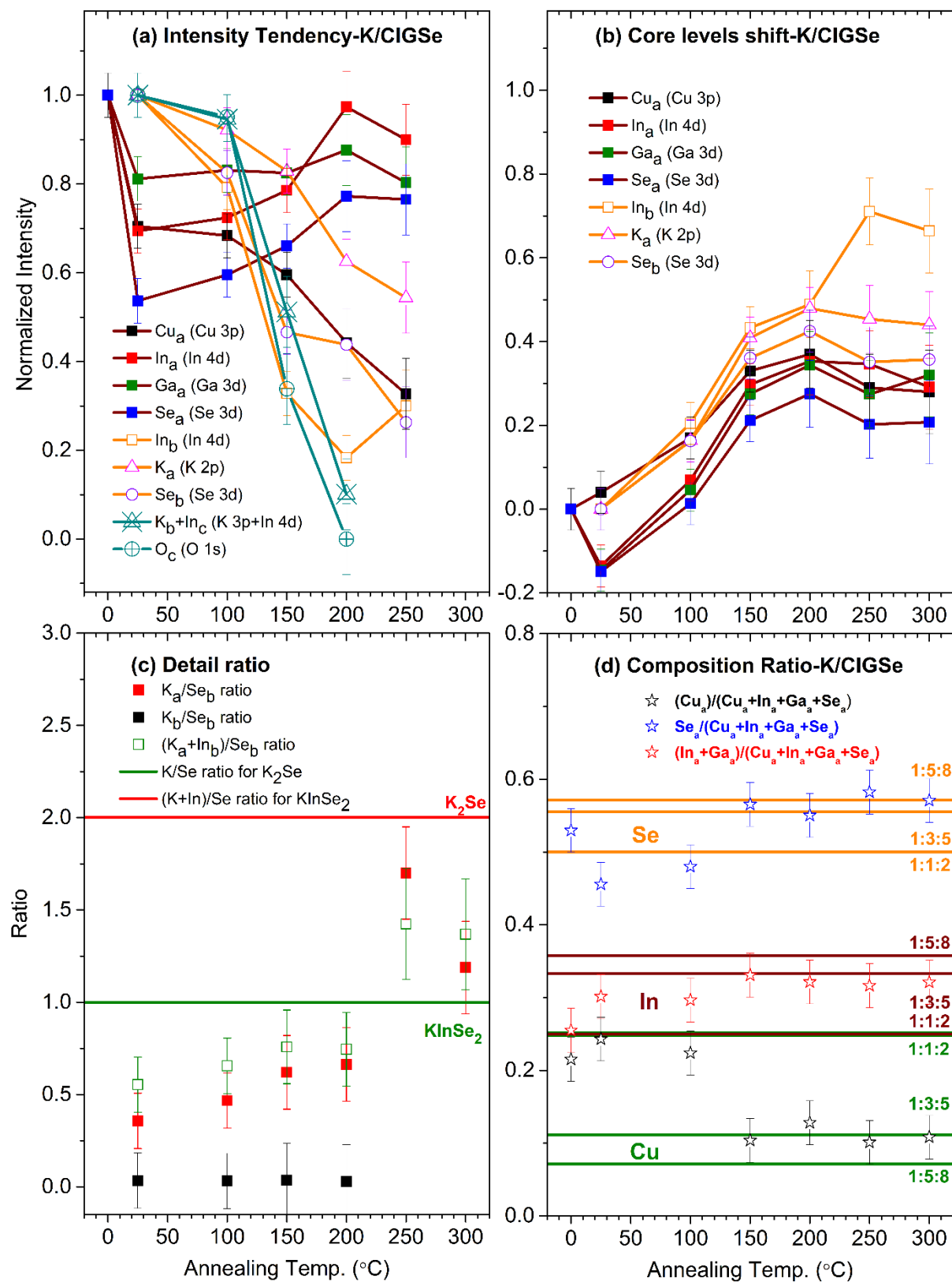


Figure 5.8. Evolution of the signal intensities (a) and BE shifts (b) of the Cu 3p, In 4d (In_a, In_b), Ga 3d (Ga_a), Se 3d (Se_a, Se_b), K 3p (K_a), and O 1s (O_c) XPS lines; (c) Evolution of the K_a/ Se_b and (K_a+ In_b)/ Se_b ratio as derived from the fit of the K 3p, Se 3d, and In 4d spectra, the K:Se ratio (2:1) of K₂Se and the (K+In):Se ratio (1:1) of KInSe₂ compositions are depicted in red and green, respectively; (d) (Cu_a)/(Cu_a+In_a+Ga_a+Se_a), Se_a/(Cu_a+In_a+Ga_a+Se_a), and (In_a+Ga_a)/(Cu_a+In_a+Ga_a+Se_a) ratios of K/CIGSe sample series as function of annealing temperature. The most common CIGSe-related stoichiometries ([Cu]:[In+Ga]:[Se] = 1:1:2, 1:3:5, and 1:5:8) for Cu, In, and Se are depicted in green, wine, and orange, respectively.

The K 2p spectra with respective fitting results are shown in Figure 5.7a to identify the chemical structure of potassium. The doublet separation of K 2p is fixed to 2.70 eV^[67]. The K 2p spectra after 250 °C annealing has the narrowest shape and that is used as a reference spectrum to represent one K species. Two K contributions (K_a and K_b) are needed to represent the K 2p spectra after K evaporation and low annealing temperatures, the binding energy of the K_b contributions (K 2p_{3/2}: 294.2 eV) is similar to the potassium oxide^[52, 136]. This component decreases with increasing annealing temperature and disappears at 200 °C, in good agreement with the K K-edge XANES (Figure 5.4). Cu 2p was also used to fit to check Cu contribution and shown in Figure 5.7b, and each spectrum can be represented by one contribution, which is in agreement with the fit of Cu 3p in Figure 5.6a.

From all the fitted Cu 3p/In 4d/Ga 3d/Se 3d/O 1s spectra, we can see all the contributions related to the chalcopyrite absorber (or potentially to other compounds) shifted due to the chemical environment change after alkali deposition. Figure 5.8 displays the intensity evolution (a), shift of respective core levels (b), and some composition ratios (c, d). Note the K_a and K_b (K 3p) contributions in Figure 5.8 a and b were calculated according to the K_a/(K_a+K_b) ratio from K 2p in Figure 5.7a, The K 3p area in Figure 5.6b is hard to separate into two K contributions with the weak K 3p signal and its significant overlap with In 4d line.

According to the fitting results in Figure 5.6 and 5.7, the intensity tendency and core levels energy shift were calculated. The values of corresponding contributions (i.e. Cu_a, In_a, Ga_a, Se_a, K_a, In_b, Se_b) were compared to detect possible relations. As shown in Figure 5.8 a, the calculated intensity of In_a, Se_a, and Ga_a components show a similar intensity evolution (i.e. all initial elements have nearly the same intensities for T > 150 °C), indicating they have a common chemical environment as discussed above. Cu is increasingly decreased with increasing annealing temperature (in

particular >150 °C), suggesting that Cu diffuses into the bulk of the CIGSe or the Cu-depleted CIGSe signal is increasingly attenuated by a formed top layer. After K evaporation, the new features of In_b , Se_b , and K_a also show similar tendency when K/CIGSe sample was evaporated and annealed, again indicating that they may be affiliated to the same component. The similar tendency of cross section corrected K_b+In_c intensity and O_c indicates the formation of K-O and In-O bonds in agreement with the K_b and In_c attribution in the previous discussion. The core level's peak center shift is shown in Figure 5.8b. The BE shifts of the In_a , Ga_a , and Se_a contributions are similar. Similar is for In_b , K_a , and Se_b , which (again) confirms this affiliation to similar chemical environment.

As in Chapter 4, in order to evaluate the attenuation behavior of the different core levels independent of analyzer transmission function and IMFP, we use the intensities of absorber-related shallow core level signals (Cu 3p, In 4d/Ga 3d, Se 3d, and K 3p) with similar (high) kinetic energies to calculate the composition ratio. First, the K_a/Se_b ratio was calculated in Figure 5.8c (red points), there is an obvious change after annealing at 250°C , which may be an artifact of the low intensity, and therefore high uncertainty at high annealing temperature. K_a/Se_b ratio is close to 1:2 at the beginning, which is contrast to the 2:1 ratio expected for a K_2Se compound (red line) but close to ratio ($K/Se = 0.5$) for $KInSe_2$ compound. Considering the presence/formation of $KInSe_2$ at the $CIGSe^{NaF+KF}$ surface has been suggested in the previous report^[33] and the existence of In species (In_b) in our sample series, we also calculated the $(K_a + In_b)/Se_b$ ratio to see if this In species can be related to $KInSe_2$ compound, as shown in Figure 5.8c (green points). The green line ($y=1$) shows the $(K+In)/Se$ ratio in $KInSe_2$ compound. According to the comparison result, and so of the two possible K-Se models described above, we would favor the “K-In-Se” model for the affiliation of K_a and Se_b species in our sample series.

It should be noted, that there are many different nonuniform compositions that could explain the findings here. Therefore, the relative $(Cu_a)/(Cu_a+In_a+Ga_a+Se_a)$, $Se_a/(Cu_a+In_a+Ga_a+Se_a)$, and $(In_a+Se_a)/(Cu_a+In_a+Ga_a+Se_a)$ ratios for the K/CIGSe sample series as function of annealing temperature are depicted in Figure 5.8d along with lines describing the expected values for different CIGSe-related stoichiometry. For the bare CIGSe sample in Figure 5.8d, the Cu_a , In_a+Ga_a , and Se_a content (open stars) approaches 1:1:2 within the experimental uncertainty. A significant change for

In_a+Ga_a and Se_a . can be observed after K evaporation, it can be attributed to the formation of K-In-Se/metallic In (In_c) components. These ratios all stabilize to 1:3:5 when the annealing temperature $T \geq 150$ °C, in the region where the fitting results in Figure 5.6 show disappearance of metallic In (In_c) and the significant Cu depletion (Figure 5.8a). Therefore, the final sample states would be more like a K-In-Se + Cu-poor CIGSe ($\text{Cu}:\text{In}+\text{Ga}:\text{Se} = 1:3:5$) mixture surface after high temperature annealing, which is in agreement with the surface structure of produced by standard NaF+KF PDT report previously.^[50]

5.3.3 Direct chemical structure comparison with CIGSe samples undergoing NaF+KF PDT

As discussed in chapter 4 and in previous report, the surface composition of CIGSe samples after NaF+KF PDT treatment ($\text{CIGSe}^{\text{NaF+KF}}$) shows the formation of a K-containing species^[26, 29, 33]. Here, we compare the evaporated and annealed K/CIGSe model system to the photoemission measurements after NaF+KF PDT. All the spectra are shown in Figure 5.9. The spectra for the $\text{CIGSe}^{\text{NaF+KF}}$ samples were adopted from Ref. ^[50] and the data for the bare CIGSe, K/CIGSe, and K/CIGSe-250°C samples are the same as in Figure 5.6.

In Figure 5.10, the binding energy are shifted to align the Cu 3p spectra to counter differences in doping level or (surface) band bending and allow a direct comparison of BE positions. As we observed, the Se_a species are aligned for K/CIGSe and K/CIGSe-250°C samples but differ from that of the bare CIGSe, in keeping with our previous conclusion from Figure 5.6 that Se_a species changes from a CIGSe absorber to K-incorporated absorber. The absolute binding energy of Se_a (CIGSe absorber) is not same as that of Se_c (CIGSe absorber), that can be induced by difference absorber preparation environment since the BE distance (0.70 eV) between Se_a and Se_b is in agreement with that (0.61 eV for Se_c and Se_d) of the $\text{CIGSe}^{\text{NaF+KF}}$ sample. There is a difference observed for In4d/Ga 3d spectra after realignment: the binding energy of In_a for bare CIGSe is close to the BE of In_c (K-In-Se species) of the $\text{CIGSe}^{\text{NaF+KF}}$ sample; considering the absorbers come from different sources, and have, e.g., very different Ga/(Ga+In) ratio (Appreciable Ga 3d lines are only detected on the K/CIGSe sample series), chemical shift is a possible explanation for the small

binding energy shift. The results of the comparison are in agreement with our previous discussion results (K-In-Se + Cu-poor CIGSe surface) about the chemical structure of evaporated and annealed K/CIGSe samples, indicating that it is a valid model system for understanding KF PDT.

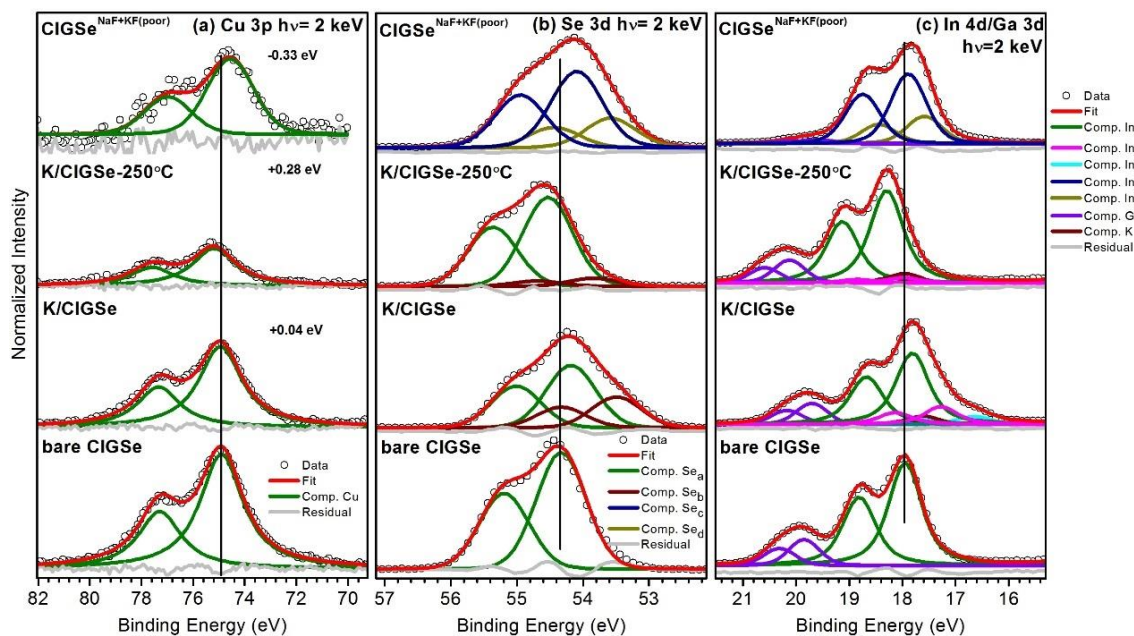


Figure 5.9. The direct comparison of Cu 3p (a), Se 3d (b) and In 4d/Ga 3d (c) spectra of bare CIGSe, K/CIGSe, K/CIGSe-250°C, and $\text{CIGSe}^{\text{NaF+KF(poor)}}$ samples with respective fitting results, all the K evaporated and PDT samples were measure at 2 keV. The residuals of the fits are also displayed. The PDT sample spectra were adopted from Ref. [50].

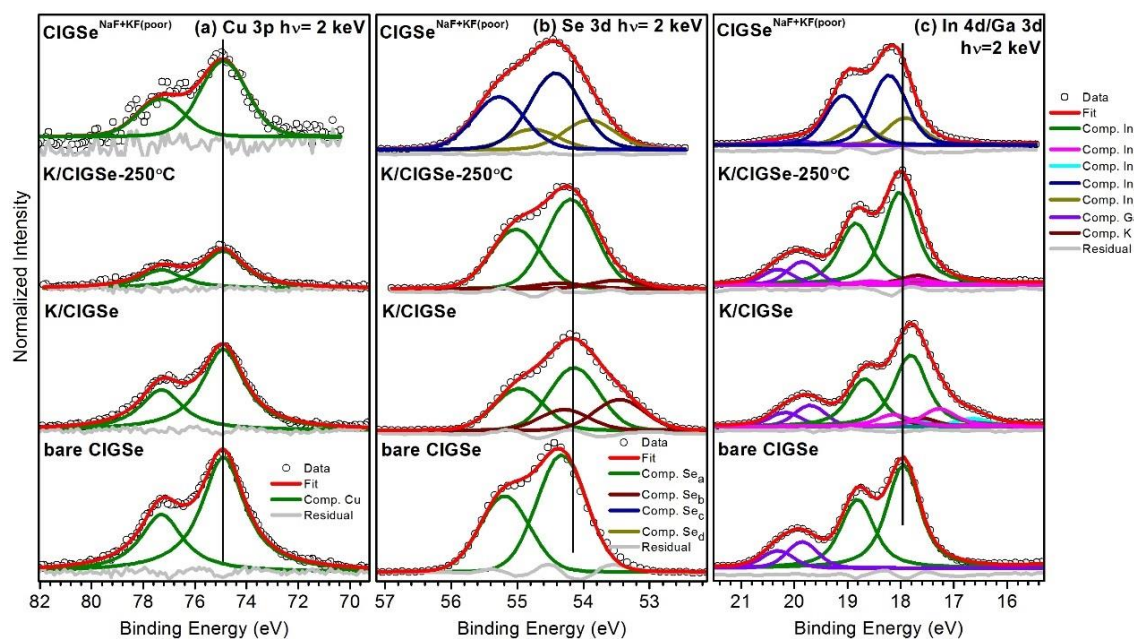


Figure 5.10. Realigned Cu 3p (a), Se 3d (b) and In 4d/Ga 3d (c) spectra by aligning the Cu 3p_{3/2} peak center to be at one BE position.

5.4 Impact of rubidium/cesium treatments on the chemical and electronic structure of CIGSe absorbers

5.4.1 Surface chemical structure

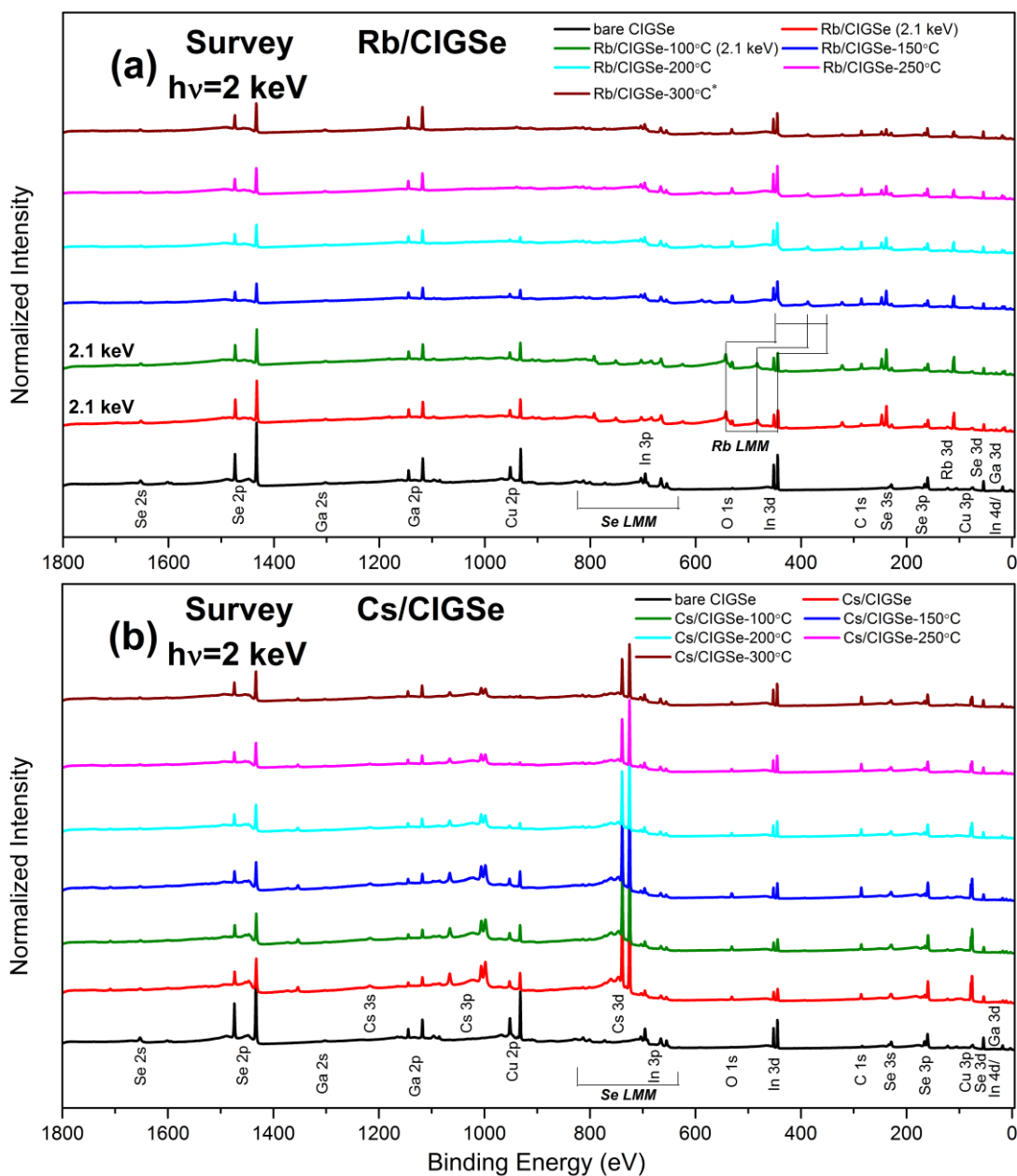


Figure 5.11. XPS survey spectra (normalized to equal intensity at a binding energy of 0 eV) of the bare CIGSe sample (bottom spectra), the alkali/CIGSe samples and all different annealing steps (100, 150, 200, 250, 300 °C), recorded with an excitation energy of $h\nu = 2$ (2.1) keV. The Rb/CIGSe and Cs/CIGSe data is shown in panel (a) and (b), respectively. All prominent photoemission and Auger lines are labeled. Spectra are vertically offset for clarity. “*” mark means the annealing and measurement for Rb/CIGSe sample at 300 °C were performed 34 days later after annealing and the measurement at 250 °C (stored in vacuum: 1×10^{-8} mbar).

The introduction of heavy alkali elements via RbF or CsF PDT improved the solar cell properties and efficiency compared to the NaF and NaF+KF PDT^[3] CIGSe absorbers. The chemical and electronic structures of CdS/CIGSe^{RbF} were investigated by Nicoara et al.^[44] and Hauschild et al.^[31], trying to explain the impact of RbF on the properties of the CIGSe surface/interface. In order to systematically study the effects of Rb metal evaporation and compare to the impact of lighter alkali elements (Na, K), we have conducted in-situ Rb and Cs deposition on CIGSe with subsequent HAXPES analysis using the HIKE end-station.

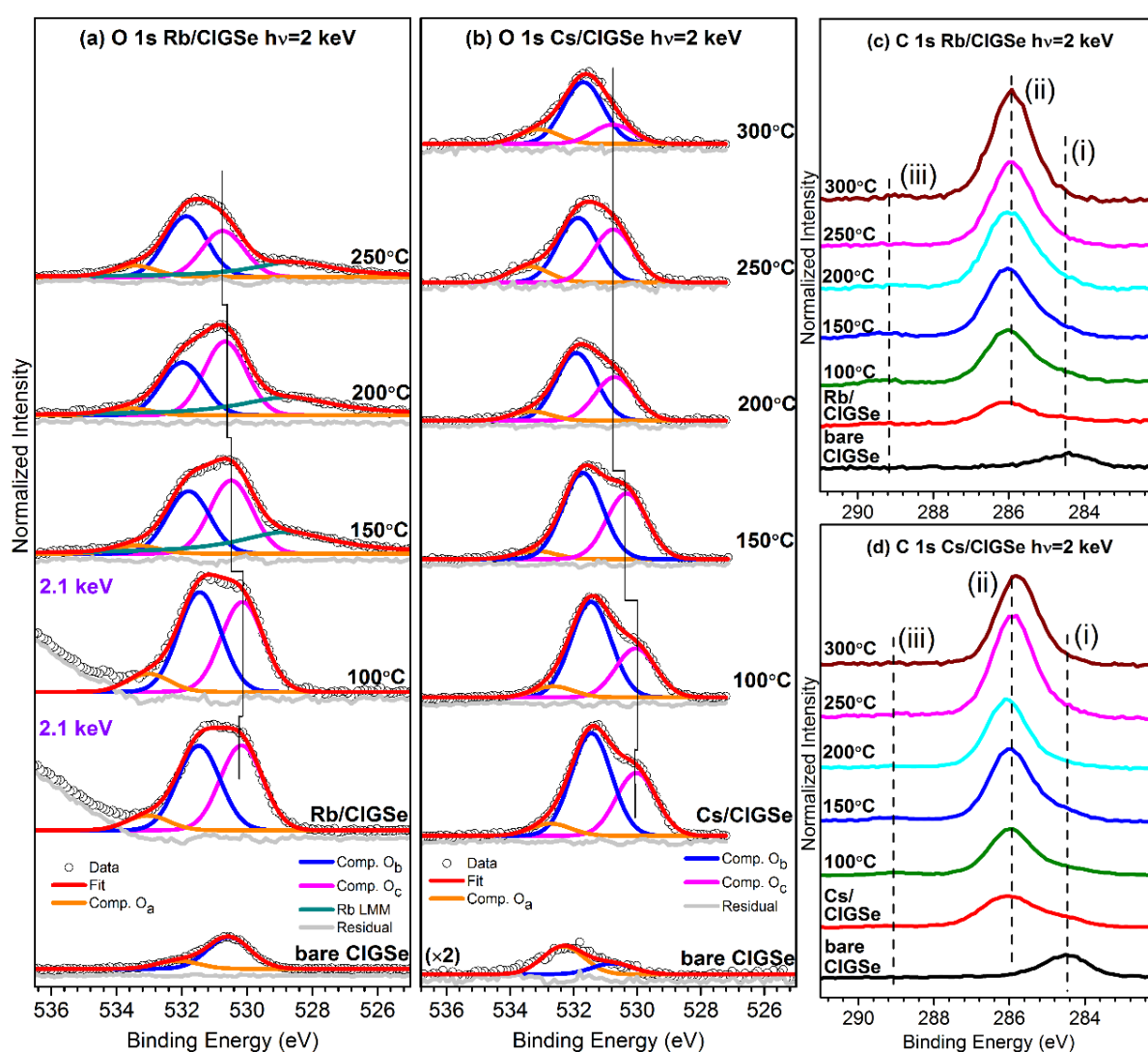


Figure 5.12. Fitted O 1s (a and b) and normalized C 1s (c and d) lines measured with excitation energies of $h\nu=2(2.1)$ keV for Rb/CIGSe and Cs/CIGSe sample series. All the spectra are background normalized. The respective fits with Voigt profiles and the residuals of the fits for O 1s are also displayed.

Figure 5.11 shows the HAXPES survey spectra of the investigated Rb/CIGSe and Cs/CIGSe sample series with an excitation energy of $h\nu = 2$ (2.1) keV, separately. As expected, all Cu, In, Ga, Se, Rb, and Cs photoemission and some Auger lines are present. The Cu, Rb, and Cs peaks decrease in intensity, and the In, Ga, and Se peaks first decrease upon alkali deposition but then increase with increasing annealing temperature. In addition, C-, and O-related XPS signals increase after Rb/Cs evaporation.

Two different excitation energies were used for the Rb/CIGSe measurement because Rb LMM Auger lines were found to overlap with O 1s when measured at 2 keV and overlapped with In 3d signals when measured with 2.1 keV. For the annealing samples from 200 °C to 300 °C, only In 3d was measured with an excitation energy of $h\nu = 2.1$ keV. The rest of the spectra were measured at 2 keV. Note that the annealing and measurement of the 300 °C Rb/CIGSe was performed 34 days after initial characterization (samples were stored in vacuum chamber at 1×10^{-8} mbar), which can explain why we can find some different features for this sample (see discussion below).

The O 1s (a and c) and C 1s (b and d) signals is depicted in more detail in Figure 5.12. The O 1s spectra for Rb at 300 °C is missing because of measurement time limitation. The “slope” at high binding energy can be attributed to Rb LMM Auger spectra^[137]. After Rb and Cs evaporation, the oxygen and carbon signals increase significantly and shift compared to the bare CIGSe sample. We see (at least) two oxygen species for both bare CIGSe samples. Moreover, additional O 1s peaks at lower binding energies and C 1s peaks at higher binding energy appear after Rb and Cs evaporation, which can be assigned to more oxygen and carbon species. Based on the O 1s fitting results, the peak at 530.0 eV (O_c) originates from metal-oxygen bonds^[90]. The dominant O 1s feature at about 531.6 eV (O_b) could be assigned to ascribed to (surface)-OH^[138] groups and the peak area decreases with increasing annealing temperature. Xu et al.^[139] reported the existence of $LiInO_2$, where O 1s peaks located at 531.5 eV. However, according to the reported syntheses temperature and time^[139-144] of $AlkInO_2$ (Alk= Li, Na, K, Cs), the time (≥ 4 h) and the temperature (≥ 600 °C) are higher than in our experiment, which excludes the presence of $AlkInO_2$ here. The small peak at 532 eV (O_a) is assigned to adsorbed oxygen species(i.e. C=O)^[145]. The C 1s also consists of three regions: i) at binding energy of 284.4 eV that corresponded to C-C bond, ii) at 285.8 eV attributed to C-O bond,

and iii) the small additional peak at 289 eV^[146] can be assigned to carbonates. Similar as potassium, the carbon and oxygen contamination could be formed by gettering residual gas remaining in the vacuum of the preparation and analysis chamber by the highly reactive alkali elements at the beamline endstation.

In the following, a detailed investigation of the chemical structure of Rb and Cs - CIGSe absorber as a function of annealing temperature will be given. Since the Rb 3d and Cs 3d spectra are the most pronounced signals for Rb and Cs core levels, we used those spectra to identify the chemical structure of the Rb or Cs species. All the spectra were normalized to the same height to compare the shape change during the annealing process. The fitting of background normalized Rb 3d/Ga 3p and Cs 3d core-level HAXPES spectra (taken at 2(2.1) keV) are shown in Figure 5.13 for all CIGSe samples. As observed in the survey spectra, the alkali signals attenuate and shift to high binding energy with increasing annealing temperature. Three Rb contributions are needed to fit the Rb 3d spectra reasonably and one Ga species is used to represent the Ga 3p line (except for the 300 °C sample). An increase of Ga 3p signal at 300 °C can be observed, which might indicate a potential diffusion process (Note that this sample was measured 34 days after the initial study.). Considering the long storage time (in vacuum) and the possible contamination by oxygen and carbon in the transfer procedure, it could be attributed to gallium oxide. Figure 5.13 shows the Rb 3d/Ga 3p and Cs 3d fitting results (note the different magnification factors). The d and p lines are composed of a doublet, the doublet separation for Rb 3d is 1.47 eV^[147] in our fitting results and 3.37 eV^[148] for Ga 3p. The third Rb (Rb_c:111.25 eV) species can be attributed to rubidium oxide^[149], however, the attribution of Rb_a and Rb_b is not straight proceed. The tendency of Rb_a and Rb_b (Rb_a decreases and Rb_b increases with increasing temperature) probably indicates an annealing induced chemical change from one Rb species into another. The fitted Cs 3d_{5/2} core-level HAXPES spectra taken at 2 keV for all CIGSe samples are shown in Figure 5.13b. According to the Cs 3d comparison, no obvious Cs 3d shape change with increasing temperature can be observed. The small Cs_b (Cs 3d_{5/2}: 726 eV) contribution can be attributed to Cs-O^[150-151]. In the main Cs peak, it is hard to distinguish if there is only one Cs contribution or two overlapping contributions as in Rb 3d. Rb and Cs contributions should be similar for Rb 4p and Cs 5p in the shallow core level region (i.e. at least

the same species should be proceed), we use the Rb 3d and Cs 3d fit results as input parameters to fit Rb 4p and Cs 5p spectral regions.

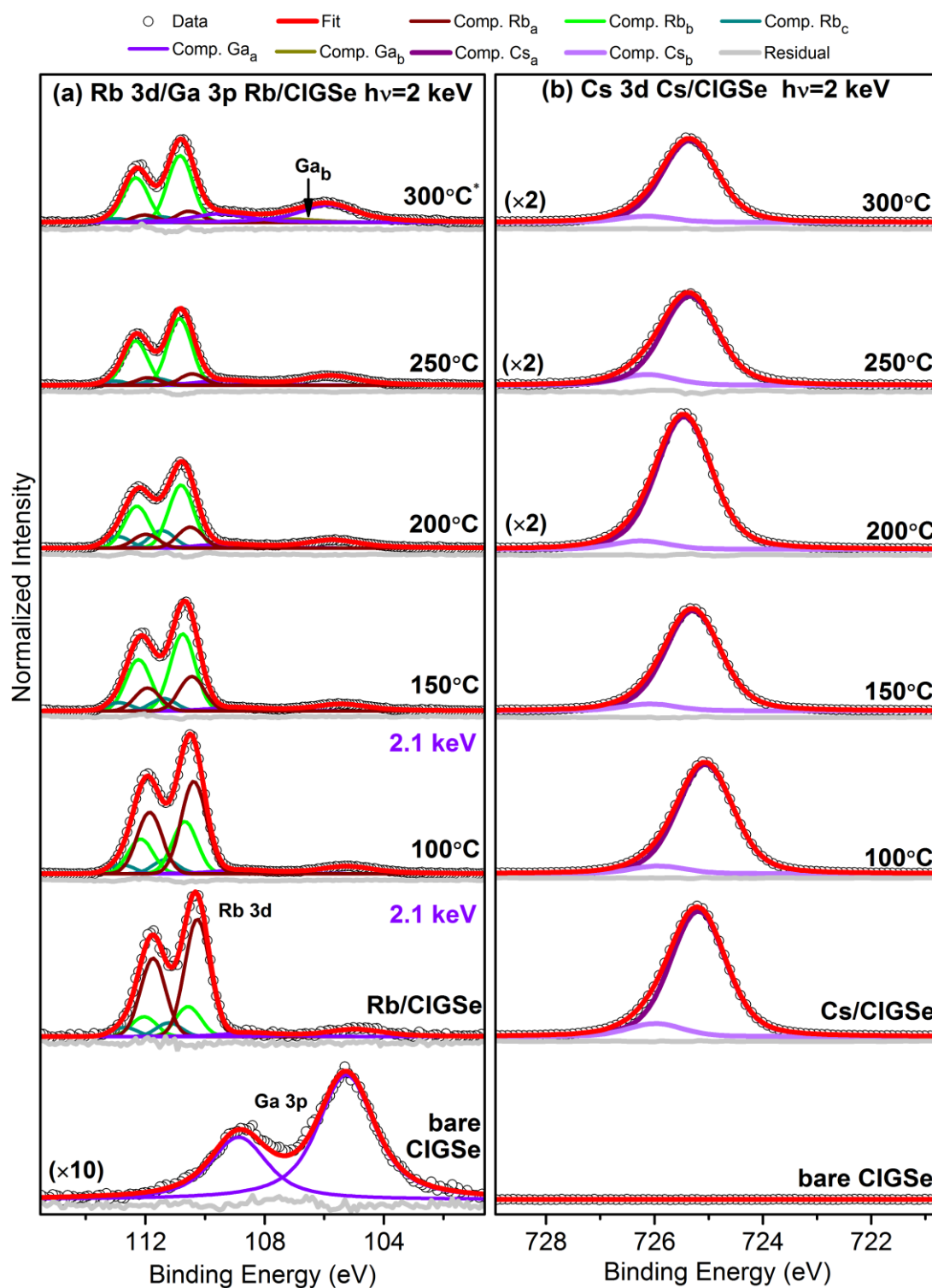


Figure 5.13. Rb 3d/Ga 3p (a) and Cs 3d (b) HAXPES data of the alkali-CIGSe sample series, recorded with an excitation energy of $h\nu = 2(2.1)$ keV. All the spectra are background normalized. For each fit, the residual is shown as well. Spectra are vertically offset for clarity. Note the different magnification factors.

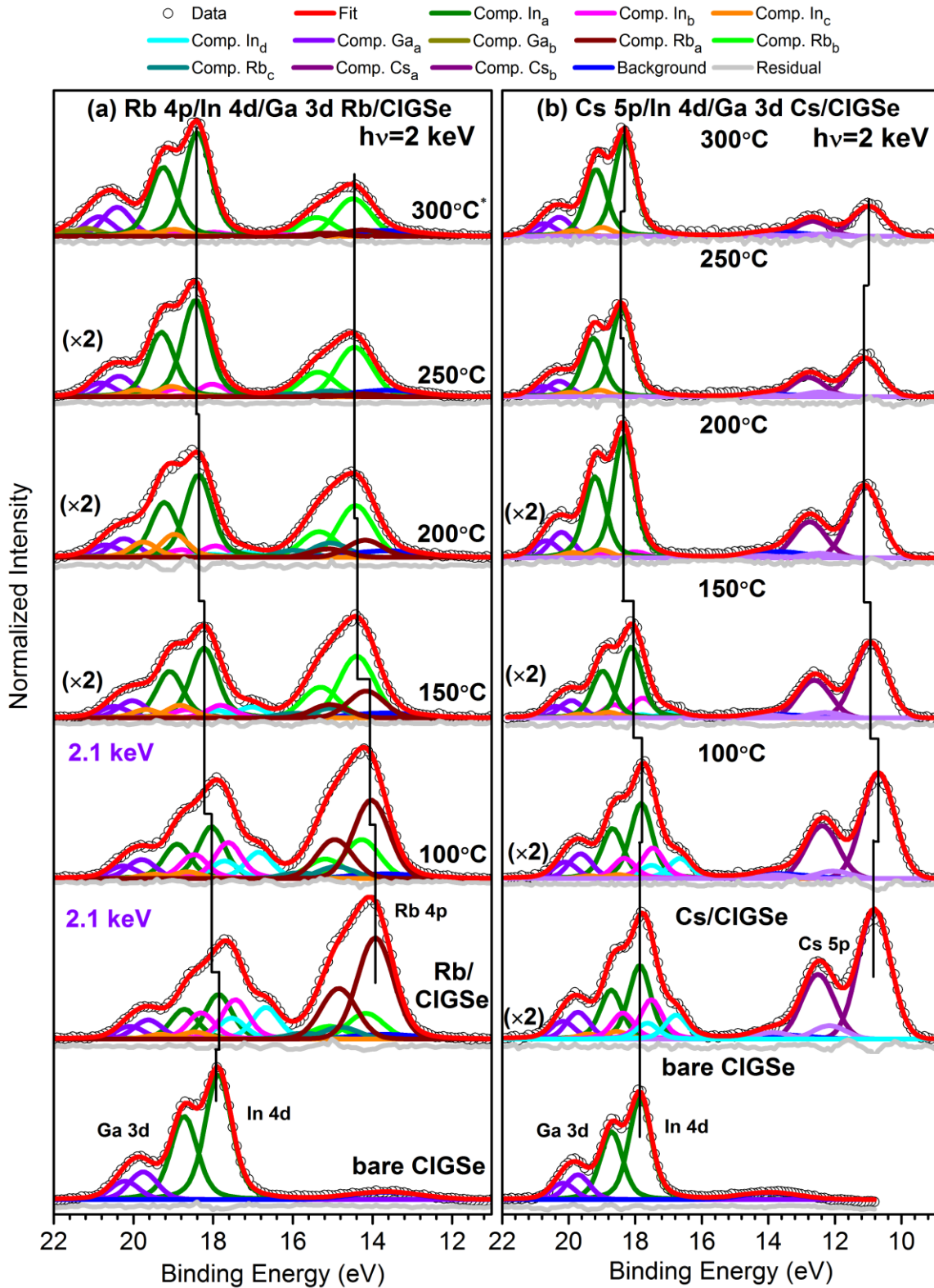


Figure 5.14. HAXPES data of alkali (Rb, Cs)-CIGSe sample series, recorded with an excitation energy of $h\nu = 2(2.1)$ keV: Rb4p/In4d/Ga 3d (a) and Cs 5p/In4d/Ga 3d (b). The respective fits with Voigt profiles (doublets) and the residuals of the fits are also displayed. Note the different magnification factors. The fitting of the Rb4p and Cs 5p spectra are based on the Rb 3d and Cs 3d fitting results in Figure 5.13. Spectra are vertically offset for clarity.

Figure 5.14 shows the fitted In 4d/Ga 3d/Rb 4p (a) and In 4d/Ga 3d/Cs 5p (b) spectra taken at 2 keV for the different alkali/CIGSe sample series. Note the background peak at around 13.69 ± 0.05 eV for all the spectra was attributed to the Se 4s contribution^[152] in previous report. The doublet separations of In 4d and Ga 3d were fixed to 0.86 eV^[82] and 0.46 eV^[83], respectively. For the bare CIGSe absorbers, the In_a 4d_{5/2}: 17.87 and Ga_a 3d_{5/2}: 19.76 eV contributions represent the chalcopyrite absorber^[131-132] (error bar would be ± 0.05 eV for all the values). The main In and Ga peak shifts to lower binding energy and then shifts to high binding energy after alkali evaporation and annealing; this is attributed to a change in chemical environment. The In 4d peak is broader than that of the bare CIGSe sample, which means at least one new In species forms upon alkali deposition.

Two new doublets, located at lower binding energy (around 14 and 11 eV, respectively), appear after Rb or Cs evaporation, which can be attributed to the Rb 4p and Cs 5p, respectively. These contributions decrease with increasing annealing temperature, indicating interdiffusion and/or incorporation process. The Rb 4p and Cs 5p doublet peak fitting is based on the Rb 3d and Cs 3d fitting results in Figure 5.13 (i.e. three Rb 3d contributions and two Cs 3d contributions). The doublet separations of Rb 4p and Cs 5p were 0.85 eV^[153] and 1.72 eV^[154], respectively. The second In 4d (In_b: 17.45 eV for Rb/CIGSe and 17.49 eV for Cs/CIGSe) peaks at low binding energy indicate an indium selenide (In_xSe_y or alk-In-Se) compound. The origin of In_c (18.48 for Rb/CIGSe and 18.56 eV for Cs/CIGSe) are suggested to be attributed to In-O bonds^[155]. In_d (In 4d_{5/2}: 16.68 eV for Rb/CIGSe and 16.76 eV for Cs/CIGSe) can be assigned to metallic In^[133] which decreases with increasing annealing temperature. The melting point of metallic indium is around 156.6 °C, which may explain the significant chemical changes observed above this temperature.

According to the In-species identification there should be corresponding Se components and the Se 3d fitting spectra are displayed in Figure 5.15. The doublet separation of Se 3d was fixed to 0.83 eV.^[84] The main Se species shift tendency is similar to In in Figure 5.14, which probably indicates a similar change of the chemical environment. For the bare CIGSe samples, the Se_a species (Se 3d_{5/2}: 54.26 eV for Rb/CIGSe and 54.28 eV for Cs/CIGSe) can be observed which agrees with Se in a chalcopyrite absorber^[131-132]. A new Se species (Se_b: 53.34 eV for Rb/CIGSe

and 53.36 eV for Cs/CIGSe) appears after Rb and Cs evaporation which decreases with increasing annealing temperature. The binding energy agrees well with the reported data of selenides^[156-157]. A third species (Se_c: 54.90 eV for Rb/CIGSe and 54.92 eV for Cs/CIGSe) can be observed after annealing at 300 °C for both sample series, which we attribute to a Se-O species. Note the different magnification factors in Se 3d.

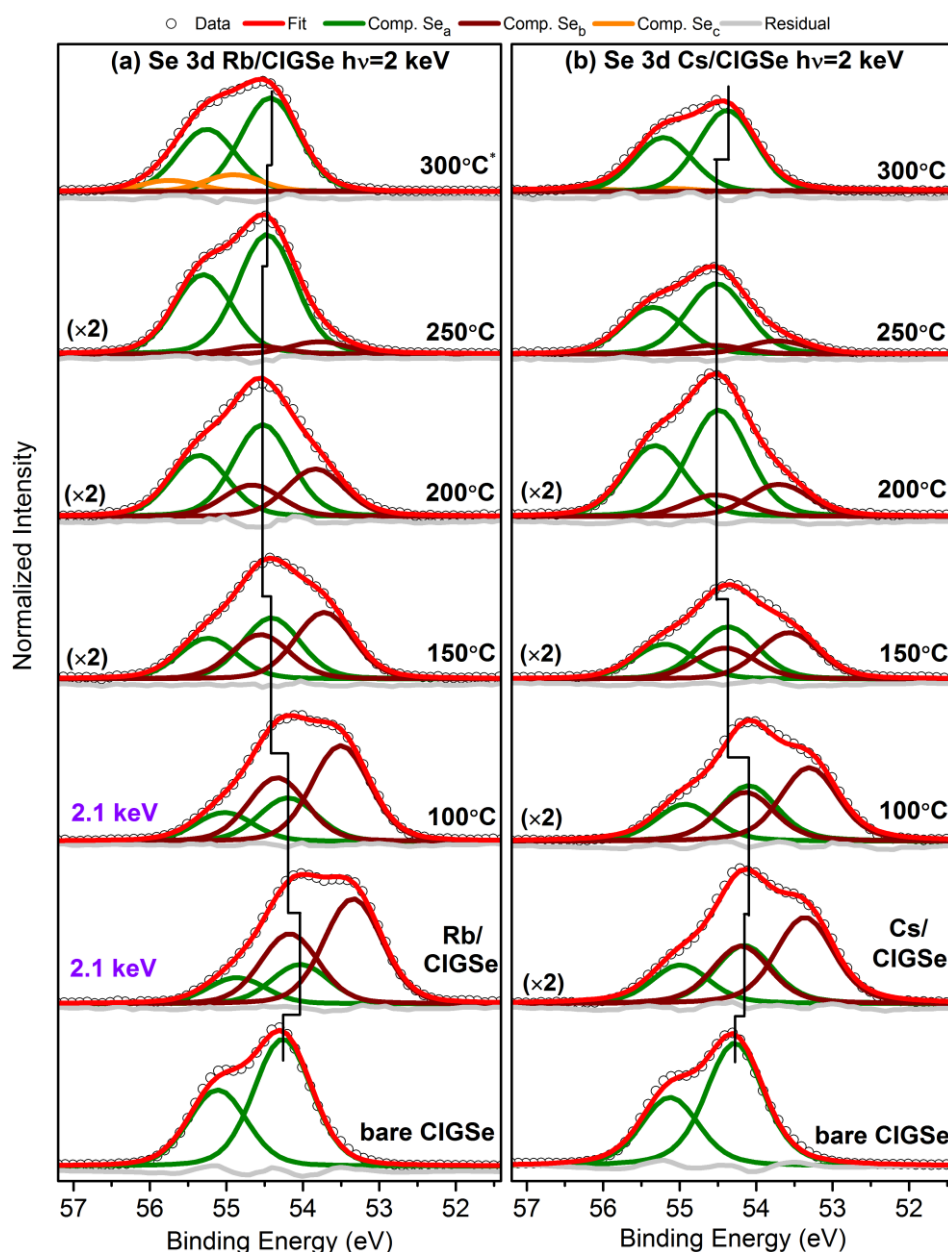


Figure 5.15. HAXPES Se 3d data of alkalis (Rb, Cs)-CIGSe sample series, recorded with an excitation energy of $h\nu = 2(2.1)$ keV: Rb/CIGSe (a) and Cs/CIGSe (b). The respective fits with Voigt profiles (doublets) and the residuals of the fits are also displayed. Note the different magnification factors. Spectra are vertically offset for clarity.

Based on the fitted In 4d/Ga 3d/Se 3d spectra, we can identify the different contributions related to CIGSe or other compounds (In-Se and Se related compound) shifted due to the chemical environment change because of the appearance of alkali elements (Rb, Cs). Rb and Cs induced similar chemical changes according to the detail spectra comparison. Since alkali (Rb and Cs) evaporation rate is not exactly same for different elements, the Rb and Cs content is not the same even though the evaporation times are similar. From the In 4d/Rb (Cs) intensity comparison in Figure 5.14, Rb content is higher than Cs content.

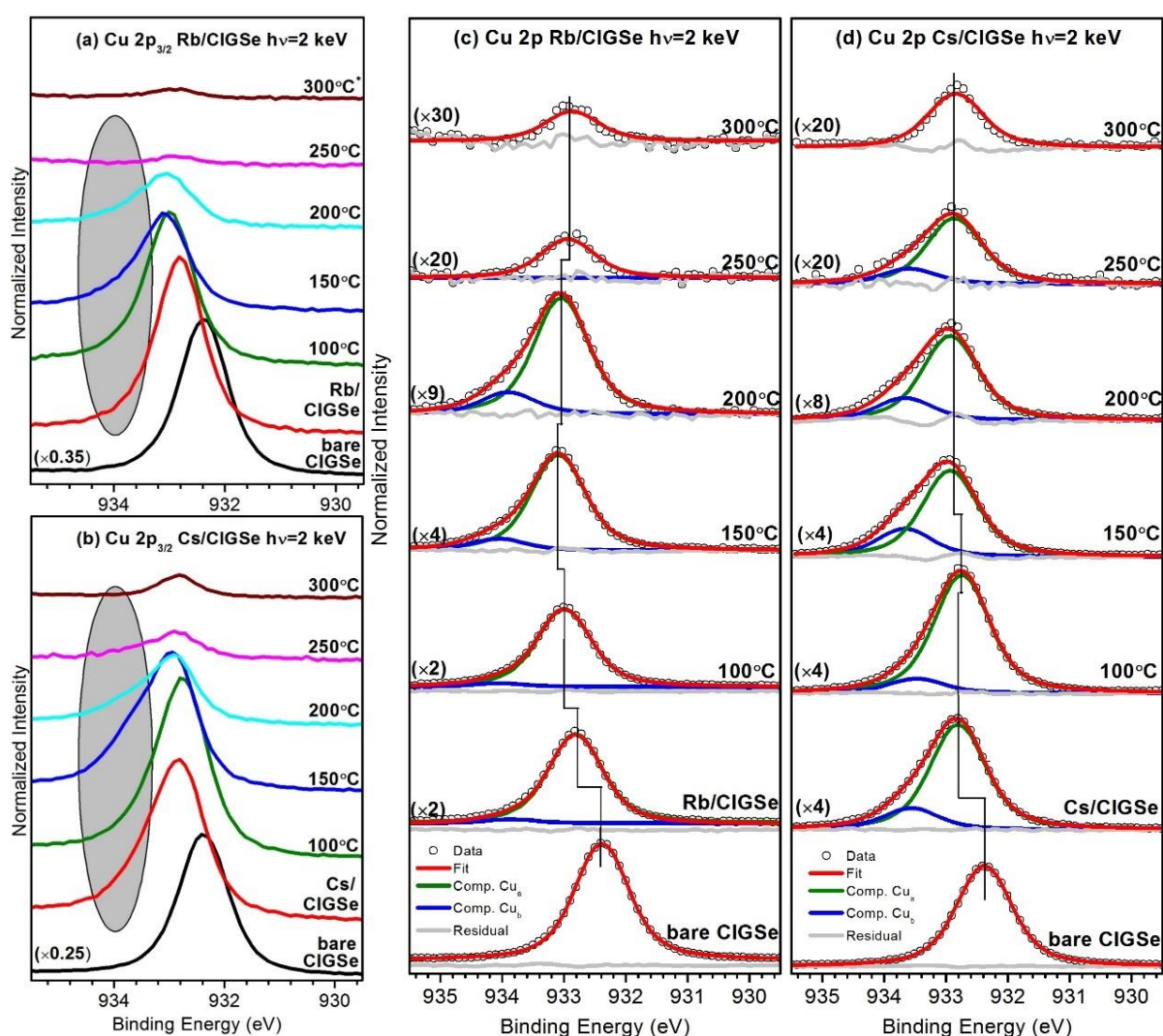


Figure 5.16. The respective Cu 2p spectra (a for Rb, b for Cs) and fitting results (c for Rb, d for Cs) with Voigt profiles, the residuals of the fits are also displayed. Note the different magnification factors. Spectra are vertically offset for clarity.

5.4.2 Detail evolution of chemical composition upon Rb/Cs deposition

Similar to what we did in chapter 5.3, we have exclusively focused on the intensity of the shallow core levels Rb 4p, Cs 5p, In 4d, Ga 3d, and, Se 3d, and Cu 3p (only for Rb/CIGSe). They have similar low binding energies and thus comparable high kinetic energies (between 1925–1995 eV for 2 keV excitation energy), that reduced the error bar and any uncertainties due to the morphology of the investigated film. Cu 2p was chosen for Cs/CIGSe because Cu 3p signals overlap by Cs 4d and the Cs signal is too strong compared to Cu 3p intensity, and it is hard to extract a meaningful Cu 3p signal from Cs 4d peak.

Before starting the fit detail analysis on this region, we discuss a significant broadening of the Cu 2p spectra (see Figure 5.16 a and b) for Rb/Cs sample series, indicating the presence of more than one Cu species. As shown in Figure 5.16, the spectra can be represented by the sum of two components. The dominant peak Cu_a at BEs from 932.4 eV to 932.9 eV is assigned to Cu in a $\text{Cu}(\text{In,Ga})\text{Se}_2$ as previous report^[158-159]. Taking the experimental uncertainty into account, the experimentally determined Cu 2p (Cu_b) peaks at 933.6 eV are in good agreement with values reported for Cu-O ^[159-161]. So only the Cu_a component of Cu 2p_{3/2} peak (located at low binding energy) was used for quantifications of the chalcopyrite-related species.

The intensity tendency of all considered absorber-related, rubidium, and cesium photoemission lines are shown in Figure 5.17 as a function of increasing annealing temperature. Note that for visual clarity, the bare sample and evaporated sample are set at 0 °C and 25 °C, respectively; in reality both were at 25 °C. In this case, the line intensities are normalized as each peak reaches one for the bare absorber layer (Figure 5.17 a and b wine lines) and new peak normalized to one for evaporated sample without annealing (Figure 5.17 a and b orange lines).

For the Rb/CIGSe sample series, a significant increase in Cu depletion can be observed at high temperature. In_a and Ga_a tendency show differences up to 150 °C, and In_a is similar to Se_a . We observe similar increases in intensity for In_a , Se_a , and Ga_a above 150 °C. For the Cs/CIGSe sample series, we observe a similar trend for Cu_a and Se_a as well as for In_a and Ga_a as for the Rb/CIGSe sample, the only difference is that the intensity increases of the In_a , Ga_a and Se_a components are more pronounced when $T > 200$ °C. The increase of the $\text{In}_a/\text{Se}_a/\text{Ga}_a$ contributions and attenuation

of Cu_a contribution can be observed when $T > 150\text{ }^\circ\text{C}$, suggesting the formation of a Cu-deficient/free In-Ga-Se compound at the surface. The “new” alkali (Rb_a+Rb_b , Cs_a), In_b and Se_b signals decline at a similar rate after annealing in Figure 5.17 a and b, suggesting the existence of a Rb-(In)-Se and a Cs-(In)-Se compound, that degrades upon annealing. Note that the attribution of In_b is still not completely clear, as its intensity trend diverges from the Se_b at some points and needs more evidence to prove.

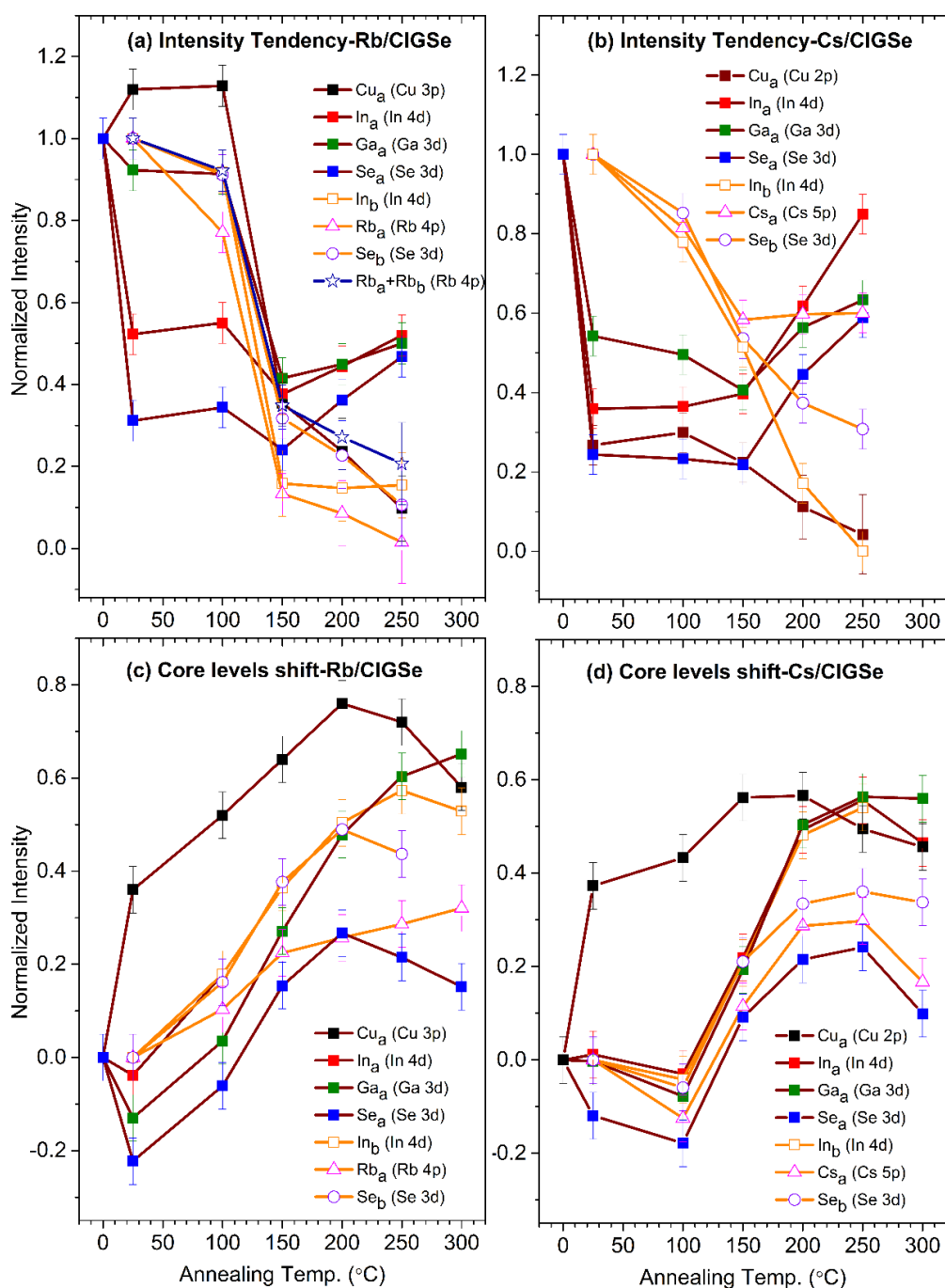


Figure 5.17. (a) and (b): Evolution of the signal intensities of the Cu 3p (Cu_a), In 4d (In_a), Ga 3d (Ga_a), Se 3d (Se_a), Rb 4p (Rb_a), Cs 5p (Cs_a) and Se 3d (Se_b) XPS lines; (c) and (d) BE shift of the Rb/CIGSe and Cs/CIGSe sets with increasing annealing temperature.

The binding energy shifts were calculated according the fitting results in Figure 5.14-5.16. Figure 5.17 c and d display shift values of respective alkali and absorber related elements with increasing annealing temperature. Cu always behaves differently (i.e. shifted to higher binding energies) at low annealing temperature compared to other elements. Note that the Cu 2p signal has a significantly lower IMFP and is the most surface sensitive measurement, which may have some impact. The magnitude of the In_a/Ga_a/Se_a shifts in Figure 5.17 c and d differ, but the tendency is similar. Different values could be induced by the complicated and varying chemical environment including the different amount of Rb and Cs. We also find In_b/Se_b (Rb) and Cs_a/Se_b (Cs) show quite similar shift tendency with increasing annealing temperature, but it is still hard to specify the compound. Since O 1s XPS position (O_c) for In-O (Figure 5.14), Cu-O (Figure 5.16), Rb-O and Cs-O (Figure 5.14), Ga-O (Figure 5.14, 300 °C), Se-O (Figure 5.15 a, 300 °C) is hard to distinguish^[90, 162], therefore the normalized intensity tendency of Rb_c, In_c, Cu_b, and Rb_c+In_c+Cu_b (from cross section corrected background normalized Rb 4p, In 4d, and Cu 3p spectra) and O_c (metal-oxide) species are compared in Figure 5.18a. Apparently, only Cu tendency is same/similar as O_c, the significant change of In_c and Rb_c at 200 °C can be attributed to the disappear of metallic In and/or the phase transition. The tendency of Rb_c+In_c+Cu and O_c show a similar situation within experimental uncertainty, indicating the attribution of In_c, Rb_c, Cu_b and O_c are possibly related. Cu_a/Cu_b (Cu 3p) area was calculated based on the Cu 2p fitting results in Figure 5.16 for composition calculation. By assumption of Cu_b and In_c were attributed to CuO and In₂O₃ (most stable Cu-O and In-O compounds), taking the IMFP, the respective photoionization cross section, and transmission function into account, the Rb_c / (O_c - O_{In-c} - O_{Cu-b}) ratio are estimated to around 1:2, which is close to the RbO₂. These results confirmed our previous Rb_c, In_c, and Cu_b attribution. Overall, the Cu 2p, Se 3d, In 4d, Ga 3d, O 1s, and Rb 4p/Cs 5p intensity behaviors suggest a “redistribution” of the former elements at the alkalis (Rb, Cs)/CIGSe surface/interface. The explanation could be alkali (Rb, Cs)-induced formation of intermixed interfaces, as will be discussed below.

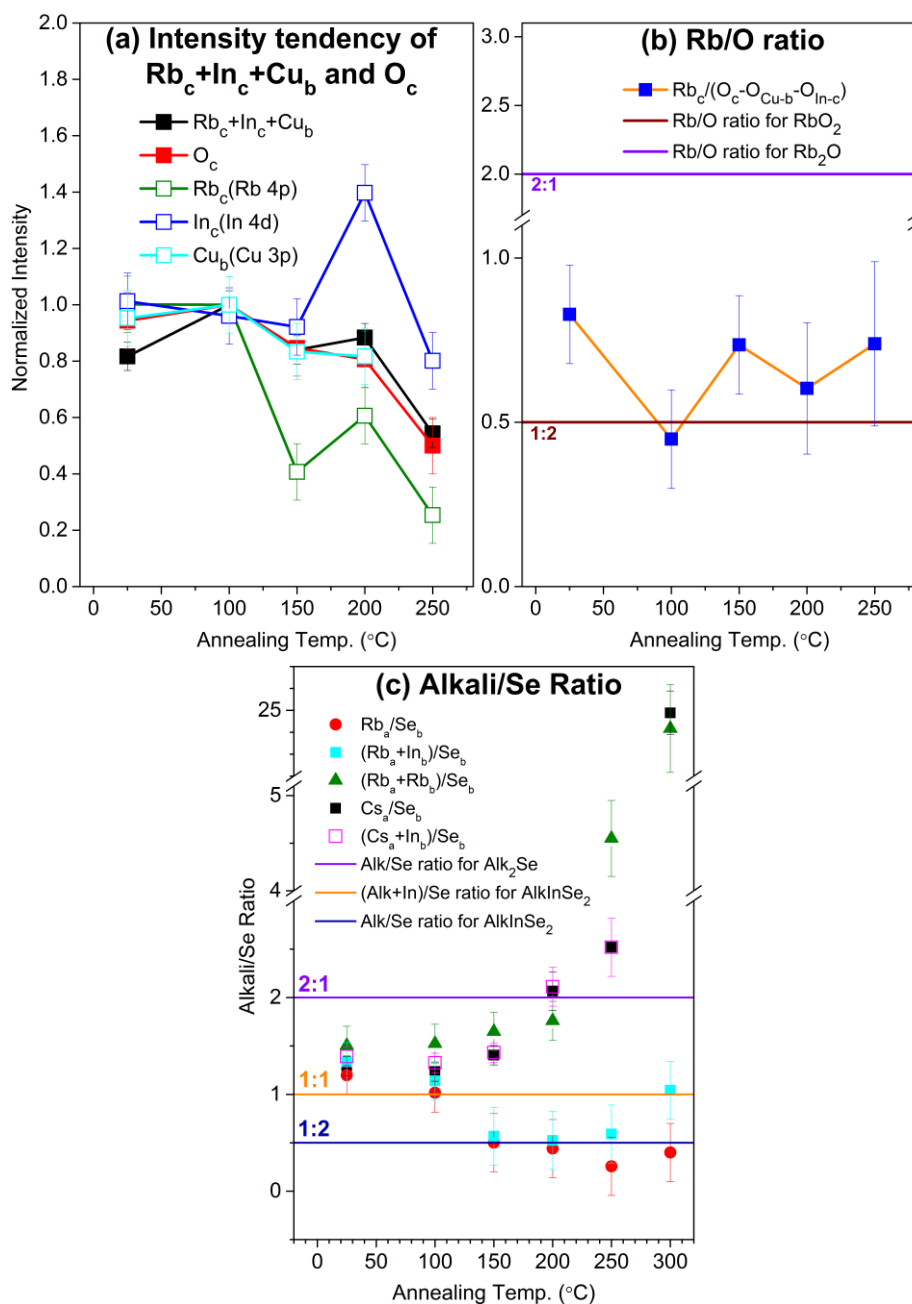


Figure 5.18. Evolution of the intensity tendency of ($Rb_c+In_c+Cu_b$) and O_c , the ratios of $Rb_c/(O_c-O_{In-c}+O_{Cu-b})$, Rb_a/Se_b , $(Rb_a+In_b)/Se_b$, $(Rb_a+Rb_b)/Se_b$, Cs_a/Se_b , and $(Cs_a+In_b)/Se_b$, as derived from the fit of the Rb 4p, In 4d, Cu 3p, O 1s, Cs 5p and Se 3d line as function of annealing temperature.

To clarify the attribution of alkalis ($Rb_a/Rb_b/Cs_a$), In_b and Se_b , HAXPES-derived (Rb_a , Rb_a+Rb_b , Rb_a+In_b , Cs_a , Cs_a+In_b): Se_b ratio is determined within error bar for all samples as a function of annealing temperature and shown in Figure 5.18c. The Rb 4p (Rb_a , Rb_a+Rb_b), Rb 4p/In 4d (Rb_a+In_b), Cs 5p (Cs_a), Cs 5p/In 4d (Cs_a+In_b), and Se 3d (Se_b) signal intensities are related to the relative quantity of the element and corrected by the respective photoionization cross-section for

2(2.1) keV excitation energy. Appendix B.2 displays the cross-sections used for the quantification of the data collected with the respective excitation energy according to Ref.^[68, 134].

As shown in Figure 5.18c, $(Rb_a+Rb_b)/Se_b$ ratio and Cs_a/Se_b ratios have very similar changes with different annealing temperature, which could indicate that the Cs could similarly have two Cs components in HAXPES spectra which overlap. The Rb_a/Se_b ratio is below 2:1 and beyond 1:1 at low temperature ($T \leq 100$ °C), indicating the Se_b could be Rb_2Se and/or Rb-(In)-Se for Rb/CIGSe sample series. At high temperature ($T \geq 150$ °C), the decrease of Rb_a/Se_b could be induced by the phase transformation (e.g. the incorporation of the melted metallic In) and its incorporation into the chemical reaction. The Rb_a/Se_b ratio close to 1:2 (\sim Rb/Se ratio in $RbInSe_2$) above 150 °C, which is an indication that a Rb-In-Se layer may be formed. However, the small change of $(Rb_a+In_b)/Se_b$ compared to Rb_a/Se_b ratio indicated the compound would be quite In-poor (if In_b is the associated species), but the stoichiometry change at 250 °C is more reasonable (the data point change with/without In_b).

As with alkali/selenide ratio, the photoemission data (Figure 5.14 and Cu 3p peak from bare CIGSe absorber) of the respective shallow core levels and respective cross sections (Figure Appendix B.2) are used to derive the relative ratio as a function of increasing annealing temperature, displayed in Figure 5.19. Here, Cu 3p (only for Rb/CIGSe sample series and bare CIGSe absorber for Cs/CIGSe) was chosen to avoid the experimental uncertainty induced by transmission function and IMFP. The Cu 3p and In 4p peak are close together, so the In 4p signal needs to be subtracted before Cu 3p signal was fitted. The details of the subtraction and related explanation are shown in Appendix B.3. After In 4p subtraction, Cu 3p fitting results for Rb/CIGSe series are shown in Figure Appendix B.4. It is known that the Cs 4d and Cu 3p signals overlap, and the Cs signal is much stronger than Cu, thereby we only use Cs 5p signal for detail composition calculation. (Cu almost disappears as shown in Figure 5.16 a and b, especially after higher temperature annealing). Large error bars were added for three annealing points, since Se_b and Cu signal still exist at this point (for Cs).

For the bare absorber, the stoichiometry of $Cu_a:(In_a+Ga_a):Se_a$ for both series is close to 1:1:2. After Rb and Cs evaporation, there are significant changes to the Cu and Se content due to Cu depletion and potential chemical reactions, but In_a+Ga_a keep mostly constant for all the samples. After

continued annealing (≥ 250 °C), the stoichiometry of $(\text{Rb}_b+\text{Cu}_a):(\text{In}_a+\text{Ga}_a):\text{Se}_a \approx 1:1:2$ (violet points for Cu_a+Alk and dark yellow points for Se_a in Figure 5.19 a and c; olive points for In_a+Ga_a in Figure 5.19 b and d), which in agreement with the nominal $\text{Cu}:(\text{In}+\text{Ga}):\text{Se}=1:1:2$ stoichiometry. This also suggests that part of Rb (Rb_b) occupies Cu vacancies after Rb evaporation. All these results suggest formation of $(\text{Rb,Cu})(\text{In,Ga})\text{Se}_2+\text{Rb}-(\text{In})-\text{Se}$ after high temperature annealing.

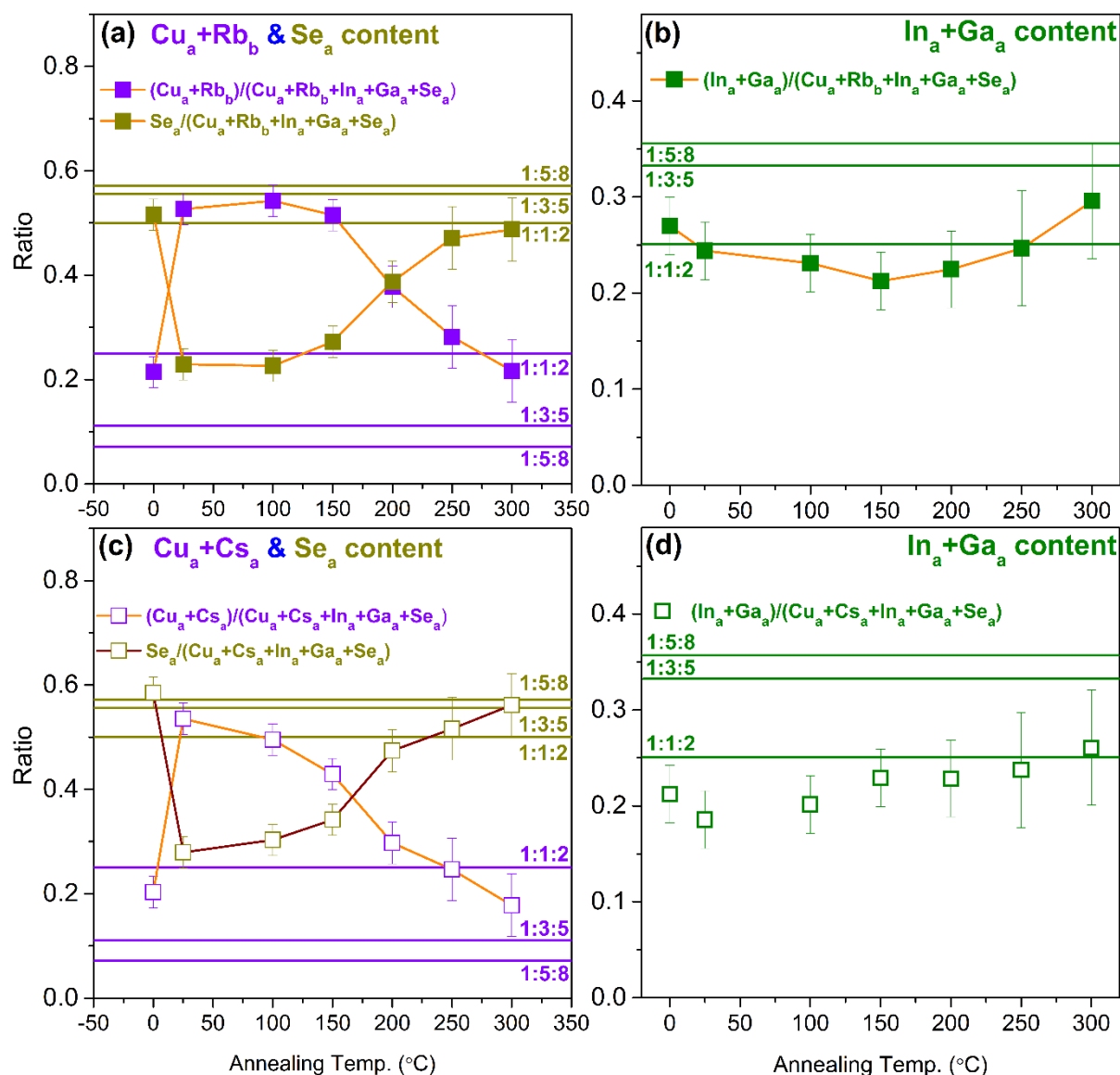
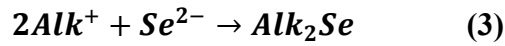
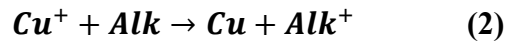
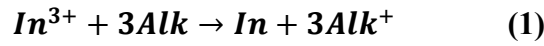


Figure 5.19. Evolution of $(\text{Cu}_a+\text{Alk})/(\text{Alk}+\text{Cu}_a+\text{In}_a+\text{Ga}_a+\text{Se}_a)$, $(\text{Se}_a)/(\text{Alk}+\text{Cu}_a+\text{In}_a+\text{Ga}_a+\text{Se}_a)$, and $(\text{In}_a+\text{Ga}_a)/(\text{Cu}_a+\text{Alk}+\text{In}_a+\text{Ga}_a+\text{Se}_a)$ ($\text{Alk}=\text{Rb}_b, \text{Cs}_a$) ratios of bare CIGSe, evaporated and annealed Rb/CIGSe (a and b) and Cs/CIGSe (c and d) samples, taken with 2(2.1) keV excitation.

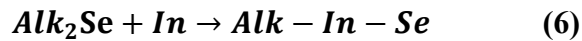
$(\text{Cs}_a+\text{Cu}_a):(\text{In}_a+\text{Ga}_a):\text{Se}_a$ tends towards 1:3:5 (Figure 5.19 c and d) after 250/300°C annealing. That means a Cu-deficient surface for Cs/CIGSe samples compared to the nominal 1:1:2 stoichiometry.

However, the possible Cs overlapping (Cs_a could be two Cs contributions) could change the calculation results. Note that these differences (e.g., 1:1:2 and 1:3:5 stoichiometry) could be impacted by experimental uncertainty.

Until now we know alkalis-(indium)-selenide, metallic indium, copper oxide, indium oxide, rubidium superoxide and cesium (super)oxide appeared after Rb/Cs evaporation (with no additional heating). Ga-O formation at 300°C can be attributed to oxygen contamination after long storage time and contamination during transport procedure. For formation of metallic indium and alkali (K, Rb, Cs) selenides upon alkali evaporation, the possible chemical processes at the absorber surface can be described by equation 1-5^[163] (Alk=K, Rb, Cs):



Alkalis (K, Rb, Cs) act as a reducing agent in this process and reduced In^{3+} to In metal. Then part of In/K/Rb/Cs/Cu metal was oxidized: even though all the evaporation process and measurement were performed in vacuum chamber; oxygen and carbon contamination still cannot be prevented. The metallic indium melts at around 150 °C, which may trigger formation of the non-uniform Alk-In-Se phase transformation by:



From HAXPES and calculation results, the disappearance of metallic indium and increase of $In_a/Ga_a/Se_a$ intensity at about 250 °C are strong indications for the phase transition from Alk-(In)-Se and CIGSe mixture.

To finalize the composition the ratios, $[Ga]/([In]+[Ga])$ (GGI) and $[Cu]/([Ga]+[In])$ (CGI) are derived and summarized in Figure 5.20 for Alk/CIGSe with increasing annealing temperature. The GGI and CGI ratios were determined by HAXPES fitting results in Figure 5.14, Figure 5.15, and respective cross sections in Appendix B.2. Figure 5.20a display a continuous Cu depletion for Rb/CIGSe series. The difference with NaF+KF PDT^[33] is that no Ga depletion appears to be

induced according to GGI results, as shown in Figure 5.20b, which may be related to the different sources of CIGSe (the absorbers are prepared by different institutes in different condition and had different starting GGI values). The CGI data points for Cs/CIGSe are missing because of the overlapping of Cs 4d and Cu 3p.

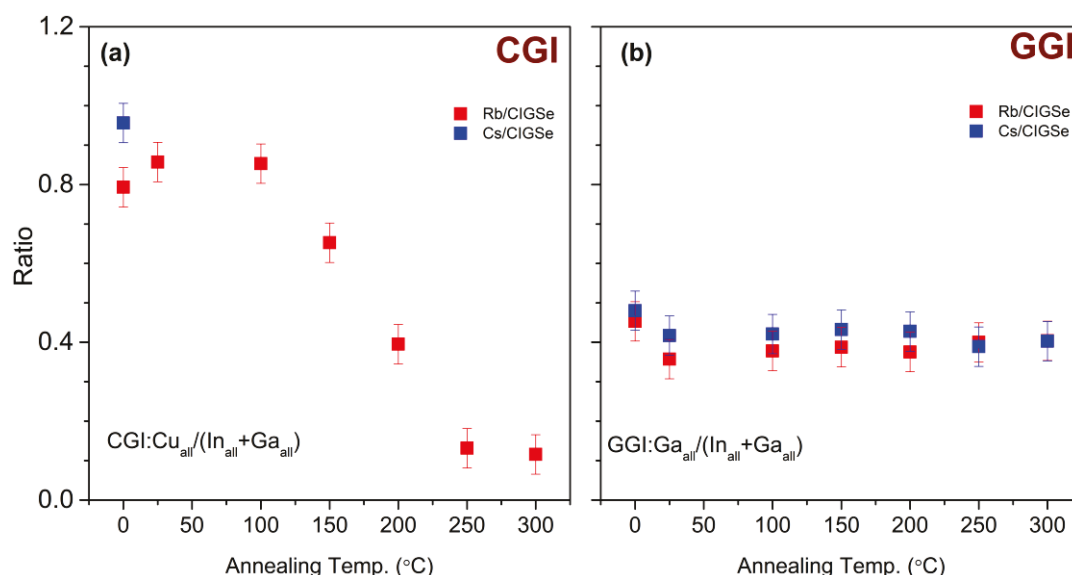


Figure 5.20. The $[\text{Cu}]/([\text{Ga}]+[\text{In}])$ (CGI) and $[\text{Ga}]/([\text{Ga}]+[\text{In}])$ (GGI) ratios are also displayed for Alk/CIGSe (Alk=Rb, Cs) series. Note that only one CGI point was calculated for Cs/CIGSe sample series because of the overlapping of Cu 3p and Cs 4d.

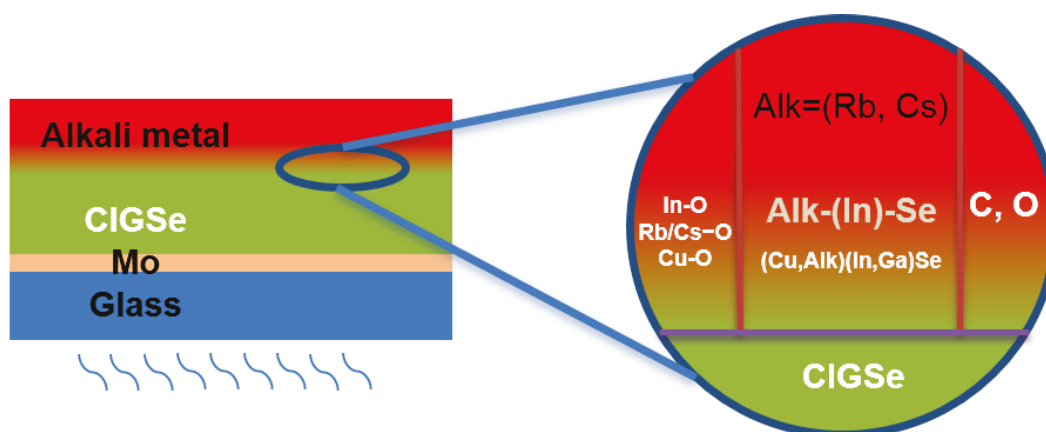


Figure 5.21. Schematic presentation of the chemical structure of the Alk/CIGSe (Alk= Rb, Cs) surface at low temperature.

With evidence for the formation of Alk-(In)-Se (Rb, Cs) and the reason for a alkali-Cu ion exchange in the annealing process, we argue that with the finding of a region with Alk-(In)-Se, Cu-O, and

In-O bonds, the HAXPES results explained an mixed Alk-(In)-Se and CIGSe material formed in the proximity of the Alk/CIGSe surface. A schematic presentation of the suggested Alk (Rb, Cs)/CIGSe surface/interface structure is depicted in Figure 5. 21.

5.4.3 Direct chemical structure comparison with RbF-PDT CIGSe (CIGSe^{RbF}) samples

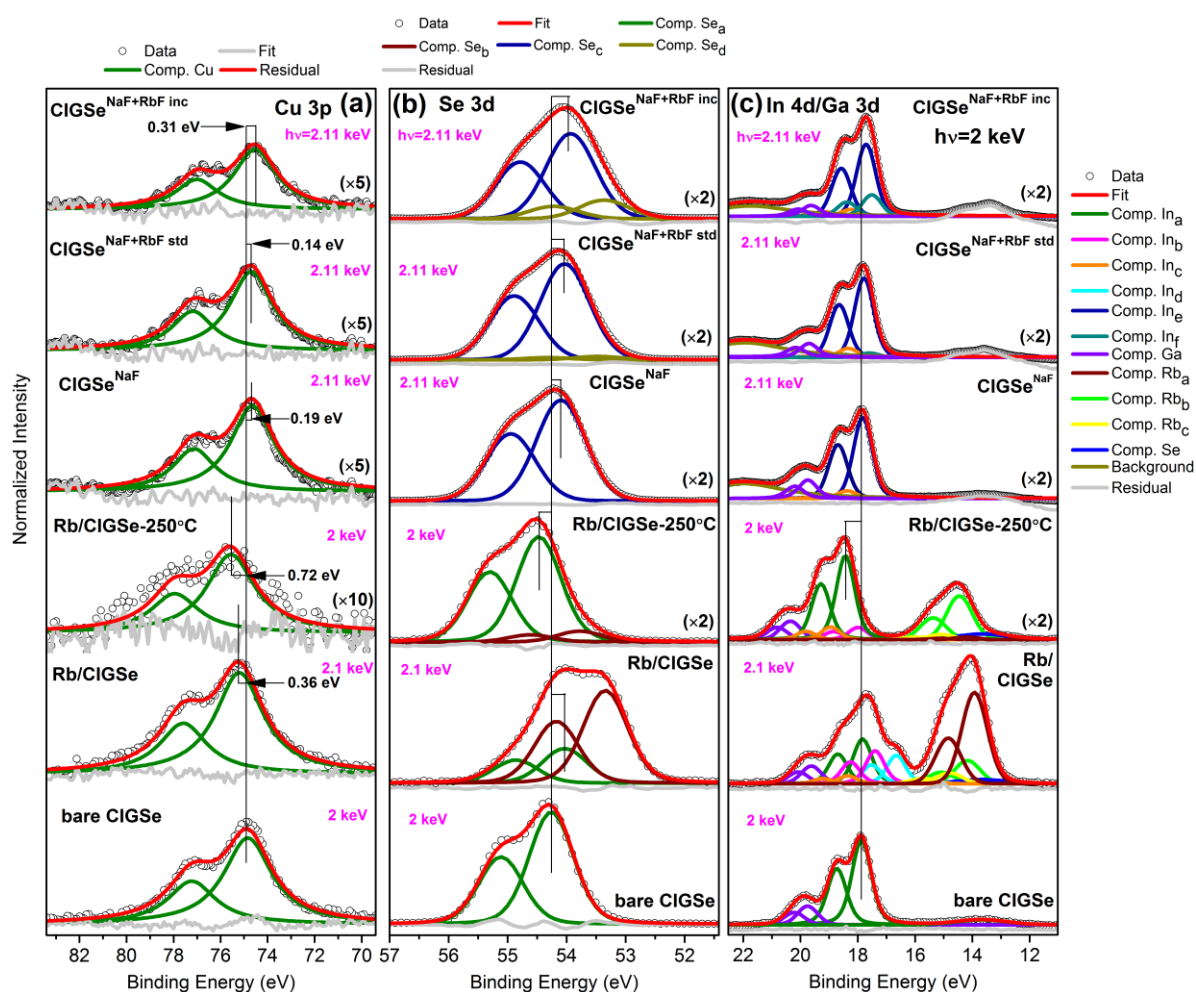


Figure 5.22. The direct comparison of Cu 3p (a), Se 3d (b) and In 4d/Ga 3d (c) spectra of bare CIGSe, Rb/CIGSe, Rb/CIGSe-250°C, CIGSe^{NaF}(PDT with NaF), CIGSe^{NaF+RbF std}(CIGSe with NaF + standard RbF PDT), and CIGSe^{NaF+RbF inc}(CIGSe with NaF + increased RbF) samples with respective fitting results, all the Rb evaporated samples were measure at 2 keV and PDT samples were measured at 2.11 keV. The residuals of the fits are also displayed.

For further chemical structure verification the effects of Rb metal deposition and successive annealing impact on CIGSe absorber layer, we compared all the core levels spectra (i.e. Cu 3p/In

4d/Ga3d/Se 3d) of Rb/CIGSe (bare CIGSe, Rb/CIGSe, and Rb/CIGSe-250°C) with alkali PDT CIGSe ($\text{CIGSe}^{\text{NaF}}$, $\text{CIGSe}^{\text{NaF+RbF std}}$, and $\text{CIGSe}^{\text{NaF+RbF inc}}$) in Figure 5.22, all the PDT spectra are adopted from Ref.^[164]. The Se_c and In_e at high binding energy represent the chalcopyrite absorber, the Se_d and In_f at low binding energy can be attributed to Rb-In-Se type species^[164]. The binding energy of In_e species are in agreement with the equivalent binding energies of In-O.

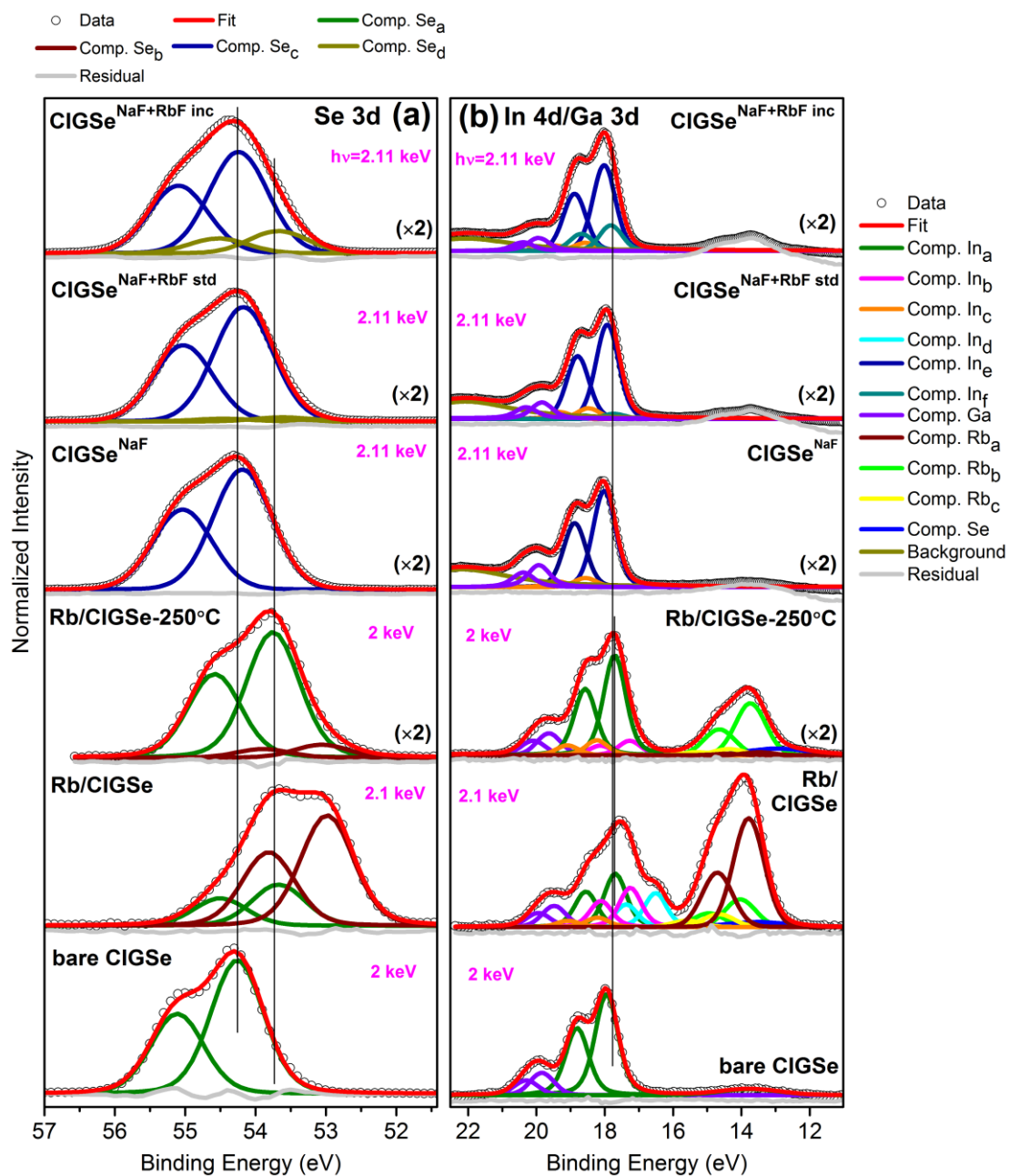


Figure 5.23. The realignment of Se 3d (a) and In 4d/Ga 3d (b) spectra of bare CIGSe, Rb/CIGSe, Rb/CIGSe-250°C, $\text{CIGSe}^{\text{NaF}}$, $\text{CIGSe}^{\text{NaF+RbF std}}$, and $\text{CIGSe}^{\text{NaF+RbF inc}}$ samples according to the shift energy values based on values in Figure 5.22a.

We use the bare CIGSe as a standard, and all the peak center values relative to this peak center are labelled in Figure 5.22a. It is observed that there is an additional species in Se 3d spectra for all Rb-containing samples compared to that of CIGSe^{NaF} sample which we attribute to Rb-In-Se species, which is also observed for In 4d/Ga 3d spectra in Figure 5.22b (Note that despite the different notation in Figure 5.22, it could be the same contribution). The doublet separation of Cu 3p, Se 3d, and In 4d/Ga 3d are the same for the fitting of both sample series. To identify and compare the detail contribution, we realigned the binding energy scales according to the energy difference in Figure 5.22a (i.e. all the Cu 3p peaks are aligned with that of the bare CIGSe absorber), as shown in Figure 5.23. As the detailed discussion about Figure 5.14 and Figure 5.15, the In_a and Se_a species before and after high temperature annealing are not exactly the same contribution: for bare sample and 250 °C, that is CIGSe absorber and (Rb,Cu)(In,Ga)Se compound, respectively. After realignment, it observed that the BE of Se_a for bare CIGSe and Se_c for CIGSe^{NaF} are almost the same, the Se_d for CIGSe^{NaF+RbF} and Se_a for Rb evaporated and annealed CIGSe sample are located at same line. Thus, we can attribute that to the same Se contribution, likely CIGSe absorber with Rb incorporation. All the comparison results confirmed our previous discussion results about the chemical structure of evaporated and annealed Rb/CIGSe samples. We don't have a detailed investigation of CsF PDT samples, so only the chemical structure of NaF+RbF PDT and Rb/CIGSe are compared.

The surface chemical structure after K/CIGSe at high temperature annealing is K-In-Se + CIGSe (1:3:5), while Rb-(In)-Se +(Rb,Cu)(In,Ga)Se (1:1:2) for Rb/CIGSe. The explanation could be K(In,Ga)Se₂ (if exist) are overlapped with CIGSe ,but also could be induced by different alkali contents (Rb content is much higher than K for the alkali evaporation samples).

5.5 Electronic structure of alkali/CIGSe (Alkali= K, Rb, Cs) and direct comparison with PDT CIGSe samples

To analyze the impact of the chemical change on the electronic structure, we now focus on the valence band maximum measurements. Alkali treated CIGSe samples showed similar changes, and the valence band spectra with linear approximations of the leading edges are shown in Figure 5.24.

The valence band spectra show six distinct main features (labeled I–VI). According to Ref.^[40, 114], feature I and III presents the antibonding and bonding hybridized Se p – Cu d states, Region II can be ascribed to nonbonding Se p states and region IV is attributed to the In s/Ga s derived states. Similar feature change can be observed with alkalis evaporation and subsequent annealing.

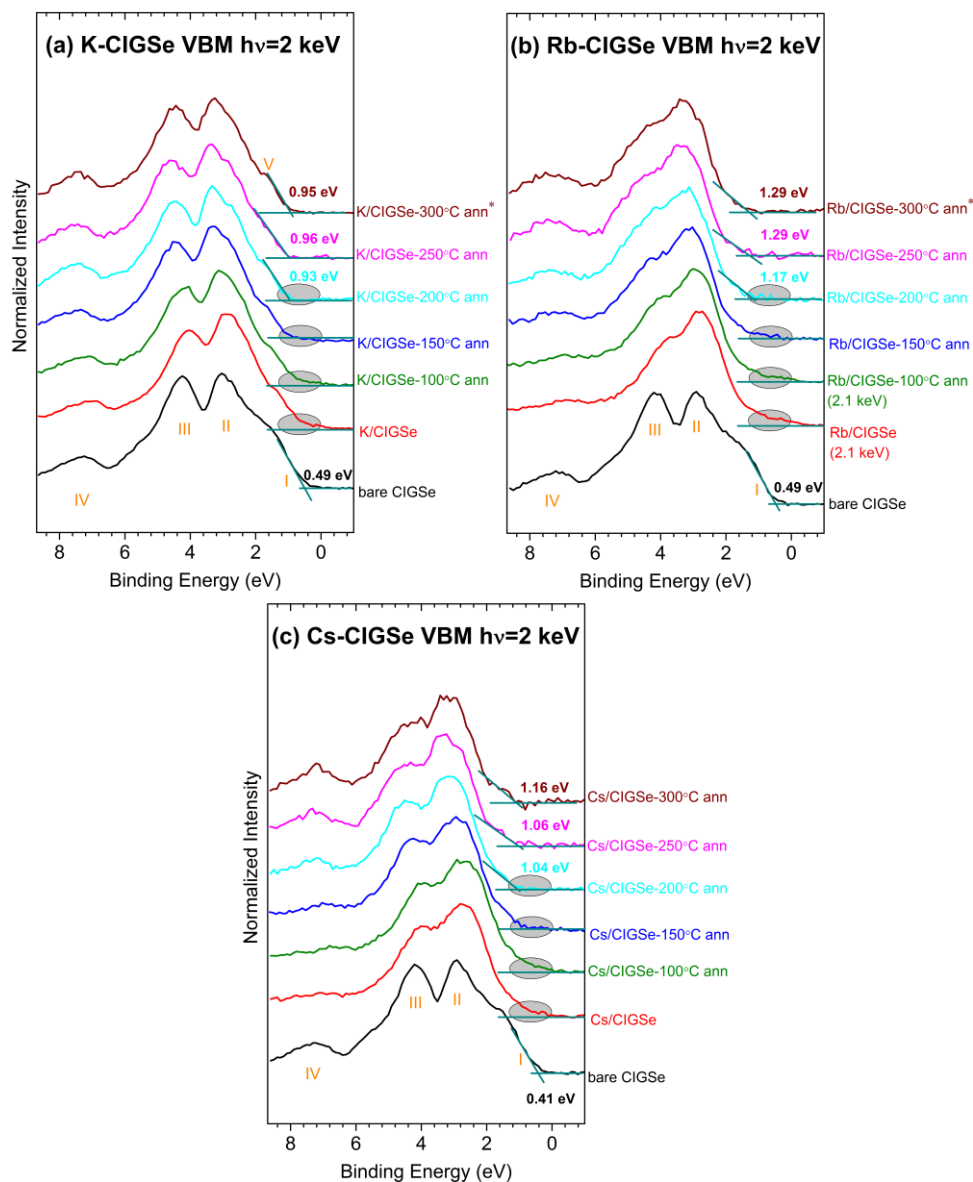


Figure 5.24. HAXPES derived valence band spectra of K/CIGSe(a), Rb/CIGSe(b), and Cs/CIGSe(c) absorbers recorded with excitation energies $h\nu = 2(2.1)$ keV. Linear approximation of the leading edges is used to determine the position of the valence band maxima. The error bar for VBM is ± 0.1 eV.

After alkali (K, Rb, Cs) evaporation, there are significant changes in the shapes of the valence band spectra. The new “bump” near 0 eV after alkali evaporation can be assigned to a Fermi edge of metallic indium. It disappears after annealing (200 °C) which agrees with the core levels in Figure

5.6 and 5.14. The decrease of feature I and III can be ascribed to Cu depletion and the presence of Alk-(In)-Se layer, the shift and decrease of feature IV can be explained by the metallic In and Ga attenuation at the interface and a corresponding change in the In s/Ga s derived states. No obvious change was observed for Feature II. In the subsequent annealing from 100 °C to 300 °C, the increase of feature IV also indicates the return of In s-Ga s derived states. The overall spectral contributions to the valence band are quite similar after alkalis evaporation, with the exception of the band edge positions toward higher binding energy.

The band gaps for $\text{Alk}_x\text{In}_y\text{Se}_z$ (Alk=K, Rb, Cs; $x=1$ or 2 , $y=0$ or 1 ; $z=1$ or 2) compounds have been calculated to be around $2\sim 2.5$ eV^[31, 45, 165-167], and the band gaps of Alk_2Se compounds are close to the band gaps of AlkInSe_2 compounds. A linear approximation of the leading edge was used to derive values for the valence band maximum (VBM) from all valence band spectra. The bare absorber shows a VBM of 0.49/0.54/0.48 eV for the absorbers, respectively, which is close to reported CIGSe absorber layer within the experimental uncertainty^[40]. After alkali evaporation and high temperature (250 °C) annealing, the VBM increase to 0.95/1.29/1.16±0.10 eV for K/CIGSe, Rb/CIGSe, and Cs/CIGSe, respectively.

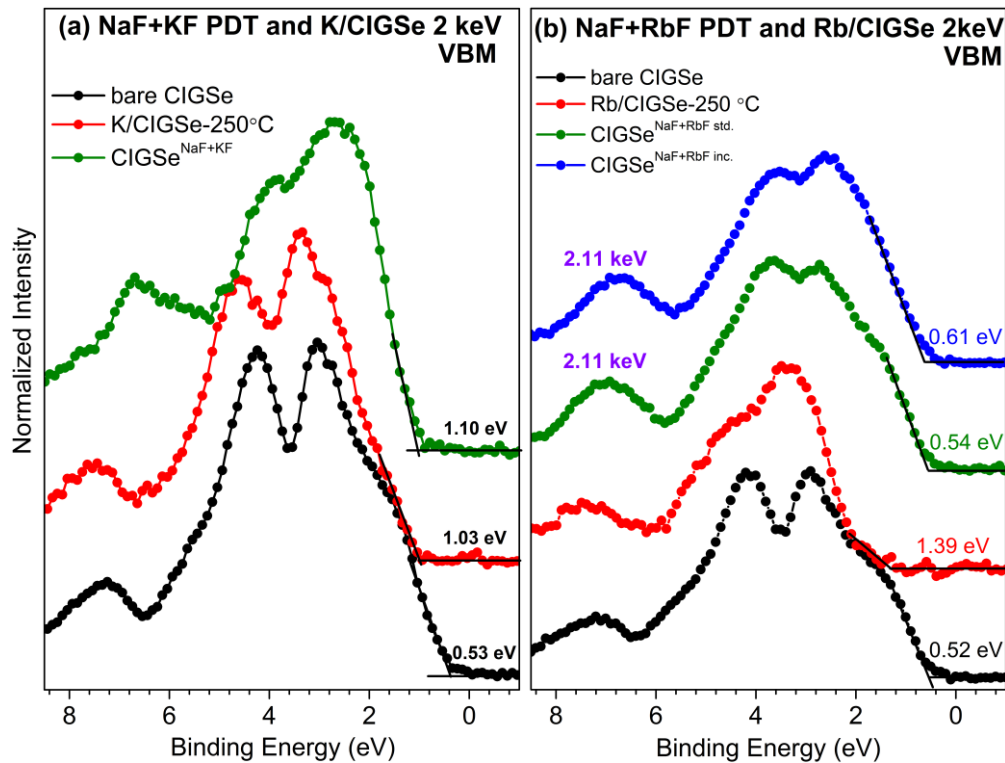


Figure 5.25. The direct comparison of VBM spectra of bare CIGSe, K/CIGSe and CIGSe^{NaF+KF}(a); bare CIGSe, Rb/CIGSe-250°C, CIGSe^{NaF+RbF std}, and CIGSe^{NaF+RbF inc} samples (b). Note that all the Rb evaporated samples were measure at 2 keV and PDT samples were measured at 2.11 keV.

In order to compare the impact of the different PDTs on the electronic structure, the direct valence band spectra for alkali/CIGSe (alk=Rb, Cs) and CIGSe absorber with PDTs (NaF+KF PDT and NaF+RbF PDT) are shown in Figure 5.25. The VBM values for K/CIGSe after 250 °C annealing are close to the NaF+KF PDT^[40] within the experimental uncertainty, which indicate a same/similar final state. Similar comparison for Rb treated CIGSe samples are shown in Figure 5.25b. The VBM value (1.29eV) for Rb/CIGSe sample is much bigger than that of the NaF+RbF treated CIGSe absorber (0.54/0.61 eV), which is also bigger than that (0.99 eV) of RbF/CIGSe absorber in the previous report^[31], the difference can be attributed to different Rb content, different amounts of Rb-In-Se, and/or different CIGSe absorber since all these absorber samples are prepared by different institutes.

As we did for the chemical structure comparison in chapter 5.3.3 (for K) and 5.4.3 (for Rb), we did same realignment for the VBM spectra, as shown in Appendix B.5. All the features have same/similar binding energies after the realignment according to Cu 3p, which is agree with the finding of (Alk-(In)-Se + (alk incorporated) absorber) in chapter 5.4.

5.6 Summary

Alkali (K, Rb, Cs) evaporation and annealing induced changes of the chemical and electronic structure of CIGSe absorber surface films have been revealed by detailed HAXPES measurements on in-system prepared model systems. We find a redistribution of K/Rb/Cs, Se, In and O in the proximity of the CIGS interface during interface formation and annealing process.

For Alk/CIGSe (Alk= K, Rb, Cs) sample series, the evolution of the detail spectra with increasing annealing temperature suggests that a Alk-(In)-Se, CuO, and In-O compound forms on the near-surface of K/CIGSe and converted to Alk-(In)-Se + Cu(In, Ga)Se surface after high temperature annealing ($T \geq 200^\circ\text{C}$). The impact of heavy alkali metal (Rb, Cs) on the CIGSe surface are shown similar change as K treated sample series. The observed decreasing Rb or Cs and respective Se contributions with increase annealing temperature, the Alk/Se and detail ratio calculation results

provide evidence for the formation of a Alk-(In)-Se and (Alk,Cu)(In,Ga)Se mixed structure. The presence of a Alk-(In)-Se on top of the alk/CIGSe absorber results in a completely modified electronic surface structure.

6. Conclusion and Outlook

For chalcopyrite-based thin film solar cell absorbers (Cu(In,Ga)Se_2), the impact of different alkali post-deposition treatments (NaF PDT and NaF+KF PDT) on the chemical structure of the CdS/CIGSe interface was studied using lab-based and synchrotron-based photoelectron spectroscopy. In order to identify the role of potassium in interface formation, the results on buffer/absorber samples sets have been compared that underwent a NaF or a NaF+KF PDT prior CdS deposition. For both sample sets we find – independent of PDT – the buffer layer to be best described by a Cd(O,OH,S) compound rather than to be a pure CdS buffer. However, while the buffer/CIGSe^{NaF} structure is formed without major interfacial interaction, significant elemental redistribution involving Cd, In, K, S, and Se in the proximity of the buffer/CIGSe^{NaF+KF} heterojunction is revealed.

When the CdS/CIGSe^{NaF} interface is formed, Cd and S are both present for even the shortest CBD times, Cd-S and Cd-O bonds are formed in the early stages of CBD, the Se chemical environment does not change, the In chemical environment does not change, and for long CBD times the buffer grows as a Cd(O,OH,S)-like compound. The CdS/CIGSe^{NaF+KF} interface structure is more complex, and the interpretation of the results is more ambiguous. When the interface is formed, Cd is initially present in much larger quantities than is S for the shortest CBD times, the Se chemical environment changes immediately upon CBD but appears stable thereafter indicating the formation of Cd-Se bonds at the interface. In is initially (i.e. for the bare CIGSe^{NaF+KF} absorber) found in two distinct chemical environments (assumed to be of Cu-In-Se and K-In-Se type). Upon CBD a change of the chemical environment of In throughout the first minute of CBD can be observed, attributed to the

formation of among others In-O bonds for CBD times of 1, 2, and 4 min. The deposited Cd is initially (i.e., for the 5 s sample) a single species which might be best described by a CdSe-like species. Between 30s and 4 min, two Cd species can be identified; one which gradually transforms from CdSe-like to CdO-like and the other one being representative for the thick Cd(O,OH,S)-like buffer compound. From the perspective of the sulfur, there is some evidence of the formation of S-In (in addition to formed S-Cd) bonds at the interface. In summary, the first stages (5s, 30s) of interface formation may be dominated by the growth of a Cd-In-(O,OH,S,Se) species with probably some Cd-In and (S,O)-Se composition gradient resulting in an In- and Se- rich composition close to the absorber, possibly formed due to modification/conversion of the existing K-In-Se layer and a Cd- and S,O-rich composition away from the absorber.

The electronic structure (i.e., the position of VBM) and the impact of the different alkali post-deposition treatments were studied HAXPES measurement. For the CdS/CIGSe^{NaF} series, the derived VBM values are 0.51, 0.58, and 1.73 (+/- 0.10) for the CIGSe^{NaF}, 5s and 15 min CdS/CIGSe^{NaF} sample, respectively. The similar VBM spectra shape at short CBD process (5s) suggesting the VB is dominated by the absorber, which agrees with our previous chemical structure results. For the CdS/CIGSe^{NaF+KF} series, the VBM values are 0.59, 0.96, 0.94, and 1.69 (+/- 0.10) for the CIGSe^{NaF+KF}, 5s, 1 min, and 15 min CdS/CIGSe^{NaF+KF} sample, respectively. The calculated VBO are -0.96 and -0.70 (±0.14) eV while the determined CBO are -0.28 (±0.14/0.51) and -0.93 (±0.14/0.51) eV for CdS/CIGSe^{NaF} and CdS/CIGSe^{NaF+KF}, respectively. However, the big CBO for CdS/CIGSe^{NaF+KF} is in conflict with working chalcopyrite-based solar cells. Taking the formation of an interface species after the CBD-CdS process on CIGSe^{NaF+KF} into account, the electronic structure brought into agreement with the simulation for high efficiency chalcopyrite-based solar cells if this interface layer is as passivation layer.

The chemical and electronic structure of alkali (K, Rb, Cs) treated surface CIGSe absorber during in-situ annealing (to mimic the thermal input similar to PDT) using photoelectron spectroscopy is monitored with an excitation energy of $h\nu=2$ (2.1) keV. For Alk/CIGSe (Alk=K, Rb, Cs) series, we find a redistribution of Alk, Se, In, Cu and O in the proximity of the CIGSe surface upon alkali metal evaporation and subsequent annealing. After K evaporation, three new In species (In_b ~ K-

In-Se species, $In_c \sim In-O$, and $In_d \sim$ metallic In), one new Se species ($Se_b \sim K-In-Se$ species), and two K species ($K_a \sim K-In-Se$ species and $K_b \sim K-O$ species). The K-O and metallic In disappear when $T \geq 150$ °C. The detail evolution of chemical contribution supports the formation of a K-In-Se and Cu-poor CIGSe (1:3:5) surface structure, which is agree with the “real” PDT sample finding in the previous report. Heavy alkali treatments (Rb, Cs) show similar chemical information as potassium evaporation: similar chemical changes (i.e. metallic In, In-O, and alkali-O) are observed, the Alk/Se ratio and related detail calculation results provide direct evidence for the formation of a Alk-(In)-Se, However, the difference with K/CIGSe would be $(Cu,Rb)(In,Ga)Se_2$ but not CIGSe (1:3:5), which could be induced by different alkali content and/or the possible overlapping between CIGSe and $(Cu,K)(In,Ga)Se_2$ in the HAXPES spectra.

The electronic structures for all the alkali/CIGSe (K,Rb,Cs) are compared and the determined VBM values are 0.95, 1.29, 1.16 eV (± 0.1 eV) for high temperature annealed K/CIGSe, Rb/CIGSe, and Cs/CIGSe, respectively. which are similar with that of (NaF+KF PDT) and different with the NaF+RbF PDT. The difference between alkali/CIGSe and the “real” PDT samples could be attributed to different amounts of alkalis being present on the CIGSe absorber surface.

All these results based on alkali treated CIGSe study (PDTs, alkali evaporation and subsequent annealing treatment) on the chemical and electronic structure provide some insights into the mechanism for underlying the formation of the alkali/CIGSe surface. The gained detailed understanding paves the way to deliberately facilitate the generation of a surface structure that enables the in-situ formation of a high-quality interface during the induction period of a chemical bath process and fully exploit it as novel approach of forming high-quality interfaces in solar cells and other energy conversion devices.

A.1. Direct In MNN spectra comparison

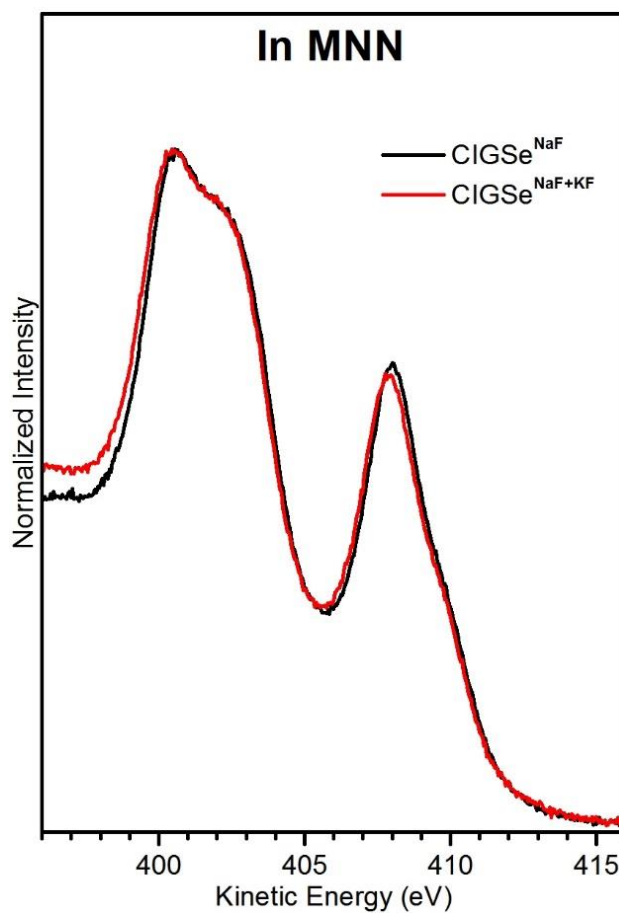


Figure A.1.1. The normalized and shifted In MNN spectra of CIGSe^{NaF} (black) and CIGSe^{NaF+KF} (red) samples, measured with an excitation energy of 1253.56 eV (Mg K_α).

A.2. Cu 3p background correction

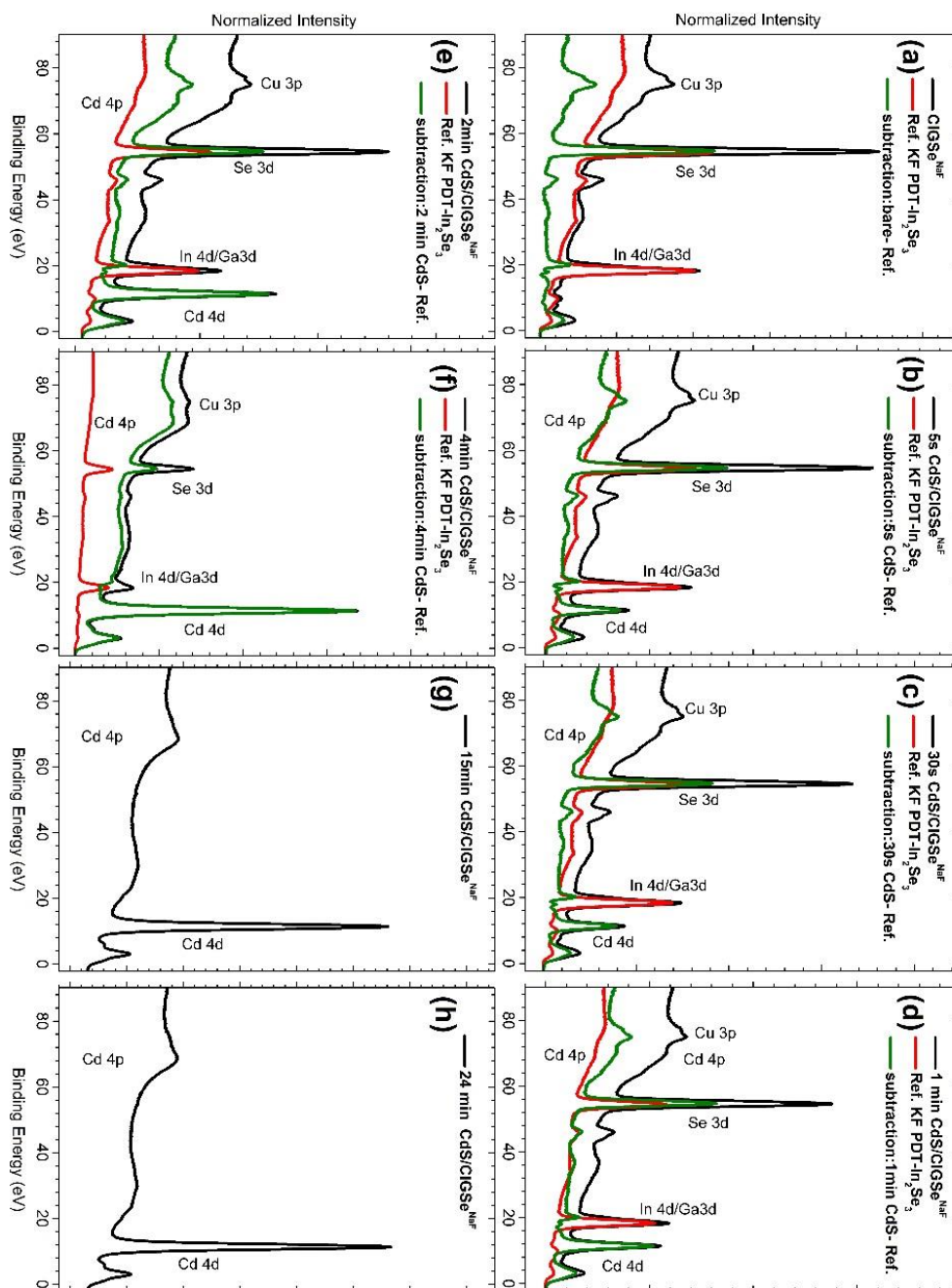


Figure A.2.1. The In 4p background correction approach for the Cu 3p line using the respectively scaled and shifted In 4d line of the KF-PDT In_2Se_3 reference spectrum employed to the data set of the $\text{CdS}/\text{CIGSe}^{\text{NaF}}$ sample series (CBD time: 0s (a), 5 s (b), 30 s, (c), 1 min (d), 2 min (e), 4 min (f) 15 min (g), and 24 min (h)), measured with an excitation energy of 1253.56 eV ($\text{Mg K}\alpha$). The as-measured spectra are shown in black, individually shifted and scaled references spectra in red, and the green spectra correspond to the resulting difference used for Cd 4p background.

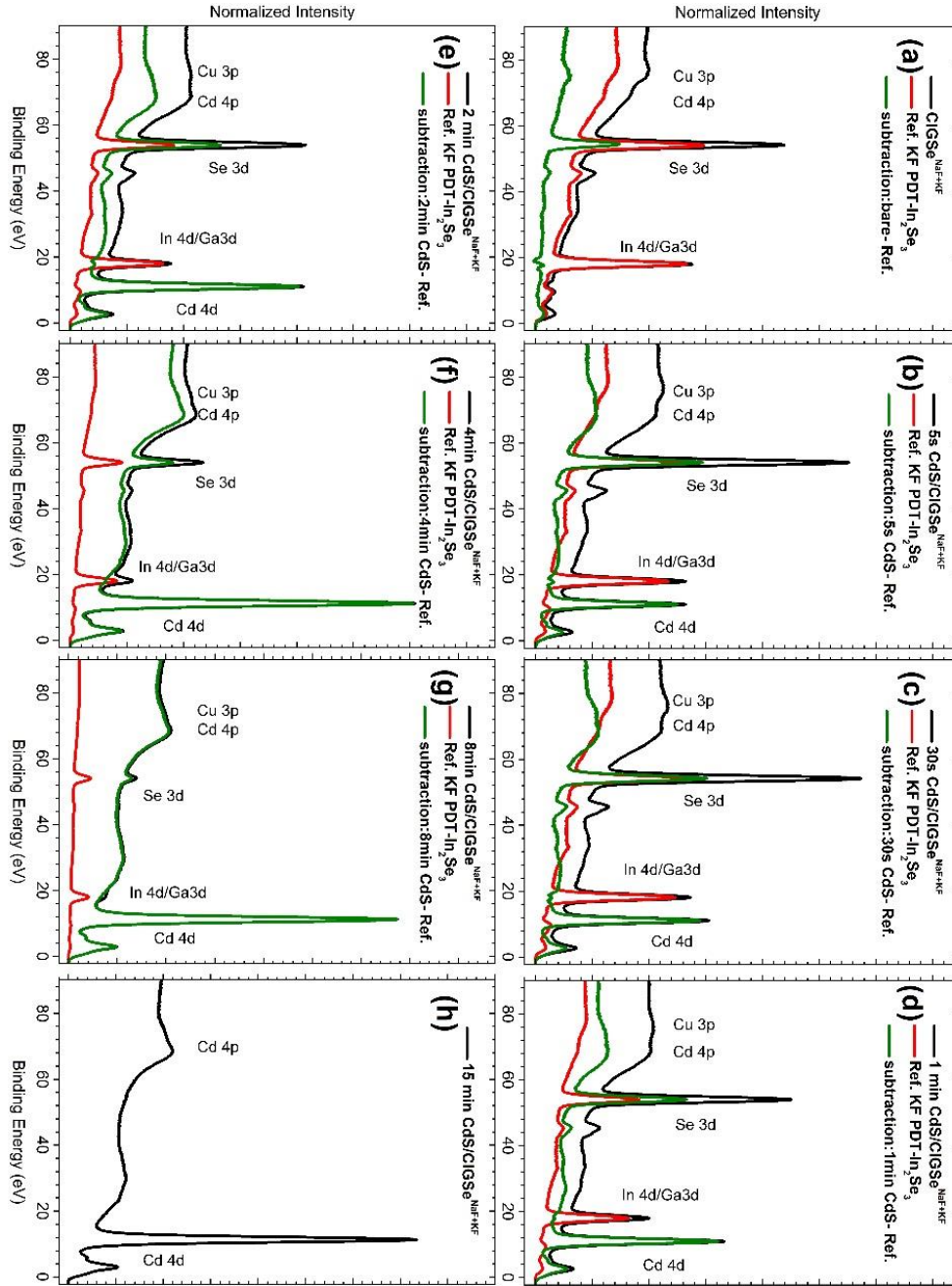


Figure A.2.2. The In 4p background correction approach for the Cu 3p line using the respectively scaled and shifted In 4d line of the KF-PDT In_2Se_3 reference spectrum employed to the data set of the $\text{CdS/CIGSe}^{\text{NaF+KF}}$ sample series (CBD time: 0s (a), 5 s (b), 30 s, (c), 1 min (d), 2 min (e), 4 min (f) 8 min (g), and 15 min (h)), measured with an excitation energy of 1253.56 eV ($\text{Mg K}\alpha$). The as-measured spectra are shown in black, individually shifted and scaled references spectra in red, and the green spectra correspond to the resulting difference used for Cd 4p background correction.

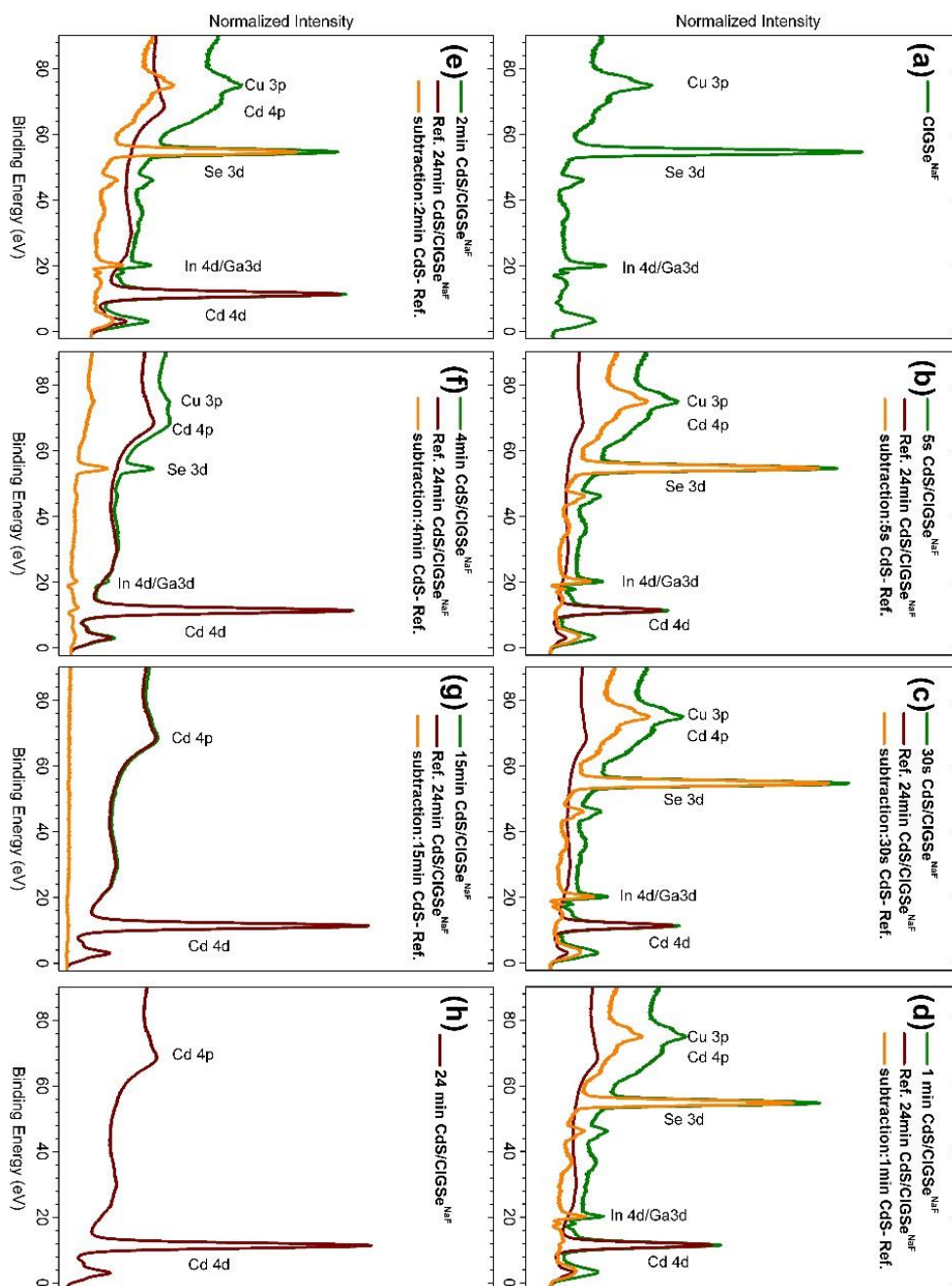


Figure A.2.3. The Cd 4p background correction approach for the Cu 3p line using the respectively scaled and shifted Cd 4d line of the 24 min CdS/CIGSe^{NaF} sample employed to the whole data set (CBD time: 0s (a), 5 s (b), 30 s, (c), 1 min (d), 2 min (e), 4 min (f) 15 min (g), and 24 min (h)), measured with an excitation energy of 1253.56 eV (Mg K α). The In 4p-corrected spectra are shown in green, individually shifted and scaled references spectra in wine, and the orange spectra correspond to the resulting difference used for further data evaluation.

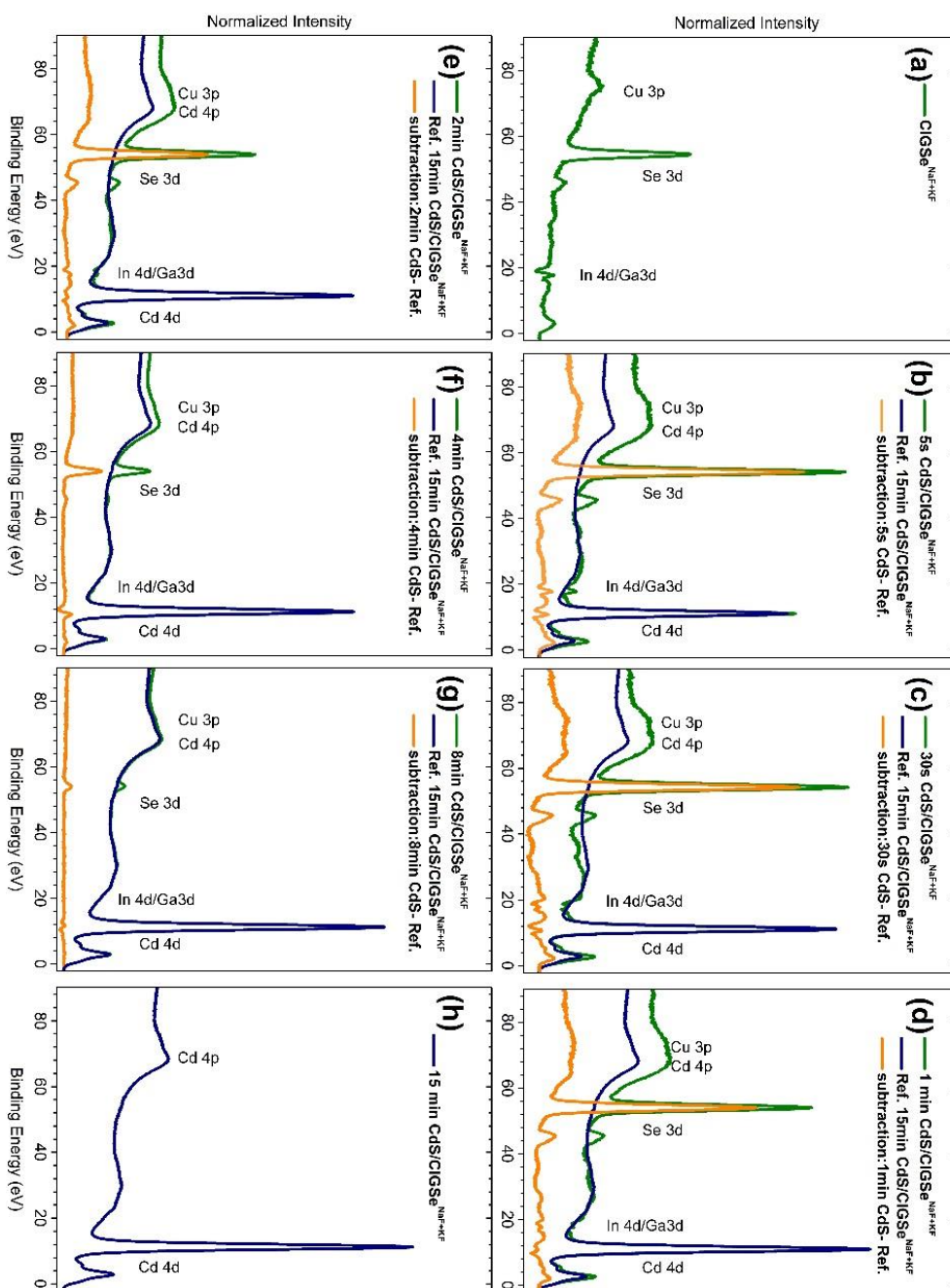


Figure A.2.4. The Cd 4p background correction approach for the Cu 3p line using the respectively scaled and shifted Cd 4d line of the 15 min CdS/CIGSe^{NaF+KF} sample employed to the whole data set (CBD time: 0s (a), 5 s (b), 30 s, (c), 1 min (d), 2 min (e), 4 min (f) 8 min (g), and 15 min (h)), measured with an excitation energy of 1253.56 eV (Mg K α). The In 4p-corrected spectra are shown in green, individually shifted and scaled references spectra in navy, and the orange spectra correspond to the resulting difference used for further data evaluation.

Figures A.2.1-A.2.4 visualize the Cu 3p background correction, subtracting (1) a properly shifted and scaled KF-PDT In₂Se₃ reference spectrum and (2) a properly shifted and scaled CdS reference spectrum (i.e., the spectrum of the thickest CdS sample of the respective sample series) to account

for the broad In 4p and Cd 4p background (between 80 and 60 eV) that overlaps with the Cu 3p signal, respectively. For the proper energy shift and scaling factor for the reference spectra were derived by bringing the In 4d and Cd 4d lines, respectively, to maximum overlap. The “negative” overshoot in the range of the In 4d & Cd 4d line in the difference spectra can be explained by different composition profiles and/or slight variations of the core level binding energies.

A.3 HAXPES spectra

A.3.1 HAXPES survey spectra

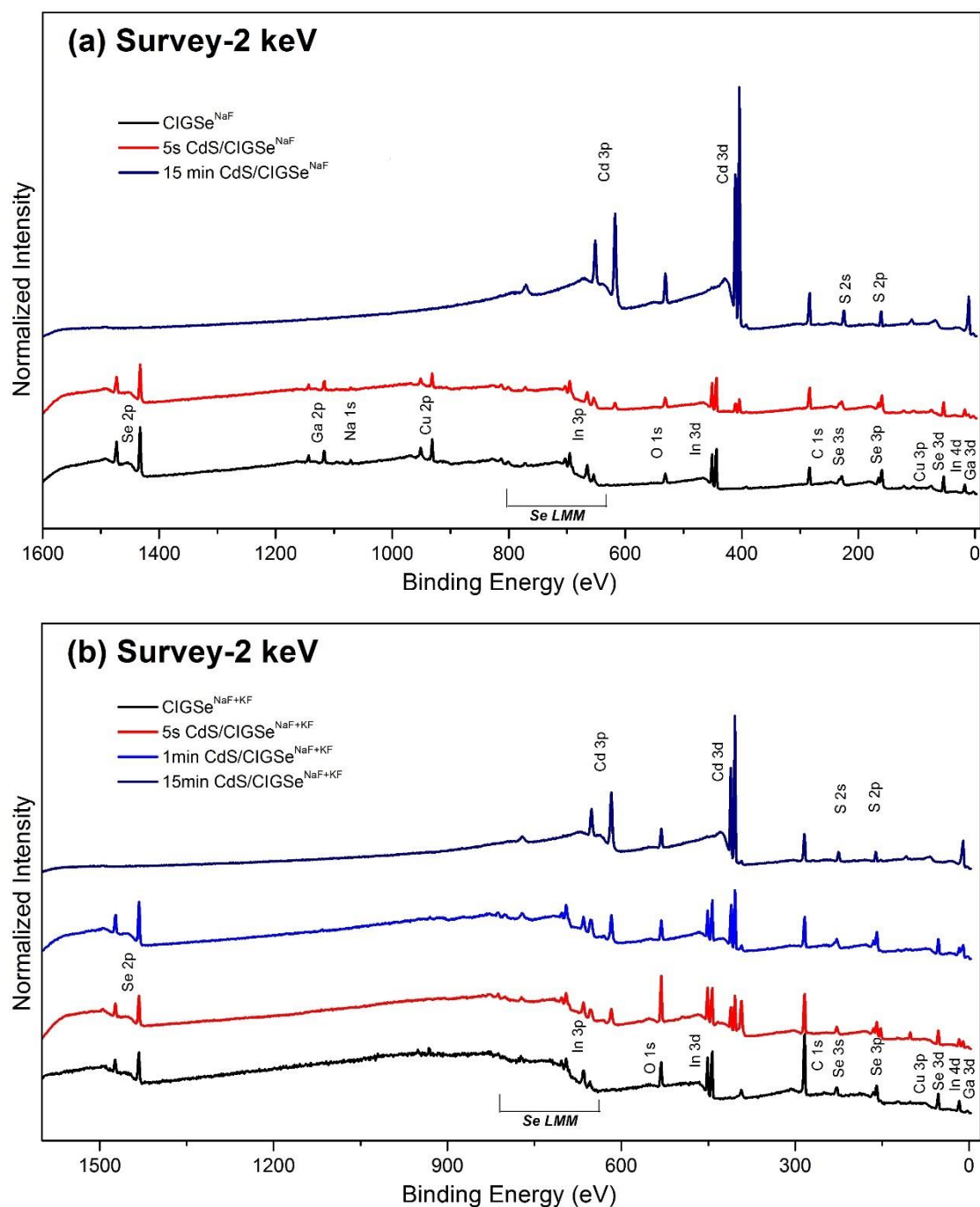


Figure A.3.1. HAXPES survey spectra (normalized to background at a binding energy of 0 eV) of CdS/CIGSe^{NaF} (a) and CdS/CIGSe^{NaF+KF} (b) with increasing CBD time (varied between 0 and 24 [15] min). All the spectra were measured with excitation energies of $h\nu=2$ keV (Mg K_{α}). All prominent photoemission and Auger lines are labeled. Spectra are vertically offset for clarity.

The HAXPES survey spectra of the two CdS/CIGSe sample series are shown in Figure A.3.1. As expected, all Cu, In, Ga, Se, Cd, and S photoemission and Auger lines are present. The Cu, In, Ga,

and Se peaks decrease in intensity, and Cd and S peaks increase with increasing CBD time, as expected. A Na-related XPS signal can only be observed for CdS/CIGSe^{NaF} samples. In addition, the presence of substantial C- and O-related XPS signals suggest surface contamination and/or incorporation of C and O into the deposited absorber and buffer layers (as discussed below). The Cu and Ga signals intensity of the bare CIGSe^{NaF+KF} is significantly lower than for the CIGSe^{NaF} absorber, consistent with a strong surface Cu depletion as previously reported^[26, 29, 69].

A.3.2 Direct comparison of HAXPES VBM spectra

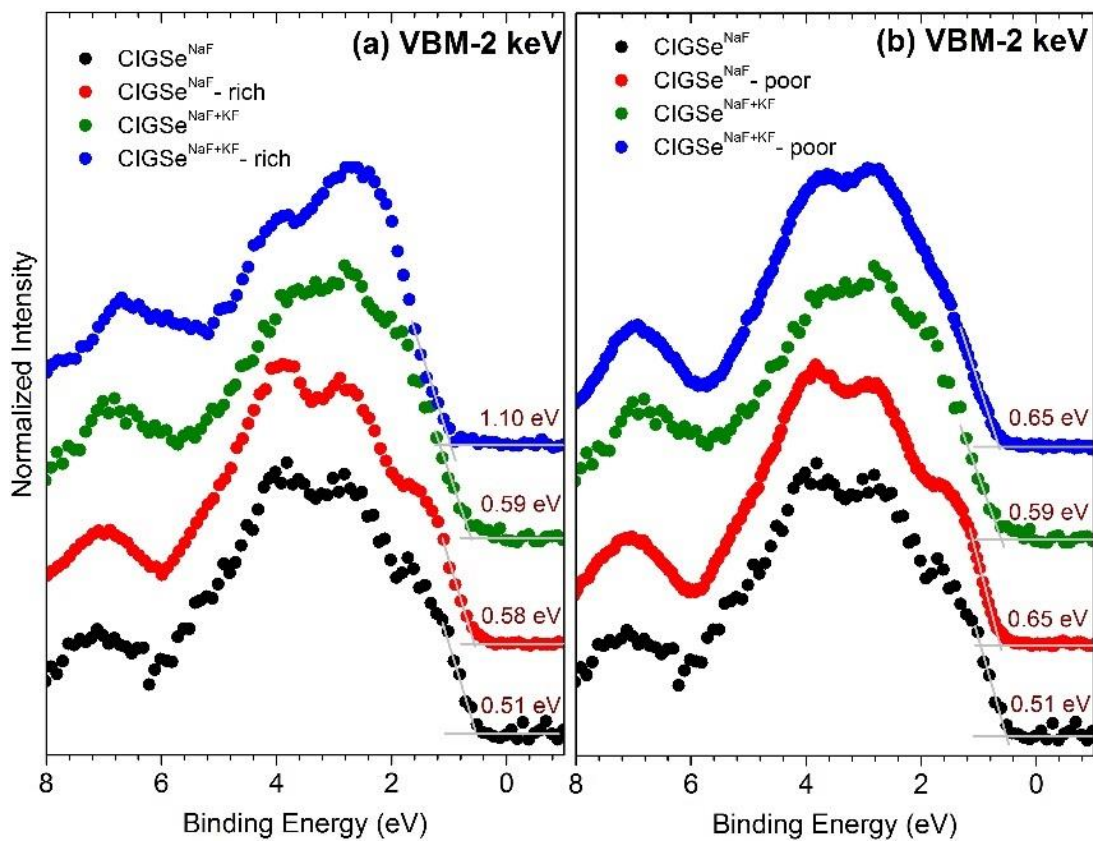


Figure A.3.2: Direct HAXPES derived valence band spectra of our CIGSe^{NaF} (black), CIGSe^{NaF+KF} (green), alkali-rich (red and blue in a), and alkali-poor (red and blue in b) CIGSe absorbers recorded with excitation energies of $h\nu=2$ keV. Linear approximation of the leading edges is used to determine the position of the valence band maxima. The alkali-rich and alkali-poor sample spectra are adapted from ^[50].

The valence band photoemission of the CIGSe^{NaF}, CIGSe^{NaF+KF}, alkali-rich, and alkali-poor reference absorbers are displayed in Figure A.3.2 with the excitation energy $h\nu=2$ keV. To derive the respective VBM values for all valence band spectra, a linear extrapolation of the leading edge

is used. For the $\text{CIGSe}^{\text{NaF}}$ and $\text{CIGSe}^{\text{NaF+KF}}$ absorbers, the VBM values are 0.51 and 0.59 (± 0.1) eV, respectively. To get more details about the impact of different treatment on the electronic structure, a direct VB spectra comparison of alkali-rich(poor), $\text{CIGSe}^{\text{NaF}}$, and $\text{CIGSe}^{\text{NaF+KF}}$ samples are shown in Figure A.3.3 a&b. Note that all the spectra in Figure A.3.3 are normalized to same height for comparison. As we can observe in Figure A.3.3 a&b, no big difference can be observed for the $\text{CIGSe}^{\text{NaF}}$ (black), alkali-rich (red in Figure A.3.3a) and alkali-poor (red in Figure A.3.3b) spectra, which indicate similar structure for all the NaF PDT related samples, which is different for all the NaF+KF PDT samples. The VB spectra of all the NaF+KF PDT related samples are directly compared in Figure A.3.3c. Features intensity change with different samples. In previous Se chemical results (Figure 4.17 and 4.18a), the K contribution (22%) are falling between alkali-rich (50%) and alkali-poor (10%), the results here is consistent with this conclusion. The decrease of Feature I and III can be attributed to Cu depletion while Feature III attenuation is induced by Ga depletion. Based on the calculation results, feature VII are dominated by Se p states in KInSe_2 compound, which indicate the alkali-rich sample have more Se (KInSe_2) contribution compare to the rest two samples.

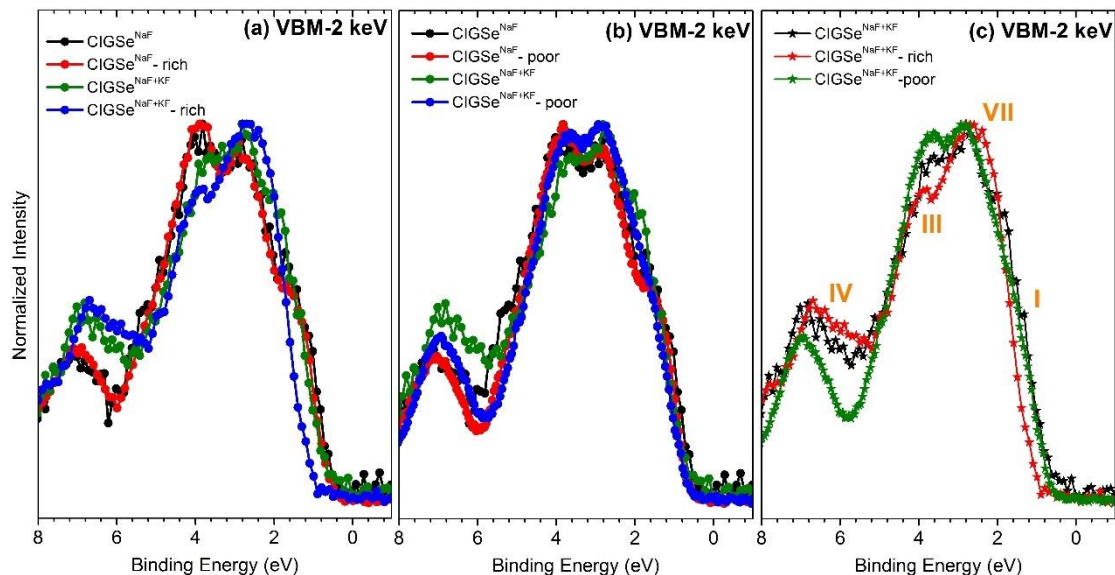


Figure A.3.3: Normalized HAXPES derived valence band spectra of our $\text{CIGSe}^{\text{NaF}}$ (black), $\text{CIGSe}^{\text{NaF+KF}}$ (green), alkali-rich (red and blue in a), and alkali-poor (red and blue in b) CIGSe absorbers recorded with excitation energies of $h\nu=2$ keV. Direct comparison about $\text{CIGSe}^{\text{NaF+KF}}$, alkali-rich and alkali-poor are shown in Figure c. The alkali-rich and alkali-poor sample spectra are adapted from [50].

B.1 In 4p background correction for K/CIGSe series

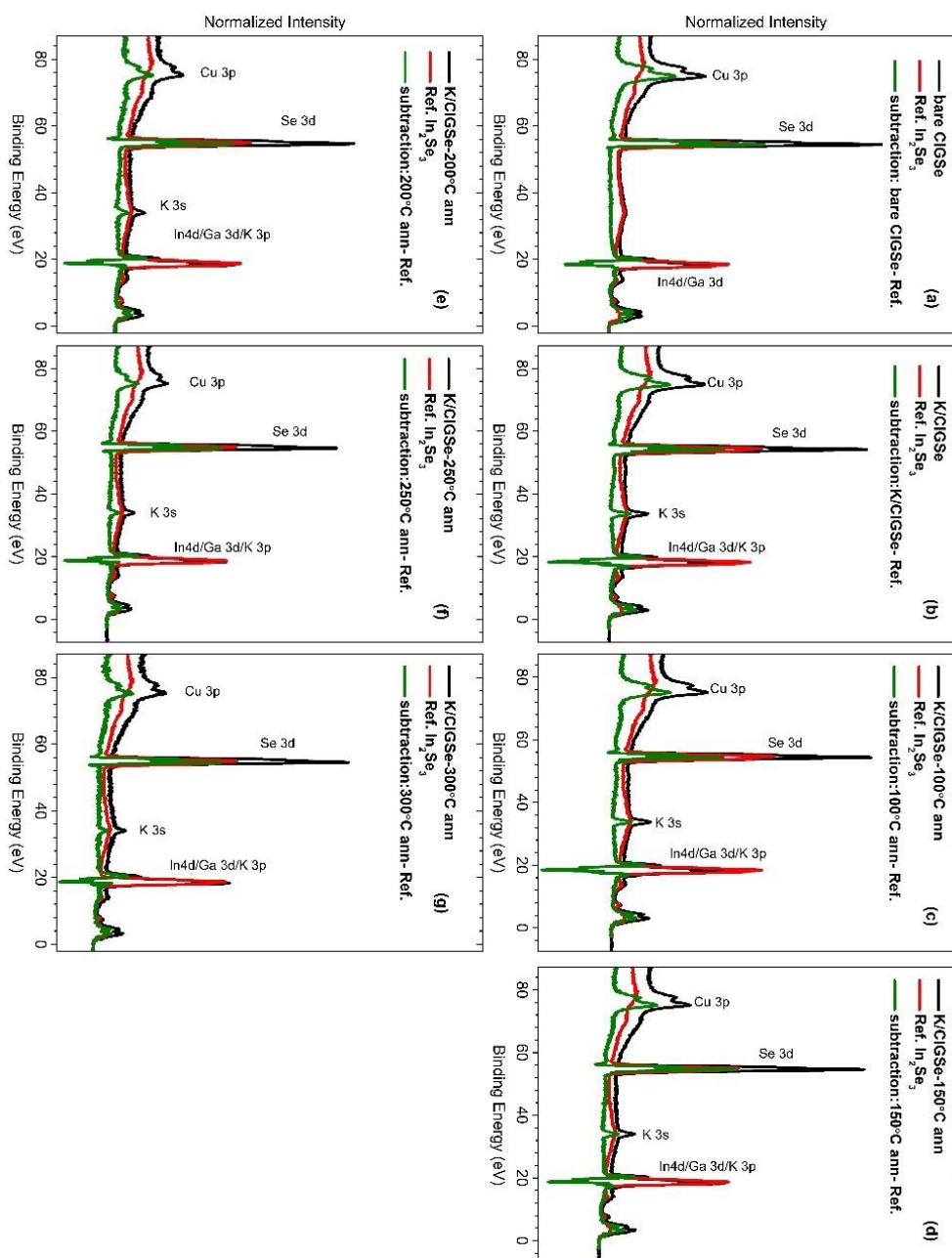


Figure B.1. The In 4p background correction approach for the Cu 3p line using the respectively scaled and shifted In 4d line of the In_2Se_3 reference spectrum employed to the data set of the K/CIGSe sample series (annealing temperature: bare (a), K/CIGSe (b), K/CIGSe-100 °C (c), K/CIGSe-150 °C (d), K/CIGSe-200 °C (e), K/CIGSe-250 °C (f), and K/CIGSe-300 °C (g), measured with an excitation energy of $h\nu=2$ keV. The as-measured spectra are shown in black, individually shifted and scaled references spectra in red, and the green spectra correspond to the resulting difference.

Figures B.1 visualize the Cu 3p background correction of K/CIGSe sample series, subtracting a properly shifted and scaled In_2Se_3 reference spectrum to account for the broad In 4p background (between 80

and 60 eV) that overlaps with the Cu 3p signal, respectively. For the proper energy shift and scaling factor for the reference spectra were derived by bringing the In 4d lines to maximum overlap. The “negative” overshoot in the range of the In 4d line in the difference spectra can be explained by different composition profiles and/or slight variations of the core level binding energies.

B.2 Cross sections.

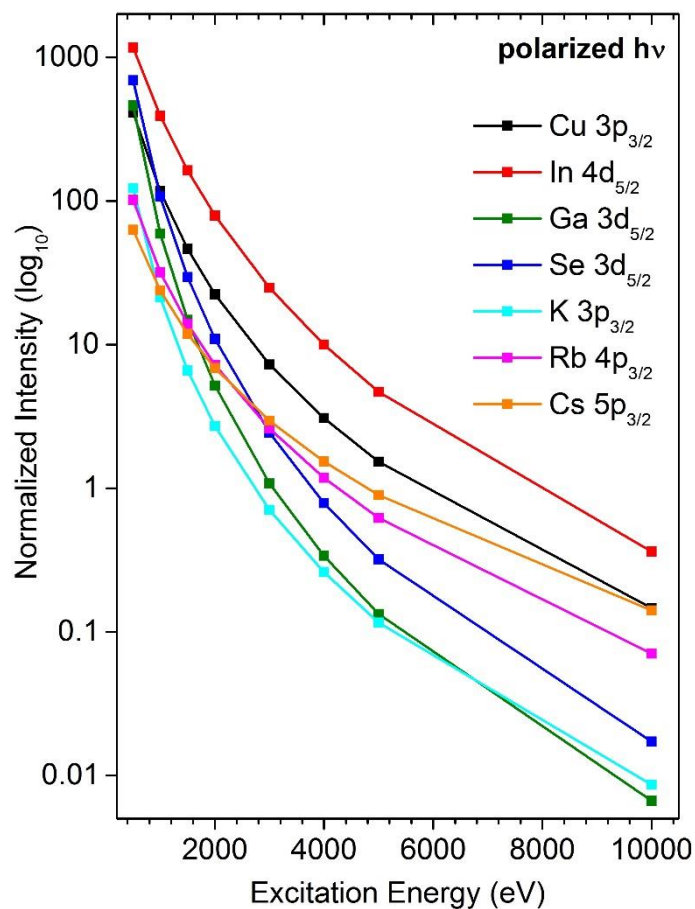


Figure B.2. Excitation energy dependent photoionization cross-section of selected shallow core levels. Cross-sections corrected for the experimental geometry of the HAXPES setups for polarized photons.

B.3 In 4p background correction for Rb/CIGSe and Cs/CIGSe sample series

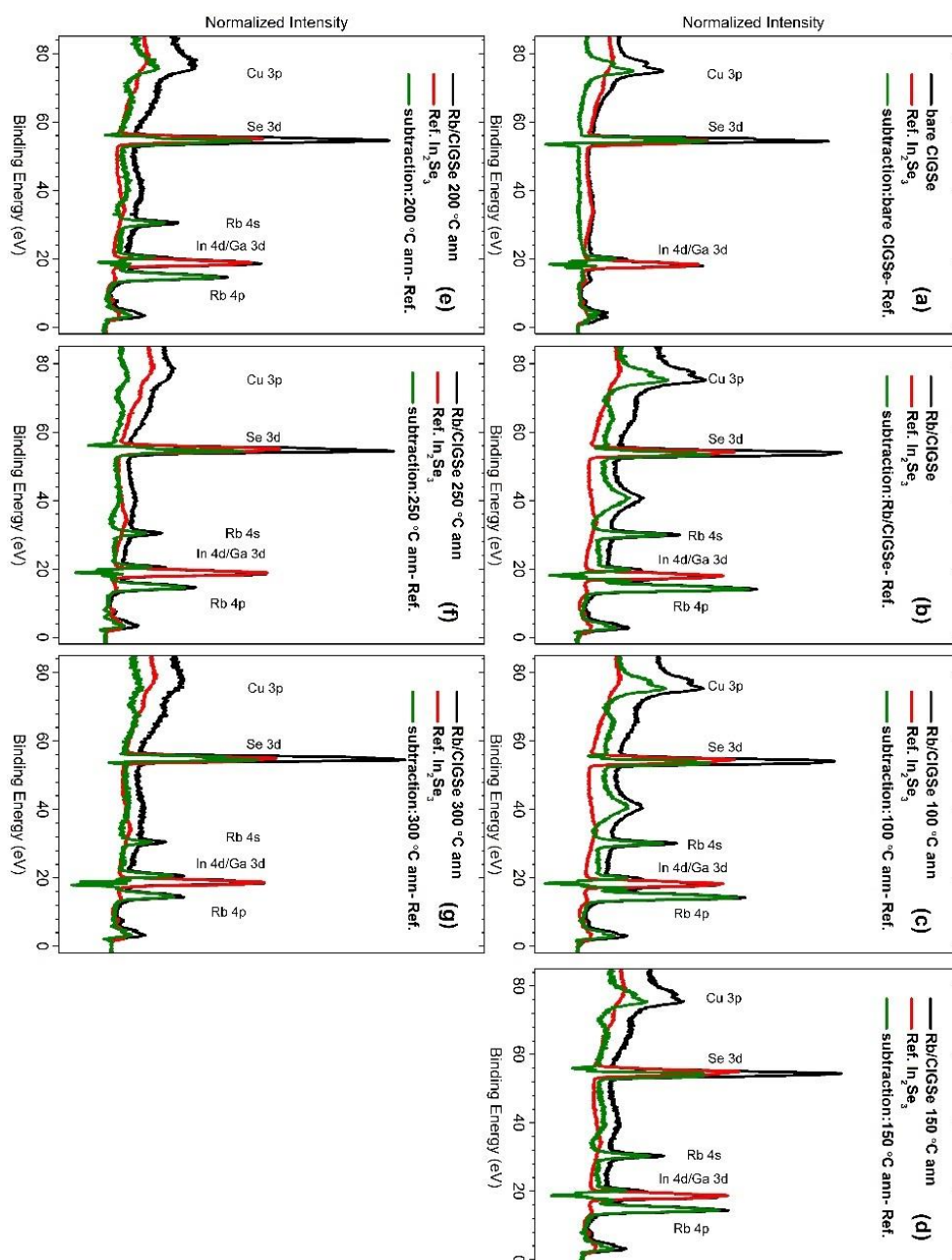


Figure B.3.1. The In 4p background correction approach for the Cu 3p line using the respectively scaled and shifted In 4d line of the In_2Se_3 reference spectrum employed to the data set of the K/CIGSe sample series (annealing temperature: bare (a), Rb/CIGSe (b), Rb/CIGSe-100 °C (c), Rb/CIGSe-150 °C (d), Rb/CIGSe-200 °C (e), Rb/CIGSe-250 °C (f), and Rb/CIGSe-300 °C (g), measured with an excitation energy of $h\nu=2$ keV. The as-measured spectra are shown in black, individually shifted and scaled references spectra in red, and the green spectra correspond to the resulting difference.

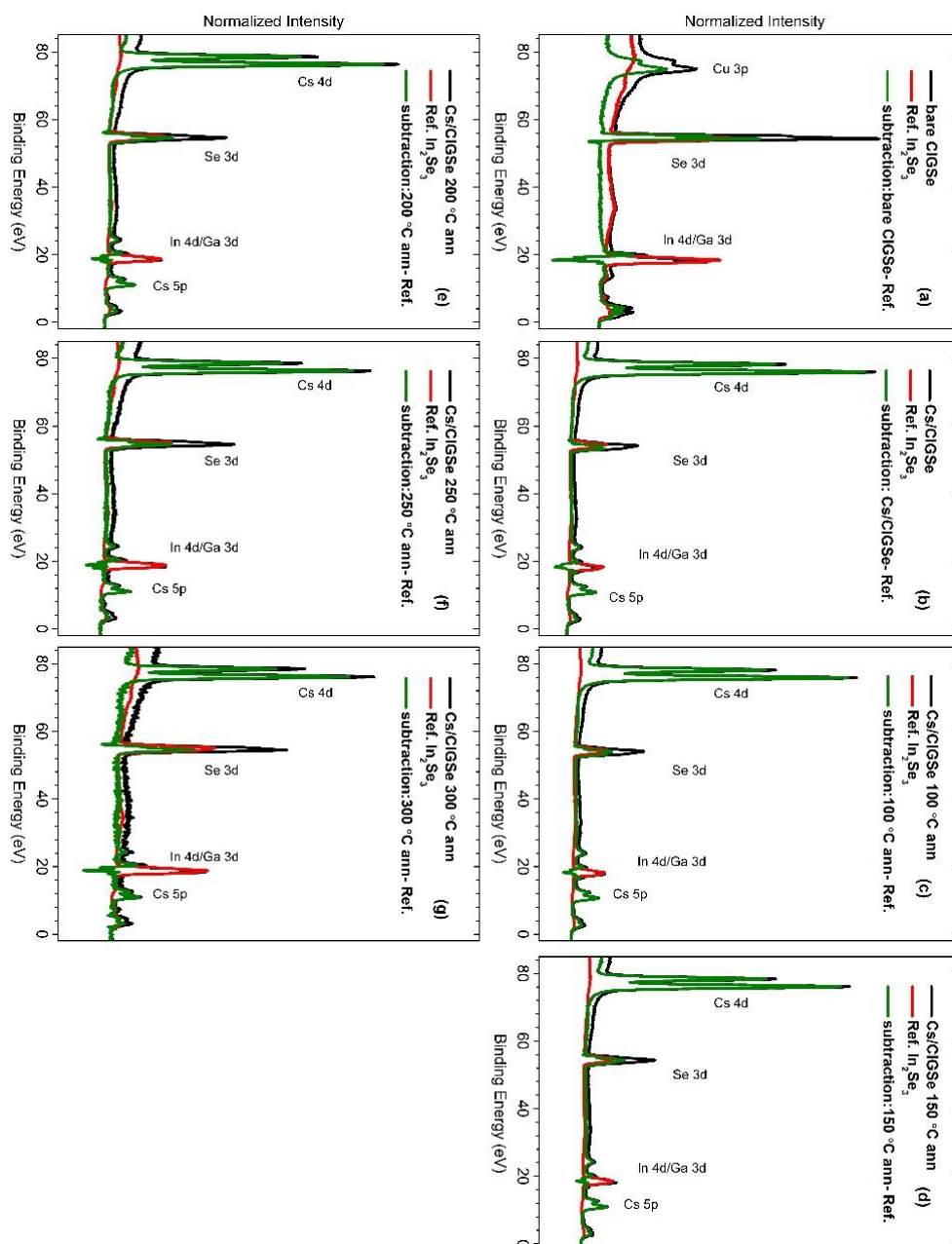


Figure B.3.2. The In 4p background correction approach for the Cu 3p line using the respectively scaled and shifted In 4d line of the In_2Se_3 reference spectrum employed to the data set of the K/CIGSe sample series (annealing temperature: bare (a), Cs/CIGSe (b), Cs/CIGSe-100 °C (c), Cs/CIGSe-150 °C (d), Cs/CIGSe-200 °C (e), Cs/CIGSe-250 °C (f), and Cs/CIGSe-300 °C (g), measured with an excitation energy of $h\nu=2$ keV. The as-measured spectra are shown in black, individually shifted and scaled reference spectra in red, and the green spectra correspond to the resulting difference.

Figures B.3.1-B.3.2 visualize the Cu 3p background correction of Rb/CIGSe (B.3.1) and Cs/CIGSe series (B.3.2), subtracting a properly shifted and scaled In_2Se_3 reference spectrum to account for the broad In 4p background (between 80 and 60 eV) that overlaps with the Cu 3p signal, respectively. For the proper energy shift and scaling factor for the reference spectra were derived

by bringing the In 4d lines to maximum overlap. The “negative” overshoot in the range of the In 4d line in the difference spectra can be explained by different composition profiles and/or slight variations of the core level binding energies.

B.4 Cu 3p fitting spectra of Rb/CIGSe sample series

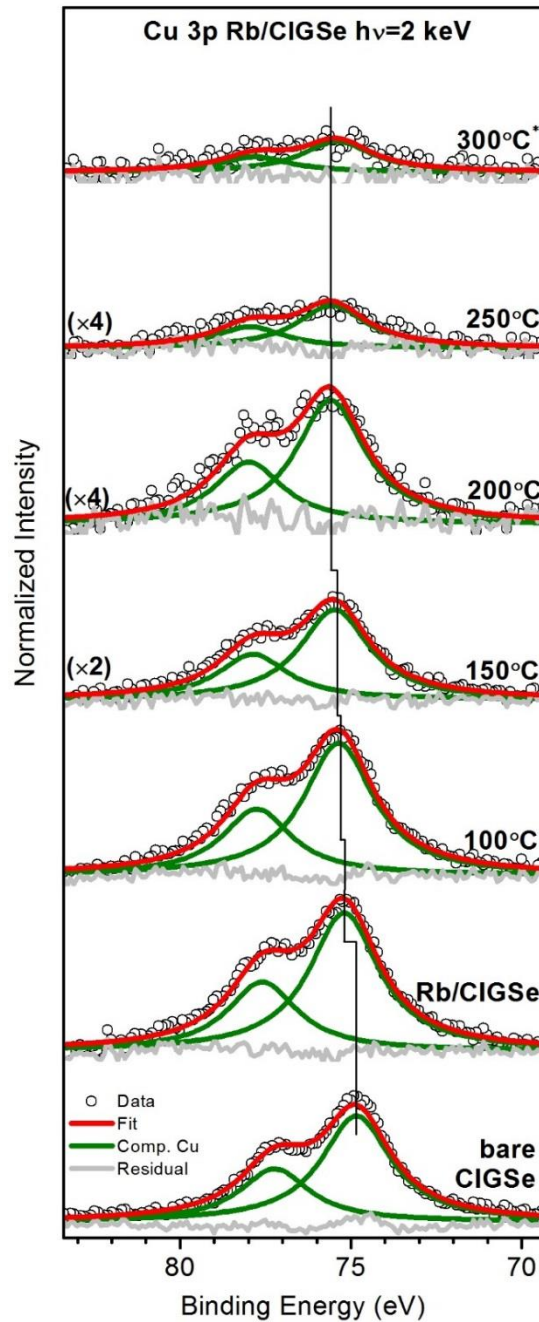


Figure B.4. Cu 3p HAXPES data with respective Voigt fits of the Rb/CIGSe sample series, measured with excitation energies of 2 keV. All spectra are displayed after subtraction of a linear background. For each fit, the residual is shown as well. Note the different magnification factors.

B.5 The direct comparison of realigned-VBM spectra for alk/CIGSe and PDTs CIGSe samples

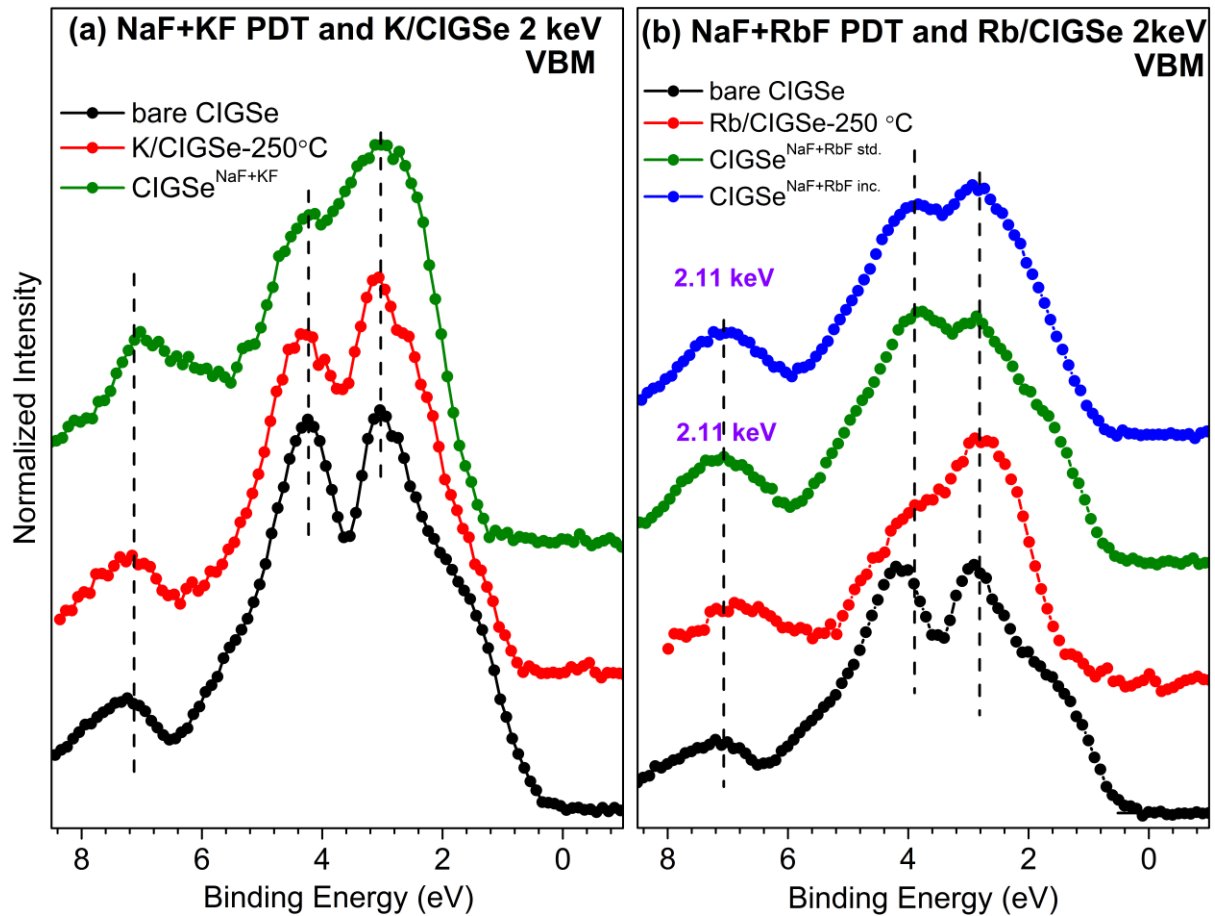


Figure B.5. The direct comparison of realigned-VBM spectra of bare CIGSe, K/CIGSe and $\text{CIGSe}^{\text{NaF+KF}}$ (a); bare CIGSe, Rb/CIGSe-250°C, $\text{CIGSe}^{\text{NaF+RbF std.}}$, and $\text{CIGSe}^{\text{NaF+RbF inc.}}$ samples (b) according to the the realigned Cu 3p. Note that all the Rb evaporated samples were measure at 2 keV and PDT samples were measured at 2.11 keV.

Bibliography

- [1] Chapin, D. M.; Fuller, C. S.; Pearson G. L. A New Silicon p-n Junction Photocell for Converting Solar Radiation into Electrical Power. *J. Appl. Phys.* **1954**, *25*, 676.
- [2] Chopra, K. L.; Paulson, P. D.; Dutta D. Thin-Film Solar Cells: An Overview. *Prog. Photovolt. Res. Appl.* **2004**, *12*, 69.
- [3] Jackson, P.; Wuerz, R.; Hariskos, D.; Lotter, E.; Witte, W.; Powalla, M. Effects of Heavy Alkali Elements in Cu(In,Ga)Se₂ Solar Cells with Efficiencies up to 22.6%. *Phys. Status Solidi RRL* **2016**, *10*, 583-586.
- [4] Solar Frontier. http://www.solar-frontier.com/eng/news/2017/1220_press.html.
- [5] Solar Frontier. http://www.solar-frontier.com/eng/news/2019/0117_press.html.
- [6] G173-03, Astm. *Standard Tables for Reference Solar Spectral Irradiances: Direct Normal and Hemispherical on 37° Tilted Surface*, ASTM International: West Conshohocken, 2012.
- [7] Hamadani, B. H.; Dougherty, B. *Solar Cell Characterization*, Springer, Cham: 2016; Vol. 218, p 229.
- [8] Wagner, S.; Shay, J. L.; Migliorato, P. CuInSe₂/CdS heterojunction photovoltaic detectors. *Appl. Phys. Lett.* **1974**, *25*, 434.
- [9] Heske, C.; Fink, C.; Umbach, E.; Riedl, W.; Karg, F. Na Induced Effects on the Electronic Structure and Composition of Cu(In,Ga)Se₂ Thin Film Surfaces. *Appl. Phys. Lett.* **1996**, *68*, 3431-3433.
- [10] Heske, C.; Eich, D.; Fink, R.; Umbach, E.; Kakar, S.; Van Buuren, T.; Bostedt, C.; Terminello, L. J.; Grush, M. M.; Callcott, T. A.; Himpel, F. J.; Ederer, D. L.; Perera, R. C. C.; Riedl, W.; Karg, F. Localization of Na Impurities at the Buried CdS/Cu(In,Ga)Se₂ Heterojunction. *Appl. Phys. Lett.* **1999**, *75*, 2082-2084.
- [11] Ong, K. H.; Agileswari, R.; Maniscalco, B.; Arnou, P.; Kumar, C. C.; Bowers, J. W.; Marsadek, M. B. Review on Substrate and Molybdenum Back Contact in CIGS Thin Film Solar Cell. *Int. J. Photoenergy* **2018**, *2018*.
- [12] Kohara, N.; Nishiwaki, S.; Hashimoto, Y.; Negami, T.; Wada, T. Electrical properties of the Cu(In,Ga)Se₂/MoSe₂/Mo structure. *Sol. Energy Mater. Sol. Cells* **2001**, *67*, 209.
- [13] Wada, T.; Kohara, N.; Nishiwaki, S.; Negami, T. Characterization of the Cu(In,Ga)Se₂/Mo interface in CIGS solar cells. *Thin Solid Films* **2001**, *387*, 118.
- [14] Mudryi, A. V.; Gremenok, V. F.; Karotki, A. V.; Zalesski, V. B.; Yakushev, M. V.; Luckert, F.; Martinc, R. Structural and optical properties of thin films of Cu(In,Ga)Se₂ semiconductor compounds. *J. Appl. Spectrosc.* **2010**, *77*, 371.
- [15] Peace, B.; Claypoole, J.; Sun, N.; Dwyer, D.; Eisaman, M. D.; Haldar, P.; Efstathiadis, H. Characterization of Cu(In,Ga)Se₂ (CIGS) films with varying gallium ratios. *J. Alloys Compd.* **2016**, *657*, 873.
- [16] Ramanujam, J.; Singh, U. P. Copper indium gallium selenide based solar cells – a review. *Energy Environ. Sci.* **2017**, *10*, 1306.
- [17] Oladeji, I. O.; Chow, L. Optimization of Chemical Bath Deposited Cadmium Sulfide Thin Films. *J. Electrochem. Soc.* **1997**, *144*, 2342.
- [18] Ortega-Borges, R.; Lincot, D. Mechanism of Chemical Bath Deposition of Cadmium Sulfide Thin Films in the Ammonia-Thiourea System In Situ Kinetic Study and Modelization. *J. Electrochem. Soc.* **1993**, *140* (12), 3464-3473.
- [19] Félix, R. Analysis and Optimization of Interfaces in “Wide-Gap” Chalcopyrite-based Thin Film Solar Cell Devices. Ph.D Thesis, BTU Cottbus-Senftenberg, 2015.

- [20] Nakada, T.; Mizutani, M. 18% Efficiency Cd-Free Cu(In, Ga)Se₂ Thin-Film Solar Cells Fabricated Using Chemical Bath Deposition (CBD)-ZnS Buffer Layers. *Jap. J. Appl. Phys.* **2002**, *41*, 2B.
- [21] Hariskos, D.; Spiering, S.; Powalla, M. Buffer layers in Cu(In,Ga)Se₂ solar cells and modules. *Thin Solid Films* **2005**, *480–481*, 99.
- [22] Bhattacharya, R. N.; Ramanathan, K.; Gedvilas, L.; Keyes, B. Cu(In,Ga)Se₂ thin-film solar cells with ZnS(O,OH), Zn–Cd–S(O,OH), and CdS buffer layers. *J. Phys. Chem. Solids* **2005**, *66* (11), 1862.
- [23] Omelianovych, A.; Kim, J. H.; Liudmila, L.; Ahn, B. T. Effect of post annealing on the characteristics of In₂S₃ buffer layer grown by chemical bath deposition on a CIGS substrate. *Curr. Appl. Phys.* **2015**, *15*, 1641.
- [24] Serhan, J.; Djebbour, Z.; Favre, W.; Migan-Dubois, A.; Darga, A.; Mencaraglia, D.; Naghavi, N.; Renou, G.; Guillemoles, J.-F.; Lincot, D. Investigation of the Metastability Behavior of CIGS Based Solar Cells with ZnMgO–Zn(S,O,OH) Window-buffer Layers. *Thin Solid Films* **2011**, *519*, 7606–7610.
- [25] Bär, M.; Bohne, W.; Röhrich, J.; Strub, E.; Lindner, S.; Lux-Steiner, M. C.; Fischer, Ch. H.; Niesen, T. P.; Karg, F. Determination of the Band Gap Depth Profile of the Pentenary Cu(In_{1-x}Ga_x)(S_ySe_{1-y})₂ Chalcopyrite from its Composition Gradient. *J. Appl. Phys.* **2004**, *96*, 3857.
- [26] Chirilă, A.; Reinhard, P.; Pianezzi, F.; Bloesch, P.; Uhl, A. R.; Fella, C.; Kranz, L.; Keller, D.; Gretener, C.; Hagendorfer, H.; Jaeger, D.; Erni, R.; Nishiwaki, S.; Buecheler, S.; Tiwari, A. N. Potassium-Induced Surface Modification of Cu(In,Ga)Se₂ Thin Films for High-Efficiency Solar Cells. *Nat. Mater.* **2013**, *12*, 1107–1111.
- [27] Unold, T.; Kaufmann, C. A. Chalcopyrite Thin-Film Materials and Solar Cells. In *Comprehensive Renewable Energy*, Sayigh, A., Ed.; Elsevier: 2012; pp 399–422.
- [28] Abou-Ras, D.; Caballero, R.; Kaufmann, C. A.; Nichterwitz, M.; Sakurai, K.; Schorr, S.; Unold, T.; Schock, H. W. Impact of the Ga concentration on the microstructure of CuIn_{1-x}Ga_xSe₂. *Physica status solidi* **2008**, *2*, 135–137.
- [29] Reinhard, P.; Bissig, B.; Pianezzi, F.; Avancini, E.; Hagendorfer, H.; Keller, D.; Fuchs, P.; Döbeli, M.; Vigo, C.; Crivelli, P.; Nishiwaki, S.; Buecheler, S.; Tiwari, A. N. Features of KF and NaF Postdeposition Treatments of Cu(In,Ga)Se₂ Absorbers for High Efficiency Thin Film Solar Cells. *Chem. Mater.* **2015**, *27*, 5755–5764.
- [30] Rudmann, D.; Brémaua, D.; Da Cunha, A. F.; Bilger, G.; Strohm, A.; Kaelin, M.; Zogg, H.; Tiwari, A. N. Sodium Incorporation Strategies for CIGS Growth at Different Temperatures. *Thin Solid Films* **2005**, *480–481*, 55–60.
- [31] Hauschild, D.; Kreikemeyer-Lorenzo, D.; Jackson, P.; Magorian Friedlmeier, T.; Hariskos, D.; Reinert, F.; Powalla, M.; Heske, C.; Weinhardt L. Impact of a RbF Postdeposition Treatment on the Electronic Structure of the CdS/Cu(In,Ga)Se₂ Heterojunction in High-Efficiency Thin-Film Solar Cells. *ACS Energy Lett.* **2017**, *2*, 2383–2387.
- [32] Contreras, M. A.; Romero, M. J.; to, B.; Hasoon, F.; Noufi, R.; Ward, S.; Ramanathan K. Optimization of CBD CdS Process in High-Efficiency Cu(In,Ga)Se₂-Based Solar Cells. *Thin Solid Films* **2002**, *403*, 204–211.
- [33] Handick, E.; Reinhard, P.; Wilks, R. G.; Pianezzi, F.; Kunze, T.; Lorenzo, D. K.; Weinhardt, L.; Blum, M.; Yang, W.; Gorgoi, M.; Ikenaga, E.; Gerlach, D.; Ueda, S.; Yamashita, Y.; Chikyow, T.; Heske, C.; Buecheler, S.; Tiwari, A. N.; Bär, M. Formation of a K-In-Se Surface Species by NaF/KF Postdeposition Treatment of Cu(In,Ga)Se₂ Thin-Film Solar Cell Absorbers. *ACS Appl. Mater. Interfaces* **2017**, *9*, 3581–3589.
- [34] Lundberg, O.; Wallin, E.; Gusak, V.; Södergren, S.; Chen, S.; Lotfi, S.; Chalvet, F.; Malm, U.; Kaihovirta, N.; Mende, P.; Jaschke, G.; Kratzert, P.; Joel, J.; Skupinski, M.; Lindberg, P.; Jarmar, T.; Lundberg, J.; Mathiasson,

- J.; Stolt, L., Improved CIGS Modules by KF Post Deposition Treatment and Reduced Cell -to-Module Losses. In *IEEE 43th Photovoltaic Specialists Conference (PVSC)*, IEEE: Portland, OR, USA, 2016 pp 1293-1296.
- [35] Khatri, I.; Fukai, H.; Yamaguchi, H.; Sugiyama, M.; Nakada T. Effect of Potassium Fluoride Post-Deposition Treatment on Cu(In,Ga)Se₂ Thin Films and Solar Cells Fabricated onto Sodalime Glass Substrates. *Sol. Energy Mater. Sol. Cells* **2016**, *155*, 280-287.
- [36] Lepetit, T. Influence of KF Post Deposition Treatment on the Polycrystalline Cu(In,Ga)Se₂/CdS Heterojunction Formation for Photovoltaic Application. Ph.D Thesis, Université de Nantes, 2015.
- [37] Khatri, I.; Sugiyama, M.; Nakada, T. Effects of Combined Additional Indium Deposition and Potassium Fluoride Post-Deposition Treatments on Cu(In,Ga)Se₂ Thin Film Solar Cells. *Prog. Photovolt. Res. Appl.* **2017**, *25*, 871-877.
- [38] Handick, E.; Reinhard, P.; Wilks, R. G.; Pianezzi, F.; Félix, R.; Gorgoi, M.; Kunze, T.; Buecheler, S.; Tiwari, A. N.; Bär M., NaF/KF Post-Deposition Treatments and Their Influence on the Structure of Cu(In,Ga)Se₂ Absorber Surfaces. In *IEEE 43th Photovoltaic Specialists Conference (PVSC)*, Portland, OR, USA, 2016; pp 0017-0021.
- [39] Pistor, P.; Greiner, D.; Kaufmann, C. A.; Brunken, S.; Gorgoi, M.; Steigert, A.; Calvet, W.; Lauer mann, I.; Klenk, R.; Unold, T.; Lux-Steiner, M.-C. Experimental Indication for Band Gap Widening of Chalcopyrite Solar Cell Absorbers after Potassium Fluoride Treatment. *Appl. Phys. Lett.* **2014**, *105*, 063901.
- [40] Handick, E.; Reinhard, P.; Alsmeyer, J.-H.; Köhler, L.; Pianezzi, F.; Krause, S.; Gorgoi, M.; Ikenaga, E.; Koch, N.; Wilks, R. G.; Buecheler, S.; Tiwari, A. N.; Bär, M. Potassium Postdeposition Treatment-Induced Band Gap Widening at Cu(In,Ga)Se₂ Surfaces-Reason for Performance Leap? *ACS Appl. Mater. Interfaces* **2015**, *7*, 27414-27420.
- [41] Mezher, M.; Mansfield, L. M.; Horsley, K.; Blum, M.; Wieting, R.; Weinhardt, L.; Ramanathan, K.; Heske C. KF Post-Deposition Treatment of Industrial Cu(In, Ga)(S, Se)₂ Thin-Film Surfaces: Modifying the Chemical and Electronic Structure. *Appl. Phys. Lett.* **2017**, *111*, 071601.
- [42] Nicoara, N.; Harel, S.; Lepetit, T.; Arzel, L.; Barreau, N.; Sadewasser, S. Impact of KF Post-Deposition Treatment on Aging of the Cu(In,Ga)Se₂ Surface and Its Interface with CdS. *ACS Appl. Energy Mater.* **2018**, *1*, 2681-2688.
- [43] Kodalle, T.; Heinemann, M. D.; Greiner, D.; Yetkin, H. A.; Klupsch, M.; Lauer mann, I.; Schlatmann, R.; Kaufmann, C. A. Elucidating the Mechanism of an RbF Post Deposition Treatment in CIGS Thin Film Solar Cells. *Solar RRL* **2018**, *2*, 1800156.
- [44] Nicoara, N.; Kunze, T.; Jackson, P.; Hariskos, D.; Félix Duarte, R.; Wilks, R. G.; Witte, W.; Bär, M.; Sadewasser, S. Evidence for Chemical and Electronic Nonuniformities in the Formation of the Interface of RbF-Treated Cu(In,Ga)Se₂ with CdS. *ACS Appl. Mater. Interfaces* **2017**, *9*, 44173.
- [45] Malitckaya, M.; Komsa, H. P.; Havu, V.; Puska, M. J. Effect of Alkali Metal Atom Doping on the CuInSe₂-Based Solar Cell Absorber. *J. Phys. Chem. C* **2017**, *121* (29), 15516.
- [46] Hertz, H. Ueber einen Einfluss des ultravioletten Lichtes auf die elektrische Entladung. *Ann. Phys.* **1887**, *267*, 983.
- [47] Einstein, A. Über einen die Erzeugung und Verwandlung des Lichtes betreffenden heuristischen Gesichtspunkt. *Ann. Phys.* **1905**, *17*, 132.
- [48] Hüfner, S. *Photoelectron spectroscopy: principles and applications*, Springer: 2013.
- [49] Hans, L. *Solid surfaces, interfaces and thin films*, Springer: 2001; Vol. 4.

- [50] Handick, E. Surface and Interface Characterization by X-ray and Electron Spectroscopies – Revealing the Peculiarities of Cu(In,Ga)Se₂ Chalcopyrite and CH₃NH₃PbI_{3-x}Cl_x Perovskite-based Thin-film Solar Cell Structures PhD Thesis, Brandenburgische Technische Universität Cottbus-Senftenberg, 2017.
- [51] Briggs, D.; Seah, M. P. *Practical Surface Analysis: Auger and X-ray Photoelectron Spectroscopy*, Wiley: New York 1983.
- [52] Moulder, J. F.; Stickle, W. F.; Sobol, P. E.; Bomben, K. D. *Handbook of X-Ray Photoelectron Spectroscopy*, Minnesota, USA, 1995.
- [53] Brown, G.; Halbach, K.; Harris, J.; Winick, H. Wiggler and Undulator Magnets – A Review. *Nuclear Instruments and Methods* **1983**, *208*, 65-77.
- [54] Attwood, D. *Soft X-rays and Extreme Ultraviolet Radiation*, Cambridge: New York, 1999.
- [55] Schaefers, F.; Mertin, M.; Gorgoi, M. KMC-1: A High Resolution and High Flux Soft X-ray Beamline at BESSY. *Review of Scientific Instruments* **2007**, *78*, 123102.
- [56] Jia, J. J.; Callcott, T. A.; Yurkas, J.; Ellis, A. W.; Himpfel, F. J.; Samant, M. G.; Stöhr, J.; Ederer, D. L.; Carlisle, J. A.; Hudson, E. A.; Terminello, L. J.; Shuh, D. K.; Perera, R. C. C. First Experimental Results from IBM/TENN/TULANE/LLNL/LBL Undulator Beamline at the Advanced Light Source. *Review of Scientific Instruments* **1995**, *66*, 1394-1397.
- [57] https://www.Helmholtz-Berlin.De/Pubbin/Igama_Output?Modus=Einzel&Sprache=En&Gid.
- [58] Wojdyra, M. Fityk: A General-Purpose Peak Fitting Program. *J. Appl. Crystallogr.* **2010**, *43*, 1126-1128.
- [59] Jackson, P.; Hariskos, D.; Wuerz, R.; Kiowski, O.; Bauer, A.; Friedlmeier, T. M.; Powalla, M. Properties of Cu(In,Ga)Se₂ Solar Cells with New Record Efficiencies up to 21.7%. *Phys. Status Solidi RRL* **2014**, *9*, 28.
- [60] Bär, M.; Weinhardt, L.; Heske, C.; Muffler, H.-J.; Lux-Steiner, M. Ch.; Umbach, E.; Fischer Ch.-H. Cd²⁺/NH₃ Treatment of Cu(In,Ga)(S,Se)₂ Thin-film Solar Cell Absorbers: A Model for the Performance-enhancing Processes in the Partial Electrolyte. *Prog. Photovolt. Res. Appl.* **2005**, *13*, 571-577.
- [61] Bär, M.; Ennaoui, A.; Klaer, J.; Kropp, T.; Sáez-Araoz, R.; Allsop, N.; Lauermann, I.; Schock, H.-W.; Lux-Steiner, M. C. Formation of a ZnS / Zn(S,O) bilayer buffer on CuInS₂ thin film solar cell absorbers by chemical bath deposition. *J. Appl. Phys.* **2006**, *99*, 123503.
- [62] Weinhardt, L.; Bär, M.; Pookpanratana, S.; Morkel, M.; Niesen, T. P.; Karg, F.; Ramanathan, K.; Contreras, M. A.; Noufi, R.; Umbach, E.; Heske C. Sulfur Gradient-Driven Se Diffusion at the CdS/CuIn(S,Se)₂ Solar Cell Interface. *Appl. Phys. Lett.* **2010**, *96*, 182102.
- [63] Pookpanratana, S.; Repins, I.; Bär, M.; Weinhardt, L.; Zhang, Y.; Félix, R.; Blum, M.; Yang, W.; Heske C. CdS/Cu(In,Ga)Se₂ Interface Formation in High-Efficiency Thin Film Solar Cells. *Appl. Phys. Lett.* **2010**, *97*, 074101.
- [64] Wilks, R. G.; Caballero, R.; Song, X.; Félix, R.; Benkert, A.; Gerlach, D.; Weinhardt, L.; Blum, M.; Yang, W.; Kaufmann, C. A.; Heske, C.; Schock, H.-W.; Bär, M. , X-ray Spectroscopic Analysis of the Growth of CBD-CdS Buffers on flexible Cu(In,Ga)Se₂ Thin-Film Solar Cell Structures In *2012 38th IEEE Photovoltaic Specialists Conference*, Austin, TX, USA, 2012.
- [65] Bär, M.; Barreau, N.; Couzinié-Devy, F.; Weinhardt, L.; Wilks, R. G.; Kessler, J.; Heske, C. Impact of Annealing-Induced Intermixing on the Electronic Level Alignment at the In₂S₃/Cu(In,Ga)Se₂ Thin-Film Solar Cell Interface. *ACS Appl. Mater. Interfaces* **2016**, *8*, 2120.
- [66] Reinhard, P.; Pianezzi, F.; Bissig, B.; Chiril, A.; Buecheler, S.; Tiwari, A. N. . Cu(In,Ga)Se₂ Thin-Film Solar Cells and Modules—A Boost in Efficiency Due to Potassium. *IEEE J. Photovoltaics* **2014**, *5*, 656-663.

- [67] Petersson, L. G.; Karlsson, S. E. Clean and Oxygen Exposed Potassium Studied by Photoelectron Spectroscopy *Phys. Scr.* **1977**, *16*, 425-431.
- [68] Trzhaskovskaya, M. B. Photoelectron Angular Distribution Parameters for Elements $Z= 1$ to $Z=54$ in the Photoelectron Energy Range 100–5000eV. *At. Data Nucl. Data Tables* **2001**, *77*, 97-159.
- [69] Pianezzi, F.; Reinhard, P.; Chirilă, A.; Bissig, B.; Nishiwaki, S.; Buecheler, S.; Tiwari, A. N. Unveiling the Effects of Post-Deposition Treatment with Different Alkaline Elements on the Electronic Properties of CIGS Thin Film Solar Cells. *Phys. Chem. Chem. Phys.* **2014**, *16*, 8843-8851.
- [70] Malitckaya, M.; Kunze, T.; Komsa, H.-P.; Havu, V.; Handick, E.; Wilks, R. G.; Bär, M.; Puska, M. J. Alkali Postdeposition Treatment-Induced Changes of the Chemical and Electronic Structure of Cu(In,Ga)Se₂ Thin-Film Solar Cell Absorbers: A First-Principle Perspective. *ACS Appl. Mater. Interfaces* **2019**, *11*, 3024-3033.
- [71] Taguchi, N.; Tanaka, S.; Ishizuka, S. Direct Insights into RbInSe₂ Formation at Cu(In,Ga)Se₂ Thin Film Surface with RbF Postdeposition Treatment. *Appl. Phys. Lett.* **2018**, *113*, 113903.
- [72] Kazmerski, L. L.; Jamjoum, O.; Ireland, P. J.; Deb, S. K. R.; Mickelsen, A.; Chen, W. Initial Oxidation of CuInSe₂. *J. Vacuum Sci. & Technol.* **1981**, *19*, 467-471.
- [73] Cahen, D.; Ireland, P. J.; Kazmerski, L. L.; Thiele, F. A. X-ray Photoelectron and Auger Electron Spectroscopic Analysis of Surface Treatments and Electrochemical Decomposition of CuInSe₂ Photoelectrodes. *J. Appl. Phys.* **1985**, *57*(10), 4761-4771.
- [74] Von Morzé, N.; Dittrich, T.; Calvet, W.; Lauermann, I.; Rusu M. Transient and Modulated Charge Separation at CuInSe₂/C60 and CuInSe₂/ZnPc Hybrid Interfaces. *Appl. Surf. Sci.* **2017**, *396*, 366-374.
- [75] Faur, M.; Jayne, D. T.; Goradia, M.; Goradia, C. XPS Investigation of Anodic Oxides Grown on P-type InP. *Surf. Interface Anal.* **1990**, *15*, 641-650.
- [76] Lin, A. W. C.; Armstrong N. R.; Kuwana, T. X-ray Photoelectron/Auger Electron Spectroscopic Studies of Tin and Indium Metal Foils and Oxides. *Ana. Chem.* **1977**, *49*, 1228-1235.
- [77] Bertrand, P. A. XPS Study of Chemically Etched GaAs and InP. *J. Vacuum Sci. & Technol.* **1981**, *18*, 28-.
- [78] Sterner, J.; Malmström, J.; Stolt, L. Study on ALD In₂S₃/Cu(In,Ga)Se₂ Interface Formation. *Prog. Photovolt. Res. Appl.* **2005**, *13*, 179-193.
- [79] Lozzi, L.; Passacantando, M.; Picozzi, P.; Santucci, S. The use of the Auger parameter in the characterisation of some silicon compounds. *J. Electron. Spectrosc. Relat. Phenom.* **1995**, *72*, 97.
- [80] Dai, M. Z.; Khan, K.; Zhang, S. N.; Jiang, K. J.; Zhang, X. Y.; Wang, W. L.; Liang, L. Y.; Cao, H. T.; Wang, P. J.; Wang, P.; Miao, L. J.; Qin, H. M.; Jiang, J.; Xue, L. X.; Chu, J. H. A Direct Method to Extract Transient Sub-Gap Density of State (DOS) Based on Dual Gate Pulse Spectroscopy. *Sci. Rep.* **2016**, *6*, 24096.
- [81] Lebugle, A.; Axelsson, U.; Nyholm, R.; Martensson, N. Experimental L and M Core Level Binding Energies for the Metals ²²Ti to ³⁰Zn. *Phys. Scr.* **1981**, *23*, 825-827.
- [82] Poole, R. T.; Kemeny, P. C.; Liesegang, J.; Jenkin, J. G.; Leckey, R. C. G. High Resolution Photoelectron Studies of the d Bands of Some Metals. *J. Phys. F: Metal Phys.* **1973**, *3*, L46-L48.
- [83] Poirier, D. M.; Weaver, J. H. GaAs(110) by XPS. *Surface Science Spectra* **1993**, *2*, 201-208.
- [84] Shevchik, N. J.; Cardona, M.; Tejeda, J. X-Ray and Far-uv Photoemission from Amorphous and Crystalline of Se and Te. *Phys. Rev. B* **1973**, *8*, 2833-2841.
- [85] Sutter, E. A.; Tong, X.; Jungjohann, K.; Sutter, P. W. Oxidation of Nanoscale Au-In Alloy Particles as A Possible Route Toward Stable Au-Based Catalysts. *PNAS* **2013**, *110*, 10519.
- [86] Shalish, I.; Shapira, Y.; Burstein, L.; Salzman, J. Surface States and Surface Oxide in GaN Layers. *J. Appl. Phys.* **2001**, *89*, 390-394.

- [87] Eom, N. S. A.; Kim, T. S.; Choa, Y. H.; Kim, W. B.; Kim, B. S. Surface Oxidation Behaviors of Cd-Rich CdSe Quantum Dot Phosphors at High Temperature. *J. Nanosci. Nanotechnol.* **2014**, *14*, 8024-8027.
- [88] Brown, M. A.; Fujimori, Y.; Ringleb, F.; Shao, X.; Stavale, F.; Nilius, N.; Sterrer, M.; Freund, H.-J. Oxidation of Au by Surface OH: Nucleation and Electronic Structure of Gold on Hydroxylated MgO(001). *J. Am. Chem. Soc.* **2011**, *133*, 10668-10676.
- [89] Kishi, K.; Ikeda, S. X-Ray Photoelectron Spectroscopic Study for the Reaction of Evaporated Iron with O₂ and H₂O. *Bull. Chem. Soc. Jpn.* **1973**, *46*, 341-345.
- [90] Kim, M. G.; Kanatzidis, M. G.; Facchetti, A.; Marks, T. J. Low-Temperature Fabrication of High-Performance Metal Oxide Thin-Film Electronics via Combustion Processing. *Nat. Mater.* **2011**, *10*, 382-388.
- [91] Tanuma, S.; Powell, C. J.; Penn, D. R. Calculations of Electron Inelastic Mean Free Paths. *Surf. Interface Anal.* **1993**, *20*, 77-89.
- [92] Islam, R.; Rao, D. R. X-ray Photoelectron Spectroscopy of Zn_{1-x}Cd_xSe Thin Films. *J. Electron. Spectrosc. Relat. Phenom.* **1996**, *81*, 69-77.
- [93] Polak, M. X-Ray Photoelectron Spectroscopic Studies of CdSe_{0.65}Te_{0.35}. *J. Electron. Spectrosc. Relat. Phenom.* **1982**, *28*, 171-176.
- [94] Banerjee, S.; Wong, S. S. Formation of CdSe Nanocrystals onto Oxidized, Ozonized Single-Walled Carbon Nanotube Surfaces. *ChemComm* **2004**, 1866-1867.
- [95] Niles, D. W.; Herdt, G.; Al-Jassim, M. An X-ray Photoelectron Spectroscopy Investigation of O Impurity Chemistry in CdS Thin Films Grown by Chemical Bath Deposition. *J. Appl. Phys.* **1997**, *81*, 1978-1984.
- [96] Bhide, V. G.; Salkalachen, S.; Rastog, A. C.; Rao, C. N. R.; Hegde, M. S. Depth Profile Composition Studies of Thin Film CdS:Cu₂S Solar Cells Using XPS and AES. *J. Phys. D: Appl. Phys.* **1981**, *14*, 1647-1656.
- [97] Riga, J.; Verbist, J. J.; Josseaux, P.; Mesmaeker, A. K. Correlation between CdS Photoanodic Behaviour and Electrode Chemical Modifications: An X-ray Photoelectron Spectroscopic Study. *Surf. Interface Anal.* **1985**, *7*, 163-168.
- [98] Wagner C. D.; Gale L. H.; Raymond, R. H. Two-Dimensional Chemical State Plots: A Standardized Data Set for Use in Identifying Chemical States by X-ray Photoelectron Spectroscopy. *Anal. Chem.* **1979**, *51*, 466-482.
- [99] O. P. Tkachenko, E. S. Shpiro, M. Wark, G. Schulz-Ekloff, N. I. Jaeger X-ray photoelectron/X-ray excited auger electron spectroscopic study of highly dispersed semiconductor CdS and CdO species in zeolites. *Journal of the Chemical Society, Faraday Transactions* **1993**, *89*, 3987.
- [100] Zhang, D. E.; Pan, X. D.; Zhu, H.; Li, S. Z.; Xu, G. Y.; Zhang, X. B.; Ying, A. L.; Tong, Z. W. A Simple Method to Synthesize Cadmium Hydroxide Nanobelts. *Nanoscale Res. Lett.* **2008**, *3*(8), 284-288.
- [101] Tkachenko, O. P.; Shpiro, E. S.; Wark, M.; Ekloff, G. S.; Jaeger, N. X-Ray Photoelectron/X-Ray Excited Auger Electron Spectroscopic Study of Highly Dispersed Semiconductor CdS and CdO Species in Zeolites. *J. Chem. Soc. Faraday Trans.* **1993**, *89*, 3987-3994.
- [102] Gaarenstroom, S. W.; Winograd, N. Initial and Final State Effects in the ESCA Spectra of Cadmium and Silver Oxides. *J. Chem. Phys.* **1977**, *67*, 3500-3506.
- [103] White, H. S.; Rocco, A. J.; Wrighton, M. S. Characterization of p-Type CdTe Electrodes in Acetonitrile/Electrolyte Solutions. Nearly Ideal Behavior from Reductive Surface Pretreatments. *J. Phys. Chem. C* **1983**, *87*, 5140-5150.
- [104] Fantauzzi, M.; Elsener, B.; Atzei, D.; Rigoldiab, A.; Rossi A. Exploiting XPS for the Identification of Sulfides and Polysulfides. *RSC Adv.* **2015**, *5*, 75953-75963.

- [105] Weinhardt, L.; Fuchs, O.; Umbach, E.; Heske, C.; Fleszar, A.; Hanke, W.; Denlinger, J. D. Resonant Inelastic Soft X-ray Scattering, X-ray Absorption Spectroscopy, and Density Functional Theory Calculations of the Electronic Bulk Band Structure of CdS. *Phys. Rev. B* **2007**, *75*, 165207.
- [106] Zhou, L.; Callcott, T. A.; Jia, J. J.; Ederer, D. L.; Perera, R. Sulfur $L_{2,3}$ and Zinc $M_{2,3}$ Soft-X-ray Fluorescence Spectra in CdS and ZnS. *Phys. Rev. B* **1997**, *55*, 5051-5061.
- [107] Bär, M.; Repins, I.; Weinhardt, L.; Alsmeier, J.-H.; Pookpanratana, S.; Blum, M.; Yang, W.; Heske, C.; Wilks, R. G.; Nouf, R. Zn–Se–Cd–S Interlayer Formation at the CdS/Cu₂ZnSnSe₄ Thin-Film Solar Cell Interface. *ACS Energy Lett.* **2017**, *2*, 1632-1640.
- [108] National Institute of Standards and Technology. <https://srdata.nist.gov/xps/>.
- [109] Meisel, A.; Leonhardt, G.; Szargan, R. *X-Ray Spectra and Chemical Binding; Springer Series in Chemical Physics*, Springer-Verlag: Berlin, 1989; Vol. 37, p 458.
- [110] Heske, C.; Eich, D.; Fink, R.; Umbach, E.; Van Buuren, T.; Bostedt, C.; Terminello, L. J.; Kakar, S.; Grush, M. M.; Callcott, T. A.; Himpfel, F. J.; Ederer, D. L.; Perera, R. C. C.; Riedl, W.; Karg F. Observation of Intermixing at the Buried CdS/Cu(In,Ga)Se₂ Thin Film Solar Cell Heterojunction. *Appl. Phys. Lett.* **1999**, *74*, 1451-1453.
- [111] Reichardt, J.; Bär, M.; Grimm, A.; Kötschau, I.; Lauermann, I.; Sokoll, S.; Lux-Steiner, M. C.; Fischer, Ch. H.; Heske, C.; Weinhardt, L.; Fuchs, O.; Jung, Ch.; Gudat, W.; Niesen, T. P.; Karg F. Inducing and Monitoring Photoelectrochemical Reactions at Surfaces and Buried Interfaces in Cu(In,Ga)(S,Se)₂ Thin-Film Solar Cells. *Appl. Phys. Lett.* **2005**, *86*, 172102.
- [112] Park, S. M.; Kim, T. G.; Chung, Y. D.; Cho, D.-H.; Kim, J.; Kim, K. J.; Yi, Y.; Kim J. W. Junction formation at the interface of CdS/CuIn_xGa_(1-x)Se₂. *J. Phys. D: Appl. Phys.* **2014**, *47*, 345302.
- [113] Yeh, J. J.; Lindau, I. . Atomic subshell photoionization cross sections and asymmetry parameters: 1<Z<103. *At. Data Nucl. Data Tables* **1985**, *32*, 1.
- [114] Kuznetsova, T. V.; Grebennikov, V. I.; Zhao, H.; Derks, C.; Taubitz, C.; Neumann, M.; Persson, C.; Kuznetsov, M. V.; Bodnar, I. V.; Martin, R. W.; Yakushev, M. V. A photoelectron spectroscopy study of the electronic structure evolution in CuInSe₂-related compounds at changing copper content. *Appl. Phys. Lett.* **2012**, *101*, 111607.
- [115] Waldrop, J. R.; Grant, R. W.; Kowalczyk, S. P.; Kraut E. A. Measurement of semiconductor heterojunction band discontinuities by x-ray photoemission spectroscopy. *Journal of Vacuum Science & Technology A: Vacuum, Surfaces, and Films* **1985**, *3*, 835-841.
- [116] Kale, R. B.; Lokhande, C. D. Systematic Study on Structural Phase Behavior of CdSe Thin Films. *J. Phys. Chem. B* **2005**, *109*, 20288-20294.
- [117] Jefferson, P. H.; Hatfield, S. A.; Veal, T. D.; King, P. D. C.; Mcconville, C. F.; Zúñiga-Pérez, J.; Muñoz-Sanjosé, V. Bandgap and Effective Mass of Epitaxial Cadmium Oxide. *Appl. Phys. Lett.* **2008**, *92*, 022101.
- [118] Gujar, T. P.; Shinde, V. R.; Kim, Woo-Young; Jung, Kwang-Deog; Lokhande, C. D.; Joo, Oh-Shim Formation of CdO Films from Chemically Deposited Cd(OH)₂ Films as a Precursor. *Appl. Surf. Sci.* **2008**, *254*, 3813-3818.
- [119] Ballipinar, F.; Rastogia, A. C. High Transmittance Cadmium Oxysulfide Cd(S,O) Buffer Layer Grown by Triton X-100 Mediated Chemical Bath Deposition for Thin-Film Heterojunction Solar Cells. *J. Appl. Phys.* **2017**, *121*, 035302.

- [120] J. Ruiz-Fuertes, D. Errandonea, F. J. Manjón, D. Martínez-García, A. Segura, V. V. Ursaki, I. M. Tiginyanu. High-pressure Effects on the Optical-Absorption Edge of CdIn₂S₄, MgIn₂S₄, and MnIn₂S₄ Thiospinels. *J. Appl. Phys.* **2008**, *103*, 063710.
- [121] Yildirim, M. Ali; Ates Aytunc;. Structural, Optical and Electrical Properties of CdO/Cd(OH)₂ Thin Films Grown by the SILAR Method. *Sens. Actuator A Phys.* **2009**, *155*, 272-277.
- [122] B. Sahin, F. Bayansal, H. M. Çakmak, S. Kahraman, H. A. Çetinkara. Effect of Heat Treatment on the Properties of Cd(OH)₂ and CdO Films Grown by Chemical Bath Deposition. *Philos. Mag. Lett.* **2013**, *93*, 101.
- [123] Minemoto, T.; Matsui, T.; Takakura, H.; Hamakawa, Y.; Negami, T.; Hashimoto, Y.; Uenoyama, T.; Kitagawa, M. . Theoretical Analysis of the Effect of Conduction Band Offset of Window/CIS layers on Performance of CIS Solar Cells using Device Simulation. *Sol. Energy Mater. Sol. Cells* **2001**, *67*, 83-88.
- [124] Avancini, E.; Carron, R.; Weiss, T. P.; Andres, C.; Burki, M.; Schreiner, C.; Figi, R.; Romanyuk, Y. E.; Buecheler, S.; Tiwari A. N. Effects of Rubidium Fluoride and Potassium Fluoride Postdeposition Treatments on Cu(In,Ga)Se₂ Thin Films and Solar Cell Performance. *Chem. Mater.* **2017**, *29*, 9695-9704.
- [125] Zhang, S. B.; Wei, S.-H.; Zunger, A.; Katayama-Yoshida, H. Defect Physics of the CuInSe₂ Chalcopyrite Semiconductor. *Phys. Rev. B: Condens. Matter Mater. Phys.* **1998**, *57*, 9642-9656.
- [126] Morkel, M.; Weinhardt, L.; Lohmüller, B.; Heske, C.; Umbach, E.; Riedl, W.; Zweigart, S.; Karg, F. . Flat Conduction-band Alignment at the CdS/CuInSe₂ Thin-film Solar-cell Heterojunction. *Appl. Phys. Lett.* **2001**, *79*, 4482.
- [127] Ramanathan, K.; Wiesner, H.; Asher, S.; Niles, D.; Bhattacharya, R. N.; Contreras, M. A.; Noufi, R. In *High-Efficiency Cu(In,Ga)Se₂ Thin Film Solar Cells Without Intermediate Buffer Layers*, Conference Proceedings of the 2nd World Conference in Photovoltaic Energy Conversion, Vienna, Austria, Vienna, Austria, 1998; pp 477-481.
- [128] <https://www.Saesgetters.Com>.
- [129] Tsai, H. M.; Asokan, K.; Pao, C. W.; Chiou, J. W.; Du, C. H.; Pong, W. F.; Tsai, M.-H.; Jang, L. Y. . Anisotropic Electronic Structure in Quasi-one-dimensional K_{0.3}MoO₃ : An Angledependent X-ray Absorption Study. *Appl. Phys. Lett.* **2007**, *91*, 022109.
- [130] Cibin, G.; Mottana, A.; Marcelli, A.; Brigatti, M. F. Potassium Coordination in Trioctahedral Micas Investigated by K-edge XANES Spectroscopy. *Mineral. Petrol.* **2005**, *85*, 67-87.
- [131] Bindua, K.; Karthaa, C. S.; Vijayakumara, K. P.; Abeb, T.; Kashiwaba, Y. . CuInSe₂ Thin Film Preparation through A New Selenisation Process using Chemical Bath Deposited Selenium. *Sol. Energy Mater. Sol. Cells* **2003**, *79*, 67-79.
- [132] Chen, H.; Yu, S.; Shin, D. W.; Yoo, J. B. Solvothermal Synthesis and Characterization of Chalcopyrite CuInSe₂ Nanoparticles. *Nanoscale Res. Lett.* **2010**, *5*, 217-223.
- [133] Procop, M. XPS data for sputter-cleaned In_{0.53}Ga_{0.47}As, GaAs, and InAs surfaces. *J. Electron. Spectrosc. Relat. Phenom.* **1992**, *59*, R1-R10.
- [134] Trzhaskovskaya, M. B. Photoelectron angular distribution parameters for elements Z=55 to Z=100 in the photoelectron energy range 100-5000eV. *At. Data Nucl. Data Tables* **2002**, *82*, 257.
- [135] Zheng, X. W.; Xie, Y.; Zhu, L. Y.; Jiang, X. C.; Jia, Y. B.; Song, W. H.; Sun, Y. P. Growth of Sb₂E₃ (E=S, Se) Polygonal Tubular Crystals via a Novel Solvent-Relief-Self-Seeding Process. *Inorg. Chem.* **2002**, *41* (3), 455-461.
- [136] Grinter, D. C.; Remesal, E. R.; Luo, S.; Evans, J.; Senanayake, S. D.; Stacchiola, D. J.; Graciani, J.; Sanz, J. F.; Rodriguez, J. A. . Potassium and Water Coadsorption on TiO₂(110): OH-Induced Anchoring of

Potassium and the Generation of Single-Site Catalysts. *The Journal of physical Chemistry Letters* **2016**, *7*, 3866-3872.

[137] Davis, L. E. Handbook of Auger Electron Spectroscopy: A Reference Book of Standard Data for Identification and Interpretation of Auger Electron Spectroscopy Data. **1976**, . .

[138] M. Vasilopoulou, A. M. Douvas, D. G. Georgiadou, L. C. Palilis, S. Kennou, L. Sygellou, A. Soultati, I. Kostis, G. Papadimitropoulos, D. Davazoglou, P. Argitis. The Influence of Hydrogenation and Oxygen Vacancies on Molybdenum Oxides Work Function and Gap States for Application in Organic Optoelectronics. *J. Am. Chem. Soc.* **2012**, *134*, 16178.

[139] Xu, K. Q.; Xu, D. F.; Zhang, X. C.; Luo, Z.; Wang, Y. T.; Zhang, S. Y. Visible-light Activity of N-LiInO₂: Band Structure Modifications through Interstitial Nitrogen Doping. *Appl. Surf. Sci.* **2017**, *391*, 645-653.

[140] Hoppe, R.; Sabrowsky, H. . Uber Scandate, Ytrate, Indate und Thallate der Alkalimetalle. *Zeitschrift fiir anorganische nnd allgenieine Chemic* **1968**, *357*, 202-214.

[141] Sato, J.; Kobayashi, H.; Saito, N.; Nishiyama, H.; Inoue, Y. . Photocatalytic Activities for Water Decomposition of RuO₂-loaded AlnO₂ (A = Li, Na) with d¹⁰ Configuration. *J. Photochem. Photobiol.* **2003**, *158*, 139-144.

[142] Kawakami, S.; Sasaki, M.; Tabata, H.; Shimooka, H.; Kohiki, S.; Matsushima, S.; Oku, M.; Shishido, T. . Comparison of Electronic Structure of LiInO₂ with NaInO₂. *J. Alloys Compd.* **2003**, *359*, 278-280.

[143] Bharathy, M.; Zhao, Q.; Loye, H.-C. Zur. Crystal Growth of KInO₂ from A Hydroxide Flux. *J. Cryst. Growth* **2010**, *312*, 3533-3535.

[144] Hsiao, Y. J.; Chang, S. C. Photoluminescent Properties of LiInO₂ Nanocrystals. *Mater. Lett.* **2011**, *65*, 2920-2922.

[145] Gan, J. Y.; Lu, X. H.; Wu, J. H.; Xie, S. L.; Zhai, T.; Yu, M. H.; Zhang, Z. S.; Mao, Y. C.; Wang, S. C. I.; Shen, Y.; Tong, Y. X. . Oxygen Vacancies Promoting Photoelectrochemical Performance of In₂O₃ Nanocubes. *Sci. Rep.* **2013**, *3*, 1021.

[146] Ruckh, M.; Schmid, D.; Kaiser, M.; Schaiffler, R.; Walter, T.; Schock, H. W. . Influence of Substrates on the Electrical Properties of Cu(In,Ga)Se₂ Thin Films. *Sol. Energy Mater. Sol. Cells* **1996**, *41/42*, 335-343.

[147] Hautala, L.; Jänkälä, K.; Mikkilä, M.-H.; Tchapyguineb, M.; Huttulaa, M. Surface Site Coordination Dependent Responses Resolved in Free Clusters: Applications for Neutral Sub-Nanometer Cluster Studies. *Phys. Chem. Chem. Phys.* **2015**, *17*, 7012-7022.

[148] Delouise, L. A. Investigation of the Mechanism of Ar⁺ Ion-assisted Cl₂ Etching of GaAs{110}: Role of Ion-induced Charge Acceptor States. *J. Appl. Phys.* **1991**, *70*, 1718-1729.

[149] Krix, D.; Nienhaus, H. Low-temperature Oxidation of Alkali Overlayers: Ionic Species and Reaction Kinetics. *Appl. Surf. Sci.* **2013**, *270*, 231-237.

[150] Hwang, C. C.; An, K. S.; Park, R. J.; Kim, J. S.; Lee, J. B.; Park, C. Y.; Lee, S. B.; Kimura, A.; Kakizaki, A. . Cesium Core Level Binding Energy Shifts at the O₂/Cs/Si(113) Surface. *J. Electron. Spectrosc. Relat. Phenom.* **1998**, *88-91*, 733-739.

[151] Wang, Y.; Lang, X.; Zhao, G.; Chen, H.; Fan, Y.; Yu, L.; Ma, X.; Zhu, Z. Preparation of Cs-La-Sb/SiO₂ Catalyst and Its Performance for the Synthesis of Methyl Acrylate by Aldol Condensation. *RSC Adv.* **2015**, *5*, 32826-32834.

[152] Satoh, K.; Takahashi, T.; Katayama-Yoshida, H.; Sagawa, T. Bound States in Copper-Based Cu-Ge and Cu-Se Alloys Studied by X-Ray Photoelectron Spectroscopy. *J. Phys. Soc. Jpn.* **1985**, *54*, 1214-1215.

- [153] Lundgren, E.; Andersen, J. N.; Qvarford, M.; Nyholm, R. Layer Dependent Core Level Binding Energy Shifts: Na, K, Rb and Cs on Al(111). *Surf. Sci.* **1993**, *281*, 83-90.
- [154] Oelhafen, P.; Dürrwächter, M.; Indlekofer, G.; Boyen, H.-G. Surface Core Level Shifts in Liquid Metals and Alloys. *Journal of Non-Crystalline Solids* **1993**, *156-158*, 219-225.
- [155] Ohashi, T.; Saito, Y.; Maruyama, T.; Nanishi, Y. Effect of Atomic Hydrogen Irradiation on Native Oxides of InN Surface. *J. Cryst. Growth* **2002**, *237-239*, 1022-1026.
- [156] Fanettia, M.; Mikulskaa, I.; Ferfoljaa, K.; Morasc, P.; Sheverdyaevac, P. M.; Panigheld, M.; Lodirizzinid, A.; Piš, I.; Nappinie, S.; Valanta, M.; Gardonio, S. Growth, Morphology and Stability of Au in Contact with the Bi₂Se₃(0001) Surface. *Appl. Surf. Sci.* **2018**, *471*, 753-758.
- [157] Peters, J. L.; Van Der Bok, J. C.; Hofmann, J. P.; Vanmaekelbergh, D. Hybrid Oleate-Iodide Ligand Shell for Air-Stable PbSe Nanocrystals and Superstructures. *Chem. Mater.* **2019**, *31*, 5808-5815.
- [158] Shin, S. W.; Gurav, K. V.; Gang, M. G.; Suryawanshi, M. P.; Patil, P. S.; Agawane, G. L.; Jeoung, C. H.; Yun, J. H.; Lee, J. Y.; Kim, J. H. Correlation between Soft Annealing Conditions and Structural, Microstructural, Morphological, and Optical Properties of CuInS₂ Thin Films Prepared by Sulfurization of Stacked Precursor. *J. Cryst. Growth* **2014**, *394*, 49-54.
- [159] Meedera, A.; Weinhardt, L.; Stresing, R.; Fuertes Marron, D.; Wurz, R.; Babu, S. M.; Schedel-Niedrig, T.; Lux-Steiner, M. Ch.; Heske, C.; Umbach, E. Surface and Bulk Properties of CuGaSe₂ Thin Films. *J. Phys. Chem. Solids* **2003**, *64*, 1553-1557.
- [160] Jiang, P.; Prendergast, D.; Borondics, F.; Porsgaard, S.; Giovanetti, L.; Pach, E.; Newberg, J.; Bluhm, H.; Besenbacher, F.; Salmeron, M. Experimental and Theoretical Investigation of the Electronic Structure of Cu₂O and CuO Thin Films on Cu(110) Using X-ray Photoelectron and Absorption Spectroscopy. *J. Chem. Phys.* **2013**, *138*, 024704.
- [161] McIntyre, N. S.; Cook, M. G. X-Ray Photoelectron Studies on Some Oxides and Hydroxides of Cobalt, Nickel, and Copper. *Analytical Chemistry* **1975**, *47*, 2208-2213.
- [162] Li, X. W.; Shao, C. L.; Lu, D. X.; Lu, G. Y.; Li, X. H.; Liu, Y. C. Octahedral-Like CuO/In₂O₃ Mesocages with Double-Shell Architectures: Rational Preparation and Application in Hydrogen Sulfide Detection. *ACS Appl. Mater. Interfaces* **2017**, *9*, 44632-44640.
- [163] Rieke, R. D. Preparation of Highly Reactive Metal Powders and Their Use in Organic and Organometallic Synthesis. *Reactive Metal Powders* **1977**, *10*, 301.
- [164] Bombsh, J. Ph. D thesis in progress. Friedrich-Alexander-Universität Erlangen-Nürnberg, 2019.
- [165] Alay-E-Abbas, S. M.; Sabir, N.; Saeed, Y.; Shaukat, A. Electronic and Optical Properties of Alkali Metal Selenides in Anti-CaF₂ Crystal Structure from First-principle. *J. Alloys Compd.* **2010**, *503*, 10-18.
- [166] Ward, M. D.; Pozzi, E. A.; Van Duyne, R. P.; Ibers, J. A. Syntheses, Structures, and Optical Properties of the Indium/Germanium Selenides Cs₄In₈GeSe₁₆, CsInSe₂, and CsInGeSe₄. *J. Solid State Chem.* **2014**, *212*, 191-196.
- [167] Huang, F. Q.; Deng, B.; Ellis, D. E.; Ibers, J. A. Preparation, Structures, and Band Gaps of RbInS₂ and RbInSe₂. *J. Solid State Chem.* **2005**, *178*, 2128-2132.

Acknowledgements

First, I would like to thank my supervisors Prof. Dr. Marcus Bär who accepted me as a PhD student, for his continued guidance, patience and support throughout this work. He had always an open door for data discussion and all the other problems. Furthermore, he provided me with the possibilities to measure at different synchrotrons and .

I am thankful to Dr. Regan Wilks for his many helpful insights in analyzing and improving the presentation of data, and for always being available to provide me feedback during the writing of this work. I am also grateful Jan-Hendrik Alsmeier who introduced me to the field of the solar cell research. Also, I have to thank all those (Dr. Roberto Felix, Dr. Leonard Köhler, Dr. Evelyn Handick, Dr. Claudia Hartmann) who have helped me in carrying out the research and given me invaluable guidance. I also want to thank all the past and present members of the “Interface Design” Department.

I am grateful to Dr. Patrick Reinhard, Dr. Stephan Buecheler, and Prof. Dr. Ayodhya N. Tiwari from Laboratory of Thin Films and Photovoltaics at Empa-Swiss Federal Laboratories for Materials and Science and Technology for providing me with the PDT sample series. I would also like to thank Dr. Dieter Greiner and Dr. Christian Kaufmann from PVcomB, Helmholtz Zentrum Berlin für Materialien und Energie GmbH for providing the chalcopyrite samples.

I gratefully acknowledge the financial support from Chinese Scholar Council (CSC) and HZB Association.

Finally, I want to thank my parents, my brother and those friends who all had an open ear for my problems and kept me optimistic through all the failures from the work as a Ph.D. student.